MASS AND OPTICAL SPECTROSCOPY OF $CF_4 + O_2$ PLASMAS AND THEIR APPLICATION TO THE ETCHING OF Si, Ge AND SiGe ALLOYS

by

Robert J. Chatfield

A thesis submitted to the University of Bristol in accordance with the requirements for the degree of Doctor of Philosophy in the faculty of Science, Department of Physical Chemistry.

March 1993

ABSTRACT

CF_4 + O_2 plasmas are widely used to etch Si in VLSI technology. Despite many investigations, much remains to be learnt of the important chemical mechanisms. We have applied Quadrupole Mass Spectrometry (QMS) with capillary sampling and Optical Emission Spectroscopy (OES) simultaneously to study this system and included the etching of Ge and SiGe alloys. The approach used was to fully characterise CF_4 + O_2 plasmas with no wafer present and then to introduce Si, Ge and SiGe substrates. SiGe alloy has recently come into prominence because it shows promise for the production of fast-switching Heterojunction Bipolar Transistors and novel optoelectronic devices.

Our investigations were carried out using a single slice 13.56 MHz Reactive Ion Etcher (Omega, Electrotech) under a variety of conditions of flow rate, power, pressure and substrate area, and also with small additions of O_2, CO, CO_2 and C_2F_6 to the process gas. For each set of conditions, detailed measurements of the plasma composition were made. Using QMS, the absolute concentrations of CF_4, O_2, CO, CO_2, C_2F_6, COF_2, F_2, SiF_4 and GeF_4 were determined by applying appropriate correction factors. In addition, OES observations in the range 6200 Å to 7400 Å allowed the measurement of emission intensities from F atoms in a variety electronically excited states.

A kinetic model involving 53 gas phase and surface reactions was constructed for the CF_4 + O_2 system with no wafer present. Using steady state considerations, it was possible to calculate [CF_3] and [F] from the QMS results over a wide range of experimental conditions. Calculations of [F] agree with trends observed by OES, but only when wall reactions involving F are included in the model. These wall reactions are shown to be inhibited by the presence of O atoms, because O atoms compete with F atoms for surface sites. The kinetic model was then tested for one specific set of conditions (40 sccm, 100 W and 85 mTorr) to see if it could reproduce the concentrations of species measured experimentally. Only 17 of the original 53 reactions are found to be important. This test also reveals the main chemical pathways, and demonstrates the importance of certain wall reactions, which when included in the model allow product distributions to be reproduced to within a factor of 3.

Si and Ge wafers were etched at various conditions of flow rate, power, pressure and exposed wafer area. Typical etch rates lie in the 1000 to 3000 Å min^{-1} range for 3" wafers, with the Ge etch rate always faster than that of Si, typically by a factor of around 1.3. The results indicate that the etching mechanisms for Si and Ge are similar, although the etching of Si relies more on ion bombardment than does the etching of Ge. F atoms are the main etchant species for both Si and Ge, and the only observed products of etching were SiF_4 and GeF_4. The Si budget is present almost exclusively as SiF_4, whereas up to 40 % of the Ge budget is present as Ge-containing species adsorbed at the chamber walls. The well-known fall in F atom emission intensity on the introduction of a wafer to the plasma is found not to be due to the direct removal of F atoms by reactions at the wafer surface during the etching process, as was previously thought. The effect is shown instead to be due to a reduction in the effective fluorine-to-carbon ratio in the plasma caused by the etching process. This results in a change in the composition of the plasma, which in turn results in an increase in the removal rate of F atoms via fast reactions in the gas phase and at the chamber walls. A mechanism is proposed which explains qualitatively the changes in the plasma composition observed by QMS when a wafer is introduced to the chamber.

OES studies show that emission from different electronically excited states of F atoms behaves differently when the experimental conditions are altered. Specifically, emission from the two halves of the 3p $^2P°$ doublet behave differently from each other, and also from all the other states observed which all exhibit the same behaviour. This observation is shown to be linked to changes in [O_2] in the gas phase; the emission from the 3p $^2P°$ states is relatively stronger in the presence of O_2. It is proposed that this effect is caused by resonant energy transfer from excited O_2 molecules in the $^1\Phi_u$ state, which has similar energy to the 3p $^2P°$ states of F. In the presence of O_2, this process competes with electron impact processes for the production of these two excited states. The magnitude of the effect is observed to be 1.8 ± 0.3 times stronger for the 3p $^2P°_{3/2}$ state than for the 3p $^2P°_{1/2}$ state. This figure is correctly predicted by calculations.

Studies into the etching of SiGe alloy layers on Si wafers with 33 and 67 mol % Ge content have also been undertaken over a wide range of experimental conditions. The purpose was to see if SiGe alloy material exhibits etching behaviour which is consistent with a simple mixture of its Si and Ge component parts, or whether it shows unexpected behaviour. We find that SiGe alloy shows the expected etching behaviour for all the conditions studied, except at low power (20 W, 85 mTorr, 5 sccm) where it exhibits novel fast etching, with corresponding changes in the gas phase composition of the plasma, viz. lower [F] and higher [C_2F_6]. The problems of endpoint detection and process control, which are crucial for the fabrication of devices, have also been addressed. It is clear that QMS monitoring can cope with both of these problems. It has also been shown that species suitable for endpoint detection must be found after the process has been optimised, because the changes observed in species concentration at the endpoint are a strong function of the experimental conditions.

How awkward is the human mind in divining the nature of things when forsaken by the analogy of what we see and touch directly.

Ludwig Boltzmann

ACKNOWLEDGEMENTS

I would firstly like to thank my supervisers Dr. D. Field and Dr. D.F. Klemperer for their help and advice throughout this work. I am particularly grateful for their expert comments and suggestions during the write up, and for the time which they have so willingly devoted to proof-reading this thesis.

There are several other people who have provided invaluable assistance during this work, without whom it all would have been much more difficult. Special thanks therefore go to Paul May, for many valuable discussions and for his friendly encouragement and continual interest in my work, to Mike Ashfold for helpful advice on spectroscopy, and also to Yiping Song, for teaching me to use some of the equipment and helping me to find my feet, and also for his friendship in the initial stages of this work.

During my time at Bristol, my life has been made much more enjoyable by those I have worked alongside, especially Andy Dickenson, Kevin Jones, Ian Hedgecock, Steve Morley and Malcolm Gray. I would like to give a mention as well to John Dunne, Austin Day, Robert Jones, Ian Wade and Ed Crewe, who also spent time in the lab while I was there.

The excellent technical support I have received from the mechanical, electrical, and glass workshops in the Chemistry Department at various stages of this work is gratefully acknowledged. Special thanks go to Gwyn Jones and to Tony Butler for their friendly advice and practical assistance, and also for their willingness to drop everything when I had problems. I am also grateful to Laurie Burbridge at the University computer centre for introducing me to the LOTUS 123 and FREELANCE software packages.

I am very grateful to Electrotech for ceding us the Omega RIE system and for providing materials, and also to VG Quadrupoles for extending the loan on the SX200 QMS to allow me to complete my work. I would like to make special mention of Jonathan Batey and Danny Smith of VG Quadrupoles for helpful discussions concerning mass spectrometry.

This work was made possible by the financial and material support of both the SERC and British Telecom Laboratories, Martlesham Heath, which I gratefully acknowledge. I would especially like to thank Derek Godfrey at BTL for his friendly advice and encouragement, and also Chris Gibbings and Chris Tuppen for growing the SiGe alloy layers for me to etch. I really enjoyed my stay at BTL, largely because of the great people I met there, particularly Scott M^{c}Rae, Simon Martin, Elizabeth Vigrass and Tony Reeder, whose company and friendship I appreciated greatly. The people in the coffee club in B40 also deserve a mention for their general good humour and famous cynicism!

I would also like to thank my family, especially my Mum and Dad, who have always taken an interest in how I've been getting on, both at work and in life in general. Special thanks should also go to Debbie for her continuing friendship and encouragement. Most of all I would like to thank Sophie, for keeping me going towards the end and for just being there with me through the difficult times. Her support throughout has been veritably cornucopic! Sophie also has the effect of making the good times absolutely wonderful, and I know that this will continue long into the future.

To mum and dad.

MEMORANDUM

The research described in this thesis was carried out by the author in the Department of Physical Chemistry at the University of Bristol under the supervision of Dr. D. Field and Dr. D.F. Klemperer.

All the work reported here is original to the author except where acknowledged by reference or special recognition. No part of this work has been submitted previously for any degree.

R. J. Chatfield

CONTENTS

CHAPTER 1

INTRODUCTION

1 INTRODUCTION

1.1 INTRODUCTION

We live in an age where semiconductor technology pervades almost every aspect of our lives, from telecommunication and computers to the most basic electronic appliances. This situation is the result of what might almost be described as the second industrial revolution, which began in 1949 with the invention of the first semiconductor transistor. In 1959, the *planar process* was developed, allowing the production of *integrated circuits*, in which many electronic devices are built simultaneously into and out of a single piece of semiconductor material, and then electrically connected together. This technology has since showed explosive expansion, with individual devices becoming increasingly complex, and also ever-smaller in size so that now, well over a million transistors are now readily produced on a single small piece of semiconductor material, or *chip*. This high level of sophistication places ever more stringent demands on the processing steps required to make such devices. One of these steps is called *reactive ion etching*. This is the process of interest in this thesis.

Reactive ion etching (RIE) is a process in which a radio frequency electrical discharge through a suitable gas is used to create a "soup" of reactive species, called a *plasma*. The species in the plasma react with and remove selected areas of the surface of a wide variety of materials relevant to the manufacture of integrated circuits. Because of the inherent complexity of RIE systems, technological advances have been made primarily by an empirical approach. This has resulted in the current state of affairs where the technological achievements far outweigh the level of scientific understanding. Indeed, RIE is often referred to as a "black art" rather than a science! Our purpose is to gain a greater understanding of (some of) the processes which occur during RIE, and so to "put some science back into the technology."

Before we discuss RIE in more detail, we first explain some of the basics of semiconductor technology, and how the integrated circuits mentioned above are fabricated. This will enable the important role played by RIE to be more clearly understood.

1.2 SEMICONDUCTOR TECHNOLOGY [1], [2]

We begin by explaining the electrical properties of semiconductors which set them apart from other materials. We will then continue in section 1.2.4 by explaining how these properties are exploited in the manufacture of electronic devices, using Si technology as an example.

1.2.1 METALS, INSULATORS AND SEMICONDUCTORS

Metals, insulators and semiconductors are distinguished by their ability to conduct an electric current. Electric current is passed through a solid by virtue of electrons moving from atom to atom. The electrons within each atom can only exist within certain energy levels, as dictated by Quantum mechanics. In a solid, the allowed energy levels form two continuous bands, which are referred to as the *valence band* and the *conduction band*. In general, the valence band consists of bonding orbitals and the conduction band consists of antibonding orbitals. Electrons in the valence band thus form the interatomic bonds which hold the solid together. The conductivity of a solid is determined by the energy difference between these two bands, called the *band gap*, and also the number of electrons which occupy them. In order for conduction to occur, the electrons in the solid must possess sufficient energy to move into an unoccupied energy level of a neighbouring atom.

Metals. In metals, the valence and conduction bands overlap (i.e. the band gap is zero) forming a single energy band, which is not completely filled with electrons. Thus the electrons in the highest occupied energy level need to acquire little energy to move into the next higher energy level and so be able to pass freely throughout the solid. Metals are therefore good conductors of electricity.

Insulators. In insulators, the valence band is completely filled with electrons, so in order to move in the solid they have to be promoted into the conduction band. However, the band gap in this case is substantial (several eV), so that at normal temperatures, the electrons do not possess enough energy to reach the conduction band. This means that insulators cannot conduct electricity.

Semiconductors. Semiconductors have a conductivity which lies between that of metals and insulators. The band gap in this case is typically around 1 eV. (Silicon has a band gap of 1.1 eV). At absolute zero, the valence band is full, and semiconductors behave as insulators. However, at temperatures greater than this, some electrons have sufficient energy to reach the conduction band and therefore are free to respond to an applied electric field, so allowing the passage of a small electric current. In addition, the promoted electrons leave behind them vacancies or *holes* (i.e. the absence of an electron) which act as positively charged particles. These may also respond to an electric field and allow the passage of an electric current. The conduction properties of semiconductors may be modified by the incorporation of impurities into the crystal lattice. This process is called *doping*. Since this thesis is concerned primarily with Si based technology, we will use Si as an example in the following discussions.

1.2.2 DOPING OF SILICON

We now consider what happens when impurities are incorporated into the Si lattice. Si atoms have 4 valence electrons, all of which are used to form the bonds which hold the lattice together, so that the valence band is full (as mentioned above). However, if for example P atoms (which have 5 valence electrons) are added to the Si lattice, the extra electrons go into the conduction band. These electrons are therefore free to move throughout the solid, allowing the Si to conduct electricity more readily. In this case, the majority charge carriers are negatively charged electrons, and the material is referred to as an *n-type* semiconductor. Alternatively, if B atoms are added (with 3 valence electrons), the effect is to reduce the number of electrons in the valence band, introducing holes. This

also has the effect of increasing the conductivity of Si. Here, the majority charge carriers are positively charged holes, and the material is a *p-type* semiconductor.

1.2.3 THE PN JUNCTION

We now consider what happens when a piece of p-type Si is brought into contact with a piece of n-type Si (see figure 1.1a). As soon as the junction is formed, some of the electrons in the n-type Si move across the boundary to fill the holes on the p-type side. In doing so, they produce a negative charge on the p-type side and leave behind a positive charge on the n-type side. This build up of charge results in a potential difference which opposes further migration of electrons. Eventually a state of equilibrium is reached, such that the region of the boundary is depleted of both holes and electrons. This region is called the *depletion layer*, and is typically < 1 μm wide.

Consider what happens when a voltage is applied to this system. In figure 1.1b, the voltage is such that the majority carriers are attracted out of the depletion layer, causing it to widen (*reverse bias*). Conduction is now small as it can now only occur via minority carriers. If the voltage is reversed (figure 1.1c), the depletion layer is narrowed and conduction is facilitated (*forward bias*). This system is therefore behaving as an electric diode (or rectifier).

This example has demonstrated that Si may be used to fabricate useful electrical devices. We now describe how transistors may also be produced from Si semiconductor material.

1.2.4 THE FABRICATION OF TRANSISTORS OUT OF Si

The bipolar transistor. Consider a system of two pn junctions sandwiched together as in figure 1.2a. Electrons in the two n-type layers will migrate and recombine with the holes in the p-type layer, forming a negative charge in the *base* (p-type layer). If a potential difference is applied between the *emitter* and the *collector*, only a small current will flow

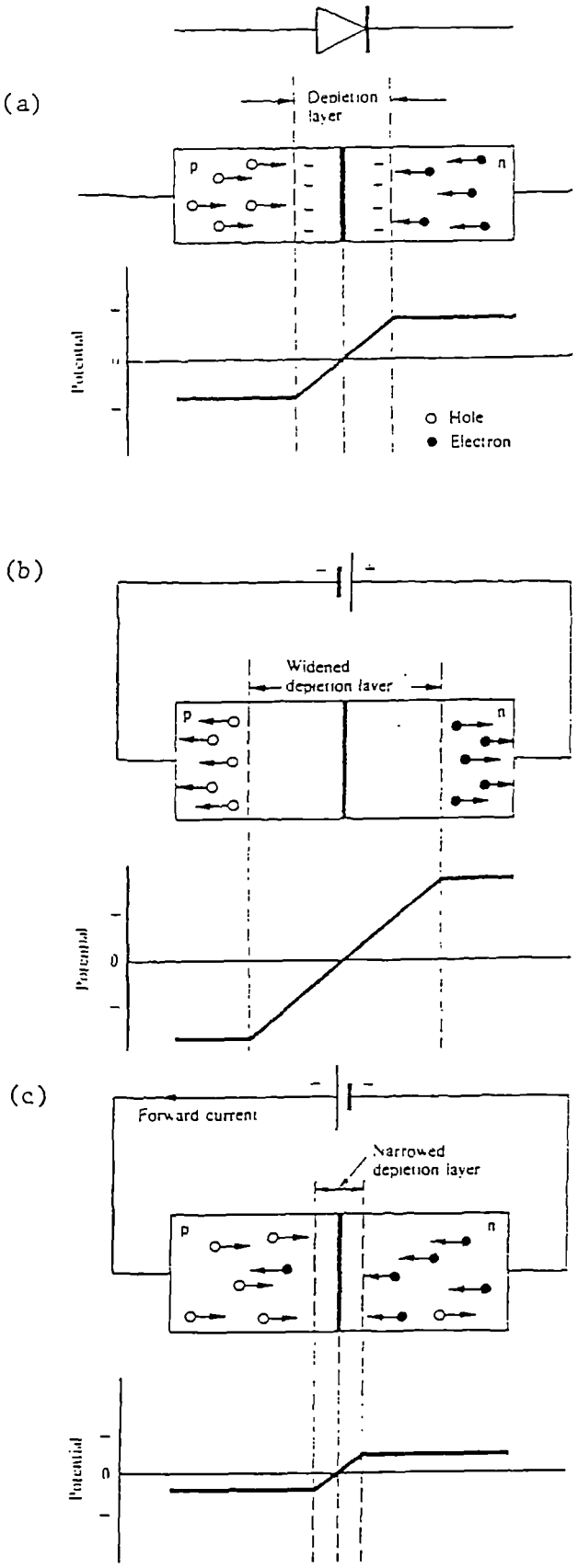

Figure 1.1. (a) The pn junction, showing the depletion layer and the variation of potential. (b) and (c) show the effect of an external DC potential on the depletion layer. The pn junction acts as an electric diode, the schematic symbol for which is shown at the top of this figure.

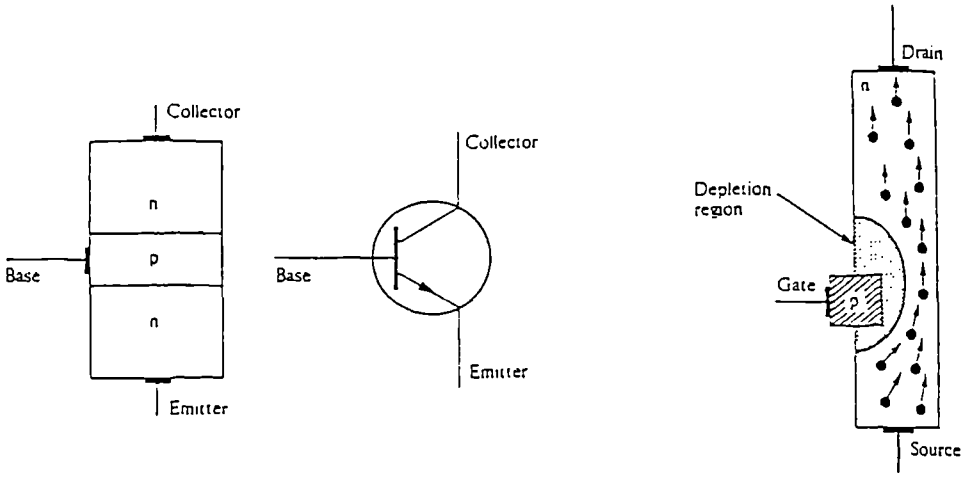

(a) (b)

Figure 1.2. (a) The npn transistor: construction and circuit diagram. (b) The unipolar or field effect transistor (FET), showing electron flow along the n-channel.

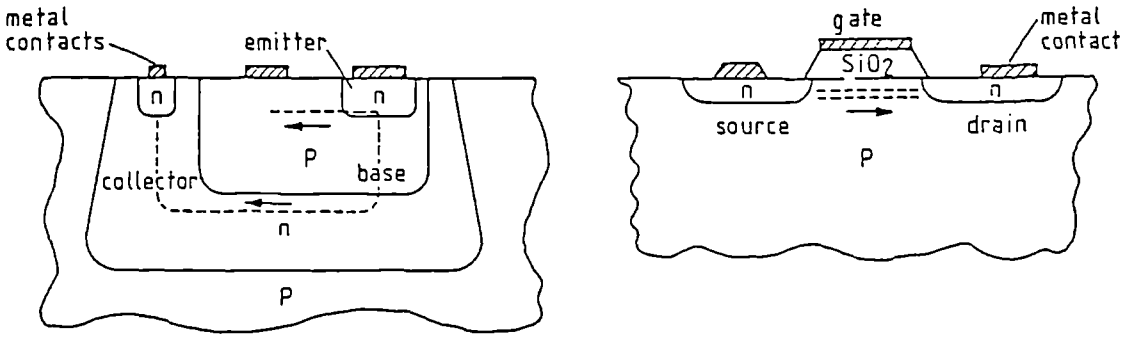

(a) (b)

Figure 1.3. Cross-sections of operational transistor devices, built into and out of the Si lattice. (a) shows a bipolar transistor, and (b) shows a MOS transistor, which is a unipolar device.

because the negatively charged base forms a potential "hill". However, if a small positive voltage is applied to the base, then the electrons forming the potential hill are depleted, reducing the size of the hill and so allowing a larger current to pass. Thus the small base voltage can be used to control the larger emitter-collector current. This system constitutes a transistor. Another type of transistor is the unipolar transistor.

The unipolar transistor. The unipolar or field effect transistor (FET) is shown schematically in figure 1.2b. Here, current may flow from *source* to *drain*, unless a small positive voltage is applied to the *gate*. In this case, the applied voltage causes the depletion layer to grow thicker, encroaching into the n-channel and so reducing the source-drain current. Again, a small voltage may be used to control a large current.

A transistor possesses two useful properties, which will make their importance readily apparent.

1) It can act as an amplifier, since a smaller voltage is used to control a larger one.

2) It can act as a very fast switch. Many transistors coupled together in a logic array lead to digital electronics and computers.

Both of the devices described above can be fabricated out of and into a single piece of Si by selectively doping the n- and p-type regions. Some more realistic devices are shown in cross section figure 1.3, and may be compared to the schematic versions shown in figure 1.2. The MOS transistor shown in figure 1.3b is a unipolar device. (MOS denotes metal-oxide-semiconductor).

1.3 INTEGRATED CIRCUITS [3, 4]

Many electronic devices such as those described section 1.2.4 can be created simultaneously from a single piece of silicon. These devices can then be inseparably connected in order that together they perform a specific useful function. The finished item

constitutes an *integrated circuit* (IC). IC's are formed by a method called *planar processing*.

1.3.1 PLANAR PROCESSING FOR IC FABRICATION

Planar processing was first used by Kilby [5] in 1959 to make the first IC. The process was later developed by Noyce and Moore [6, 7], and is now the major production method for Si IC's. Planar processing involves the fabrication of many layers of materials with different electrical properties, which are then patterned so that the entire structure forms all the various circuit elements including rectifiers, transistors, resistors and capacitors. These circuit elements are finally connected together by a patterned conducting layer (the interconnect) to make the finished IC. The fabrication process may involve up to 15 layers and up to 200 processing steps [8].

1.3.2 STARTING MATERIALS

IC's are fabricated on single-crystal wafers of semiconductor material. Si wafers are manufactured from raw silica by the *zone refinement* method [9]. Single crystal ingots are then grown by the Czochralski [10] or the floating zone [11] method. The ingot is then sawn into thin wafers which are then lapped, polished and chemically cleaned to produce a mirror finish. Si wafers are usually around 0.5 mm thick, and the diameter has increased from 75 mm to 200 mm over the last ten years.

1.3.3 PROCESS STEPS

In this section, we describe briefly the main steps involved in planar processing. These include film formation, doping and implantation, photolithography and etching, all of which may be repeated many times during the manufacture of a single chip. We then take the example of the fabrication of an MOS transistor on a Si wafer, as shown in figure 1.3b, in order to illustrate how the processing steps are used to create finished devices.

1.3.3.1 FILM FORMATION

An important requirement in each cycle of the fabrication process is the formation of thin films of different materials on the wafer surface. SiO_2 layers can be formed on the Si wafers by simply oxidising the surface in an oven with O_2 or steam flowing through it. However, all other layers must be made by alternative means. Some of the more common methods used are described below.

Spin-on and spray-on processes. These methods involve the use of suitable reagents dissolved in a carrier solvent. This mixture is applied to the wafer surface either as a spray, or alternatively it is poured onto the centre of a rapidly spinning wafer. When the solvent evaporates, the reagents can react to produce the required film. This is the method generally used for the application of photoresist (section 1.3.3.3), but is now rarely used for other films as a result of various practical difficulties.

Chemical Vapour Deposition (CVD) [12]**.** CVD is the most commonly used method for thin film formation. Using this technique, suitable reactive gases are brought together over a hot substrate wafer on which they react to form a solid thin film. The stoichiometry of the film may be accurately controlled by adjusting the proportions of the reactant gases. CVD is performed either at Atmospheric Pressure (APCVD) or at Low Pressures of 0.1 to 1 Torr (LPCVD), with each pressure regime having its own advantages and disadvantages. A more recent advance is Plasma Enhanced CVD (PECVD), in which a plasma is used to increase the film deposition rates of standard CVD processes. Another addition is Metal-Organic CVD (MOCVD), which involves the pyrolysis of a vapour phase mixture of reactants which includes a volatile organometallic reagent.

Sputtering [13]**.** Using this technique, a suitable target material is bombarded by high energy inert gas ions (usually Ar^+) in a vacuum chamber, causing sputtering of target atoms. The sputtered atoms then deposit onto a nearby substrate wafer, gradually forming a thin film. Sputtering is often used to grow metallic films.

Evaporation. In this technique, the target material is heated to high temperatures in a vacuum chamber, causing atoms to evaporate. The vaporised atoms then condense onto a nearby substrate wafer as in the sputtering technique above. As with sputtering, this method is useful for the formation of metallic films.

Molecular beam epitaxy (MBE) [14]. This technique is finding an increasing number of applications because of its ability to produce very thin films (down to monolayer thickness) of elements, compounds and alloys. The MBE technique employs effusive beams of thermal energy atoms and molecules which impinge onto a heated substrate wafer under ultra high vacuum conditions. The films formed in this way are epitaxial, that is, the film adopts the crystal structure of the substrate rather than forming an amorphous layer or adopting its own usual crystal structure. The film composition may be accurately controlled by co-evaporating several different materials simultaneously and allowing them to impinge on the same substrate. This technique may be used, for example, to produce SiGe alloy epitaxial layers (section 1.4) with variable composition onto a Si substrate, using Si and Ge effusive beam sources [15].

1.3.3.2 DOPING AND IMPLANTATION

Having produced the thin films, it is then necessary to ensure that the films have the correct electrical properties, in terms of type (i.e. holes or electrons) and degree of conductivity. This is achieved by the process of doping (see section 1.2.2). Until recently, dopant material was introduced into the semiconductor lattice using high temperature diffusion techniques. Dopant material was first deposited onto the semiconductor surface, and then caused to diffuse into the film by a *drive-in* step. This involved heating the substrate to a high temperature (typically around 1000°C). However, as device dimensions have fallen, it has become increasingly important to control more accurately the precise dopant concentration profiles. The preferred technique for dopant introduction is now ion implantation.

In the ion implantation technique, the substrate is bombarded by dopant ions with energies in the range one to several hundred keV, which then penetrate the layer surface. The areas to be implanted are defined by a masking layer such as SiO_2 or photoresist. Using this technique, the dopant concentration and also the concentration profile may be carefully controlled by adjusting the ion current and ion energy. The implantation step is then followed by a high temperature anneal to repair any damage caused to the crystal lattice by the bombarding ions, and also to electrically activate the dopant (i.e. to ensure substitutional siting within the lattice). This is achieved by laser annealing to a very high temperature (typically > 1000 °C) for a short time period from 100 s down to ns, which is long enough to repair the damage to the lattice but short enough so that diffusion of the dopant is kept to a minimum. A typical ion implantation step is the introduction of B^+ ions into a Si lattice to produce a p-type layer [16].

1.3.3.3 PHOTOLITHOGRAPHY

The photolithography step defines the pattern which will later be transferred to the substrate by an etching step. The layout of all the devices on the chip is first designed on a large scale drawing, which is then reduced in size by a large camera to produce a real size template mask. The surface of the substrate is then coated with a thin layer of *photoresist* (or simply *resist*) and irradiated with UV light through the mask to print the pattern. The photoresist is made of light sensitive material which is either made more resistant (*negative* resist) or less resistant (*positive* resist) to chemical attack by a suitable solvent, called the *developer*. The irradiated wafer is then immersed in the developer, so that the exposed (or unexposed) areas of resist are removed, producing the pattern. Features on the resist pattern are typically 2-3 μm high with near vertical sidewalls. The patterned wafer is then baked in an oven typically at around 100 °C to harden the resist layer. The layer then serves as a mask for a subsequent etching step which will transfer the pattern to the wafer.

After the etching step, the resist pattern is removed either by immersing the wafer in a chemical bath (such as fuming nitric acid) or by exposing the wafer to an O_2 plasma (called *plasma ashing*).

1.3.3.4 ETCHING

Etching is the removal of material from the substrate surface. Only material which is not covered by the resist mask will be etched, so that the pattern is transferred to the underlying layer. The two main methods used are wet etching and dry etching.

1.3.3.4.1 WET ETCHING [3]

The wet etching process involves immersing the wafer in a bath of an appropriate solvent which reacts at the surface to produce a soluble product. This product will then dissolve into the bath, and so material is removed from the wafer surface. A useful feature of wet etching is that it can exhibit high *selectivity* for layers of different chemical composition. This means that the top layer may be removed without etching into the underlying layers. However, wet etching techniques tend to be *isotropic*. This means that etching proceeds at the same rate in all directions, so that the depth of the etch is around the same as the lateral etching distance, resulting in undercutting of the resist mask (figure 1.4a). For large features (say $> 10\ \mu m$) this poses no problem, but as devices grow smaller ($< 2\ \mu m$) wet etching can no longer provide the required feature resolution. This has led to the development of dry etching techniques, which are capable of providing the required directional or *anisotropic* etching (figure 1.4b). Wet etching is generally now only used for resist removal, cleaning steps or for large scale features.

1.3.3.4.2 DRY ETCHING

In dry etching, the wafer is generally brought into contact with a reactive gas which reacts with the surface to produce a volatile product. This product then evaporates, and so the surface is removed. Directional etching is obtained in dry etching techniques by

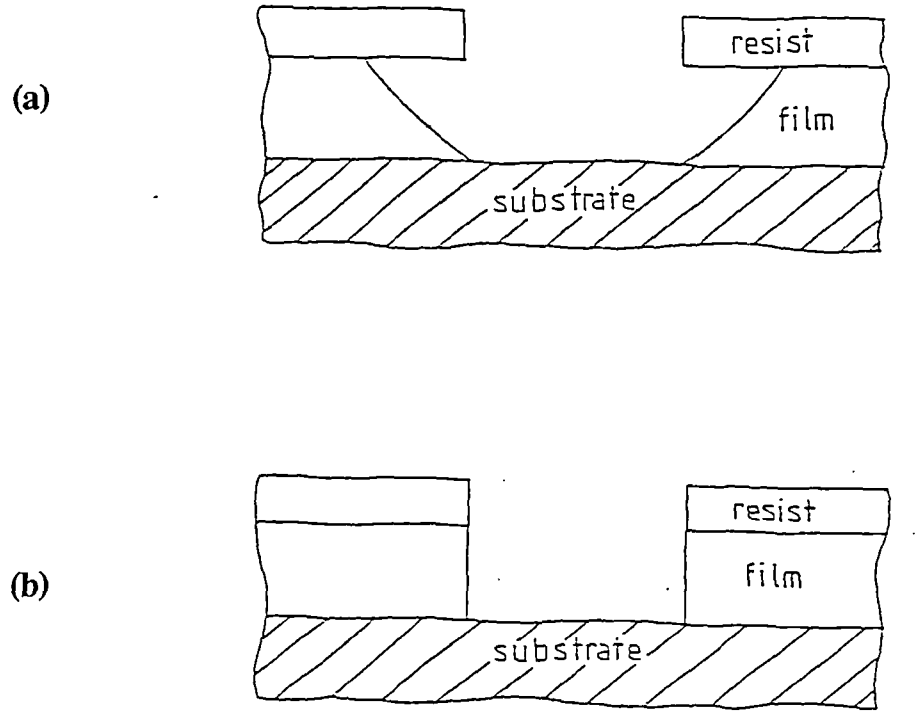

Figure 1.4. Sidewall profiles obtained after (a) isotropic and (b) anisotropic etching.

bombardment of the reacting wafer surface by high energy ions of normal incidence. This enhances the etch rate vertically but not laterally, allowing anisotropic etch profiles to be produced (figure 1.4b).

Other advantages of dry etching over wet etching techniques include the following. Firstly, there is no problem with uncontrolled overetching because etching stops as soon as the power source is switched off. Also, typical gases used for dry etching (e.g. freons and O_2) are cheaper and much safer to handle than wet etching chemicals, which also produce dangerous fumes and waste. In addition, dry etching is inherently much cleaner, which dramatically reduces wafer contamination. However, there are also a few disadvantages. The necessary equipment is very expensive, and etch selectivity is often difficult to obtain. In addition, the ion bombardment during etching can produce lattice damage, which may affect device performance. However, the advantages far outweigh the disadvantages, so that dry etching techniques are now used in almost every cycle of the IC fabrication process.

Dry etching techniques are generally classified according to the relative amounts of chemical and physical (ion enhanced) etching. Three broad headings are often used, which are *ion beam etching* (purely physical etching), *plasma etching* (mainly chemical) and *reactive ion etching* (chemical and physical), which is a development of plasma etching. A description of all these techniques will be given in section 1.5.

1.3.4 FABRICATION OF AN MOS TRANSISTOR

Having described the individual processing steps necessary for the fabrication of IC's, we now illustrate the fabrication process by the use of an example. We describe the fabrication of an MOS transistor (see section 1.2.4, figure 1.3b). This device gets its name from its basic layer structure, that is; Metal (the gate) on top of an Oxide dielectric on top of a Semiconductor substrate. (This name is still used, despite the fact that the "metal" gate is now made from highly doped polycrystaline Si, which is a good electrical conductor). The steps involved in MOS fabrication are illustrated in cross section in figure 1.5. The

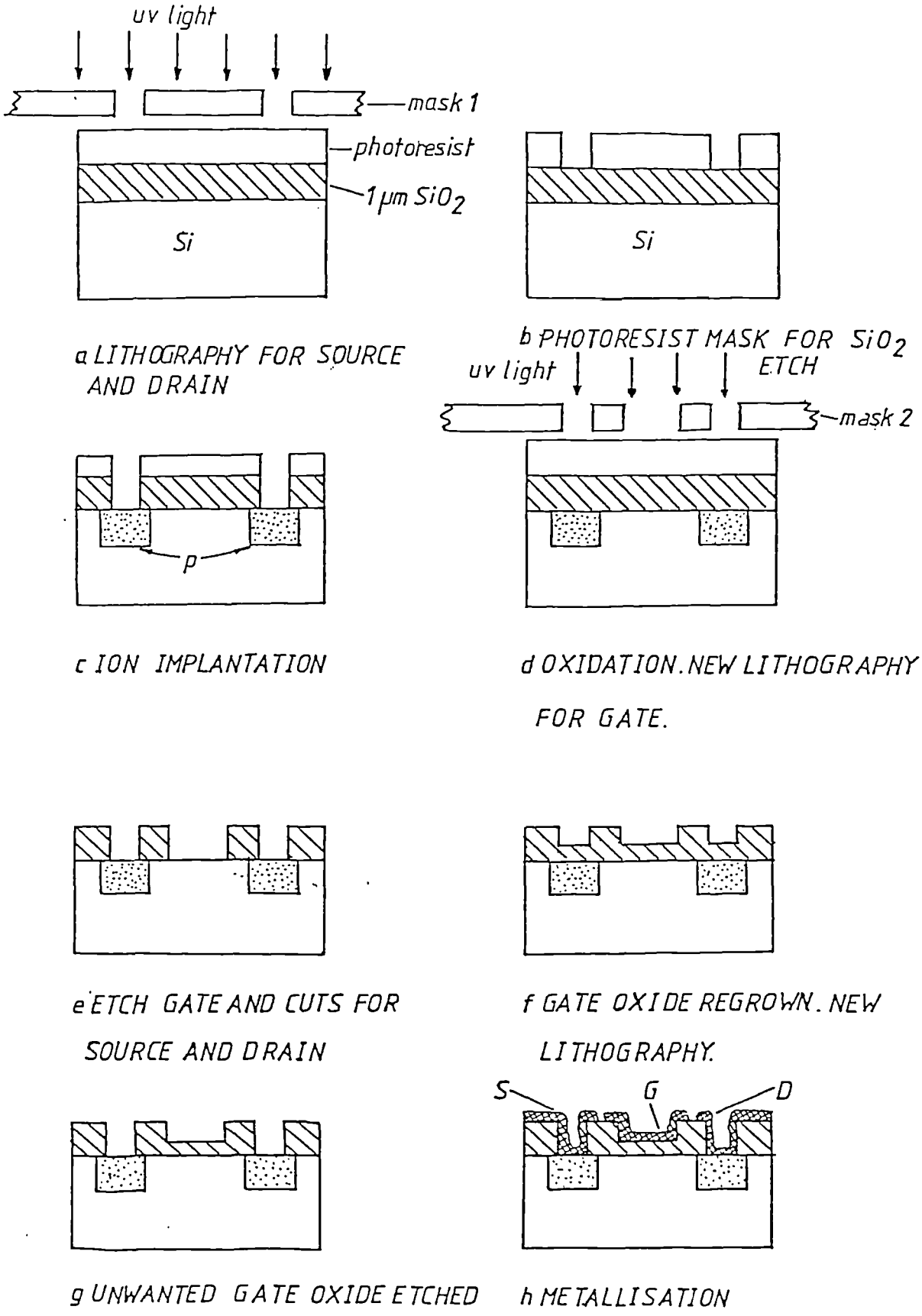

Figure 1.5. (a) to (h) show the process sequence used for the fabrication of a p-channel MOS transistor.

process starts with a resist layer on an SiO_2 layer on a Si wafer, and the process steps are described below.

Firstly, photolithography steps are performed in order to define the source and drain regions of the MOS transistor (Figures 1.5a and 1.5b). The SiO_2 layer is then etched away, and B dopant is implanted through the etched channels into the exposed Si, the remaining resist and SiO_2 acting as a mask (figure 1.5c). The whole wafer is then covered in a thick oxide layer ($\approx$ 1 to 2 μm), which isolates the transistors and so prevents electrical problems which would otherwise occur later. The photolithography steps are then repeated, but with a different mask which defines the gate and also the access holes which will allow electrical contact to the doped Si source and drain regions (figure 1.5d). These regions are then exposed by etching the SiO_2 layer down to the Si surface (figure 1.5e). After etching, a thin ($\approx$ 0.1 to 0.15 μm) gate oxide layer is grown (figure 1.5f). Further lithography steps (not depicted) using a third mask are then performed which allow the unwanted gate oxide in the source and drain regions to be removed by another etching step (figure 1.5g), finally forming the finished device.

These steps will produce many such devices in the Si surface, which are all fabricated at the same time. The individual devices so formed are then connected together by a conducting layer of Al, which is patterned by further lithography and etching. The resultant structures, with Al "wiring", called *the interconnect* or *metalisation*, form the finished IC. It is easy to see how chips can be fabricated with literally millions of electrical devices on them, allowing the production of very complicated integrated circuits with, for example, all the elements required for a whole computer on a single chip. When devices reach this scale, the technology is referred to as *very large scale integration*, or *VLSI* [17], and the field is referred to as *microelectronics*. Lately the industry has entered *ultra high scale integration*, or *ULSI*.

1.4 SiGe ALLOYS; ELECTRICAL AND MATERIAL PROPERTIES AND APPLICATIONS [18]

Having described how some simple electronic devices are made from Si, and how IC's are fabricated, we now turn to the discussion of SiGe alloys. These materials have electrical properties which make them promising for the fabrication of future microelectronic devices. We now discuss both the electrical and the material properties of SiGe alloy layers grown on Si, and then describe some of their potential applications.

Growth and material properties of SiGe alloy layers. Using molecular beam epitaxy (MBE) (section 1.3.3.1) it is possible to grow high quality SiGe alloy layers on Si wafer substrates. Although there is a lattice mismatch of 4.2 % between bulk Si and bulk Ge, it is possible to grow the layers epitaxially provided the layers are sufficiently thin [15]. The resulting epitaxial layers are strained, because some of the Si atoms in the lattice have been replaced by the larger Ge atoms. It is the strain in these layers which gives rise to the useful electrical properties of these materials. However, if SiGe alloy layers are grown thicker than the *critical thickness*, they begin to relax due to the propagation of dislocations [19]. The critical thickness depends on the Ge content, amongst other factors, and gets lower as the Ge content increases. Reported values for the critical thickness vary in the literature, but it appears that for SiGe alloys with a Ge content above around 10 %, the critical thickness is less than around a micron, and falls off rapidly with larger Ge content. For electronic applications, SiGe alloy layers with only a low Ge content are used.

Electrical properties of SiGe alloy strained layers on Si. The band gap of bulk unstrained SiGe alloy material is reduced relative to that of pure Si. However, as a result of the strain in epitaxial SiGe, a given band gap reduction is obtained with a much lower Ge content compared with unstrained material. The band gap reduction in strained epitaxial SiGe is proportional to the Ge content of the layers [20], and so the band gap may be tailored as required by simply adjusting the SiGe alloy composition. In addition, the lower Ge content required for a significant band gap reduction means that epitaxial SiGe layers of

sufficient thickness to be useful for device fabrication may be grown on Si. These possibilities have benefits for the fabrication of electronic devices, as below.

1) **Faster switching devices.** The electron and hole mobility (i.e. the conductivity) may be enhanced in the SiGe-on-Si system using the *modulation doping effect* [21], which involves the selective doping of whichever material has the higher energy conduction band edge. This means that electrical devices fabricated using this system will be able to work faster. For example, bipolar transistors (section 1.2.4) fabricated using a SiGe alloy base have recently been demonstrated to exhibit faster switching than devices made using conventional Si technology [22]. Bipolar transistors such as these, which have junctions between layers of different materials, are called *heterojunction bipolar transistors* (HBT).

2) **Optoelectronic devices** [23]**.** Light may be emitted by some semiconductor materials when electrons fall from the conduction band to the valence band. The wavelength of the emitted photons corresponds approximately to the band gap energy. This forms the basis for the field of optoelectronics, which involves the construction of "electronic" devices which use light instead of electricity to pass signals. The light pulses are controlled by altering the refractive index of the semiconductor material. For example, a reverse voltage applied to a pn junction sweeps out free carriers and increases the refractive index. Optoelectronic systems are of great interest for communications networks via fibre-optic light pipes, because light can carry more signals in a single cable than electricity can. In addition, they could potentially provide computers which work up to a factor of 10^4 faster than conventional electronic ones [23].

SiGe alloys are ideal materials for optoelectronic applications because the refractive index is a function of Ge content [24], allowing greater freedom in the nature of the devices which may be fabricated. In addition, the fundamental

(indirect) band gap of SiGe alloy spans the 1.30 μm to 1.55 μm range, making SiGe alloy materials very attractive for long wavelength optoelectronic applications [18]. Although indirect band gap materials such as Si and SiGe do not emit light efficiently, recent theoretical work [25] has indicated that light emission may be possible using Si / Ge short period superlattices (i.e. many alternating thin layers of Si and Ge, each of just a few monolayers).

The technology of III-V materials (e.g. GaAs, InP) can also provide both optoelectronic and fast switching devices, but the devices cannot be interfaced with conventional Si based technology. On the other hand, as we have seen, SiGe materials can easily be interfaced with conventional Si based technology. This is another very important advantage of SiGe alloys. Thus they offer considerable potential for enhancing the existing Si based IC technology, which makes up the vast majority of the semiconductor devices in use today.

****

So far, we have outlined several major aspects of the semiconductor industry. We have described some of the properties of semiconductor materials, and then described how electrical devices are made from them. We have explained how many such devices may be fabricated on a single Si substrate using the planar process, and also each of the main processing steps involved, including film formation, doping, photolithography and wet and dry etching. We have also outlined the important properties of SiGe alloys which make them a promising new material for microelectronic applications.

The purpose of this thesis is better to understand the chemical processes involved in one of the dry etching processes, namely reactive ion etching. We therefore now outline the main types of dry etching technique and then describe in detail the processes which occur within the plasmas of the sort used for reactive ion etching.

1.5 DRY ETCHING

Dry etching was introduced in section 1.3.3.4.2 earlier. We now return to discuss in more detail the three main types, which range from the purely physical ion beam etching, to plasma etching which is largely chemical, and reactive ion etching which lies between these two extremes.

1.5.1 ION BEAM AND SPUTTER ETCHING

In these techniques, the wafer is bombarded by a highly directional beam of inert gas ions (usually Ar^+) at kinetic energies of typically several hundred eV. This causes etching by simply knocking or *sputtering* atoms off the surface by momentum transfer. Ion beam etching uses an ion gun to produce a beam of ions which are accelerated towards the wafer by collimators. Sputter etching uses an RF discharge to produce ions, which are then accelerated through the sheath potential (see section 1.6.5) to strike the wafer surface. Both techniques are performed at pressures of typically 10^{-2} to 10^{-5} Torr. The ion beam is directional, so the etching is anisotropic, allowing very high feature resolution [3]. However, these techniques have several disadvantages. Firstly, since the sputter yields of most materials are fairly similar at these ion energies, selectivity is hard to achieve. Also, the high energy ion bombardment can cause intense heating, and may also result in lattice damage and ion implantation into the substrate. In addition, sputtered material may be redeposited onto etch sidewalls and photoresist. For these reasons, ion beam etching is rarely used for the manufacture of IC's.

1.5.2 PLASMA ETCHING

In plasma etching, a reactive "soup" containing atoms, radicals, electrons and ions is generated by an electric discharge through a flowing gas at low pressure (typically 100 to 500 mTorr). This is achieved in a vacuum chamber with two equal-area electrodes to produce the discharge. The wafer to be etched is placed on the lower electrode which is earthed (the cathode), and the upper electrode (the anode) is powered at radio frequency

(RF) through a capacitor. The typical power level is a few W cm^{-2} at an RF frequency of between 50 kHz to 20 MHz. The reactive species then diffuse to the wafer surface where they react to form a volatile product which is pumped away. As an example, F atoms produced in a CF_4 plasma will react with a Si surface to produce volatile SiF_4 product. A typical plasma etcher is illustrated in figure 1.6.

In plasma etching, the wafers are subjected to a modest amount of ion bombardment from ions which are accelerated through the sheath potential (see section 1.6.5). These ions may assist in producing anisotropic etching. However, the geometry of the chamber is such that ion energies are typically only a few volts, so that isotropic etching caused by the reactive chemical species more usually predominates (although anisotropic etching can be obtained under some circumstances [26]). This problem has lead to the development of reactive ion etching.

1.5.3 REACTIVE ION ETCHING (RIE)

RIE is in a refinement of plasma etching. The purpose of the development of RIE was to combine the advantages of physical etching (e.g. anisotropy, fast etch rates) with the advantages of chemical etching (e.g. low lattice damage, selectivity). This is achieved by changing the plasma etcher configuration so that the wafer sits on the powered cathode, and by arranging that the cathode is much smaller than the earthed anode. This results in a large DC bias potential between the plasma and the cathode (section 1.6.6) which accelerates ions onto the wafer surface with energies of typically several hundred eV. This enhances the vertical etch rate, helping to give anisotropic etching. Anisotropic etching is further encouraged by the use of lower gas pressures, typically < 100 mTorr. This reduces the probability of ions being deflected by collisions with neutral molecules before they reach the wafer surface. A typical RIE system is shown in figure 1.7.

RIE is now the dominant etching technique used in the semiconductor industry. However, for such a widely used technique, remarkably little is known about the

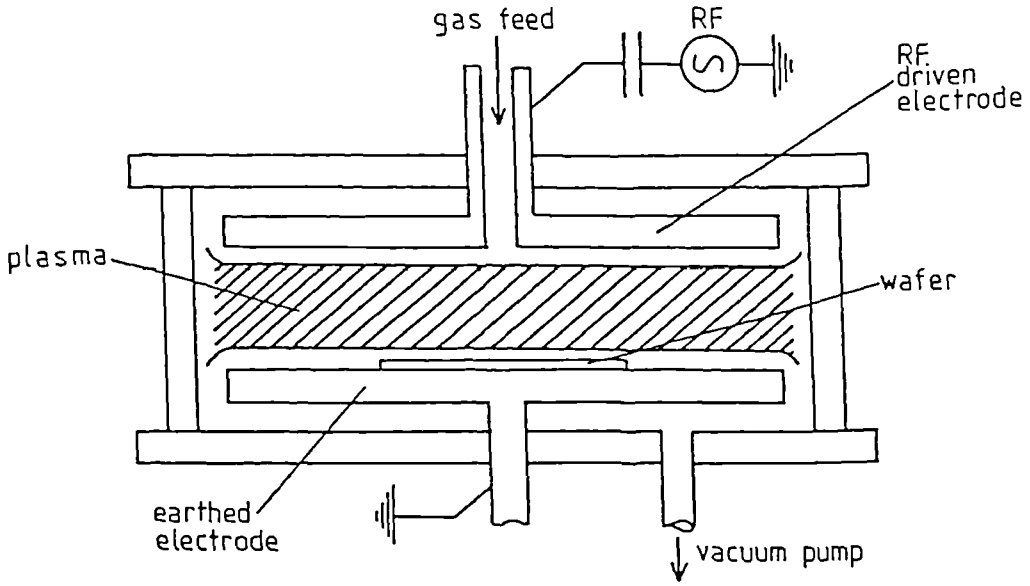

Figure 1.6. A schematic diagram of a typical plasma etcher.

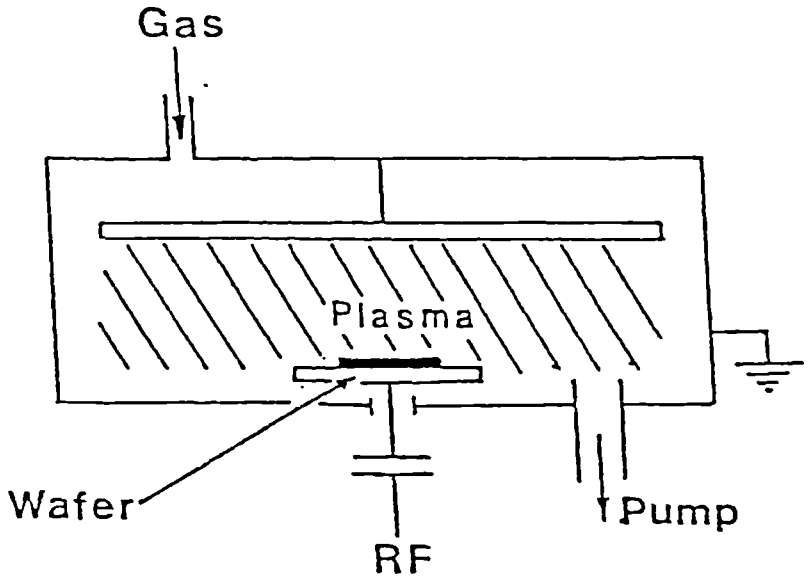

Figure 1.7. A schematic diagram of a typical reactive ion etcher.

fundamental processes which occur in the plasma and at the wafer surface during etching. This lack of understanding has motivated the work contained in this thesis.

1.5.4 FUTURE DRY ETCHING SYSTEMS

At present, there appears to be a move towards high-density (i.e. high ionisation efficiency), low pressure plasma sources [27]. These allow fast, anisotropic etching, but with minimum lattice damage. The current interest seems to be centred on electron cyclotron resonance (ECR), in which RF or microwave discharges are used to excite the plasma. The plasma is surrounded by a strong magnetic field, which causes the electrons in the plasma to follow spiral trajectories, and therefore to undergo more ionising collisions than in conventional RF reactors. Consequently, ECR plasmas can operate at very low pressures ($<$ 1 mTorr), with the resultant benefits mentioned earlier. However, there are now a range of alternative sources available which also have these attributes, including inductively coupled plasmas (ICP), transmission coupled plasma (TCP), helicons, M = 0 resonant induction (MORI), helical resonators and hollow anode sources [27]. At present, it is unclear which of these techniques (if any) will provide the next generation of plasma-based etching reactors.

1.6 PLASMA PHYSICS

The low pressure plasmas dealt with in this thesis consist of a partially ionised gas containing atoms, molecules, electrons, positive and negative ions and photons. The plasma has overall charge neutrality, so that the number of positive and negative particals are on average equal. The degree of ionisation in the plasma is typically 10^{-4} [28], so the plasma consists mainly of neutral molecules and radicals. The plasma region is equipotential, and is always the most positive thing in the chamber, resulting in a potential drop or *sheath* between the plasma and the chamber walls. The physical and chemical processes maintaining the plasma result in the system reaching a non-equilibrium steady state, which is determined by the rates of production and loss of active species.

1.6.1 INITIATION AND MAINTENANCE OF THE DISCHARGE

Initiation of the discharge. When the electric field is applied between the two electrodes, the discharge will be initiated by (a) ionisation of a neutral species by cosmic rays or by background radiation, or by (b) field emission caused by strong electric fields around a sharp point at the powered electrode surface. The electrons so produced will be accelerated by the applied electric field, causing them to collide with gas molecules in the chamber. Eventually the electrons will possess enough energy to cause ionisation of gas molecule through inelastic collisions. This ionisation process produces other electrons, which will then also be accelerated in the electric field, so starting a chain reaction which sets up the discharge. As mentioned above, the degree of ionisation in the plasma is typically 10^{-4} of the total gas number density [28].

Maintenance of the discharge. Electrons will be lost from the plasma at the chamber walls and in collisions with other species. Therefore in order to maintain the discharge, the rate of loss of electrons must be compensated for by the rate of generation of electrons in the plasma. The main process by which sufficient electrons are generated to sustain the plasma is thought to be secondary electron emission from electrode surfaces due to the impact of positive ions [29]. The electrons so produced will be accelerated through the sheath (section 1.6.5) back into the plasma, where they undergo further ionising collisions.

For high frequency plasmas (> 1 MHz), another sustaining mechanism can occur [29]. Field fluctuations in the body of the plasma can accelerate electrons, raising the overall electron temperature. Most of these electrons will not have sufficient energy to cause ionisation, but electrons in the high energy tail of the distribution have energies up to tens of eV, and so can cause ionisation. Although these electrons will represent only a small fraction of the total number of electrons in the plasma, it appears that they do have an important role to play in high frequency plasmas [29].

1.6.2 THE USE OF RF

The main reason that radio frequency plasmas are used in preference to DC ones is that RF plasmas can operate over insulators, such as SiO_2. If a DC plasma were used for this purpose, the insulator would rapidly charge up, eventually causing the plasma to extinguish. By using RF, the negative charge which develops on the substrate surface during one half cycle can be neutralised by ion bombardment during the next half cycle. Providing the frequency is greater than a few tens of kHz, a continuous discharge may be sustained.

Using RF has other advantages. The transfer of energy to the plasma is more efficient in RF plasmas than in DC ones. This results in more ionisation and a denser plasma, leading also to greater concentrations of radicals and atoms compared with a DC discharge operating at the same pressure and field strength. These effects mean that greater etch rates can be obtained.

1.6.3 THE ENERGIES OF ELECTRONS, IONS AND NEUTRALS IN THE PLASMA

The particles in the plasma receive energy either directly or indirectly from the applied electric field. We now consider the energies which electrons, ions and neutrals attain as a result of this energy input.

For systems at equilibrium, the energy distribution of particles will be of Maxwell-Boltzmann form. The plasma, however, is not an equilibrium system, and so the Maxwellian distribution may be expected not to apply. In fact, it turns out that the energy distributions are closely approximated by a Maxwellian type distribution (see also section 1.6.4), which therefore allows us to speak of a *temperature*. This is often quoted in Kelvin, or may be converted to eV using

$$\text{Kinetic Energy} = (3/2)\, k\, T / e \qquad 1.1$$

where k is the Boltzmann constant, T is the temperature in Kelvin and e is the electronic charge.

Electrons. The plasma region is equipotential, and therefore can be considered to be field free (see section 1.6.5). However, the edges of the plasma oscillate, producing field waves which propagate into the plasma [28]. Electrons are very light, so they gain energy very rapidly from fluctuating electric fields. In addition, secondary electrons which are emitted from the electrode surfaces are accelerated through the sheath region into the plasma with high energies (see section 1.6.5). Moreover, electrons which are reflected off the moving plasma-sheath boundary are raised in energy [8]. These mechanisms result in very high electron temperatures in the plasma, typically of the order of 20,000 K ($\approx$ 2 eV).

Ions. Ions receive energy from electric fields much less efficiently than do electrons as a result of their greater mass. Consequently, they have a temperature which is only slightly above ambient, typically $\approx$ 400 K ($\approx$ 0.05 eV). Note however that ions are accelerated to energies of several hundred eV by the sheath potential near the cathode (see section 1.6.5).

Neutrals. Neutral gas molecules only gain energy inefficiently, usually via collisions with ions. Consequently they remain close to ambient temperature, typically $\approx$ 300 K ($\approx$ 0.04 eV).

1.6.4 THE ELECTRON ENERGY DISTRIBUTION

We mentioned in the previous section that the energy distribution of particles in the plasma can be described by a Maxwellian distribution. This will be a reasonable approximation for the relatively massive ions and neutrals, but large deviations might be expected for the lighter electrons. With this in mind, Druvestyn and Penning [30] calculated a theoretical distribution of energies for electrons moving in a weak electric field, predicting a distribution similar to Maxwellian, but with fewer electrons in the high energy

tail. However, experimental evidence indicates that the real energy distribution is in fact much closer to Maxwellian than the Druvestyn and later models had predicted [28].

1.6.5 THE PLASMA POTENTIAL AND THE SHEATH POTENTIAL

We now consider what happens when an electrically isolated substrate is inserted into the plasma. Due to the higher mobility of electrons, the substrate will initially be struck by more electrons than ions, causing it to charge up negatively. This has the result of repelling further electrons and attracting positive ions. Eventually, the substrate will "float" to a potential at which the electron and ion flux balance. This potential is called the *floating potential*, V_f. The excess positive charge density surrounding the substrate is referred to as the *sheath*.

A further consequence of the high mobility of electrons in the plasma is that electrical disturbances within the bulk of the plasma (away from perturbations such as described above) are small; generally fractions of a volt. The bulk of the plasma can therefore be considered to be at equipotential, and it resides at a potential known as the *plasma potential*, V_p. The potential difference across the sheath formed between a floating substrate and the plasma will therefore be $(V_p - V_f)$. This is the energy which an electron must surmount in order to strike the floating substrate.

All the surfaces which are in contact with the plasma are surrounded by a sheath region, including the reactor walls and the electrodes. At any earthed surface, such as the anode in RIE, the sheath potential is equal to the plasma potential, V_p. However, the powered electrode is capacititively coupled to the power generator. The potential at this electrode therefore oscillates on the RF timescale. This has the result that the sheath potential at the RF powered electrode may be large (several hundred volts), and it oscillates in magnitude with the applied voltage. The sheath region will also expand and contract with the RF.

Positive ions which diffuse into the sheath region surrounding a surface are accelerated towards the surface by the sheath potential. The ions which strike the powered electrode may therefore possess high energies as a result of the large sheath potential (see also the following section). It is this property of RF plasmas which allows the possibility of anisotropic etching when wafers are placed on the powered electrode. The situation for electrons is different. Electrons are repelled from sheath regions, so that only the highest energy electrons can strike the electrode for most of the RF cycle. This results in a region of low electron density surrounding any surfaces in contact with the plasma. Since electrons give rise to the glow observed from plasmas, all sheath regions are observed as a region of low light intensity, and are referred to as the *dark space*. The dark space surrounding the electrodes ($\approx$ sheath width) is typically of the order of a few mm thick [8].

1.6.6 THE VOLTAGE DISTRIBUTIONS IN RF PLASMAS

As mentioned earlier, the RF power in RIE systems is generally coupled to the plasma through a capacitor (as it is in the system used in the present work). This capacitor prevents DC current from flowing while allowing RF current to pass, with the result that no net current can flow during one whole RF cycle. In other words, the total charge passed during one whole RF cycle must sum to zero. We recall that in RIE, the areas of the electrodes are not equal, the powered electrode (on which the wafer sits) being smaller than the earthed electrode. The only way for the system to fulfil the zero net-current requirement is to have different sheath potentials at the two electrodes in order to balance the electron and ion currents. The result of this is that the powered electrode charges negatively to reduce the electron current to its surface. This negative potential is referred to as the *DC bias*, V_{DC}, and may be several hundred volts depending on the electrode area ratio. The relationship between the applied RF power, V_0, and V_{DC} is illustrated in figure 1.8, where V_{DC} appears as an offset to the sinusoidally varying V_0. Note that V_0 is positive for only a small fraction of the whole RF cycle. This is the only time during which electrons can strike the cathode.

Song et al [31] have recently derived expressions for the relationship between the electrode area ratio and the various sheath potentials in RIE systems, obtaining excellent agreement with experimental results. The variation of the anode and cathode sheath potentials with time, calculated in that work, are illustrated in figures 1.9a and 1.9b respectively. It is clear from figure 1.9 that the cathode sheath potential is much larger than the anode sheath potential (≡ plasma potential), and is also greater than its minimum potential for a larger proportion of the RF cycle. These factors result in larger ion bombardment energies being found at the cathode, on which the wafers are placed. The smaller anode sheath potential is in antiphase with the cathode sheath potential. The time averaged potentials found across the plasma are shown schematically in figure 1.10. The plasma potential is always the most positive potential in the chamber.

1.7 PLASMA CHEMISTRY

Having described some of the important aspects of the physics of the plasma, we now turn to the chemical aspects which are of greater interest in this work. Many of the important chemical processes are discussed in detail in references 28, 32 and 33.

In etching plasmas, a principal requirement is to dissociate unreactive molecules into species which will react with the substrate surface. It is therefore these reactive species which are our primary concern. However, these species are produced primarily by electron impact processes, and in turn the electrons rely on the ionisation process for their sustenance. Clearly the processes occurring in the plasma are inherently closely interrelated, and can not therefore easily be separated and categorised. Nevertheless, we attempt some form of categorisation in the following sections in order to aid our understanding. We describe many of the important collision processes which occur in the plasma between ions, electrons and neutral atoms and molecules, highlighting the processes which are thought to be the major production and loss mechanisms for each species. An important point to note, is that in order to maintain steady state concentrations in the plasma, the production and loss mechanisms for each type of species must balance. This

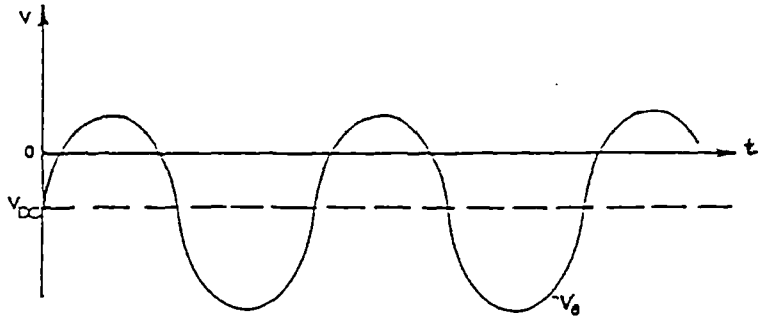

Figure 1.8. The variation of V_0 with time for an RIE system, showing the DC bias offset voltage, V_{DC}.

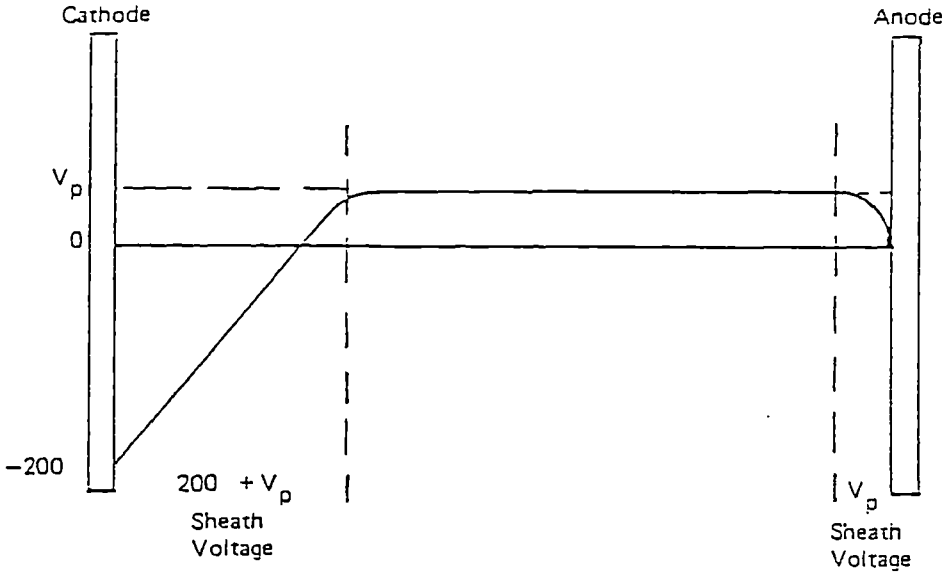

Figure 1.10. The time-averaged sheath potentials versus location in an RIE reactor.

(a)

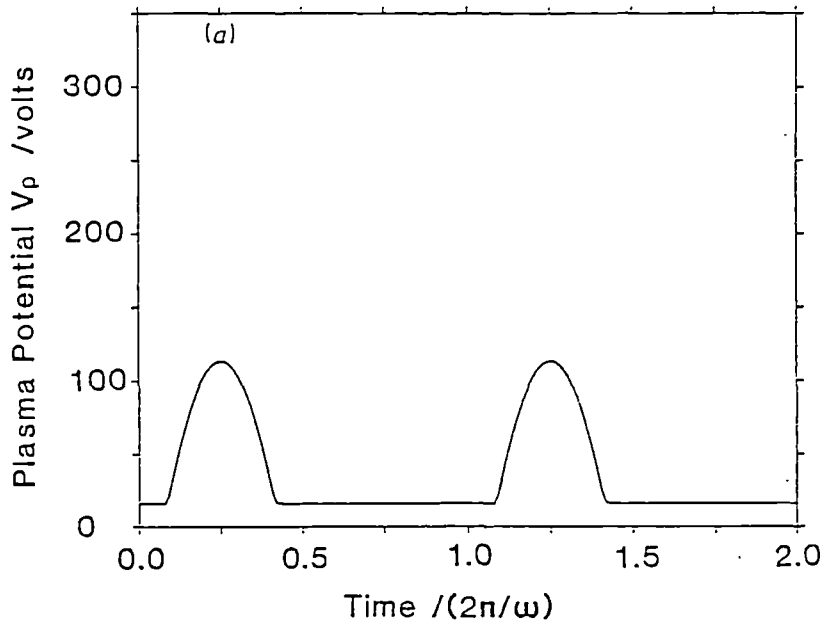

(b)

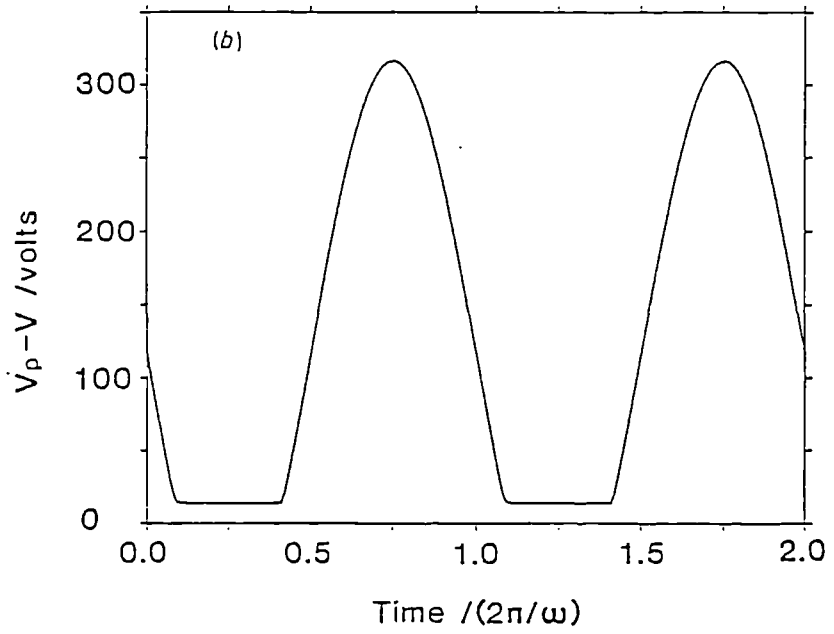

Figure 1.9. The variation of the sheath potential for (a) the anode and (b) the cathode of a 13.56 MHz RIE plasma.

principle is used in the kinetic calculations contained in chapter 4. Noting that $\approx$ 99.99 % of the plasma is made up of neutral gas molecules, we first describe some of the basic properties of gases which are of relevance to the plasma, in order to give a feel for the physical regime.

1.7.1 BASIC PROPERTIES OF GASES

Mean speed of molecules. Gas molecules in the plasma will have a Maxwellian distribution, for which the mean speed, c, (in m s^{-1}) is given by

$$c = \{(8\ k\ T / \pi\ m)\}^{½} \qquad 1.2$$

where k is the Boltzmann constant (in J K^{-1}), T is the temperature (in K) and m is the mass of the molecule (in kg). For CF_4 gas at 298 K, c $\approx$ 300 m s^{-1}.

Mean free path. The mean free path of molecules in the plasma, d, (in cm) (i.e. the average distance molecules move before colliding with other molecules), is given by

$$d = 1 / (\sqrt{2}\ \sigma\ n_i) \qquad 1.3$$

where σ is the collision cross section (in cm^2) and n_i is the gas number density (in molecules cm^{-3}). For CF_4 at a pressure of 85 mTorr (where $n_i \approx 3 \times 10^{15}$ molecules cm^{-3}), d $\approx$ 0.03 cm.

Residence time. This is the average time for which molecules remain in the chamber before being pumped away, t_{res}, (in s) and is given by

$$t_{res} = (V\ n_i) / Q \qquad 1.4$$

where V is the chamber volume (in cm^3) and Q is the gas flow rate through the chamber in molecules s^{-1} (and $Q = 4.48 \times 10^{17} q$ where q is the flow rate in sccm). For typical values of $V = 5000\ cm^3$, $q = 40$ sccm and $n_i = 85$ mTorr, then a value for $t_{res} \approx 1s$ is obtained.

Random walk distance. This is the RMS distance, $<r^2>^{½}$, (in cm) which molecules will move from their start position in a given time period following a simple random walk and is given by

$$<r^2>^{½} = (6\ D\ t)^{½} \qquad 1.5$$

where t is time (in s) and D is the diffusion coefficient (in $cm^2\ s^{-1}$). D is given [34] by

$$D = 0.599\ d\ c\ . \qquad 1.6$$

If we take typical values of $D \approx 500\ cm^2\ s^{-1}$ (for CF_4 at 85 mTorr), then during a residence time of 1s, molecules will on average move a distance of ≈ 50 cm from their starting points. If the trajectory were straightened out, the total distance moved (at 300 m s^{-1} for CF_4 at 298 K) would of course be 300 m. One could therefore envisage the trajectory of the molecule as represented by a ball of string 300 m long, coiled into a 50 cm radius ball. Since plasma chambers are generally smaller than this, it is easy to see that each molecule will visit every part of the chamber many times in the 1s before being pumped away.

1.7.2 IMPORTANT PRODUCTION PROCESSES IN THE PLASMA

In this section, we discuss some of the more important production mechanisms for photons, electrons, ions and neutrals.

1.7.2.1 ELECTRON IMPACT EXCITATION

Electronically excited states of atoms and molecules are formed in the plasma by electron impact processes, which may be written

$$e + A \longrightarrow A^* + e \text{ (lower KE)} \qquad 1.7$$

where A^* denotes an excited atom or molecule and e denotes an electron. The electron energies required for such processes are high (typically of the order of 10 eV for atoms), but lower than the corresponding ionisation process for a given atom or molecule. For example, excitation of F atoms may occur at 12.7 eV, whereas ionisation requires 17.4 eV [35]. Clearly only electrons within the tail of the electron energy distribution can cause electronic excitation (or ionisation) at the mean electron energies typically encountered in etching plasmas (around 2 eV - see section 1.6.3).

Once excited atoms and molecules are formed, they may release their excess energy in the form of a photon by a process called *fluorescence*:

$$A^* \longrightarrow A + \text{photon} \qquad 1.8$$

This is the process which gives rise to the glow exhibited by etching plasmas. The wavelength of the emitted photon is determined by the energy difference between the upper and lower states of A, and so will be characteristic of the species A. The light emitted from the plasma can therefore be used as a diagnostic for determining which species are present in the plasma. This diagnostic is called optical emission spectroscopy and is described in section 1.9.2.

If the de-excitation process involves an allowed transition, then the *radiative lifetime* of the excited state, i.e. the time before fluorescence occurs, will be very short (typically 10^{-8} to 10^{-9} s). However, if the transition is not allowed as a result of the quantum selection rules, the state will have a much longer radiative lifetime (up to 1s).

Such excited states are referred to as *metastable*. Metastable states are more likely to lose their excess energy during a collision with other species or with the chamber walls than by emitting a photon.

1.7.2.2 PRODUCTION OF ELECTRONS AND IONS

Electrons. Once the plasma has been initiated, as described in section 1.6.1, further electrons are produced through electron impact processes such as ionisation and dissociative ionisation:

$$e + A \longrightarrow A^+ + 2e \qquad 1.9$$

$$e + AB \longrightarrow A^+ + B + 2e\,. \qquad 1.10$$

Another process which is likely to be important for the production of electrons in the plasma is secondary electron emission from surfaces within the plasma (see section 1.6.1). Although secondary electron emission is unlikely to contribute greatly to the total electron production, secondary electrons can be accelerated into the plasma with high energies by the sheath potential and can therefore cause ionisation via processes such as 1.9 and 1.10 above. Indeed, as mentioned earlier (section 1.6.1), secondary electron emission from the electrode surfaces due to bombardment from ions is thought to be important in sustaining the discharge [29], although we note that bombardment by metastables and electrons may also produce secondary electrons [8], [32].

Positive ions. The main mechanism for the production of positive ions in the plasma is by electron impact ionisation of neutral molecules through processes such as 1.9 and 1.9 above. The ionisation of atoms and molecules in this way typically requires > 15 eV, and is therefore caused by electrons in the high energy tail of the distribution, as with excitation discussed above. Other possible routes for production of positive ions are discussed below.

The ionisation of metastables requires less energy than ionisation of ground state species.

$$e + A^* \longrightarrow A^+ + 2e \qquad 1.11$$

However, the concentration of metastables is usually much smaller than that of ground state species, so processes such as 1.11 are not a major source of positive ions.

Another mechanism for positive ion production is the process of Penning ionisation, in which a metastable transfers energy to a neutral species.

$$A^* + B \longrightarrow A + B^+ + e \qquad 1.12$$

Clearly such processes can only occur if the internal energy of the metastable is larger than the ionisation potential of the neutral species.

Positive ions may also be produced by photoionisation, as in

$$A + \text{photon} \longrightarrow A^+ + e \qquad 1.13$$

The photons which may perform such processes are in the far UV or soft X-ray region, being produced predominantly by the impact of ions and electrons on chamber and electrode surfaces [28].

Negative ions. Negative ions may be formed in the discharge through processes such as electron attachment and dissociative attachment [36], as in

$$e + A + M \longrightarrow A^- + M \qquad 1.14$$

$$e + AB \longrightarrow A^- + B \qquad 1.15$$

where M is a third body.

Negative ions can only be important in plasmas of electronegative gases, i.e. ones which have a high electron affinity. For example, in CCl_4 plasmas the number of electrons may be up to 100 times less than the number of negative ions, with overall charge neutrality being maintained through the large number of negative ions [37]. This may result in the plasma becoming unstable and non-uniform because there are fewer electrons to sustain the discharge. By contrast, in electropositive gases such as Ar, the number of electrons is approximately equal to the number of positive ions, resulting in a stable, uniform plasma. The case for CF_4 lies somewhere between these two extremes. It is possible therefore that negative ions may be important in $CF_4 + O_2$ plasmas in that they may modify the electrical characteristics of the discharge [38]. However, negative ions are not likely to be involved directly in the etching process because the electrode sheath will reflect them back into the plasma, preventing them from reaching the substrate.

1.7.2.3 PRODUCTION OF RADICALS AND ATOMS

A possible process by which atoms and radicals are produced in the plasma is through dissociative ionisation (1.10), mentioned earlier. However, the main production mechanism for radicals and atoms is likely to be through direct electron impact dissociation of neutral species. In such processes, the electron collides with a neutral molecule, raising it into an excited state which then dissociates before it can lose the excess energy by other means (such as fluorescence, as in section 1.7.2.1, or through collisions). These processes may be written

$$\begin{aligned} e + AB &\longrightarrow (AB)^* + e \\ (AB)^* &\longrightarrow A + B\,. \end{aligned} \qquad 1.16$$

Such processes may occur if the electron impact event excites the molecule to

(i) a repulsive excited state.

(ii) the repulsive part of an upper bound state.

(iii) an upper bound state which intersects and mixes with a repulsive state (called *predissociation*).

In processes such as 1.16, the electron must have more energy than the dissociation energy, which is typically just a few eV. Thus more electrons will have sufficient energy to perform such reactions than will be able to perform dissociative ionisation (needing typically around 15 eV).

1.7.3 IMPORTANT LOSS MECHANISMS IN THE PLASMA

We now discuss the processes by which electrons, ions and neutrals are removed in the plasma.

1.7.3.1 REMOVAL OF ELECTRONS

The main loss processes for electrons in the plasma are likely to be diffusion to the walls (charge outflow), and also recombination processes in the gas phase such as 1.14 and 1.15

Another possible gas phase loss process is dissociative recombination [36]

$$e + AB^+ \longrightarrow A + B \qquad 1.17$$

which is a two-body collision since the two products can conserve both energy and momentum. Such processes may be rapid due to the strong Coulombic attraction between the ion and the electron, although this rapidity is offset by the low concentrations of these species (each $\approx 10^{-4}$ of the total gas concentration).

1.7.3.2 REMOVAL OF POSITIVE IONS

Positive ions are lost from the system by diffusion to the walls (charge outflow). Gas phase processes which may also be important for removing positive ions are recombination with electrons, as in 1.17, and ion-molecule reactions [39].

Charge exchange reactions. When ions collide with neutrals, the charge may transfer from the ion to the neutral. Such processes may be symmetrical or asymmetrical, as in

$$A^+ + A \longrightarrow A + A^+ \qquad 1.18$$

$$A^+ + B \longrightarrow A + B^+ . \qquad 1.19$$

The reaction probability is usually much higher for the symmetrical (1.18) than for the asymmetrical (1.19) case. The overall effect of these reactions is to preserve the total ion and neutral concentrations, but in asymmetric transfer, the balance is upset in favour of particular ions and neutrals. Both processes become important in the sheath regions at higher pressures (> 30 mTorr) [8], [40], where charge exchange may have a moderating effect on the energies of ions striking the electrode.

1.7.3.3 REMOVAL OF ATOMS AND RADICALS

It is the radicals and atoms in the plasma which are responsible for the chemical etching process. Their presence also determines the gas composition of the plasma. It is therefore of great importance to consider how such species react and are removed, once they have been formed by the processes described in section 1.7.2.3. The reactions involving atoms and radicals which are important in the plasma can be classified into two main types. These are two-body and three-body reactions. We now discuss each of these.

Two-body reactions. These are processes such as

$$AB + C \longrightarrow A + BC\,. \qquad 1.20$$

The excess energy released in such reactions appears as increased kinetic (or internal) energy of the product species. As a result, energy and momentum are conserved. Two-body reactions exhibit second order kinetics and the reaction rate, in $cm^{-3}\ s^{-1}$, is given by

$$\text{Rate} = k^{2nd}\,[AB]\,[C] \qquad 1.21$$

where k^{2nd} is the second order rate coefficient in $cm^3\ s^{-1}$, and [AB] and [C] are the concentrations of AB and C in cm^{-3} respectively. (Note that gas kineticists by convention omit to use "molecules" as a unit, so that concentrations expressed in "cm^{-3}" refer to "molecules cm^{-3}". We adhere to this convention throughout this work). The value of k^{2nd} increases with the gas temperature, because at higher temperatures more of the reacting molecules will possess sufficient energy to overcome the activation energy. At the temperatures encountered in etching plasmas, typical values for k^{2nd} vary from $\approx 10^{-10}$ $cm^3\ s^{-1}$ for the fastest reactions to $< 10^{-20}$ $cm^3\ s^{-1}$ for the slowest.

Three-body reactions. These are processes such as

$$A + B + M \longrightarrow AB + M \qquad 1.22$$

where M is a third body (i.e. any other molecule). The third body is required because the AB^* complex formed initially has no way to release the excess energy derived from the exothermicity of the reaction. It therefore possesses sufficient energy to dissociate back to (A + B), which it will do unless the excess energy can be transferred to a third body through a collision. This will stabilise the AB^* complex and so allow the reaction to occur. Three-body processes exhibit third order kinetics (except at high pressures - see later), and the reaction rate in $cm^{-3}\ s^{-1}$ is given by

$$\text{Rate} = k^{3rd}\,[A]\,[B]\,[M] \qquad 1.23$$

where k^{3rd} is the third order rate coefficient in $cm^6\ s^{-1}$, and square brackets [ ] denote concentrations in cm^{-3}.

The rate of such processes depends on the total gas pressure (i.e. [M]), and also the dissociative lifetime of the AB^* complex. This lifetime tends to be longer for large molecules because the excess energy can be distributed amongst the vibrational modes of the molecule. At sufficiently high pressures, quenching of AB^* by collisional de-excitation will always occur before dissociation. The reaction then becomes pseudo second order, and the reaction rate may be described by an effective second order rate coefficient, whereupon the rate equation becomes the same as equation 1.21.

Three body reactions may therefore exhibit both third and second order kinetics, depending on the pressure. The third order rate coefficients (i.e. low pressure limit) tend to have values of up to $\approx 10^{-23}\ cm^6\ s^{-1}$ for the fastest reactions, and values $< 10^{-40}\ cm^6\ s^{-1}$ for the slowest. The effective second order rate coefficients (i.e. high pressure limit) of three-body reactions have values similar to those for the "normal" second order reactions discussed earlier in this section. In between these two pressure extremes, the reactions are said to be in the *fall off* region, whereupon behaviour somewhere between true second and true third order kinetics is exhibited.

For reactions in the fall off region, it is possible to calculate an effective second order rate coefficient using methods developed by Troe [41] (see section 4.4). This is useful for modelling purposes [42], [43] as will become clear in chapter 4 where we construct a detailed kinetic model for the chemical reactions occurring in plasmas through $CF_4 + O_2$ mixtures.

Rule of thumb for determining the importance of gas phase reactions in etching plasmas. The results presented in chapter 4 indicate the approximate reaction rates necessary for a given reaction to be considered as important in the plasma. Those results show that, as a general rule of thumb, only reactions with a two-body rate coefficient of more than around $10^{-14}\ cm^3\ s^{-1}$ are likely to be important.

Reactions at surfaces [44]. For reactions at surfaces, rate coefficients are superseded by sticking coefficients and reaction probabilities (see section 4.4). The rates of such reactions depend strongly on the nature of the surface involved. For example, the reaction probability for recombination of O atoms at surfaces to form O_2 varies from 0.2 to 10^{-4} depending on the nature of the surface [45]. It has also been shown that the sticking probability of F atoms at surfaces (including Si wafers as well as the reactor walls and electrodes) is affected strongly by the presence of O atoms in the plasma because O atoms compete with F atoms for surface sites [46] (see section 4.5.1.2).

The nature of the surfaces exposed to the plasma is particularly uncertain due to the large number of reactive species which may adsorb there. Nevertheless, the results of chapter 4 have shown clearly the reactions which occur at the chamber walls are important in determining the overall plasma composition.

1.8 MODELLING THE PLASMA

The problem of computer modelling of the processes which occur in etching plasmas has recently been reviewed by Kline and Kuschner [47] and also by Plumb and Ryan [43]. We therefore mention this subject only briefly.

The difficulties involved in attempting to model the plasma will now be clear from the many complex processes described in the preceding sections. A complete model requires knowledge of many factors, including discharge currents and voltages as a function of time and position, electron and ion kinetics data, gas phase chemical kinetics data, surface chemical kinetics data, and gas mixture and flow geometry, along with many other factors. The overall problem is often broken down into three sub-models [47], which are; the discharge kinetics model, the chemical kinetics model and the surface science model. A complete model is at present beyond the scope of current knowledge and computer power. Simplifications are therefore required.

In order to model the chemistry of the plasma, as is one of the objectives of the present work (see chapter 4), the model may be simplified by separating the discharge kinetics model from the chemical kinetics model. Using this approach, it is assumed that the electron impact rate coefficients may be determined from an appropriate discharge kinetic model. Further simplifications may then be made. Firstly, the number of important spatial dimensions may be reduced by considering a discharge through a fast flowing gas, and then assuming "plug flow", in which "plugs" of gas are assumed to convect downstream with a specified convective velocity. Diffusion between adjacent plugs and variations in the convective velocity in the boundary layers adjacent to the walls are ignored (see for example [42]). Alternatively, a "stirred tank" approach may be adopted, where the concentrations of species are assumed to be uniform, with no variation along the flow direction. The second assumption is a closer approximation to the situation found in typical etching plasmas, where residence times are long. This approach has therefore been adopted in the present work (see section 4.4).

1.9 PLASMA DIAGNOSTIC TECHNIQUES

We have now described much of the physics and the chemistry of importance in plasmas of the type used for etching. We next describe some of the methods by which such systems may be studied in order to inquire further into their nature. The aim of such studies is to aid in the development of new etching processes, and also to improve existing ones. Emphasis will be placed on quadrupole mass spectometry and optical emission spectroscopy, which are the techniques employed in this work.

1.9.1 MASS SPECTROMETRY

Mass spectrometry is a technique which may be used to identify and determine the concentrations of gas phase molecules. In brief, a mass spectrometer consists of an ion source to ionise the neutrals, an analyser which separates the ions according to their mass-to-charge ration (m/q), and a detector which effectively counts the number of mass-filtered

ions. There are many types of mass spectrometer, but the quadrupole mass spectrometer (QMS) is often used (as in the present work) because of its convenience and flexibility. This discussion is therefore confined to the QMS.

A schematic diagram of a QMS is shown in figure 1.11. The gas sample is directed (see later) into the ion source. Here, electrons are produced by thermionic emission from a hot filament (usually tungsten or thoriated iridium) and accelerated typically to 70 eV, which represents a maximum in the ionisation efficiency curve for most atoms and molecules [48]. The positive ions are produced by electron impact (as in equations 1.9 and 1.10 in section 1.7.2.2), and are directed by electric fields through an aperture and into the analyser section of the QMS.

The analyser section contains four symmetrically arranged and precisely aligned parallel metal rods which act as electrodes. Opposite pairs of electrodes are electrically connected together. Mass analysis is achieved by applying appropriate varying potentials to these pairs of electrodes as follows. To one pair is applied a DC voltage U with an RF voltage V cos ft superimposed. To the other pair is applied the opposite potential; - U - V cos ft. There are two possible fates for an ion entering such an arrangement. Firstly, it may oscillate symmetrically and continuously about the central axis of the rods and succeed in travelling along the entire length of the electrodes, where it may be detected (ions a^+ in figure 1.11). Alternatively, it may suffer unstable motion which forces it to depart from the central axis and strike one of the electrodes, where it is neutralised (ions b^+ in figure 1.11). The motion exhibited by the ion is determined by its mass-to-charge ratio (m/q). By a judicious choice of U, V and f, the system may be arranged so that only ions within a small m/q range can reach the detector, thus allowing effective mass filtering. The entire mass range may then be scanned by varying V and U while keeping U / V constant, or alternatively by varying the frequency, f. In this way, ions of varying m/q (typically 0 to 200 amu) may be brought to the exit of the quadrupole rods in turn. As the ions emerge from the rods, they are accelerated by a high negative voltage (typically 2 to 3 kV) towards the entrance of a channeltron or secondary electron multiplier (SEM), which will give

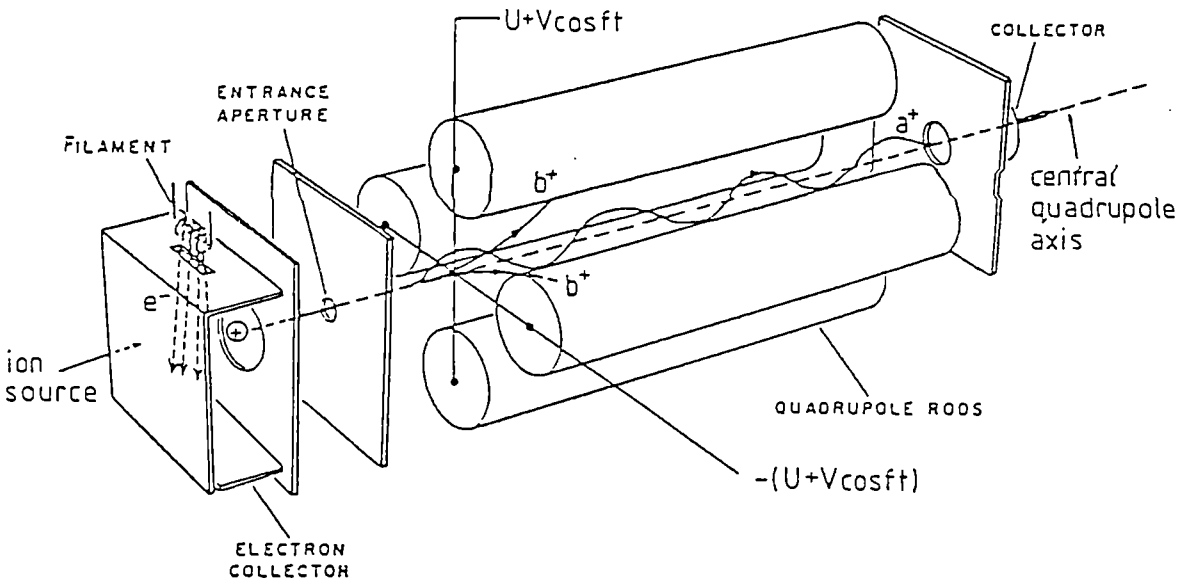

Figure 1.11. A schematic view of a quadrupole mass spectrometer.

current amplification of typically 10^5. The output signal may be recorded on a chart recorder or oscilloscope, or else transferred to a computer for display on the monitor. The mass spectrum so produced consists of a plot of ion current (or partial pressure) vs m/q.

Quadrupole mass spectrometers operate at low pressures of typically $< 10^{-6}$ Torr. This low pressure is necessary because firstly, there must be no collisions of ions with neutrals within the analyser and secondly, the sensitivity of SEM type detector degrades rapidly if used at higher pressures. Low pressure is also necessary to avoid oxidation of tungsten thermionic filaments.

Analysing the plasma by QMS. We now discuss how a gas sample may be extracted from the plasma for analysis by QMS. The QMS (at 10^{-6} Torr) must be connected to the plasma chamber (at 10^{-2} to 10^{-3} Torr) in such a way as to preserve the different pressure regimes. This may be achieved by the use of a small orifice, which may be a simple effusion hole, or by the use of a fine capillary. Several different methods of attaching a QMS to the plasma chamber are illustrated in figure 1.12.

The simplest approach is to attach the QMS to the effluent line downstream from the plasma. This type of analysis may be used to identify the overall product species. However, since the analysis is remote from the discharge, the measurements do not truly represent the gas present in the plasma, which greatly limits its value (cp section 3.3.4). By the use of an effusion hole, the QMS housing can be made to form part of the chamber wall [49] or electrode [50], [51]. The gas effusing through the hole may be modulated using a chopper, and the signal detected using phase sensitive detection. This ensures that only those species which travel directly to the ion source from the plasma without suffering collisions with the walls en-route are detected [49]-[51]. An alternative sampling method is to locate the QMS within the discharge itself [52], although this approach is certain to introduce a large disturbance to the plasma and so disrupt species concentrations.

In the case of gas sampling with the QMS as part of the electrode, ions from the discharge may be sampled directly by simply switching off or removing the ion source.

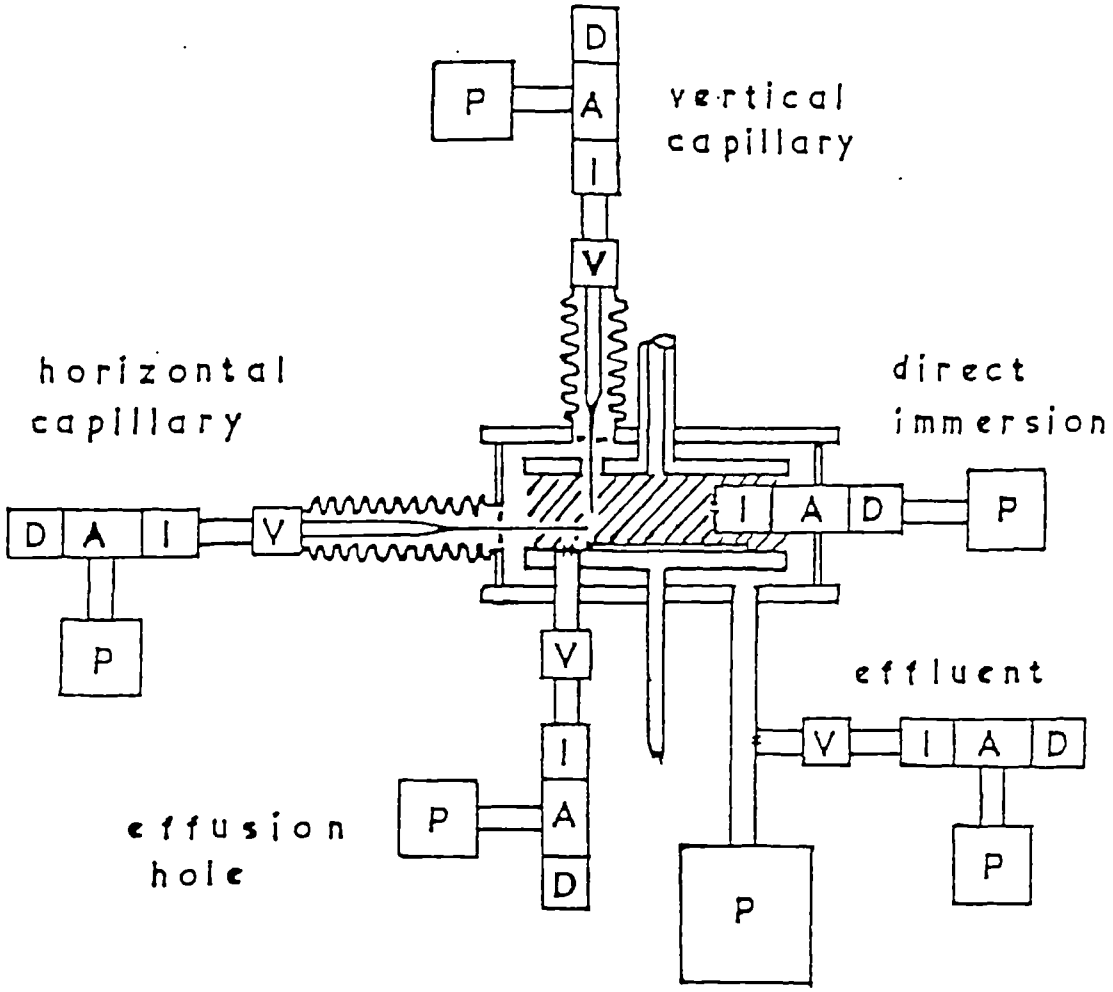

Figure 1.12. The various ways in which a mass spectrometer may be attached to a plasma reactor. V = valve, I = ion source, A = analyser, D = detector and P = pump. Effluent sampling involves an analysis which is remote from the discharge. A closer approximation to genuine sampling of the plasma is afforded by direct immersion, although the resulting disturbance to the plasma is large. Effusion holes and capillaries offer a reduced plasma disturbance, and the latter may be made movable through the chamber for a spatially resolved analysis.

The sampled ions may be analysed according to identity and energy. Ion identification is performed in the usual way with the QMS. Some methods of energy analysis are described later in section 1.9.7. However, we note that the interpretation of such results is more difficult than for neutral species detection because the energies and trajectories of the ions may be significantly altered by the potential sheaths which form around the sampling orifice.

An alternative method of sampling the plasma for analysis by QMS, which has been adopted by this laboratory, is to sample gas from the plasma via a thin capillary which is inserted directly into the plasma [53]-[55]. This method allows gas from within the discharge region to be sampled while introducing minimal disturbance to the plasma. The benefits of the capillary probe sampling system, and also the difficulties which must be overcome, are discussed in more detail in the experimental section of this thesis, and also in chapter 3.

Some factors affecting the analysis of QMS results. The factors which affect the analysis of QMS results are discussed in more detail in experimental section 2.6.4. Briefly, they include (a) distortion of the plasma or the gas sample by the capillary probe, (b) variation in the performance of the QMS from run to run, (c) the need to account for the overlap of the cracking patterns of different species in the plasma, and (d) the need to account for the different sensitivity of the QMS towards different species.

1.9.2 OPTICAL EMISSION SPECTROSCOPY

In section 1.7.2.1 we described how excited species formed within the plasma may emit light of a wavelength which is characteristic of that species. Optical emission spectroscopy (OES) is a technique by which the emitted light is analysed by wavelength, allowing the identity of fluorescing species to be determined. Light from the plasma passes through a suitable quartz window and is transmitted to the entrance slit of a monochromator either by means of a fibre optic cable, or by simply positioning the monochromator as close

to the plasma as possible. Dispersion of the light is achieved by a diffraction grating within the monochromator, so that only a narrow wavelength spread appears at the exit slit. The nearly monochromatic light which passes through the exit slit then falls onto a photomultiplier, which produces a small photocurrent which is approximately proportional to the intensity of the light falling on it. In order to produce a spectrum of a selected wavelength range, the grating is rotated with high precision using a stepper motor. The amplified output of the photomultiplier is then displayed on a y-t plotter.

The spectral resolution obtained by such an arrangement depends on the grating and on the optical path length; for example a 2400 lines per mm grating in a 0.5 m spectrometer will give a resolution of 8 Å for a slit width of 1 mm. For serious spectroscopic studies, a typical resolution of around 1 Å or less is required in order to distinguish successfully the emissions from the many different species which arise in plasma systems. The spectral range which may be observed depends on the grating, photomultiplier and the fibre optic, but is typically 2000 Å to 8000 Å.

OES has been used extensively for monitoring many RIE and plasma etching systems due largely to its relative ease of implementation and because it allows the observation of important reactive species such as F atoms which are difficult to observe by other means [46]. This makes it an ideal technique to complement an analysis by QMS, which is very effective at monitoring the stable, unreactive molecules present in the plasma. Examples of systems which have been studied by OES include (a) $CF_4 + O_2$ etching of Si and its compounds [53], [56]-[58], (b) Cl_2 and CCl_4 etching of Si and Al [59]-[61] and (c) CCl_2F_2 etching of GaAs [62].

The power of the OES technique can be greatly increased by the use of a monochromator with a photodiode array detector instead of the conventional PMT and exit slit arrangement described above. This type of detector consists of an array of tiny photodiodes housed within the monochromator, onto which the light diffracted by the grating falls. This type of detector permits real-time monitoring of wide regions of spectrum (perhaps 2000 Å at 1Å resolution), allowing emission from a greater number of

different species to be monitored simultaneously. It also allows data to be stored on computer disk for later analysis, aiding the interpretation of the results.

However, the OES technique has its drawbacks. The main problem is that, it is difficult to relate OES results, which monitor emission from species in transient excited states, to the concentration of ground state species. The intensity of emission at a specific wavelength, I, for a given excited species, X^*, is given by

$$I(X^*) = A[X^*] \qquad 1.24$$

where A is a constant (the Einstein coefficient) and $[X^*]$ is the concentration of X^*. However, $[X^*]$ depends not only on the concentration of ground state X species, [X], from which X^* is formed by electron impact (section 1.7.2.1), but also on parameters such as the electron density and distribution function, and on the collision cross section for excitation. These factors may vary according to the process conditions, which means that the emission intensity can not be simply related to the concentration of ground state species. A development of the OES technique which attempts to allow for the above factors is called *actinometry*.

Actinometry. This technique, first used by Coburn and Chen [63], [64] and d'Agostino et al [57], involves the observation of emission from an inert tracer gas (e.g. Ar, N_2), called the *actinometer*, which is added in small known amounts to the plasma. Since this gas is inert, its concentration is unaltered by the action of the plasma. The assumption is then made that the same electrons excite the actinometer as excite the species of interest (lines with a similar excitation threshold are used where possible). The ratio of emission intensities of the two species should therefore give a more reliable indicator of concentration. Actinometry is reported to be successful for measurements of [F] in the CF_4 + Ar system [65], [66], but is found to fail for [O] in the CF_4 + O_2 system [67], for [Cl] in the Cl_2 + Ar system [68], for [CCl] in the CCl_4 + N_2 system [69]. Where actinometry fails, it is often because excited state species are formed by direct dissociation of polyatomic parent species.

At any event, it is clear that actinometry needs to be verified against an independent measurement technique before it can be used safely.

Despite the difficulties in obtaining absolute concentrations of species using OES, the technique is useful for extracting ratios of concentrations as the etch parameters vary, especially on passing through an endpoint or comparing no wafer with a wafer. This will become clear in chapter 5.

1.9.3 LASER INDUCED FLUORESCENCE

The laser induced fluorescence (LIF) technique uses a laser beam of a suitable wavelength to excite ground state species into higher states by absorption of a photon. The subsequent decay by fluorescence is monitored using conventional OES techniques (see previous section). Because the excited state is produced by a laser beam which is controlled by the experimenter, rather than by electrons in the plasma, the intensity of emission can more easily be related to the concentration of ground state species. For example, Hancock [46] has measured ground state concentrations of O, CF and CF_2 in a plasma of $CF_4 + O_2$. LIF has other advantages in that it is highly species-selective, can be spatially selective by using directed lasers, and is extremely sensitive (species with concentrations of only 10^7 cm^{-3} may be detected [70]). However, LIF is experimentally difficult to use, and can only be applied to certain species because of limitations in the wavelength range accessible with current laser technology, and because many polyatomic species dissociate on absorption. Nevertheless, LIF provides perhaps the best method for measuring absolute ground state concentrations of reactive species, which are otherwise difficult to obtain.

1.9.4 LANGMUIR PROBES

A Langmuir probe consists, in the simplest case, of a wire inserted into the plasma to measure the potential at different locations. This provides information concerning the ion and electron temperatures and densities, along with the plasma potential [37], [71].

Langmuir probe techniques have recently been reviewed by Kuschner [72], Clements [73] and Swift and Schwar [74].

One of the main problems with Langmuir probe measurements is that the signal is modulated by the oscillating plasma potentials. This can be overcome in part by applying a compensating voltage directly to the probe (81, 82) in the hope that the effects will cancel out. However, this assumes that the plasma potential may be represented by a sinusoidal function, which is not correct [31]. Another problem of the interpretation of Langmuir probe measurements occurs when using corrosive gases in which the probe tip etches away. These factors mean that Langmuir probe measurements are subject to uncertainty. However, they are useful for providing order-of-magnitude estimates for ion and electron temperatures and densities etc. which are difficult to obtain by other means.

1.9.5 SURFACE ANALYSIS TECHNIQUES [75]-[77]

After etching, the surface of the wafer may be examined to identify the chemical constituents of the uppermost surface layers. There are many techniques available with which to probe the surface, such as XPS, SIMS, AES, UPS and RBS. Most of the various surface analytical techniques involve bombarding the surface with a flux of particles or radiation of known energy (e.g. X-rays, electrons, ions, neutrals etc.) and observing the secondary particles which are ejected. The type and energy of the ejected particles is measured, yielding information about the chemical nature of the surface. In addition, each of these techniques is capable of giving a compositional depth profile when used in conjunction with an Ar ion gun to sputter the surface layer by layer. We now describe briefly some of the more commonly used surface analytical techniques.

X-ray photoelectron spectroscopy (XPS) [75]. XPS employs a monochromatic beam of X-rays to probe the surface. Photoelectrons are emitted, and their energy distribution yields qualitative and quantitative information about the chemical elements present in the surface layers ($\approx$ 30 to 100 Å). XPS is a particularly valuable technique as it also yields information concerning the chemical environment of the surface species. For example,

many workers have observed SiF_x (x = 1 to 3) at the surface of Si wafers which have been etched in fluorine-based systems [78]-[81].

Auger electron spectroscopy (AES). In AES, the surface is bombarded by electrons. This results in the emission of Auger electrons [75] which are characteristic of the elements present at the surface. This allows elemental analysis to be performed, as with XPS. An advantage of AES is that a compositional "map" of the surface may be obtained by combining AES with scanning electron microscopy. However, information concerning the chemical environment of surface atoms is difficult to obtain using AES.

Secondary ion mass spectrometry (SIMS). In SIMS, the surface is probed by a beam of ions. Ions are directly sputtered from the surface and detected by mass spectrometry. SIMS has the advantage of high surface sensitivity, allowing the surface monolayer to be studied. It also has the highest atomic fractional sensitivity of any surface technique [77]. A disadvantage is that SIMS is destructive, since it requires the surface to be removed during analysis, but this does mean that a depth profile is automatically obtained.

There is no "perfect" surface analytical technique; each has its own advantages and disadvantages. The best that can be done is to combine several techniques in order to obtain the advantages of each. Modern surface spectrometers can now combine several techniques in the same apparatus, allowing more detailed surface analyses to be carried out.

1.9.6 ETCH RATE MEASUREMENT

Etch rate measurement represents one of the simplest methods for obtaining information about the plasma, and can be obtained by several methods.

A convenient way to measure the etch rate is by using a surface profiler, in which a sensitive stylus is dragged across the surface, connected to instrumentation which measures its vertical position. The stylus is dragged over raised etch features, formed by resist masked areas, and the height of the step is recorded to allow determination of the

etch rate. Commercially available surface profilers (such as a Tallysurf or Dektak) can measure step heights down to 10 Å.

For the study of fundamental plasma properties, the use of organic resists is not advisable because they are not usually completely plasma resistant and will therefore introduce contaminants into the plasma. This means that the above techniques can not be used for etch rate measurements. As in the present work, the etch rate may then be measured by the method of weight loss, i.e. simply weighing the wafer before and after etching and then calculating the etch rate from the etch time and the substrate density and surface area. Alternatively, the time taken to etch through a layer of known thickness can be determined (section 2.8.2). Other methods by which etch rates may be determined include laser interferometry (see section 1.9.7), or the use of a quartz crystal microbalance [77], in which the loss of material is recorded as a change in the oscillating frequency of a quartz crystal.

1.9.7 MISCELLANEOUS TECHNIQUES

There are many other diagnostic techniques which have been used to study the plasma. We now mention briefly some of these.

Scanning electron microscopy (SEM) [82]. An SEM is a microscope which rasters a beam of electrons across a sample enclosed in a vacuum chamber. Resolution down to 10 nm may be obtained, making SEMs ideal for examining etch profiles and surface roughness etc.. As a result, SEM's are widely used by process engineers when developing new etch processes.

Ellipsometry [83]. In this technique, the polarisation state of a laser beam which is reflected from a substrate surface is measured. This can be related to the thickness of thin surface films. Ellipsometry can be used as a real-time in-situ monitor of the wafer being

processed, giving information on etch rates, end-points, presence of residual layers, surface roughness and polymer formation. This technique has recently been used successfully in the SiGe-on-Si system to determine endpoints, and to provide a compositional depth profile of the SiGe alloy substrate during etching [24].

Titration. Gas phase titration has been used to determine the concentration of F atoms downstream from a $CF_4 + O_2$ plasma using Cl_2 gas [65].

Molecular beam studies [83]**.** In these studies, the substrate surface is exposed to a molecular beam of reactive species under UHV conditions. The initially desorbed products may be determined by QMS, and the post-exposure surface may be studied by XPS or other surface techniques. In addition, an ion beam can be superimposed onto the molecular beam in order to study the effects of ion bombardment on etching. These techniques allow the fundamental surface processes to be studied in a "clean" system, without the added complication of a plasma.

Ion energy analysis. In the simplest case, this involves drilling a small hole in the electrode of a RIE or plasma etching system, and allowing ions which have been accelerated by the sheath to be energy analysed outside the plasma. Both the energy and the identity of detected ions may then be determined by the use of a mass spectrometer [85], [38] (section 1.9.1). Smaller detectors have also been used to measure ion energy distributions (IED's), such as a retarding field analyser (RFA) [86] or a parallel plate energy analyser [87]. The RFA also allows the ion angular distribution to be measured [86]. Recent computer models have allowed comparisons to be made with experimental IED's [40], [88], [89].

Fabry-Perot interferometry. This is a method by which emission lines may be observed at resolutions as low as 0.01 Å. The kinetic energies of emitting species may then be

determined by measuring the Doppler linewidths [8]. Investigations are currently underway in this laboratory to measure the broadening of F atom emission lines in CF_4 + O_2 plasmas.

CHAPTER 2

EXPERIMENTAL

2 EXPERIMENTAL

2.1 INTRODUCTION

A Reactive Ion Etcher (RIE) has been used in a study of the chemical processes occurring in radio frequency discharges through mixtures of CF_4 and O_2, and to study their application to the etching of Si, Ge and SiGe alloy wafer substrates. Simultaneous Quadrupole Mass Spectrometry and Optical Emission Spectroscopy were used to monitor gas phase species present in the plasma. Later in this chapter we describe the apparatus (sections 2.3 to 2.6), materials (section 2.7) and experimental procedures used (section 2.8), and also the methods used to calculate species concentrations from raw mass spectroscopic data (section 2.9). First, we explain the strategy and tactics which have been employed during this study by way of an overview, and also to help give perspective to the descriptions given later in the chapter.

2.2 EXPERIMENTAL STRATEGY AND TACTICS

We have mentioned before that the initial impulse behind the work was to gain a greater understanding of the chemical processes which occur during the etching of SiGe alloy substrate material in CF_4 + 8 vol % O_2 plasmas. We now explain the strategy which has been adopted to achieve this aim.

A huge amount of work has been published concerning plasmas of CF_4 and O_2 mixtures and their use for etching Si. This system is probably the best understood of all the plasma-based etching systems which are used. Nevertheless, due to the phenomenal complexity of the processes which occur in the plasma, even this system is not understood in detail (see for example reference 47). Often there are many opposing views offered in published work, partly due to difficulties inherent in the study of plasma systems, and partly because factors which are important in one etching machine may not be important in another due to differences of reactor geometry and experimental operating conditions etc.. The strategy adopted was therefore first to build up a database of information concerning

CF_4 + O_2 plasmas and then to study the etching properties of pure Si and pure Ge. This was done in order to gain a better understanding of these systems and also to fully characterise the Omega RIE reactor used in this work, before beginning the study of the etching of SiGe alloy. The tactics employed toward this end are described below.

As mentioned above, plasma systems are very complex. This is due to the large number of interrelated parameters which are important in influencing their behaviour. It is necessary to have information concerning a significant number of these parameters in order to gain a detailed understanding of plasma systems. The tactics we have employed are therefore to simultaneously measure the largest possible number of important parameters given available equipment, and to measure these parameters over the largest possible process parameter space. Using QMS, we have measured the concentrations of all the important unreactive molecules present in the plasma, and using OES we have measured emission intensities from F atoms in a variety of excited states (which can be related to the concentration of F atoms in the gas phase). In addition, during etching experiments the etch rates of wafer substrates have been determined.

All these measurements have been performed on CF_4 + 8 vol % O_2 plasmas for a wide range of conditions of gas flow rate, rf power and gas pressure with no wafer present, and also with pure Si and pure Ge wafers present in the chamber. For Si and Ge etching, the effect of varying the wafer surface area exposed to the plasma was also investigated. In addition, the effect of changing the feed gas mixture was studied with no wafer present in order to reveal the role of some of the species present in the plasma. These experiments allowed a greater understanding to be gained concerning the chemical processes occurring in CF_4 + O_2 plasmas and also during the etching of Si and Ge wafers. Only after this detailed study was completed were measurements performed on the etching of SiGe alloy material. This placed us in a better position to discover if SiGe alloy shows etching behaviour consistent with a simple mixture of Si and Ge, or whether it shows novel etching behaviour.

2.3 THE OMEGA REACTIVE ION ETCHER

2.3.1 OVERVIEW

The etcher used for this work was an Electrotech Omega RIE reactor. A schematic diagram of our system is shown in figure 2.1, and a photograph is shown in figure 2.2. Briefly, it consists of a vacuum chamber into which gas flows through a series of small holes called the shower head. Gas passes through the chamber and is pumped out by vacuum pumps, while keeping the pressure constant and below around 100 mTorr. The plasma is produced by a powered electrode on which wafers to be etched are placed. A port in the chamber lid allows the plasma to be monitored simultaneously by Quadrupole Mass Spectrometry and by Optical Emission Spectroscopy (see section 2.4).

This section is now split into 4 sub-sections to describe the Omega RIE reactor in more detail. They are; the vacuum chamber, the gas inlet system, the pumping system and the rf power supply.

2.3.2 THE VACUUM CHAMBER

The main chamber body consists of two parts: the chamber lid in which the plasma is confined and a "dead space" below the plasma. The chamber body is earthed except for an 88 mm cathode pedestal on which wafers to be etched are placed. The cathode is capacitatively connected to a 13.56 Mhz radio frequency power supply to produce the discharge, and is electrically isolated from the rest of the chamber by a ceramic spacer. The process chamber and the port (mentioned above) are shown in cross section in figure 2.3.

The chamber lid can be raised and lowered pneumatically to allow the insertion of a wafer for etching. When lowered, the lid and powered cathode form an approximately 5 litre cylindrical volume which contains the plasma. Gas enters this volume through the showerhead, and exits through 16 equally spaced pumping holes into the approximately 7

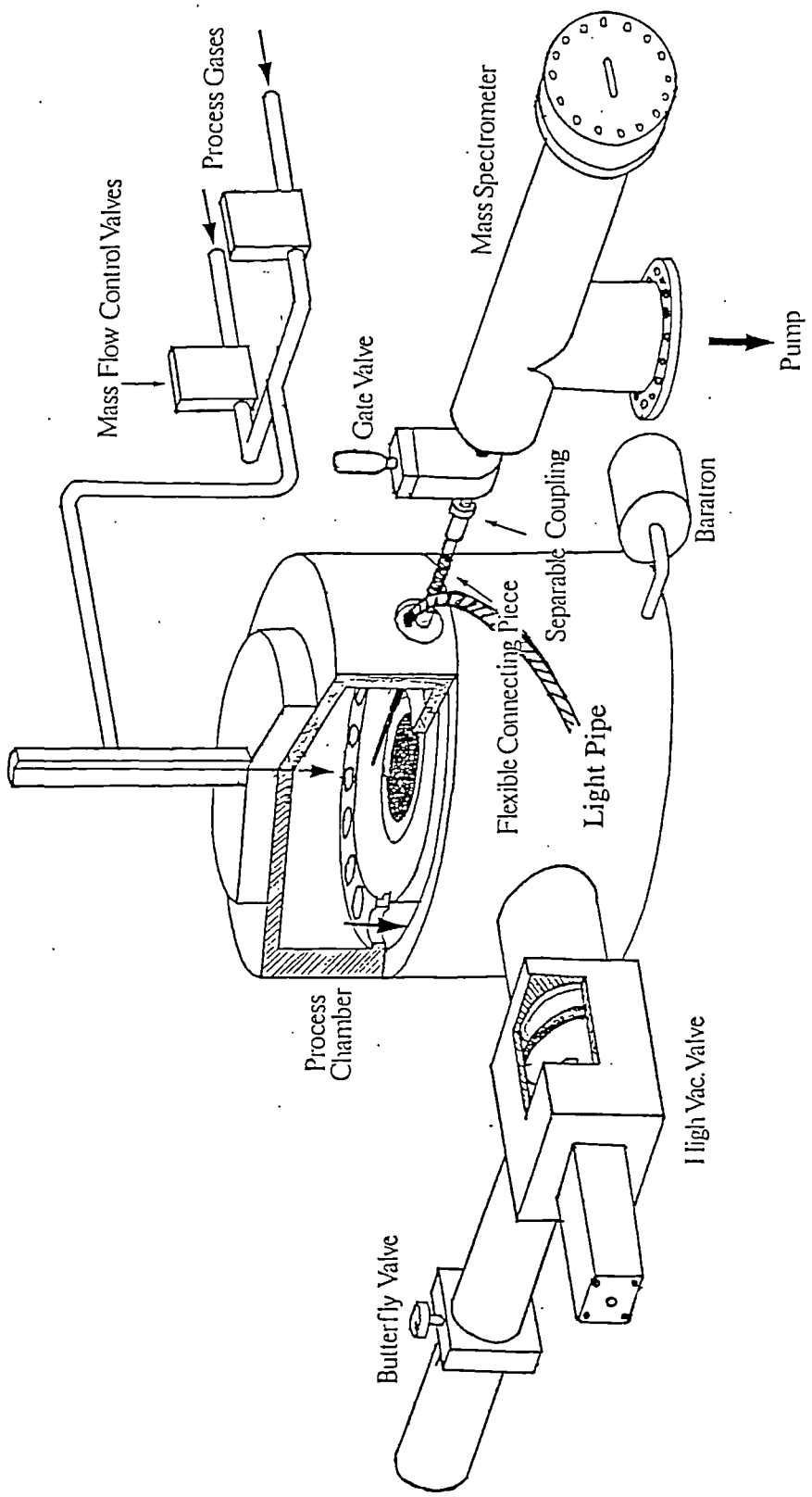

Figure 2.1. Schematic diagram of the Omega RIE etching system and the QMS. The light pipe used for optical sampling is also shown. The relative positions, approximate sizes and connections of most of the important parts of the system are shown. For clarity, the baratron has been displaced from its normal position opposite the high vacuum valve. Some valves, mainly isolation ones, and some of the extraneous connecting pipes have been omitted.

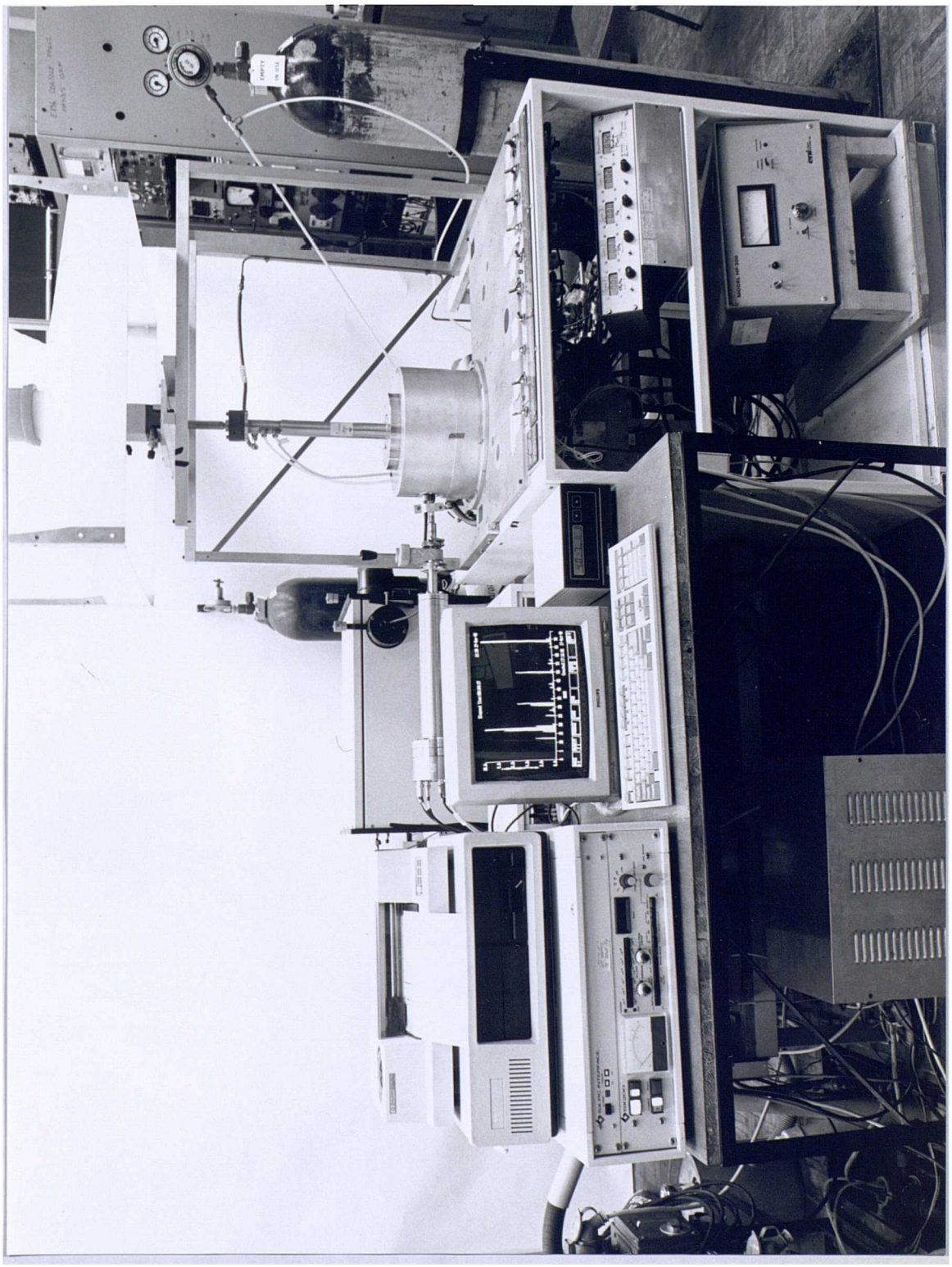

Figure 2.2. Photograph showing our experimental system.

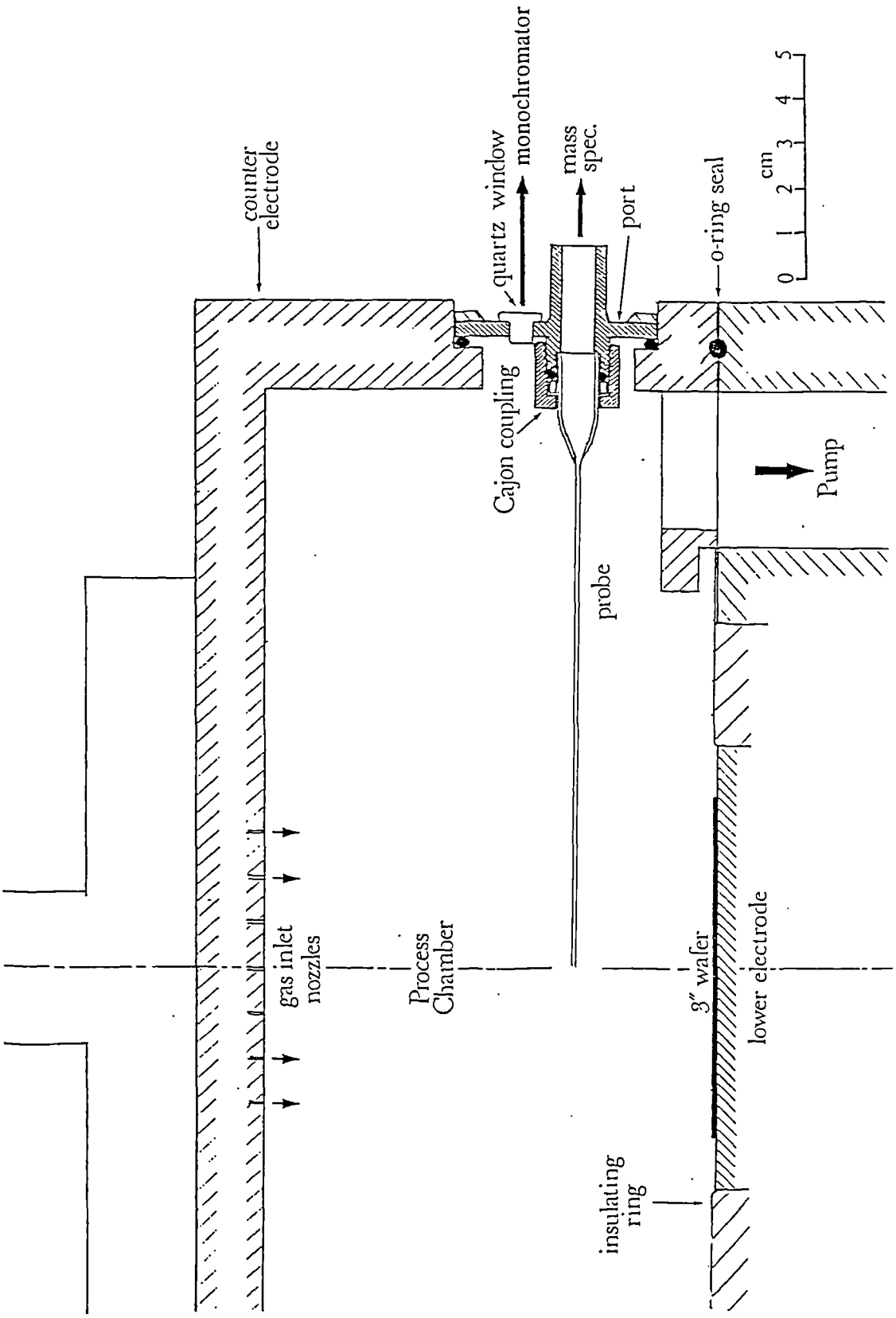

Figure 2.3. Scale diagram of the process chamber, capillary probe and sampling port.

litre dead space below from which it is removed by vacuum pumps via the main pumping port situated at the base of the vacuum chamber. It is possible to isolate the chamber from the pumps using a pneumatically operated "high vacuum" valve, situated in the pumping line. This allowed the chamber to be vented to atmospheric pressure with dry N_2 from a cylinder, ready for wafer insertion. During the experiments in which SiGe alloy thin layers were etched, the entire chamber lid was enclosed in a large polythene bag. This was flushed with dry N_2 while SiGe alloy wafers were inserted into the chamber in order to reduce contamination by water vapour from the air (see section 7.2). In all experiments, the walls of the chamber and the rf powered cathode were water cooled in order to maintain a constant temperature during etching.

The chamber pressure is monitored using a Baratron capacitance manometer (MKS instruments) connected to the chamber via 1/4 inch stainless steel tubing. This allowed pressure measurements to be made from a few mTorr to around 1.2 Torr. All vacuum seals were made by lightly greased O-rings, resulting in a pressure rise of only $\approx$ 0.2 mTorr per minute with the evacuated chamber isolated from the pumps at the high vacuum valve.

2.3.3 THE GAS HANDLING LINES

All the process gases used in this work were obtained from cylinders, the details of which are given in section 2.7.2. The flow rate of gas into the chamber was controlled and monitored using 2 Mass Flow Controllers (MFCs)(Tylan, type FC 260) to deliver flow rates between 2 and 50 standard cubic centimetres per minute (sccm). MFCs are calibrated for one specific gas (usually N_2 or Cl_2) and so a correction factor is applied when using other gases [90]. The correction factors used are given in table 2.3 in section 2.7.2. The MFC outlets connect to a common gas inlet line which runs to the showerhead situated in the chamber lid. The showerhead helps to distribute the gas evenly in the chamber. The MFCs could be by-passed via a connecting tube to allow direct evacuation

back to the gas cylinders and also to allow the chamber to be vented with dry N_2 from a cylinder.

All connecting tubing is ¼-inch stainless steel or plastic (Enots) tubing except for a 45 cm long flexible stainless steel bellows which connects from the gas inlet line directly to the chamber. This allows the lid to be raised and lowered without disconnecting the gas supply.

2.3.4 THE PUMPING SYSTEM

The vacuum chamber was pumped by a rotary vane pump (Alcatel, type 2033 C) which in general provided a sufficient pumping speed for our purposes. Where higher pumping speeds were required (e.g. in experiments with high flow rates or low pressures), a Roots booster pump (Alcatel, type MV 350) was added in series with the rotary vane pump. The pumping speed, and hence the chamber pressure, was controlled by a butterfly throttle valve located just behind the chamber pumping port (figure 2.1). A valve next to the rotary vane pump provided the additional throttling necessary with the lowest flow rates used.

The base pressure to which we could evacuate the chamber was $\approx$ 5 mTorr.

2.3.5 THE RF POWER SUPPLY

RF power was provided by a power supply (ENI, model HF 300), capable of providing 0 to 300 W of rf power at 13.56 Mhz. The power supply was connected to a matching network consisting of two variable air capacitors and an inductor. By varying the capacitances it was possible to make the plasma, of unknown impedance, appear as a 50 Ω load to the power supply, and so allow maximum transfer of power. For all the conditions used in this work, the power reflected back to the generator was less than around 1 % of the forward power. The capacitor through which the power was supplied to the plasma acts

as a high pass filter, preventing any DC current from flowing. This allows a DC bias of typically several hundred volts to build up on the cathode (see section 1.6.6).

2.4 SAMPLING THE PLASMA

Diagnostics for the plasma were made using a 40 mm diameter port located in the side of the chamber lid. This port allows the attachment of the Plasma Diagnostics Assembly. This is shown in position in the process chamber in figure 2.3. Figure 2.4 shows the connection between the Omega reaction chamber and the QMS.

The Plasma Diagnostics Assembly bears a small quartz window which allows light from the plasma to be collected for analysis by Optical Emission Spectroscopy (section 2.5). It also bears Cajon coupling which holds a fine capillary probe protruding into the plasma (figure 2.3). This probe, with appropriate connecting tubing (figure 2.4), allows gas to be sampled for analysis by Quadrupole Mass Spectrometry (section 2.6). The arrangement allows the plasma to be monitored by Optical Emission Spectroscopy and Quadrupole Mass Spectroscopy simultaneously. Figure 2.5 shows the port and QMS connecting pipe with the light pipe positioned at the quartz window. Note that while taking data, the light pipe is held in a set position by a clamp (not shown in figures 2.4 or 2.5), to ensure that light originating from the same volume of the plasma is sampled in all experiments.

2.5 OPTICAL EMISSION SPECTROSCOPY

In this work we report a detailed study of the emission from F atoms in a range of electronically excited states in the wavelength range 6200 Å to 7400 Å using optical emission spectroscopy (OES). We now describe the optical system used for this work.

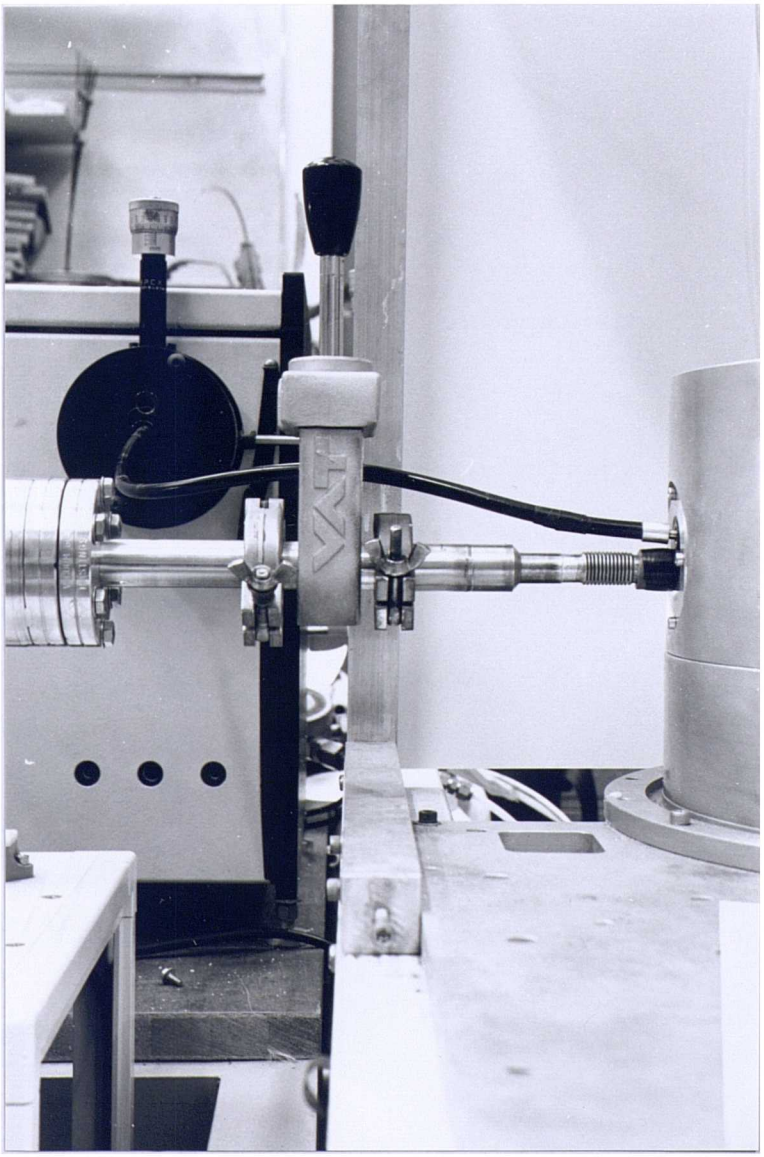

Figure 2.4. Photograph showing the connection between the Omega reaction chamber and the QMS. The light pipe is shown positioned at the quartz window.

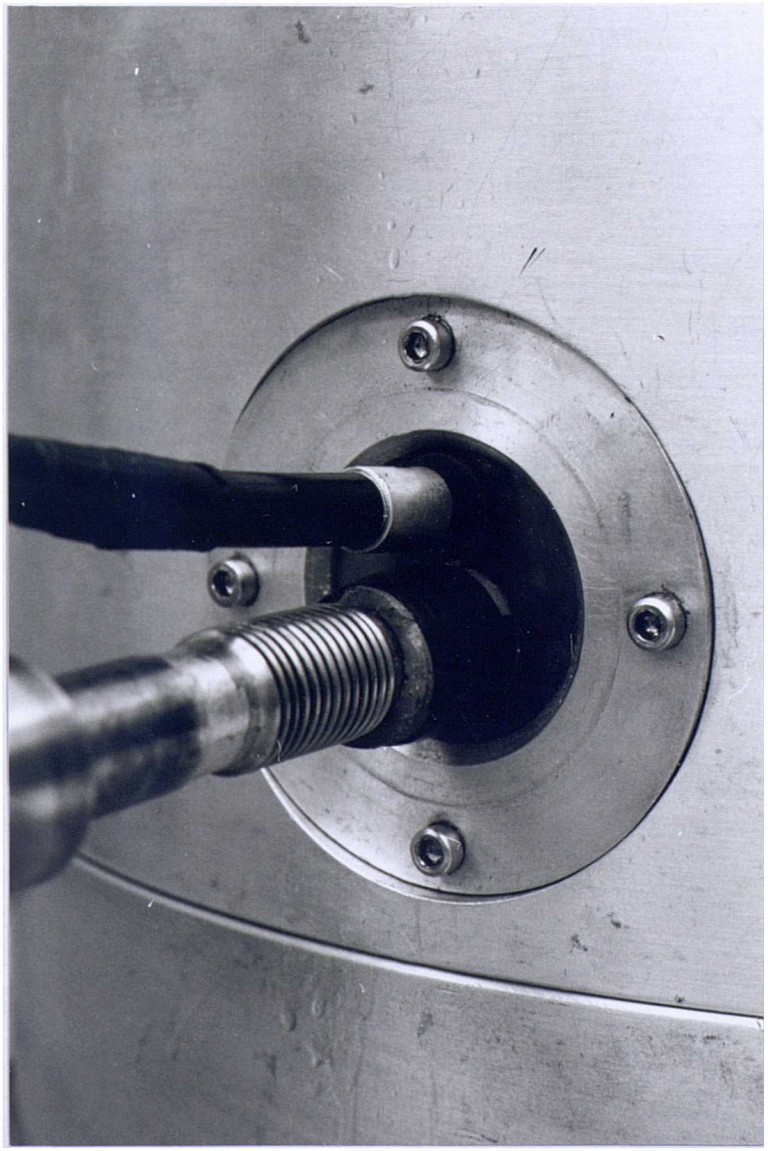

Figure 2.5. Close up photograph showing the port in the chamber lid and QMS connecting pipe, with the light pipe positioned at the quartz window.

2.5.1 THE OPTICAL SYSTEM

Light is sampled from the plasma through a small quartz window in the Plasma Diagnostics Assembly, which was described in section 2.4. Light is collected from this window by an optical fibre (Schott Glass Ltd.) capable of transmitting light down to 1900 Å, and allowed to fall onto the entrance slit of the optical spectrometer. The light from the plasma which reaches the detector originates from a large conical shaped volume defined by the acceptance angle of the optical fibre, which means that bulk rather than spatially selective spectra are recorded.

The spectrometer used was a 0.5 m SPEX (model 1870), incorporating a Czerny-Turner optical system, a 2400 lines per mm holographic grating giving 8 Å per mm dispersion, and a photomultiplier tube (Hammatsu, R955) suitable for the 1900 Å to 7500 Å wavelength range. The grating is scanned by a linear stepper motor. Spectra are recorded using a slit width of 125 μm and a slit height of 2 cm, giving a resolution of 1 Å. Light entering the spectrometer is chopped by an eight aperture light chopper (Rofin, model 7500) set at a chopping frequency of around 515 Hz. The resulting photomultiplier signal is then recorded using phase sensitive detection with a lock in amplifier (Brookdeal, model 9503-SC). Spectra are recorded at a scan speed of 0.25 Å s^{-1}, with fast output smoothing and a time constant of 1s. The amplifier output is then fed to a chart recorder (JJ Instruments, model PL4) to obtain a permanent record of spectra from which F atom emission line intensities can later be measured.

This optical arrangement does not allow the easy inclusion of filters to cut off second order harmonics. However, experiments conducted using a larger quartz window in place of the Plasma Diagnostics Assembly which allowed the use of filters showed that no shorter wavelength emissions are of sufficient intensity to give significant second order peaks in the spectral range of interest. The spectra measured in this work can therefore be considered as first order. Wavelength calibration of the spectra is achieved using Hg and Ne reference lamps. Spectral assignments were then made using data collated in references 91-94.

2.6 QUADRUPOLE MASS SPECTROMETRY

A commercial Quadrupole Mass Spectrometer (QMS) (VG Quadrupoles, model SX200) with SPECTRALAB PC software control was used in this work to measure the partial pressures of gas phase species sampled from the plasma. Its operating range of 0-200 amu with unit resolution was quite sufficient to monitor all the important unreactive molecules encountered in $CF_4 + O_2$ plasmas and when etching Si, Ge or SiGe alloy wafer substrates.

2.6.1 THE QMS ASSEMBLY

The QMS housing is constructed from stainless steel, with knife-edge Conflat flanges forming the vacuum seals. The housing is pumped continually by a turbomolecular pump (Balzers, model TPU 050, with TCP 121 controller) backed by a rotary vacuum pump (Alcatel, model 2002 BB), achieving a typical base pressure of less than $\approx 10^{-9}$ Torr with the QMS housing isolated from the Omega etcher. When sampling gas during etching, with a pressure of 85 mTorr in the Omega reaction chamber, the pressure inside the QMS housing rises to around 5×10^{-7} Torr, which is sufficiently low to allow safe operation of the QMS secondary electron multiplier (see later).

Ions are produced from neutral gas molecules in the ion source by electron impact with electrons produced by thermionic emission from a hot filament. The nominal electron energy used for ionisation was 70 eV. Ions thus produced are accelerated into a mass filter consisting of 4 parallel rods, each 125 mm long and 6.3 mm wide. Detection of ions is by means of either a Faraday Cup or a wide-bore channeltron Secondary Electron Multiplier (SEM). The SEM detector was used for all partial pressure measurements throughout this work due to its higher sensitivity and better signal-to-noise ratio.

2.6.2 EXTRACTING A GAS SAMPLE FOR ANALYSIS BY QMS

Gas for mass spectrometric analysis is sampled from the centre of the plasma via a fine capillary probe drawn out from a 8 mm diameter quartz tube. The probe has a total length of 130 mm. The capillary section ($\approx$ 110 mm long) has an outer diameter of around 1.1 mm and an internal diameter of around 0.8 mm. The wider 8 mm end which is held by the Plasma Diagnostics Assembly is made as short as possible ($\approx$ 15 mm) in order to minimise the disturbance to the plasma. The effects of the probe on the plasma and the gas sampled through it are discussed in section 2.6.4. Connection from the capillary to the QMS is made by a short connecting pipe containing a flexible bellows (see figure 2.4). The bellows allows the pipe to be manipulated and so facilitates its connection via a separable coupling to a gate valve, which in turn connects to the QMS. This valve is used to isolate the Omega reaction chamber from the QMS assembly in order to allow the chamber to be vented to atmospheric pressure without the need to break the vacuum inside the QMS.

2.6.3 COMPUTER CONTROL OF THE QMS: THE SPECTRALAB PC SOFTWARE

The SX200 QMS is interfaced to an IBM compatible SPECTRALAB PC computer from which all operations of the QMS are controlled. This has the effect of speeding up data collection and it also allows data to be stored on computer disk for later analysis. We now describe the modes of operation of the QMS using the menu driven SPECTRALAB PC software [95], and the way in which each was used in this work.

2.6.3.1 THE COMMAND PAGE

This screen is used to set up the QMS ready for an experiment and is split into different functions. From this screen, filament emission is obtained. Before taking data, the filament must be left for 15 minutes to stabilise. The total pressure can be measured using the Faraday cup, and provided the pressure is sufficiently low ($< 10^{-6}$ Torr), the SEM detector can be switched on and the detection voltage set. The voltage necessary for

suitable ion signal intensities was ≈ 1800 V (although this needed to be raised in stages throughout this work up to ≈ 2200 V because the response of SEM type detectors fades with use). The filament degas option can be selected to remove deposits from the filament surface by thermal desorption. This was found to be necessary in this work in order to obtain reproducible results (see section 2.6.4.2). In degas mode, the filament power is automatically ramped from 2 to 8 W over a period of 15 minutes to give the desorbed gases time to be pumped away.

2.6.3.2 ANALOGUE SCAN AND HISTOGRAM SCAN MODES

Analogue scan mode. In analogue scan mode, the mass spectrum is displayed "raw", ie. as it would appear if the detector output were displayed directly on an oscilloscope or chart recorder, with the mass scale on the x-axis and partial pressure in mbar on the y-axis. This allows the true peak shape and resolution to be viewed throughout the entire mass range. The mass range of interest can be selected and viewed at the required sensitivity (only one user-selected decade of partial pressures can be viewed at a time in analogue scan mode). The QMS then scans the selected mass range repeatedly, updating the screen continuously. The spectrum can be improved by the use of signal averaging, which is set to obtain a good compromise between the speed of data collection and the signal-to-noise ratio.

Histogram scan mode. In histogram scan mode, instead of scanning the selected mass range continuously, a single measurement is recorded by the QMS at a position where the top of each mass peak is assumed to be. The data is then presented as a histogram. The mass scale can be aligned by calibrating the instrument at two known, well separated mass peaks; the positions of all the other masses are then found by interpolation. In practice, however, there is still some non linearity in the mass scale, causing some measurements to be recorded on the peak shoulder and not at the peak top. This results in a false reading, although relative changes in intensity of mass peaks are still correctly indicated. In histogram scan mode, as with analogue scan mode, the signal can be averaged to improve the signal-to-noise ratio. A useful feature of histogram scan mode is that the partial

pressure axis may be displayed in logarithm format, allowing simultaneous observation of species which have very different partial pressures (the partial pressures of species in the QMS span the range 10^{-7} to 10^{-13} mbar).

In the initial stages of this work, it was necessary to identify species of interest, ie. ones arising from or removed by the action of the discharge, and ones involved in the etching of Si, Ge and SiGe alloys. Such species can be recognised by observing which species change in concentration when a plasma is switched on or off, or when a wafer is introduced to the plasma, and also with reference to previous work on similar systems [65], [28], [94]. Analogue and histogram scan modes were used for this purpose since all the masses 1 to 200 inclusive could be monitored quickly and easily. Once the important species had been identified, all subsequent data was recorded using Multiple Ion Monitoring mode, described below.

2.6.3.3 MULTIPLE ION MONITORING MODE

In Multiple Ion Monitoring (MIM) mode, the partial pressures of up to 16 different masses can be monitored simultaneously. The mass peaks to be monitored are entered into a "recipe", which can be stored on computer disk for future use. The recipe specifies the mass to charge ratio (m/q), a suitable species name for easy reference, and the number of cycles to be averaged to produce a value for the partial pressure. It was found that averaging over 16 cycles produced the best compromise between speed of data collection and signal-to-noise ratio. A single MIM recipe which contains details of all the important species was used for all the concentration measurements concerning CF_4 + O_2 plasmas. This recipe contained details of ion signals used to monitor the following parent species; CF_4, O_2, CO, CO_2, COF_2, C_2F_6, C_2F_4, F_2, SiF_4 and GeF_4.

Before taking data in MIM mode, the mass peaks to be monitored undergo a peak-lock routine which finds the location of the peak top. This is the point at which the subsequent partial pressure measurements will be recorded. This avoids the problems caused by non-linearities in the mass scale which occur in histogram scan mode. When the

run is started, the masses specified by the MIM recipe are scanned repeatedly, updating the screen at the end of each cycle. The data is presented either as a table of partial pressures, or as a trend graph of partial pressure versus time. In trend mode the partial pressure axis can display one linear decade or a user selected range of decades in logarithmic format.

MIM mode has several advantages over analogue and histogram scan modes. It allows observation of only the important mass peaks, and thus speeds up data collection by avoiding time wasted on the measurement of irrelevant mass peaks. It also displays data in real time as a graph, making it possible to see by visual inspection any changes in the partial pressure of monitored species as they occur. Furthermore, it allows the partial pressures to be presented in numerical form in a table from which data can later be extracted for further analysis (see section 2.9).

All data recorded using the SPECTRALAB PC software can be stored on computer disk. Using the Data Disk Operations facility, stored data can be reviewed later. This facility is particularly useful for results recorded in MIM mode. In this case, the results can be scanned through, one cycle at a time, to see numeric partial pressures and the exact time that each cycle was recorded. Selected data cycles can then be transferred to a separate file on computer disk, by the use of appropriate software. In this way, the data can easily be manipulated to allow the calculation of species concentrations (see section 2.9).

2.6.4 FACTORS AFFECTING THE QMS RESULTS

WE now discuss some of the factors which affect the analysis of the results obtained by QMS.

2.6.4.1 PROBE SAMPLING

The question which we ask here is this; does the gas which is sampled by the probe accurately represent the gas present in the plasma? This question can be split into three parts, which are considered below.

1) **Distortion of the plasma caused by the presence of the probe.** Some distortion of the plasma will occur due to the formation of a sheath potential around the probe. This sheath will cause an electrical disturbance extending a few Debye lengths into the plasma which could affect the local concentration of species near to and hence sampled by the probe. Previous work from this laboratory [53], [96], [54] has indicated that this effect is small, and, in addition, the rapid rates of diffusion in these plasmas would tend to reduce any gas phase inhomogeneities. For these reasons, electrical disturbances caused by the probe on the plasma are not expected to affect the partial pressures of gases sampled by it.

2) **Differential sampling by the probe.** It is possible that species of different mass are differentially sampled by the probe. However, gas entering the probe exhibits neither true viscous nor true molecular flow since the mean free path of gas molecules in the chamber ($\approx$ 0.3 mm at 85 mTorr) is comparable to the internal diameter of the capillary ($\approx$ 0.8 mm), making it very difficult to predict the exact sampling characteristics [97]. This problem is solved by the measurement of sensitivity factors (see sections 2.6.4.3 and 2.8.3.1) which take account of both QMS and probe sampling characteristics. This means that raw data can be adjusted later to correct for these effects (see section 2.9).

3) **Distortion of the sampled gas by chemical reactions within the probe.** The question here is this; does the composition of the gas sample alter due to chemical reactions occurring between the probe tip and the mass analyser? The gas flow regime is expected to change from near viscous flow as the gas enters the chamber to molecular flow after the gas has travelled only a short distance along the probe. Consequently, it seems very unlikely that gas phase reactions will occur in the probe since gas molecules will collide much more frequently with the probe inside walls than with each other. Therefore the only reactions which could be important are heterogeneous reactions occurring on the internal surfaces of the probe. It is

difficult to estimate *a priori* the importance of this effect, so several experiments were performed in order to test the effects of transit through the probe on the sampled gas. These experiments are described in section 2.8.3.2, and the results are presented in chapter 3. The results indicate that radical species are not detected, and that minimal perturbation is caused to the concentrations of unreactive species in transit along the probe. This means that the true concentrations of unreactive species present in the chamber can be determined (see section 2.9).

2.6.4.2 VARIATION IN THE QMS PERFORMANCE

It was found that the QMS sensitivity and the measured cracking patterns could vary from run to run or even during a single run. The QMS performance in this respect was monitored by observing the absolute and relative intensities of the CF_3^+ and O_2^+ ion signals (due to CF_4 and O_2 parent molecules) with CF_4 + 8 vol % O_2 process gas present in the chamber with no plasma running. Clearly the signal strength and the ratio of the CF_3^+ and O_2^+ ion signals is fixed by the feed gas pressure and composition. Any deviation in the CF_3^+ or O_2^+ ion signals therefore gives an indication that the QMS performance is changing. In practice, the ion signal intensity ratio of CF_3^+ / O_2^+ is observed to change slowly with each plasma run, accompanied by a gradual loss in overall instrument sensitivity.

This problem was found to be due to contamination of the filament, probably caused by the build up of polymer on its surface. It was solved by ensuring that the filament was degassed at regular intervals (section 2.6.3.1), typically after around 10 hours of running time. In this way signal reproducibility of within $\approx \pm 8$ % was ensured throughout the QMS experimental results, determined using the CF_3^+ / O_2^+ ion signal intensity ratio (which was measured before and after every run). Note that the measurements of the plasma composition are only affected by changes in relative signal intensities; an overall loss in instrument sensitivity can be corrected for later (see section 2.9).

2.6.4.3 CRACKING PATTERNS AND SENSITIVITY FACTORS

In order to convert raw QMS data into true partial pressures and concentrations of species, it is necessary to take into account cracking patterns and sensitivity factors, as we now explain.

Sometimes two different species may produce a signal at the same (m/q). For example both COF_2 and SiF_4 produce a signal at (m/q)=47 due to the ions COF^+ and SiF^+ respectively. In cases where the cracking patterns of more than one species overlap it is necessary to deconvolute the two signals to obtain true partial pressures.

In addition, the QMS has a different sensitivity towards different species, ie. for the same partial pressure of different species, a different signal strength is obtained. This could be due, for example, to different ionisation efficiencies [98] or differential probe sampling (section 2.6.4.1). This means that scaling factors need to be applied to obtain the true partial pressures.

Raw data from the QMS can thus be corrected by simple numerical adjustment provided the cracking patterns and sensitivity factors of all the relevant species are known. Some of this information is listed in reference [99] for sector field mass spectrometers. However, due to differences in mass spectrometer design and gas sampling characteristics it does not correspond accurately to the SX200 QMS and probe sampling system used in the present work (see section 3.2). Consequently, it was necessary to measure cracking patterns and sensitivity factors for pure samples of each species of interest using our system, in order to account for its unique characteristics. The methods used to measure these parameters are described in section 2.8.3.1, and the results are presented in section 3.2.

2.7 MATERIALS

2.7.1 WAFERS

Full details of the Si and Ge wafers used for etching are given in table 2.1 below. For some experiments, whole wafers were cleaved to obtain smaller pieces.

Wafer	Diameter	Type	Dopant	Resistivity / Ω cm	Thickness / mm	Supplier
Si(100)	3"	p	B	14-20	0.36-0.41	Monsanto Co.
Ge(100)	3"	n	not specified	6.2-9.4	0.2-0.3	Hoboken

Table 2.1. Details of the Si and Ge wafers used.

The SiGe alloy layers used for etching experiments were grown to our specification by Dr. Chris Gibbings and Dr. Chris Tuppen at BTL by Molecular Beam Epitaxy (MBE, see section 1.3.3.1) using a VG Semicon V80 MBE system fitted with Airco Temescal electron beam evaporators and a Sentinal flux control system (a description of the MBE system is given in [19]). These layers were grown onto 3" Si (100) substrate wafers to a nominal thickness of 2 μm. This thickness is greater than the critical thickness, and the layers are therefore relaxed (see section 1.4). During MBE layer growth, the sample holder protects a $\approx$ 1 mm wide ring around the edge of the wafer from the molecular beam. This results in a step which allowed the actual layer thickness to be measured later at Bristol using a Tallysurf (Taylor-Hobson) surface profiler (see section 1.9.6). SiGe alloy layers were grown with 33 mol % and 67 mol % Ge content (both $\pm \approx$ 3 %). 7 wafers of each composition were grown. Full details of these layers are given in table 2.2 below.

mol % Ge content	Thickness / μm $\pm$ 5 %	mol % Ge content	Thickness / μm $\pm$ 5 %
33	2.2	67	2.15
33	2.35	67	2.2
33	3.1	67	2.25
33	2.2	67	2.1
33	2.2	67	2.1
33	2.1	67	2.1
33	2.3	67	2.1

Table 2.2. Thickness and composition of the SiGe alloy layers.

2.7.2 GASES

The process gas used throughout most of this work was CF_4 + 8 vol % O_2. Other gases which were added to the feed gas for some experiments were O_2, CO, CO_2 and C_2F_6. Details of all the gases used in this work are listed below in table 2.3. Cracking pattern and sensitivity factor measurements were made for all the gases listed.

Gas	Container	Source	purity / %	MFC correction factors
CF_4 / O_2	cylinder	BOC (Electra II)	99.7	0.42
CF_4	cylinder	BOC (Electra II)	99.7	0.42
O_2	cylinder	BOC (Electra II)	99.98	1.00
CO	cylinder	BOC	99.5	1.00
CO_2	cylinder	BOC	99.5	0.74
C_2F_6	cylinder	BOC (Electra II)	99.5	0.24
COF_2	gas bulb	Made in-house	≈ 98	-
C_2F_4	gas bulb	Fluorochem	≈ 97	-
SiF_4	gas bulb	Cambrian Chemicals	≈ 99	-
GeF_4	gas bulb	Made at Birmingham University	* not known	-

* = the mass spectra revealed only insignificant impurity levels.

Table 2.3. Details of the gases used. The GeF_4 was kindly made available by Dr. R.P. Tuckett, Chemistry Dept., University of Birmingham. The GeF_4 was prepared at Birmingham by Dr. A.J. Edwards, by passing F_2 over a sample of finely ground Ge in a stainless steel reaction vessel. The GeF_4 product was then purified by trap-to-trap distillation and pre-mixed in a 0.3 litre lecture bottle with He at a pressure of 650 psi (≈ 20 % mixture). Thanks are due to Karl O'Mahoney, Chemistry Dept., University of Bristol, for providing C_2F_4 and SiF_4 gas samples, for transferring the GeF_4 sample to the gas bulb, and for general assistance with the handling of the gases contained in gas bulbs during the cracking pattern and sensitivity factor measurements. He also kindly prepared the COF_2 sample, using a corona discharge through C_2F_4 and O_2. The MFC correction factors are given relative to N_2 [90].

2.8 EXPERIMENTAL PROCEDURES

2.8.1 SIMULTANEOUS QMS AND OES MONITORING OF THE PLASMA

In this section we describe the experimental procedures used to operate the Omega RIE apparatus and to monitor the plasma by QMS and OES. Three types of experiment are described. We first describe the experiments which were performed using CF_4 + 8 vol % O_2 process gas with no wafer (NW) present and with Si and Ge wafers present, in which the plasma composition was monitored as a function of the experimental conditions of flow rate, rf power, gas pressure and the surface area of Si and Ge exposed to the plasma (section 2.8.1.1). We then describe the experiments in which the plasma composition was monitored as a function of feed gas composition with NW present (section

2.8.1.2). Finally, we describe the experiments in which SiGe alloy layers were etched using CF_4 + 8 vol % O_2 process gas (section 2.8.1.3).

2.8.1.1 THE EXPERIMENTS WITH NW, Si AND Ge PRESENT

The experimental parameter space which has been covered with each of NW, Si and Ge present is summarised in table 2.4 below.

Experiment name	Variable parameter	Fixed parameters
FLOW RATE	2 - 50 sccm	100 W, 85 mTorr, Const. area
PRESSURE	10 - 85 mTorr	5 sccm, 100 W, Const. area
AREA AT 5 sccm	0 to 1 wafer	5 sccm, 100 W, 85 mTorr
AREA AT 50 sccm	0 to 1 wafer	50 sccm, 100 W, 85 mTorr
POWER AT 5 sccm	10 - 200 W	5 sccm, 85 mTorr, Const. area
POWER AT 50 sccm	10 - 200 W	50 sccm, 85 mTorr, Const. area

Table 2.4. Table showing the experimental conditions used for the NW, Si and Ge etching experiments.

We now describe in detail the procedures used for the collection of these results.

The procedural steps described below begin with the apparatus set up prior to the run as follows. The chamber, with no wafer present, is initially pumped down to base pressure ($\approx$ 5 mTorr) right back through the vent line to the shut off valve of the CF_4 + 8 vol % O_2 gas cylinder, and the water cooling is on. The gate valve between the QMS and the plasma chamber is open and the QMS housing is at a pressure of typically 2 x 10^{-8} Torr, with the QMS ion source filament switched off. The optical detection system is switched on with the PMT set to 700 V, and the optical fibre is clamped in place at the quartz viewing window, but with the slits of the optical spectrometer closed.

1) **Setting up the gas flow and the chamber pressure.** First, the vent line is closed off, and the CF_4 + 8 vol % O_2 process gas is allowed to flow into the chamber through the MFC, which is set to the required flow rate. The chamber pressure is

then adjusted using the throttle valve to $\approx$ 5 % lower than the required pressure (to allow for a rise in pressure due to dissociation in the plasma). The pressure in the QMS housing now rises typically to $\approx 5 \times 10^{-7}$ Torr (for $\approx$ 85 mTorr chamber pressure).

2) **Data collection using the QMS.** Once the pressure in the chamber and in the QMS housing has stabilised, the QMS filament is switched on to obtain emission, and the SEM voltage is then set. Before any data is collected, the filament is left on for at least 15 minutes to stabilise. MIM mode (section 2.6.3.3) is then selected, and QMS scanning is started using the MIM recipe which contains all the species of interest.

3) **Switching on the plasma.** The plasma is now ignited by ramping the rf power to the required setting. This generally causes an initial pressure overshoot by typically $\approx$ 30 % of the steady state pressure due mainly to the initial desorption of water and its reaction products from the chamber walls. The pressure then falls slowly as the plasma approaches the steady state.

4) **Weathering the chamber.** While the plasma is running, with the QMS scanning continuously, the slits of the optical spectrometer are opened to 125 μm x 2 cm (in order to avoid problems of backlash, the slits are first opened wider than 125 μ, then closed down to this setting). The spectrometer is then tuned to observe the strong F atom emission line at 6856 Å as the plasma approaches the steady state. The approach to the steady state, which we refer to as "weathering", is thus monitored by both QMS and OES. It may take up to an hour or even longer for concentrations to stabilise depending on the process conditions. Weathering is mainly due to the need to remove water from the chamber, and to a lesser extent due to the need to passivate the walls of the chamber (this process is discussed in more detail in section 7.2). The plasma is always allowed to reach a steady state

before collecting the data which will be used for determining the plasma composition.

5) **Recording OES data.** Once the steady state is reached, the optical spectrometer is set to 6200 Å, and is scanned through to 7400 Å to observe F atom emission line intensities. Data was collected by scanning rapidly at 2.5 Å s^{-1} between the F atom emission lines to save time, and then reducing the scan speed to 0.25 Å s^{-1} to observe each individual line at better signal to noise. The sensitivity of the lock-in amplifier is adjusted as necessary to allow for the different intensities of these lines. The procedure takes around 30 minutes to complete. During this time, the QMS takes data continuously, storing them on computer disk for later analysis.

6) **Plasma shut-down.** Once all the data has been collected, the rf power is turned off, noting the time for which the plasma has run (typically between 60 and 120 minutes in total). The QMS is allowed to continue scanning for several more minutes to allow background concentrations to be measured. The QMS is then shut down by switching off the SEM and the filament, and by closing the gate valve between the QMS and the plasma chamber. The slits of the optical spectrometer are closed as a precaution against stray light, and the gas flow to the chamber is stopped, allowing the chamber to return to base pressure.

7) **Introducing a wafer to the chamber for etching.** The Baratron is isolated from the chamber by a Nupro valve to prevent it being damaged by a sudden jump in pressure. The chamber is then isolated from the pump at the high vacuum valve, and brought to atmospheric pressure using dry N_2 from a cylinder, admitted via the vent line. The separable coupling between the plasma chamber and the QMS is disconnected, and a plastic cap is quickly placed over the end of the pipe which connects between the separable coupling and the chamber. This is done in order to reduce the adsorption of water onto the internal surfaces of the pipe and so to

reduce the pump-down time of the QMS housing when the gate valve is later re-opened. The chamber lid is then raised pneumatically, with N_2 still flowing through the chamber to reduce the in-flow of water from the air, and a wafer is inserted as quickly as possible using wafer tweezers. The chamber lid is then closed, the separable coupling is re-made, the N_2 flow is stopped and the chamber is pumped down again. Once the pressure in the chamber has fallen below around 20 mTorr, the gate valve is opened. This results in a transient increase of pressure in the QMS housing to around 10^{-4} Torr due to the higher pressure in the connecting pipe. The QMS pressure then falls slowly back to the 10^{-8} Torr range while the pressure in the chamber falls back to $\approx$ 5 mTorr. This typically takes around 30 minutes, but depends on how much water was admitted while the wafer was inserted. Note that this delay time was reduced greatly for the SiGe alloy etching experiments by enclosing the entire chamber lid in a large N_2-filled polythene bag to help exclude water (see section 7.2). The apparatus has now been returned to the same state that it was in prior to step 1, but with a wafer present.

8) **The Si and Ge wafer etching experiments.** Steps 1 through 7 are now repeated with a wafer substrate present using the same operating conditions.

9) **Preparing the apparatus for the next set of experiments.** After each set of experiments, the chamber lid is unbolted and removed from the etcher to allow the process chamber to be cleaned ready for the next set of experiments. This is done to prevent the build up of polymer which may accumulate after many runs, and so to ensure that the chamber is in the same state prior to each set of experiments (although in hindsight, it appears that this precaution is not necessary for reproducible results). The filament of the QMS ion source is now degassed if necessary, usually after around 10 hours of running (see section 2.6.4.2). The apparatus is then reassembled and pumped down overnight ready for the next set of experiments.

Using the experimental procedures described above, a given set of process conditions in the flow rate, power and pressure variation experiments could be examined in a single day for NW, 3" Si and 3" Ge wafers present. In the area variation experiments, two days were necessary because more runs were performed with wafers of different areas.

The method by which species concentrations are calculated from the raw data recorded during these experiments is described in section 2.9.1, and the results are presented in section 4.2 and in section 5.2.3.

2.8.1.2 THE GAS ADDITION EXPERIMENTS

In the gas addition experiments, the composition of the feed gas mixture was varied by flowing two different gases through separate MFCs at variable rates, while all the other experimental parameters remained constant. Actual gas flow rates were determined by dividing the indicated flow rate by the appropriate correction factors, given in table 2.3 (section 2.7.2). In one experiment, O_2 was added in various proportions (0 to 20 vol % additions) to pure CF_4 process gas. In another series of experiments, various proportions of CO, CO_2 and C_2F_6 (0 to 40 vol %) were added to CF_4 + 8 vol % O_2 process gas. All these experiments were performed with no wafer present at conditions of 5 sccm total flow, 100 W and 85 mTorr.

All the gas composition measurements for each system of gases were performed during one plasma run, by changing the gas mixture without extinguishing the plasma. The different feed gas mixtures were run in random order to reveal specious results. Many of the experimental procedures used for the gas addition experiments are similar to those described in steps 1 to 9 in section 2.8.1.1 above. We now describe these procedures with reference to steps 1 to 9, highlighting the differences where they occur.

Before each experiment, the chamber is weathered using CF_4 + 8 vol % O_2 process gas (steps 1 to 4). The plasma is then switched off, and the QMS is re-started with process gas flowing, but with no plasma running in order to obtain background signals.

The plasma is then re-started and allowed to stabilise ready for data collection. Gas composition data is recorded as in step 5, except that optical spectrometer is scanned within the narrower wavelength range of 6800 Å to 7150 Å. This range contains all the F atom emission lines which have been found to be of interest (see chapter 6). Once the OES data has been collected for each gas mixture, the MFC settings are altered to give the next gas mixture, keeping the total flow rate constant at 5 sccm. The plasma is again allowed to stabilise (usually taking < 5 minutes) and the OES scan is repeated. All the different feed gas mixtures were run in this way, with the QMS scanning continuously. The run ends with CF_4 + 8 vol % O_2, as at the start of the experiment, allowing a check on reproducibility. The plasma is then switched off as in step 6. The method by which species concentrations are calculated from raw QMS data recorded during the gas addition experiments is described in section 2.9.2, and the results are presented in section 4.2.

2.8.1.3 THE SiGe ETCHING EXPERIMENTS

In the SiGe alloy etching experiments, the seven pairs of SiGe alloy layers (33 mol % and 67 mol % Ge content) on 3" Si wafers were etched at sets of different conditions which cover the widest possible process parameter space. Each set of conditions has also been used to etch Si and Ge, allowing the results to be compared. Full details of the SiGe layers and the experimental conditions used for etching are given in table 7.1 in section 7.3.

In the SiGe alloy etching experiments, it was necessary to reduce the time needed to weather the chamber. This is because the plasma must reach the steady state before the underlying Si is exposed in order to allow true steady state concentrations over SiGe alloy to be measured. As discussed earlier, the main cause of the need for weathering is contamination of the chamber by water, which is introduced when wafers are inserted. In order to reduce this contamination in the SiGe alloy etching experiments, the entire chamber lid was enclosed in a large polythene bag which was flushed with dry N_2 from a

cylinder while wafers were inserted. The problems of weathering in the SiGe alloy etching experiments are discussed in more detail in section 7.2.

As with the gas addition experiments, many of the experimental procedures used for the SiGe alloy etching experiments are similar to those described in steps 1 to 9 in section 2.8.1.1. We now describe these procedures, again with reference to steps 1 to 9, highlighting the procedural differences where they occur.

The chamber is first weathered to CF_4 + 8 vol % O_2 process gas at the selected process conditions (steps 1 to 4). Then, half a 3" Si and half a 3" Ge wafer are introduced to the chamber and etched together until the steady state was reached. This was done in an attempt to reduce the weathering time in the subsequent SiGe alloy run (see section 7.2). Then, the SiGe alloy layers are etched. In each case, the SiGe layer was completely removed, monitoring the endpoint by QMS, and etching was continued into the underlying Si substrate. During each experiment, the plasma was monitored continuously by QMS from several minutes before the plasma was switched on to several minutes after it was switched off in order to obtain species concentrations and to measure background signals. Before the endpoint was reached, the F atom emission intensity at 6856 Å was measured by OES. The intensity of this emission line has been shown to be a reliable indicator of [F] in the plasma (see section 6.3.1). The methods by which species concentrations were calculated from the raw QMS data recorded during the SiGe alloy etching experiments are described in section 2.9.3, and the results are presented in section 7.4.1.

2.8.2 THE MEASUREMENT OF ETCH RATES

The etch rates of Si and Ge wafers were determined by the method of weight loss. Each wafer substrate was weighed prior to and after the etching process, and the etch rate was calculated using the etch time, the substrate density and the substrate surface area exposed to the plasma. For SiGe alloy material, the etch rate was determined by measuring the time taken to etch through the SiGe layers (section 7.4.2). The layer thickness was

measured using a surface profiler, as mentioned earlier, and the endpoint time was determined by QMS (see section 7.4.1).

2.8.3 EXPERIMENTS PERFORMED IN ORDER TO CHARACTERISE THE QMS TECHNIQUE

We discussed in section 2.6.4 some of the factors which affect the QMS results. We now describe the experiments which were performed in order to characterise the QMS technique. These include the measurements of cracking patterns and sensitivity factors, and also the experiments which were performed in order to prove that the capillary probe allows a minimally distorted sample of gas to be transmitted to the QMS ion source.

2.8.3.1 THE MEASUREMENT OF CRACKING PATTERNS AND SENSITIVITY FACTORS

Cracking patterns and sensitivity factors were measured for CF_4, O_2, CO, CO_2, COF_2, C_2F_6, C_2F_4, SiF_4 and GeF_4. This was necessary in order to isolate a single ion signal which would act as a monitor of each parent species of interest. It also allowed the raw QMS data to be corrected later for the overlap of cracking patterns from different species and for the different sensitivity of the QMS diagnostic system towards different species (see section 2.6.4.3). Cracking patterns were measured by recording a mass spectrum with the pure gases present in the chamber at a pressure of 85 mTorr. Sensitivity factors for the ion signal of interest were measured relative to CF_3^+ (from CF_4 parent molecules) = 1 by calibrating with a CF_4 standard before and after each cracking pattern measurement. The procedures used for these measurements are detailed in steps 1 to 5 below.

1) **Calibration of the QMS to a CF_4 standard.** The chamber was brought to a pressure of 85 mTorr with CF_4 + 8 vol % O_2 flowing through the chamber with no plasma running. The QMS was set to MIM mode and the intensity of the CF_3^+ ion signal (from CF_4 parent species) was measured. This was used as the standard for

the sensitivity factor measurements. The presence of the O_2 allowed the performance of the QMS to be checked by observing the CF_3^+ / O_2^+ intensity ratio (see section 2.6.4.2). (Note that the CF_3^+ ion signal was corrected later for the 8 vol % O_2 dilutant in the CF_4 standard).

2) **Admitting the test gas to the chamber.** The chamber was pumped out to base pressure, and then returned to 85 mTorr with the gas to be tested. The gases were admitted by different methods depending on whether they were contained in gas cylinders or in gas bulbs. Gases contained in pressurised cylinders (CF_4, O_2, CO, CO_2 and C_2F_6) were admitted to the chamber through a MFC and the pressure was set to 85 mTorr by balancing the throttle valve position and the flow rate. The remaining gases (COF_2, C_2F_4, SiF_4 and GeF_4) were contained in 565 cm^3 gas bulbs with Young's Taps to isolate the gas. The gas bulbs also had a cold finger to allow the gas to be frozen using a liquid N_2 bath. These gases were admitted to the chamber as follows. The gas bulb was connected to the chamber via a glass coupling joint (B 14) which in turn was connected via a specially made connecting pipe directly to the gas inlet line, through a Nupro isolation valve. The gas sample was then frozen, and the gas bulb was opened to the chamber to pump out any residual gases. The vacuum pump was then isolated at the high vacuum valve, and the liquid N_2 bath was removed from around the cold finger to allow it to warm up. As the temperature rose and the frozen sample began to evaporate, the chamber pressure slowly increased. When the pressure reached 85 mTorr, the gas bulb was isolated from the chamber using the Nupro valve.

3) **Measuring the mass spectrum.** Once the test gas was present in the chamber at a pressure of 85 mTorr, the mass spectrum of the test gas was recorded. This was done in MIM mode (section 2.6.3.3), using a recipe containing all the important mass fragments. (Note that these measurements were made in less than $\approx$ 5 minutes

so that the gas samples used from gas bulbs were not contaminated by air leaks by more than $\approx$ 1 %).

4) **Measuring background signals.** The test gas was pumped out, and the chamber was returned to base pressure. This was done while still monitoring with the QMS in order to measure backgrounds so that they could be subtracted later.

5) **Re-checking the QMS calibration.** Step 1 was then repeated in order to check that the QMS performance had not changed during the measurements.

The results of the cracking pattern and sensitivity factor measurements are presented in section 3.2.

We note that the gases sampled from the plasma during etching are not pure gases, as were used in the measurements above, but will be transmitted to the QMS in a carrier gas of (mostly) CF_4. In addition, some etching experiments were performed at pressures other than 85 mTorr (which was the pressure used for the above measurements). It might therefore be expected that gas molecules of different masses would be differentially sampled, causing a distortion to the calculated concentrations of plasma species when using sensitivity factors measured by the methods described above. However, this can be shown not to be the case by considering the O_2^+ ion signal measured from the CF_4 + 8 vol % O_2 process gas with no plasma running. In this case, the calculation of the concentration of O_2 in the chamber using the sensitivity factor for O_2 (measured as above using pure O_2) agrees with the 8 vol % O_2 known to be present in the feed gas, for all the pressures studied in this work.

2.8.3.2 TESTING THE EFFICACY OF THE PROBE SAMPLING TECHNIQUE

1) **Probe coatings.** In order to study the effectiveness of the probe sampling technique, several internal capillary probe surface coatings were tested. These were PTFE (as a colloidal dispersion, Dupont, Vydax 550), Silver Dag colloidal silver paint and Photoresist (Shipley S1818). These coatings were all applied as follows. The probe capillary was first cleaned with acetone and rinsed with distilled water and dried. The coatings were then sucked through the entire length of the probe and allowed to drain. To avoid clotting of the capillary, dry N_2 was passed through the probe for $\approx$ 1 hour while the coatings hardened. The probe was then baked in an oven at $\approx$ 80 °C for an hour. The findings of these tests are discussed in section 3.3.1.

2) **Probe conductance experiments.** In order to test the effects of different probe conductances, several probe capillaries with different internal diameters were made. The composition of the plasma was measured by QMS for conditions of 5 sccm, 100 W and 85 mTorr with no wafer present using each of these probes in order to prove that different probe conductances did not affect the measured plasma composition. The results of these experiments are given in section 3.3.3.

3) **Sampling within the effluent vs within the plasma.** An experiment was performed to make a comparison of the gas composition measured by QMS when sampling with the probe tip within the plasma with that measured with the probe tip within the effluent. As with 2) above, conditions of 5 sccm, 100 W and 85 mTorr with no wafer present were used for this comparison, and the following procedure was adopted. The composition of the plasma was first measured by QMS with the probe tip within the plasma. The Plasma Diagnostics Assembly was then unbolted from the chamber lid and the probe was removed from the Cajon coupling. The probe was then bent in a hot flame by an angle of 90° at the point where the 8 mm

wide section of the probe narrows to form the capillary section. This bend made it possible to manoeuvre the probe tip into the effluent through one of the 16 pumping holes between the plasma and the dead space, allowing gas to be sampled at a point $\approx$ 80 mm downstream from the plasma. The results of this experiment are presented in section 3.3.4.

2.9 CALCULATIONS OF ABSOLUTE SPECIES CONCENTRATIONS FROM RAW QMS DATA

In this section, we describe the method by which concentrations of gas phase species present in the plasma were calculated from raw QMS data. This requires corrections for background signals, cracking pattern overlap and for different sensitivity factors. The raw QMS data was always collected in MIM mode (section 2.6.3.3), and all calculations were performed using the spreadsheet software package LOTUS 123. The method of calculating species concentrations was similar for the experiments with NW, Si and Ge, the gas addition experiments and the SiGe alloy etching experiments. We first explain how concentrations were calculated for the NW, Si and Ge etching experiments and then highlight the differences in the method used for the gas addition and SiGe alloy etching experiments.

2.9.1 THE NW, Si AND Ge ETCHING EXPERIMENTS

The raw QMS data is stored in separate data files; one file for each set of experimental conditions and for each different wafer substrate (NW, Si or Ge). These data files contain typically 300 data cycles which were recorded during the experiment. Each cycle contains the partial pressures of each of the species included in the recipe, and the time at which the cycle was recorded. The calculations of species concentrations from this raw QMS data were carried out as follows for each of these data files.

1) **Transfer selected data cycles from the raw QMS data files to LOTUS 123.** Selected cycles of data were transferred from files containing the raw MIM data to separate data files. These cycles were; 12 data cycles with process gas only ("no plasma") which were recorded after the plasma was switched off at the end of the run, and 12 cycles with a plasma running ("plasma on") recorded just before the plasma was switched off (i.e. after the steady state was reached). Thus data cycles which were recorded only $\approx$ 2 minutes apart were used for the calculations, during which time the QMS performance did not change significantly. The two sets of 12 data cycles were then transferred into LOTUS 123 for the calculations.

2) **Take an average of the data cycles to obtain partial pressure readings.** The sets of 12 data cycles were averaged to produce values for the partial pressures of each (m/q) in the MIM recipe, both with a plasma running, and also with no plasma to obtain background signals.

3) **Subtract the backgrounds.** For species formed by the action of the discharge, the "no plasma" background signal (usually small) was subtracted from the "plasma on" signal. For gases present in the feed (ie. CF_4 and O_2), the "plasma on" signal was taken directly.

F_2 requires special attention because CF_4 molecules in the feed gas produce a background signal at (m/q)=38, corresponding to F_2^+, which can be large compared with the F_2^+ signal from F_2 parent molecules. When wafers are present in the chamber, $[F_2]$ is reduced to very low levels, which results in the F_2^+ signal from CF_4 parent molecules being up to an order of magnitude stronger than the F_2^+ signal from F_2 parent molecules themselves, introducing large uncertainties into the calculation of $[F_2]$. Therefore, $[F_2]$ data is only presented with no wafer present where $[F_2]$ in the plasma is larger.

4) **Normalise the partial pressure readings.** The overall sensitivity of the QMS varied slightly from run to run (section 2.6.4.2), so it was necessary to calibrate all the data to some common standard to allow comparison of data from different runs. The pressure and composition of the CF_4 + 8 vol % O_2 feed gas in the chamber with no plasma running is known, and was measured in each case, so the CF_3^+ ion signal (from CF_4 in the feed gas) was used to calibrate the QMS sensitivity. The standard used was, arbitrarily, CF_3^+ measured partial pressure = 10^{-7} mbar with 81 mTorr of CF_4 + 8 vol % O_2 feed gas present in the plasma chamber. When a plasma is struck, the pressure rises by $\approx$ 5 % (a value which is fairly independent of plasma conditions). 81 mTorr is the initial feed gas pressure necessary to give an 85mTorr plasma. The results from plasmas run at pressures other than 85 mTorr were scaled to this standard.

5) **Adjust the partial pressures for cracking pattern overlap.** The data was adjusted for the cracking pattern overlap of some species (section 2.6.4.3) using the measured cracking patterns given in table 3.1 in section 3.2.

6) **Apply sensitivity factors.** Sensitivity factors, relative to CF_3^+ (from CF_4 parent molecules) = 1, were then applied (see section 2.6.4.3) to bring the data for different species onto the same relative partial pressure scale.

7) **Convert partial pressures to the required units of concentration.** The partial pressures were then converted to the desired units using the relationship that an ion signal of 10^{-7} mbar corresponds to (81 x 0.92) = 74.5 mTorr of gas in the plasma chamber. The species concentrations calculated in this work are presented as mole percentage compositions in all cases since the numbers obtained are easier to conceptualise. However, units of molecules cm^{-3} have been used for the kinetic calculations of chapter 4.

Using this process, the concentrations of species present in the discharge are calculated from the raw data recorded during the NW, Si and Ge etching experiments. The results of the calculations are presented as graphs of mole percentage composition vs varying process parameter in sections 4.2 and 5.2.3.

2.9.2 THE GAS ADDITION EXPERIMENTS

The methods used to calculate species concentrations from raw data recorded during the gas addition experiments are similar to the methods described in the previous section for NW, Si and Ge etching data (steps 1 to 7). The only differences are due to changes in the QMS performance during each run as a result of the longer duration of these experiments, as we now explain.

In the calculations described in the previous section, all of the raw data cycles which were used to determine species concentrations were recorded only $\approx$ 2 minute apart, during which time the QMS performance does not change significantly. However, the duration of the gas addition experiments was much longer, taking more than 2 hours to collect all the data for all the gas mixtures studied. During this time the QMS performance may change slightly (see section 2.6.4.2), although usually by less than $\approx$ 10 % as measured using the CF_3^+ and O_2^+ ion signals. In addition the background signals were sometimes found afterwards to have changed by small factors during the run. To take account of these effects, it was assumed that the background ion signals with no plasma running change linearly throughout the run. Thus the "no plasma" data cycles which were recorded before and after the time when plasma was running were transferred from the raw data files to separate files and then into LOTUS 123, where linear interpolation was used to find the background signals at the intermediate times when the plasma was on. This procedure was necessary for background signal subtraction (step 3), and also for normalising the data using the CF_3^+ ion signal (step 4).

12 raw "Plasma on" data cycles were transferred for each different feed gas composition using data which was recorded just before the experimental gas flow rates

were adjusted to the next feed gas composition. This procedure and that described above for the "no plasma" ion signals, replace step 1 from the calculations in the previous section. Species concentrations are then calculated using steps 2 to 7. The results of the species concentration calculations for the gas addition experiments are presented in section 4.2.

2.9.3 THE SiGe ETCHING EXPERIMENTS

The SiGe etching results were required to be presented in two forms. Firstly as species concentrations vs time (temporal results) and secondly as steady state species concentrations over SiGe alloy (i.e. before the endpoint is reached) vs varying process conditions. The steady state concentrations were calculated using the same approach as that used for the gas addition experiments above. (Note however that the steady state was not always reached before the endpoint. This is discussed in section 7.5). In order to obtain temporal results, selected data cycles were transferred from the raw "plasma on" data but were not averaged for the calculation of species concentrations because we wish to observe changes in species concentrations with time. The results of the species concentration calculations for the SiGe alloy etching experiments are presented in section 7.4.1.

CHAPTER 3

THE APPLICATION OF THE MASS SPECTROMETRY TECHNIQUE

3 THE APPLICATION OF THE MASS SPECTROMETRY TECHNIQUE

3.1 INTRODUCTION

In this chapter, we describe some important aspects of the use of the QMS to measure the concentrations of species in the plasma. In section 3.2, we present the results of the cracking pattern and sensitivity factor measurements, which are essential for quantitative results. Then, in section 3.3, we discuss the probe sampling technique in detail. We provide evidence that an uncoated silica probe allows a minimally distorted sample of gas to be transmitted from the plasma to the QMS. We then show clearly the advantages of sampling within the plasma using the capillary sampling technique over effluent gas sampling. Finally, in section 3.4, we comment on the overall accuracy of the QMS results.

3.2 CRACKING PATTERNS AND SENSITIVITY FACTORS

In this section we present the results from the measurements of cracking patterns and sensitivity factors. As we noted in section 2.6.4.3 these alter from mass spectrometer to mass spectrometer, so it was necessary to measure them using our SX200 QMS in order to allow the calculation of species concentrations (represented by [ ]) using methods described in section 2.9. The concentrations are presented in this work in units of mole percent (mol %), although units of molecules cm^{-3} are used for the kinetic calculations. Cracking patterns measured using the SX200 QMS are presented in table 3.1 for CF_4, O_2, CO, CO_2, COF_2, C_2F_6, C_2F_4, SiF_4 and GeF_4. The cracking patterns of CF_4 and O_2 are presented along with values from the literature [99] in order to highlight the differences between different mass spectrometers. The cracking pattern of F_2 is taken from reference 38, because a suitable sample of F_2 was not available.

In order to monitor absolute concentrations of parent species present in the discharge it was necessary to isolate one single ion signal for each parent species of interest

CF_4	(m/q)	69	50	31	19	12	25	70	34.5	51
	This work	1000	105	69	40	31	29	11	7	1
	Ref. 99	1000	118	49	67	-	39	10	12	1

O_2	(m/q)	32	16
	This work	1000	93
	Ref. 99	1000	36

CO	(m/q)	28	12	16	29	14
	This work	1000	32	17	13	4

CO_2	(m/q)	44	28	16	45	22
	This work	1000	106	74	12	9

COF_2	(m/q)	47	66	28	31	12	50	16	19	48
	This work	1000	287	207	43	39	35	21	18	12

C_2F_6	(m/q)	69	119	31	50	70	19	12	120
	This work	1000	336	334	147	11	9	9	7

C_2F_4	(m/q)	31	81	51	100	69	12	24	43	19
	This work	1000	433	241	212	40	24	23	10	10

SiF_4	(m/q)	85	28	47	33	86	87	19	104	66
	This work	1000	260	57	54	53	35	28	21	10

GeF_4	(m/q)	131	129	127	130	19	93	74	112	56
	This work	1000	797	619	254	188	131	120	80	59

F_2	(m/q)	38	19
	Ref. 38	1000	347

Table 3.1. The results of the cracking pattern measurements for CF_4, O_2, CO, CO_2, COF_2, C_2F_6, C_2F_4, SiF_4 and GeF_4. Literature values for CF_4 and O_2 are also given for comparison [99]. The cracking pattern for F_2 is taken from reference 38. m/q is the relative molar mass to charge ratio in arbitrary units. The strongest peak intensity is given a value of 1000 in each case.

which would act as a measure of parent concentration. This ion signal would preferably be unique to that parent, although in some cases it was necessary to subtract contributions from the cracking fragments of other parents using the data in table 3.1 (see section 2.6.4.3). Table 3.2 shows the ion signals used to monitor each parent, along with measured sensitivity factors relative to CF_3^+ (from CF_4) = 1. (The sensitivity factor for F_2 is set equal to 1 because no F_2 sample was available for measurements). In cases where cracking patterns overlap, the small contributions from other parent species are also shown. Absolute concentrations of species in the discharge were then calculated using the sensitivity factors, with adjustments for cracking pattern overlap where necessary. The full procedure for obtaining absolute concentrations from raw QMS data is described in section 2.9.

3.2.1 ARE RADICAL SPECIES DETECTED ?

The detection of radical species directly by QMS was not attempted in this work for the following reasons. Firstly, as we show later, radical concentrations are very low; typically « 1 % of the total gas in the plasma. These concentrations will also be significantly attenuated during transport along the probe due to their removal by reactions at the walls. In addition, the mass peaks expected from radical species always coincide with a much larger peak due to unreactive molecules. For example, the CF_3^+ peak due to CF_3 radicals is obscured by signals from CF_4 parent molecules which are typically more than 50 times stronger. Under these circumstances, it is impossible to make reliable direct measurements of the concentrations of radical species. The mass spectrometric studies performed in this work are therefore restricted to unreactive molecules only. However, as we show in chapter 4, we can in some cases calculate radical concentrations from the measured concentrations of unreactive molecules by using gas kinetic considerations.

Species to monitor	Details of measured signal (m/q)	Ion	Sensitivity factor	Other parent species contributing to the measured ion signal (brackets).
CF_4	69	CF_3^+	1.00	C_2F_6 (CF_3^+)
O_2	32	O_2^+	1.61	-
CO	28	CO^+	1.65	COF_2 (CO^+), SiF_4 (Si^+)
CO_2	44	CO_2^+	1.95	-
COF_2	47	COF^+	1.09	SiF_4 (SiF^+)
C_2F_6	119	$C_2F_5^+$	0.388	-
C_2F_4	100	$C_2F_4^+$	0.189	C_2F_6 ($C_2F_4^+$)
SiF_4	85	SiF_3^+	0.891	-
GeF_4	129	$^{72}GeF_3^+$	0.136	-
F_2	38	F_2^+	1 (assumed)	CF_4 (F_2^+)

Table 3.2. Ion intensity signals used to measure the concentration of each parent species, along with sensitivity factors and contributions due to the overlap of the cracking patterns of other parents. Note that the gas sensitivity of ionisation pressure gauges is normally proportional to the number of electrons in the molecule [98]. This is not the case here (compare for example CF_4 and CO). Clearly other factors are involved, for example the relative flow of different gases down the capillary, or the relative pumping speed of different gases by the QMS pumping system.

3.3 PROBE SAMPLING

As we have seen, there are difficulties inherent in the probe sampling technique used in this work (section 2.6.4.1). Consequently, this technique was studied in some detail to ascertain its effectiveness. Several different internal probe surface coatings (PTFE, Silver Dag, Photoresist) were tested to find one which would allow a minimally distorted sample of gas to be transmitted from the plasma to the QMS. In this section we compare these different probe coatings and show that an uncoated silica probe has better sampling characteristics than any surface coating tested. We then demonstrate the validity of the probe sampling technique used in conjunction with quadrupole mass spectrometry (QMS). Finally, we compare results obtained by sampling within the plasma to those obtained by sampling within the effluent, showing clearly the advantages of the capillary probe sampling technique.

3.3.1 PROBE COATINGS

Previous workers in this laboratory have used the capillary probe sampling technique with a probe coated with PTFE (Clarke et al [55]). This was done in an attempt to reduce chemical reactions inside the probe and so to convey as many unreacted radicals as possible from the plasma to the mass analyser. However, this type of probe was found to be unsatisfactory in the present work for the reasons discussed below.

The problem is that PTFE is not very resistant to the $CF_4 + O_2$ discharges used in this work. It etches at a rate of around 10,000 Å min^{-1} when placed on the powered electrode (around 5 times faster than Si or Ge wafers). When electrically floating in the discharge (suspended from the probe), thus with much reduced ion bombardment, that is, to mimic as closely as possible the environment of the probe, PTFE still etches at more than 300 Å min^{-1} (although we note that the PTFE etch rate inside the capillary will be slower due to the lower pressure found there). As a result of this etching, the PTFE coating was found to recede from the probe tip along the inside of the probe after just a few experiments. Clearly this situation is unsatisfactory since the surface properties of the probe

are bound to change with time. In addition, PTFE etch products produced within the probe are sampled too and will most likely distort the results. When the PTFE-coated probe was used to sample the plasma, the QMS signals were seen to reach a steady state long after the plasma had been shown by OES to have stabilised, indicating that the PTFE coating does indeed have an effect on the results. The PTFE coating was thus rejected.

The silica material from which the probe was made was also found to etch, albeit slowly, at around 50 Å min^{-1} (dangling from the probe). This was fast enough to produce a significant SiF_3^+ signal in the QMS with no Si wafer present, so an etch resistant coating for the probe surface was sought. The coatings tested were a Photoresist (Shipley S1818), which is designed to resist plasmas, and Silver Dag colloidal silver paint (silver fluorides are involatile, so silver is not expected to etch in fluorine-based plasmas). These coatings also proved to be unsatisfactory as they both became "flaky" due to the action of the discharge and so did not adhere well to the probe.

It was therefore decided to use a silica probe with no surface coating. Although the probe etches slowly, its surface is more durable than any of the surface coatings tested. In addition, any surface effects are not likely to change with time and should therefore be easy to characterise. Experiments were performed to determine the effects of the probe on the gas sampled through it. In the following sections we present evidence from these experiments which shows that the silica probe with no surface coating does allow a minimally distorted sample of unreactive gas molecules to be transmitted to the QMS.

3.3.2 CONSEQUENCES OF THE SLOW ETCHING OF THE PROBE

In this section we discuss the effects that the etching of the probe might have on the results. We show that SiF_3^+ signals produced by the etching of the probe can generally be neglected, and that no oxygen-containing products of probe etching are observed. We then show that ion signals detected from higher fluorocarbon species cannot be used to monitor the concentrations of higher fluorocarbon species in the plasma chamber.

SiF_3^+ signals. As stated in the previous section, an SiF_3^+ signal appears in the mass spectrum even with no silicon wafer present. This is produced from SiF_4 parent species etched from the probe surface, presumably by the action of F atoms present in the sample extracted from the discharge. Evidence for this view is presented below.

It can be shown directly that the SiF_4 detected with no wafer present is produced within the probe and not by reactions in the main chamber body (as would be the case if it were produced by the etching of the small quartz optical window, for example). This is achieved by scanning the SiF_3^+ signal rapidly as the plasma is extinguished. Species produced within the chamber can be seen to fall off in concentration relatively slowly as they are removed by the pump. The SiF_3^+ signal, however is seen to fall off by about 90 % at a rate around 25 times faster than that for other species. This shows that it has its origins within the probe itself and not the main chamber body. The diagram below shows this behaviour, along with that of $C_2F_5^+$ from C_2F_6 parent molecules which are produced within the chamber, for comparison. (Note that the rapid fall-off of SiF_3^+ also gives an indication of the sampling response time; around 0.4 s for signals to fall to half their original values).

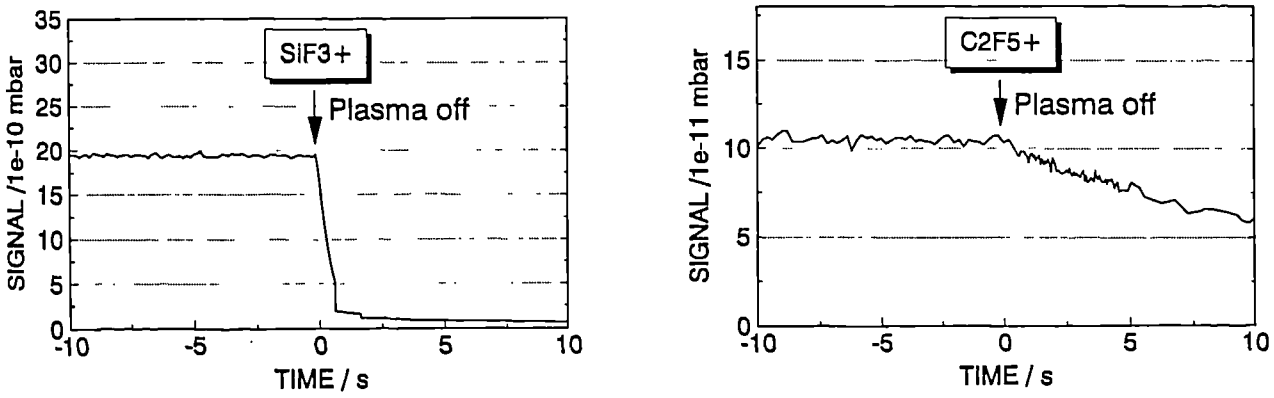

Figure 3.1. Graphs showing the rate of fall-off of signals due to $C_2F_5^+$ and SiF_3^+ on extinguishing the plasma.

Further evidence for probe production of SiF_4 is found by considering cases where the F atom concentration in the gas sampled by the probe is lower, as shown below.

a) **Sampling within the effluent.** The first case which we consider is where the tip of the sampling probe is situated in the effluent line. Here, the SiF_3^+ signal is found to be around a factor of 6 lower than that found when sampling within the plasma. This is because the F atom concentration in the effluent is lower than in the plasma due to recombination, resulting in much slower etching of the probe, and so the smaller SiF_3^+ is signal observed. (Results obtained when sampling in the effluent are discussed in more detail in section 3.3.4).

b) **Etching Ge.** The second case considered is that of etching a Ge wafer at low flow rates. The F atom concentration is much lower in this case due to the removal of F atoms from the chamber as a result of the Ge etching process. Here, the SiF_3^+ ion signal falls to insignificant levels, showing that the etching of the probe has effectively stopped.

These observations show that SiF_3^+ ion signals observed with NW and Ge wafer present are an artifact of the probe sampling system and not representative of SiF_4 in the plasma, and are therefore neglected in this work. We now consider the case of etching Si wafers.

The etch rates of Si and Ge are similar, so it is expected that the SiF_3^+ ion signal from the probe will be insignificant when etching Si at low flow rates, as with Ge etching. The SiF_3^+ ion signal observed in this case is therefore due to SiF_4 parent molecules etched from the Si wafer surface, and is not artificially enhanced by signals from the etching of the probe. This is confirmed by rapid scanning of the SiF_3^+ ion signal as the plasma is extinguished with a Si wafer present, where a slow fall in SiF_3^+ intensity which is consistent with removal of SiF_4 from the chamber through pumping is obtained, in contrast to the rapid 10 fold fall observed with no wafer present (figure 3.1). However, at higher flow rates, some artificial enhancement of the SiF_3^+ ion signal does occur, as indicated by the SiF_3^+ ion signal during Ge etching. The errors caused to the value for the concentration of SiF_4 when etching Si will be discussed in section 5.2.3.1.

Oxygen-containing products. Having shown that the silica probe walls etch to give SiF_4 product molecules, it may be expected that oxygen-containing products due to etching of the SiO_2 probe walls will also be detected. However, by considering the total oxygen budget (ie. the sum of all the oxygen detected; as O_2, CO, CO_2 and COF_2) it can be shown that no such products are observed. If oxygen-containing products of the etching of the probe were detected in addition to oxygen-containing species from the plasma, this would result in an inflated total oxygen budget. However, a comparison of results obtained when sampling within the plasma to those obtained when sampling within the effluent (where the probe etch rate is slower), show that the measured total oxygen budget is exactly the same in each case despite differences in the relative proportions of the oxygen-containing molecules (see table 3.3 in section 3.3.4). In addition, the total measured oxygen budget observed from CF_4 + O_2 plasmas is consistent with the 8% oxygen initially present in the feed gas in all our experiments. It is not clear why oxygen-containing molecules etched from the probe are not detected. However, it is clear that the oxygen-containing molecules which are detected in the QMS do indeed originate in the plasma and not in the probe.

$C_xF_y^+$ type species. At this point, it is appropriate to comment on the long term sampling properties of the probe. The same sampling probe was used throughout this work and so was "conditioned" to CF_4 + O_2 plasmas. It was therefore important that the sampling characteristics remained the same. This was found to be the case for CF_4, O_2, CO, CO_2, COF_2, C_2F_6 and F_2 by comparing results from an unused probe with results from the conditioned sampling probe after it had been used for many experiments. However, small signals attributed to $C_2F_4^+$, $C_3F_7^+$, $C_4F_7^+$ and a range of other higher fluorocarbon species were found to be considererably larger when using the conditioned probe. This indicates that these species have their origins within the probe and not within the plasma. Perhaps they arise from higher fluorocarbon parent species produced as a result of the etching of plasma deposited species from the inside surfaces of the probe. Consequently these ion signals were not used as indicators of gas phase species present in the plasma. Further support for discounting these signals can be found in section 4.5.2, where the concentration of C_2F_4 is calculated using kinetic considerations. Those calculations result

in a value more than three orders of magnitude lower than that indicated by measurements using the $C_2F_4^+$ ion signal. Clearly the $C_2F_4^+$ signal does not originate from C_2F_4 parent molecules within the plasma.

3.3.3 THE EFFECT OF DIFFERENCES IN THE PROBE CONDUCTANCE

In order to test further the sampling properties of the probe, experiments were performed using probes with different internal diameters, and hence different gas conductances, to monitor a CF_4 + 8 vol % O_2 discharge (5 sccm, 85 mTorr, 100 W, no wafer present). These experiments would be expected to show up variations in the concentration of species produced by radical recombination at the walls of the probe because different diameter probes have different internal surface areas, different transit times and, in addition, molecules are expected to strike the walls more frequently while traversing narrower probes. Any effects of differential sampling due to the different probe conductances would also be highlighted. The pressure reading from the QMS Penning gauge with no plasma running was taken as a measure of probe conductance, rather than the capillary internal diameter, i.e. the lower the Penning gauge pressure, the lower the tube conductance and the lower the tube diameter. This procedure was adopted because travelling microscope measurements of the internal diameter of the capillary opening were not representative of the conductance of the probe as a result of variations in the internal diameter of the probe along its length. The results from these experiments are presented in figure 3.2 and the observations are discussed below.

a) The measured concentrations of CF_4, O_2, CO, CO_2, COF_2 and C_2F_6 are constant within experimental error for all the different probe internal diameters tested. This indicates that these species are all produced within the plasma and that the probe is transmitting a representative sample of gas to the QMS without altering the relative concentrations of these species.

PROBE CONDUCTANCE EFFECTS

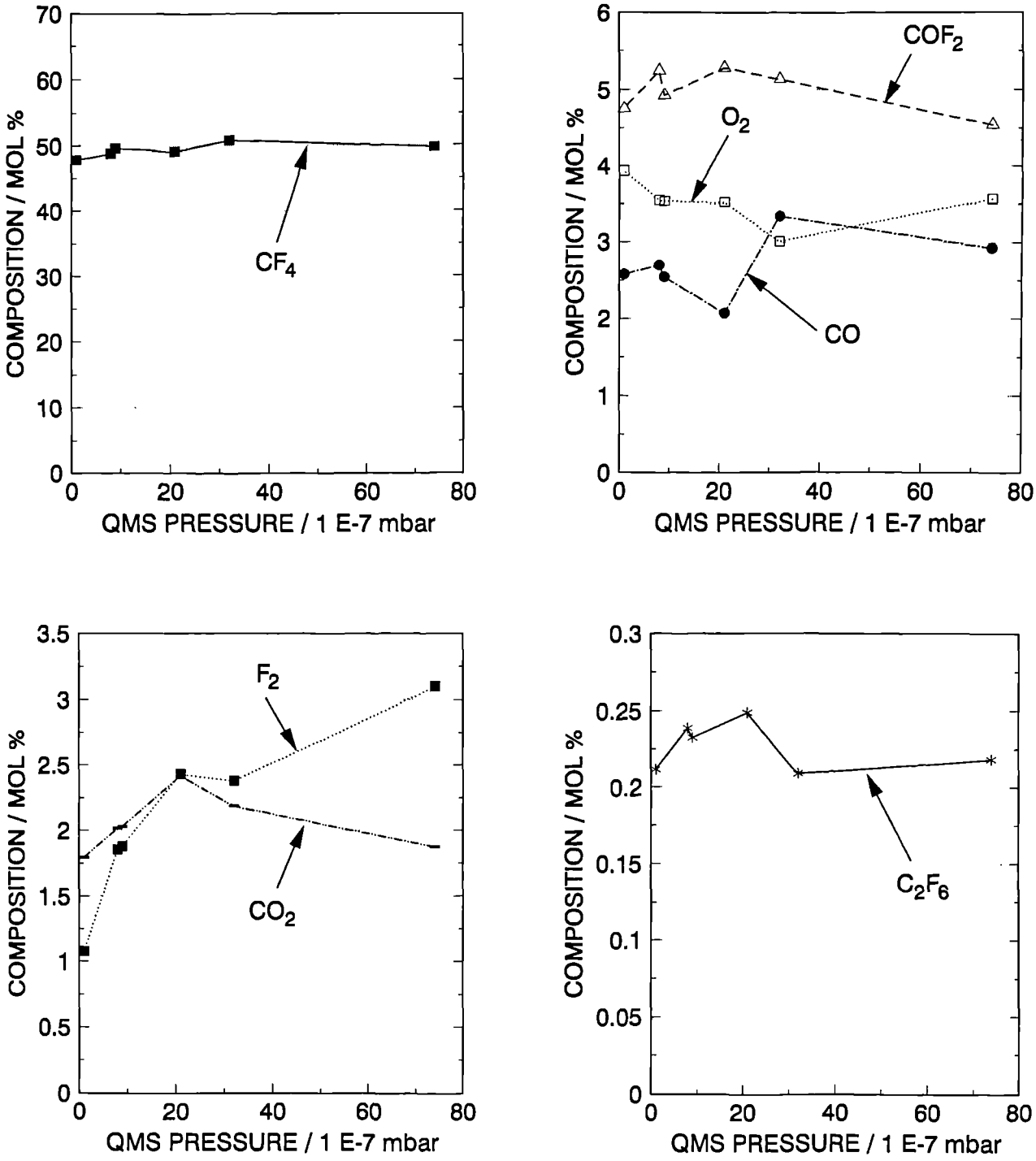

Figure 3.2. Graphs showing the mol % composition of species (ordinates) at conditions of 5 sccm, 100 W and 85 mTorr, measured using sampling probes with different conductances. QMS pressures (abscissae) measured by the Penning gauge are a measure of tube conductance. Results are shown for 6 different tubes.

b) The F_2 signal is lower with the narrowest probes used. This is attributed to removal of F_2 by reactions at the probe walls as a result of the high reactivity of F_2. Consequently the measured F_2 signal can not be taken as an accurate measure of the concentration of F_2 in the discharge. (In fact this would be the case anyway since no F_2 sensitivity factor data was available)

These observations further confirm that the QMS measurements using the uncoated silica probe give true concentrations of unreactive gas molecules present in the plasma.

3.3.4 PLASMA VERSUS EFFLUENT SAMPLING

As discussed in section 1.9.1, sampling within the plasma is to be preferred to sampling downstream in the effluent. In this section we compare results obtained using both these methods to illustrate this point further.

Table 3.3 shows the gas composition measured both in the effluent and in the plasma. The total oxygen budget, calculated by summing the contributions from O_2, CO, CO_2 and COF_2, is also given to show that no products of SiO_2 probe etching are detected (see section 3.3.2).

Species	mol % composition	
	Plasma	Effluent
CF_4	46	65
O_2	2.5	1.2
CO	2.3	3.7
CO_2	2.5	2.4
COF_2	6.4	7.8
C_2F_6	0.29	0.41
F_2	2.7	6.5
Total O-Budget	19	19

Table 3.3. The gas composition measured in the plasma and in the effluent.

It can be seen from table 3.3 that there are differences between the gas composition in the plasma and in the effluent. This is due to radicals recombining as they leave the plasma region, although the exact details are difficult to determine. Whilst gas sampled from the effluent may indicate the overall products of the action of the plasma, it does not accurately represent the gas present within the discharge region. It is of course the gas in the discharge region which is of most interest in etching studies since this is the gas which the wafer "sees". This shows clearly the value of the capillary probe sampling technique.

3.4 THE OVERALL ACCURACY OF THE QMS RESULTS

Having shown that the QMS with probe sampling is a valid technique for measuring concentrations of species in the plasma, we now discuss the overall accuracy of the QMS results.

It is very difficult to determine *a priori* the accuracy of the absolute species concentration results as there are many factors which may affect them. The performance of the QMS does vary slightly from run to run (see section 2.6.4.2), and given the sensitivity of the plasma to the exact experimental conditions, it is also likely that there will be genuine changes in the concentration of species present from run to run. In addition, there are differences in accuracy from species to species due to their different signal strengths. Consequently the best indicator of the accuracy of the results is their consistency. We estimate that throughout the QMS results presented in this work, the errors are in general no more than about $\pm$ 20% in the worst cases, and in most cases much better than this (unless otherwise mentioned in the text).

CHAPTER 4

THE CHEMISTRY OF $CF_4 + O_2$ PLASMAS

4 THE CHEMISTRY OF CF_4 + O_2 PLASMAS

4.1 INTRODUCTION

This chapter is concerned with unravelling some of the complex chemical processes occurring in CF_4 + O_2 plasmas with no wafer present. This is achieved using the Quadrupole Mass Spectrometry (QMS) results and the Optical Emission Spectroscopy (OES) results, with reference to a detailed kinetic model. We now explain the origin of the model used, and then outline how the subsequent sections of this chapter are arranged.

Plumb and Ryan [42] have constructed a detailed kinetic model of the chemistry of CF_4 + O_2 plasmas and used the experimental results of Smolinsky and Flamm [100] to test its validity. Smolinsky and Flamm used a tubular alumina fast-flow reactor with external brass electrodes to produce the discharge, and measured gas-phase product distributions downstream by QMS. The model of Plumb and Ryan predicted the distribution of F atoms and unreactive molecules correctly to within a factor of 2. Since our own experimental conditions are very different to those of Smolinsky and Flamm, it is of interest to see if a similar chemical model is applicable to our results. (We note also that the Omega reactive ion etcher used in this work is more relevant to the etching processes used by the semiconductor industry than the reactor used by Smolinsky and Flamm).

The system modelled by Plumb and Ryan was operated under conditions of very high gas flow rate. Plumb and Ryan performed time dependent concentration calculations using methods developed by Davies and Smith [101], assuming simple plug flow (see section 1.8), thus ignoring any effects on concentrations brought about by diffusion. In the present work, the residence times employed are around three orders of magnitude longer, so that diffusion causes concentrations to become uniform throughout the chamber. The kinetic calculations in this work are therefore performed in the steady state, using the "stirred tank" approach (see section 1.8).

By equating the production and loss rates for each species in the plasma with reference to a kinetic model, steady state equations are derived (cp [102]). From these equations, the concentrations of species present in the plasma can be calculated and compared with experimental measurements to determine to what extent the kinetic model is self consistent. In addition, the relative importance of the reactions which contribute to the production and loss processes can be directly recognised. The objective of this section is therefore to produce a kinetic model of the plasma and then to test its validity using steady state equations, and so to expose the important reaction pathways occurring in plasmas of $CF_4 + O_2$.

The model of Plumb and Ryan uses only gas phase reactions to explain product distributions. However, in section 4.3, we present direct evidence that reactions at the chamber walls are important in the plasma. This is done by considering total atom budgets, calculated using the QMS results which are presented in section 4.2. We show later that surface reactions are indeed essential to the understanding of our QMS results. We therefore adopt the set of gas phase reactions used in the kinetic model of Plumb and Ryan, but we extend it to include important wall reactions where necessary. The kinetic model used in this work is described in section 4.4. Then in section 4.5 we explain how steady state equations are derived, and how they are used to calculate species concentrations and to indicate the most important reaction pathways in the plasma.

In section 4.5.1, we determine the concentrations of important reactive species (CF_3, CF_2, F, O and COF) present in the discharge which could not be measured directly by QMS. These species control much of the chemistry which occurs in the plasma, so a knowledge of their concentrations is an essential requirement for calculating reaction rates. For CF_3 and F, concentrations could be calculated directly from the QMS results for a wide range of experimental conditions. [CF_3] was calculated using the steady state equation for C_2F_6. It was then possible to calculate [F] using the steady state equation for CF_4. However, agreement of calculated [F] with F atom OES results could only be obtained by including a reaction which produces CF_4 at the chamber walls. This reaction is found to be

inhibited by O atoms because they compete with F atoms for surface sites. With this reaction included, good agreement of calculated [F] with OES results was obtained for a wide range of experimental conditions. We find also that the reaction rate required to obtain a fit with the emission results is consistent with the rate indicated by the earlier atom budget considerations.

Similar methods to those used for [CF_3] and [F] could not be used to calculate [CF_2] and [O]. For these species, values for concentrations were adopted from the literature [46] for one specific set of conditions (40 sccm, 100 W and 85 mTorr). Using these literature values for [CF_2] and [O] along with values for [CF_3] and [F] calculated for those conditions, [COF] could be calculated using the steady state equation for COF. Values have thus been obtained for the concentrations of all the major reactive species present in the discharge at conditions of 40 sccm, 100 W and 85 mTorr. All subsequent calculations were then performed at this set of conditions.

In section 4.5.2, we calculate the concentrations of other species which might be present in the discharge but were not detected or could not be measured directly. These species include FO_2, FO, CF_3O_2, O^-, $O(^1D)$, CF, C_2F_3, C_2F_5 and C_2F_4. All of these species are shown to be present at concentrations which are too low to be important in the plasma.

We now have values for the concentrations of all the important reactive and unreactive species present in the plasma. In sections 4.5.3 and 4.5.4 , we use the steady state equations for each of these species to provide independent calculations of their concentrations. Clearly if the kinetic model is correct then the calculated concentrations will agree with the measured concentrations, and thus the consistency of the model is tested directly. These calculations indicate that wall reactions involving O atoms are important in the plasma in addition to the wall reactions already discussed. With these processes included in the model, calculated concentrations are within a factor of three of measured concentrations for all these species. Given the complexity of the plasma system, this agreement represents good self consistency, and indicates that the kinetic model is valid.

In section 4.6, a reaction scheme important in CF_4 + O_2 plasmas is given. The steady state equation calculations show that, of the 53 reactions considered in the kinetic model initially, only 17 have important consequences on the chemistry of the plasma. The role of all the important species is discussed, and the main consequences of the model are outlined. Then in section 4.6.3, we use the reaction scheme to explain qualitatively the trends observed in the QMS results of section 4.2. Finally, in section 4.7, the main conclusions from this chapter are summarised.

We now present the results taken by QMS during the study of discharges of CF_4 and O_2 with no wafer present.

4.2 THE QMS RESULTS FOR CF_4 + O_2 PLASMAS

The results of the QMS study of CF_4 + O_2 discharges with no wafer present are shown in figures 4.1 to 4.8. The composition of unreactive molecules in the plasma, expressed as mole percentages (mol %), have been calculated using methods described in section 2.9. Mole percentage compositions are presented for a wide range of conditions of flow (2-50 sccm), power (10-200 W) and pressure (10-105 mTorr), all using CF_4 + 8 vol % O_2 process gas. The effects of varying the feed gas composition have also been studied for conditions of 5 sccm total flow rate, 100 W and 85 mTorr. Figure 4.5 shows the effects of varying the proportions of O_2 and CF_4 in the feed gas. Figures 4.6 to 4.9 show the effect of the addition of other gases normally produced by the action of the plasma (CO, CO_2 and C_2F_6) to the CF_4 + 8 vol % O_2 process gas. (Note that in the CO, CO_2 and C_2F_6 addition experiments, the flow rates of CF_4 and O_2 vary slightly because the total flow rate was held constant). The observed trends in these results are discussed later in section 4.6.3 with reference to the reaction scheme which is proposed in section 4.6.

The measurements of $[C_2F_6]$, $[CF_4]$ and $[O_2]$ are used in the calculations of $[CF_3]$ and [F] presented in sections 4.5.1.1 and 4.5.1.2 respectively. All subsequent kinetic calculations are then performed for conditions of 40 sccm, 100 W and 85 mTorr to allow

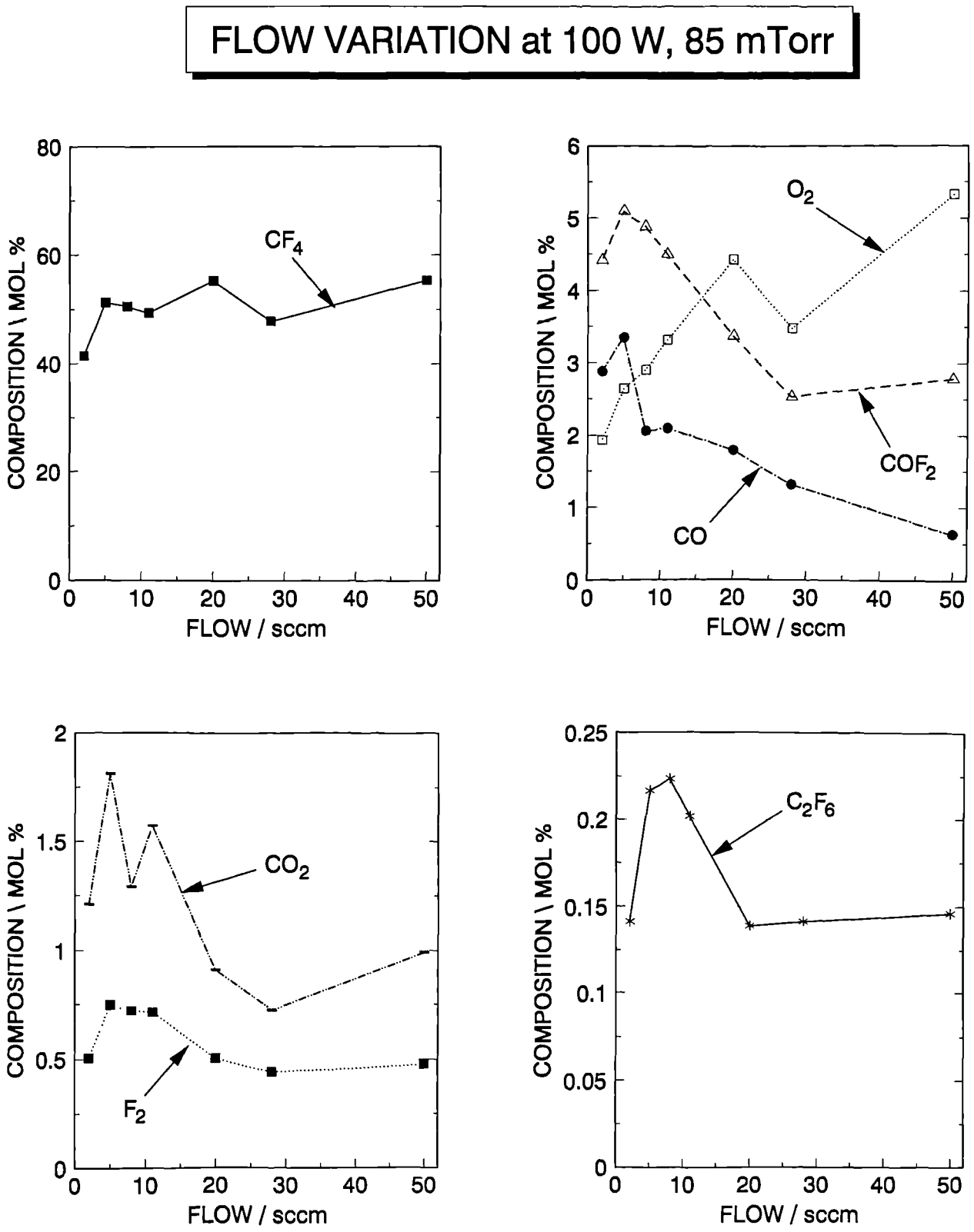

Figure 4.1. Graphs showing the Mass Spectrometry results for flow rate variation of CF_4 + 8 vol % O_2 process gas at conditions of 100 W and 85 mTorr with no wafer present.

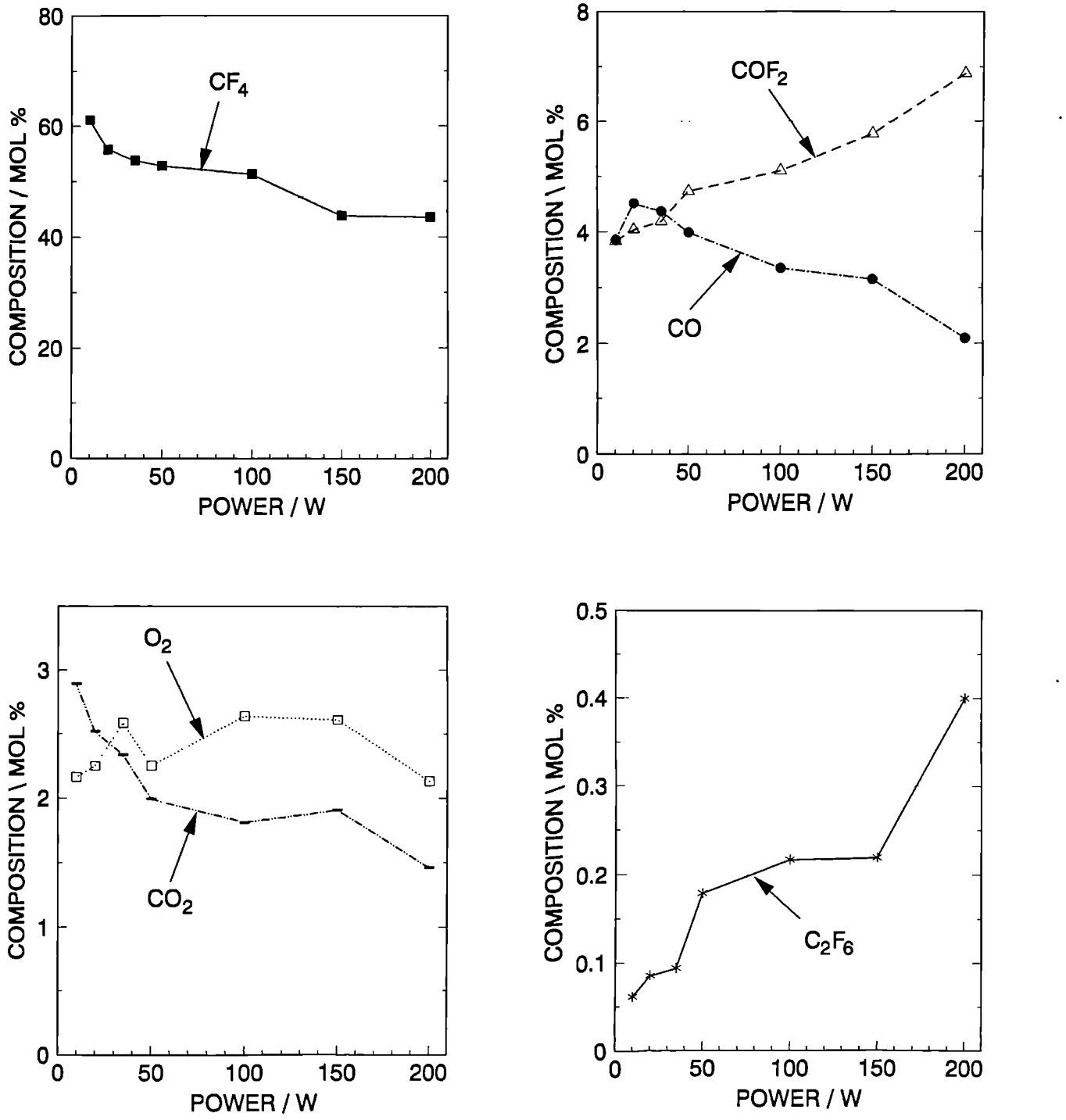

Figure 4.2. Graphs showing the Mass Spectrometry results for power variation, using CF_4 + 8 vol % O_2 process gas at conditions of 5 sccm and 85 mTorr with no wafer present.

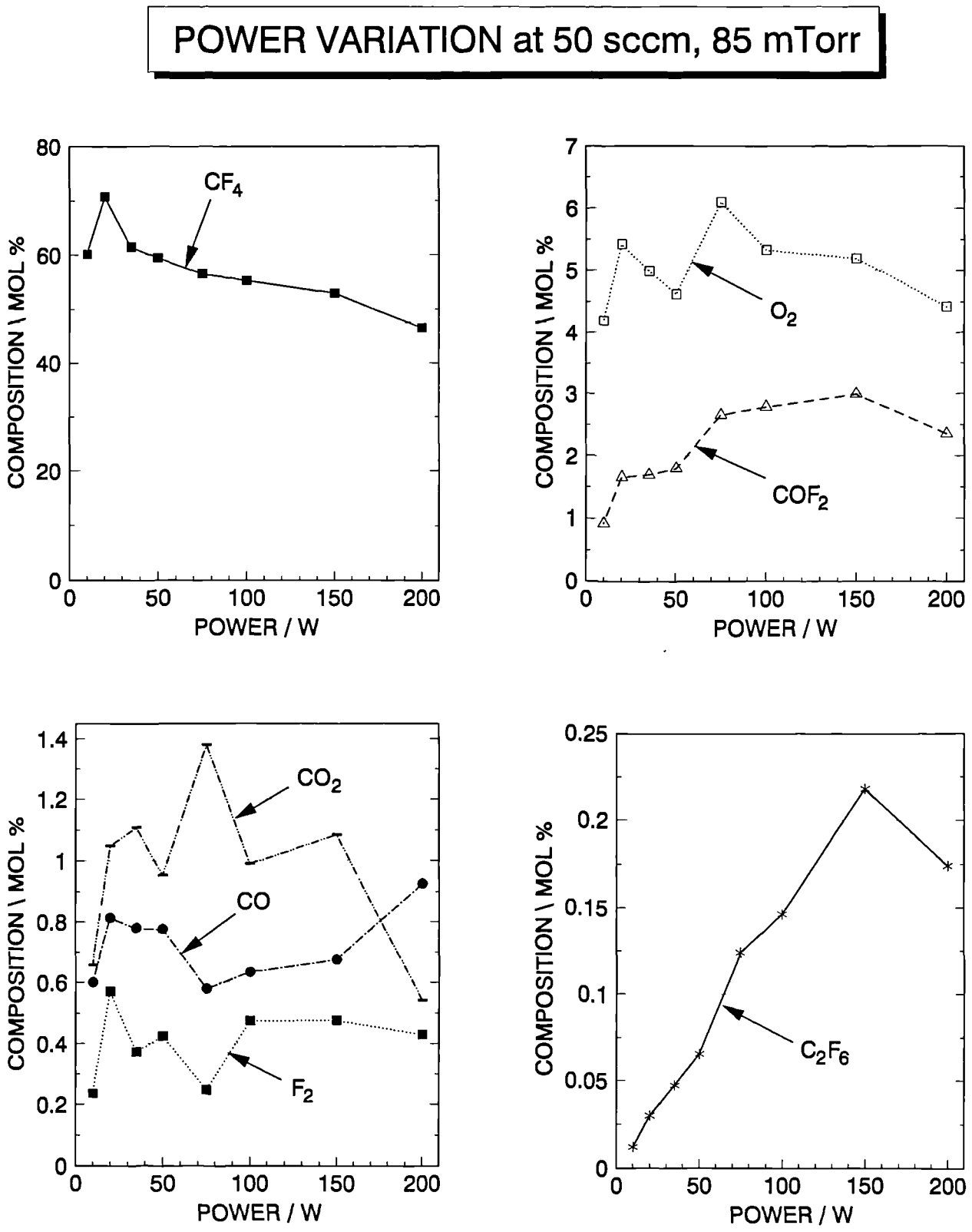

Figure 4.3. Graphs showing the Mass Spectrometry results for power variation, using CF_4 + 8 vol % O_2 process gas at conditions of 50 sccm and 85 mTorr with no wafer present.

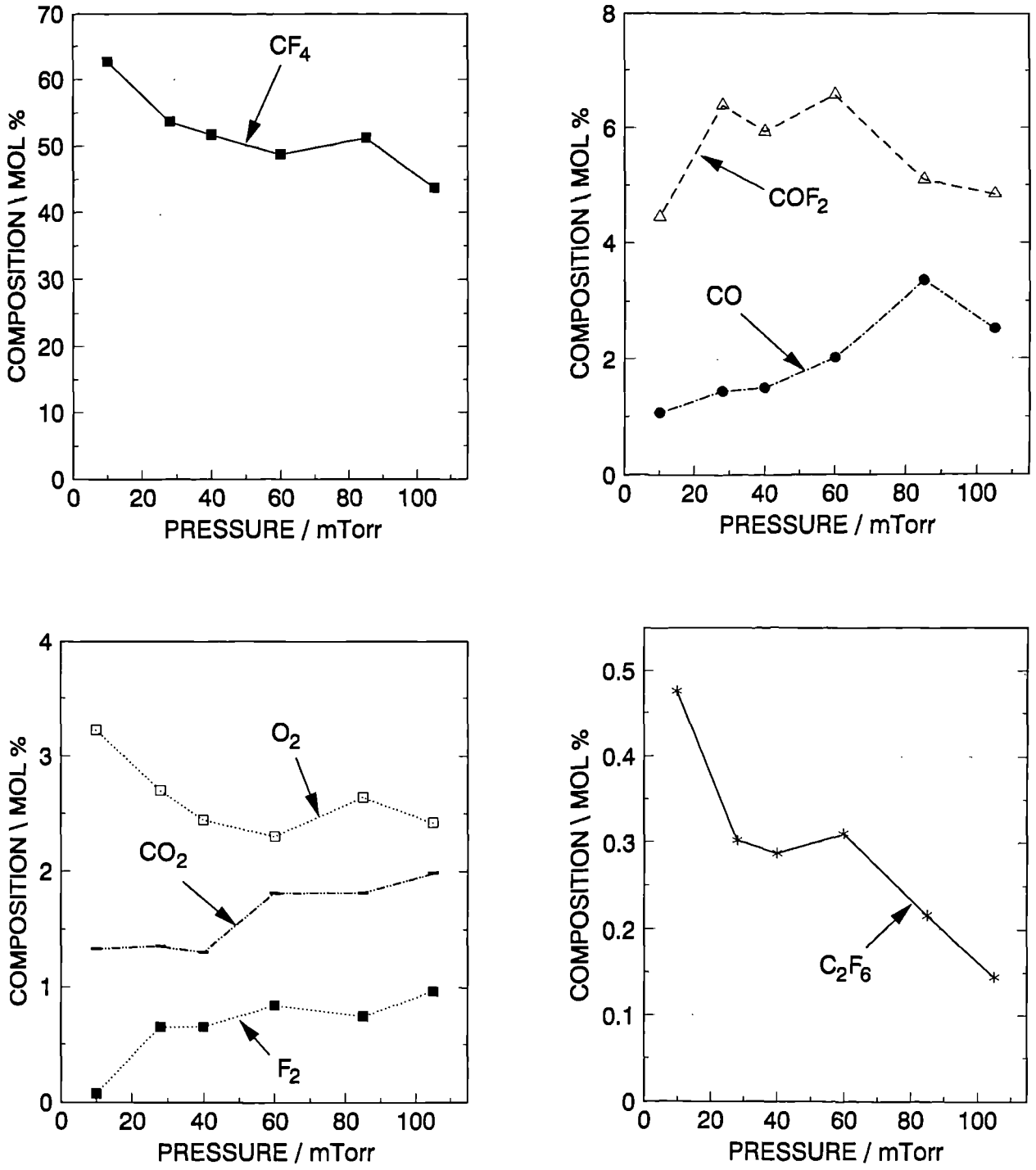

Figure 4.4. Graphs showing the Mass Spectrometry results for pressure variation, using CF_4 + 8 vol % O_2 process gas at conditions of 5 sccm and 100 W. Note that the ordinates show percentage composition but not true concentration because the pressure changes.

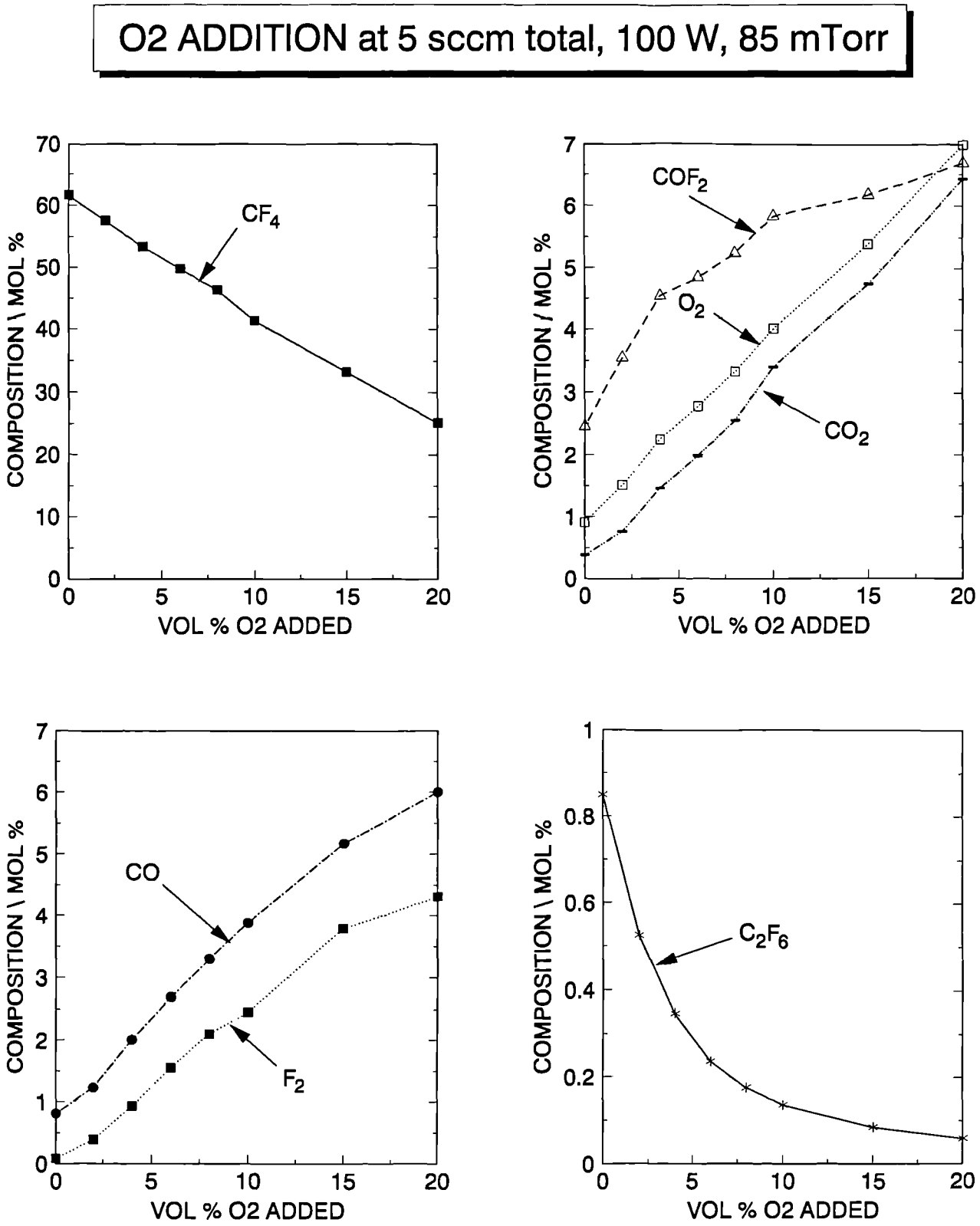

Figure 4.5. Graphs showing the Mass Spectrometry results for variation of the volume percentage of O_2 added to CF_4 process gas, at conditions of 5 sccm, 100 W and 85 mTorr with no wafer present.

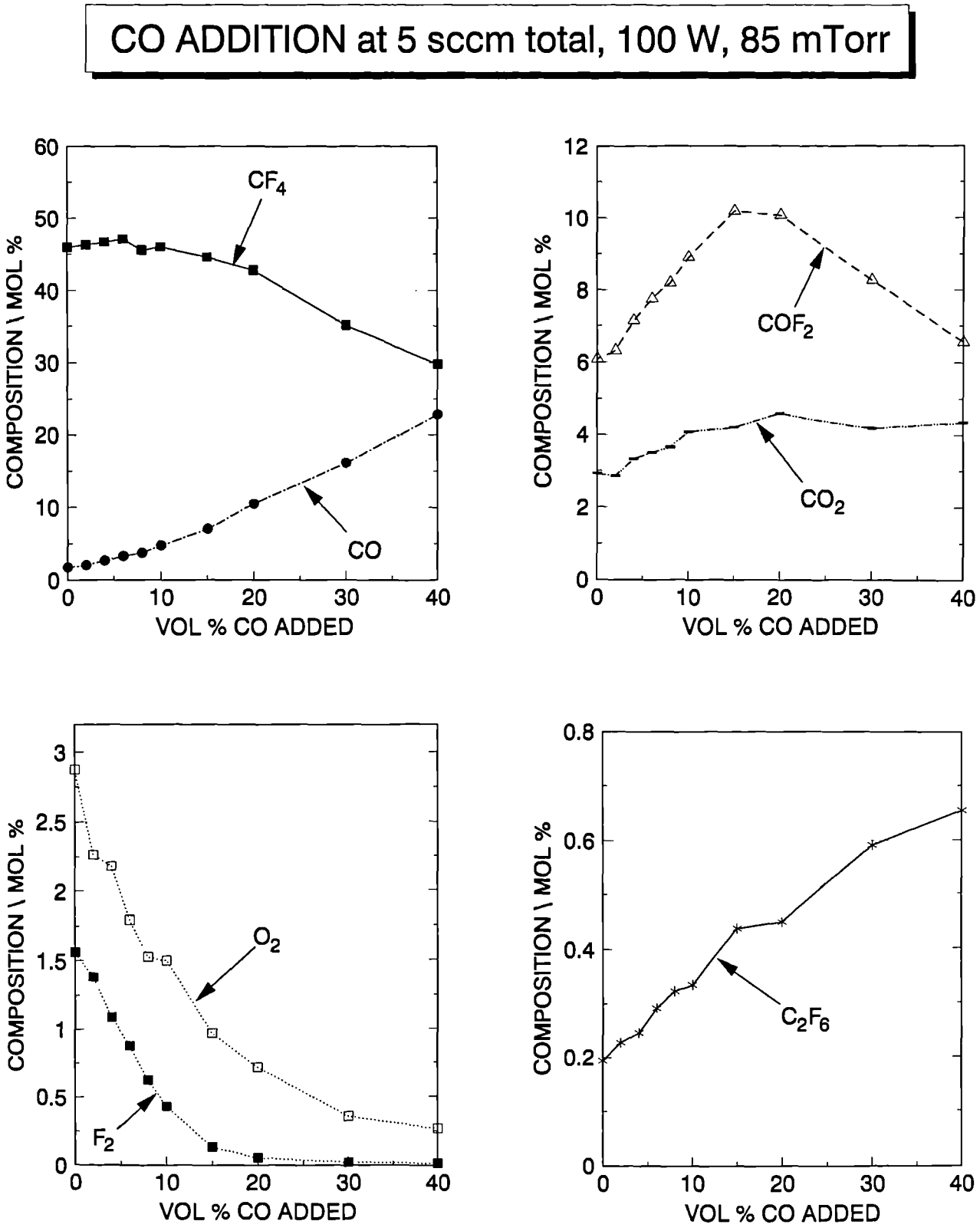

Figure 4.6. Graphs showing the Mass Spectrometry results for variation of the volume percentage of CO added to CF_4 + 8 vol % O_2 process gas, at conditions of 5 sccm, 100 W and 85 mTorr with no wafer present.

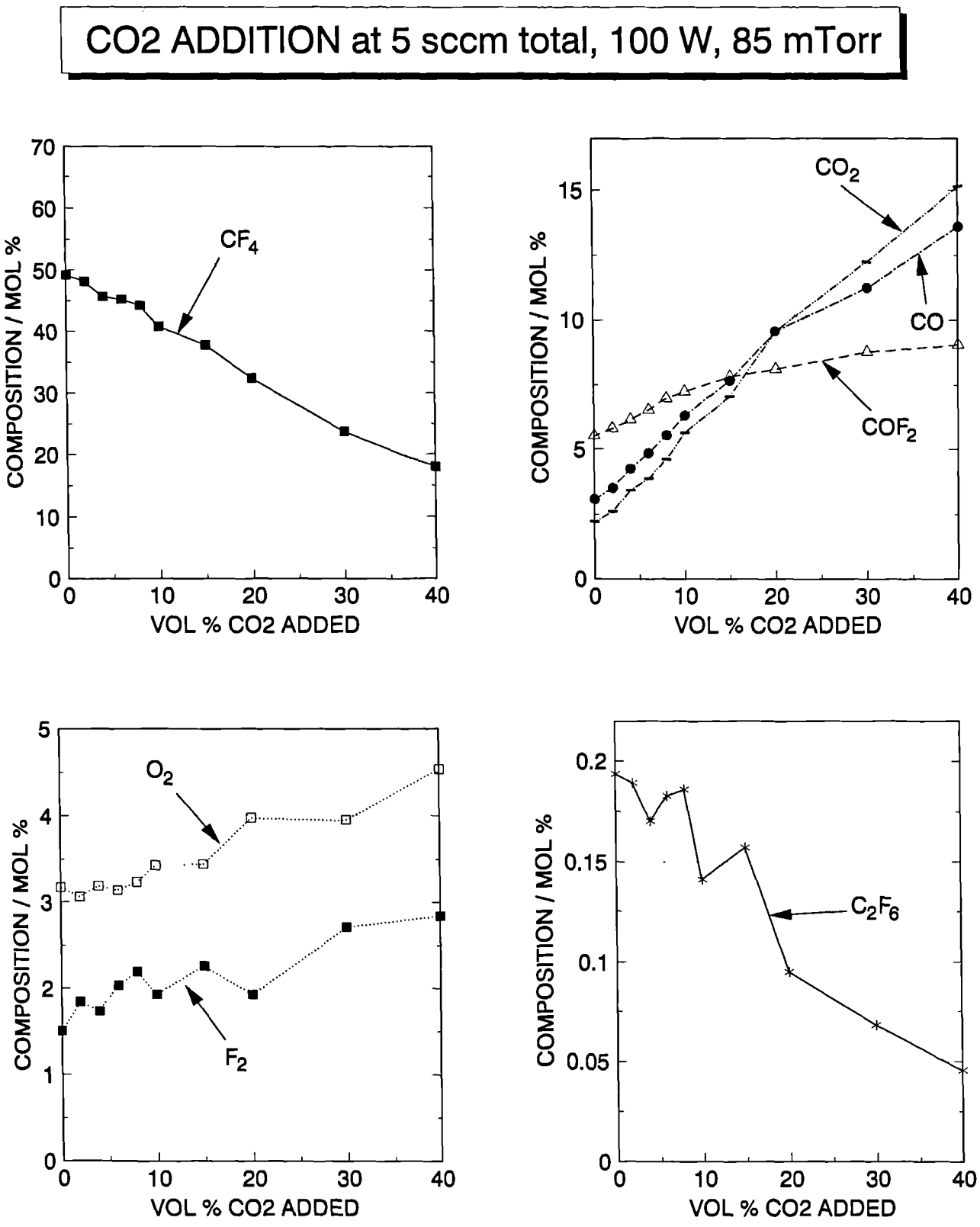

Figure 4.7. Graphs showing the Mass Spectrometry results for variation of the volume percentage of CO_2 added to CF_4 + 8 vol % O_2 process gas, at conditions of 5 sccm, 100 W and 85 mTorr with no wafer present.

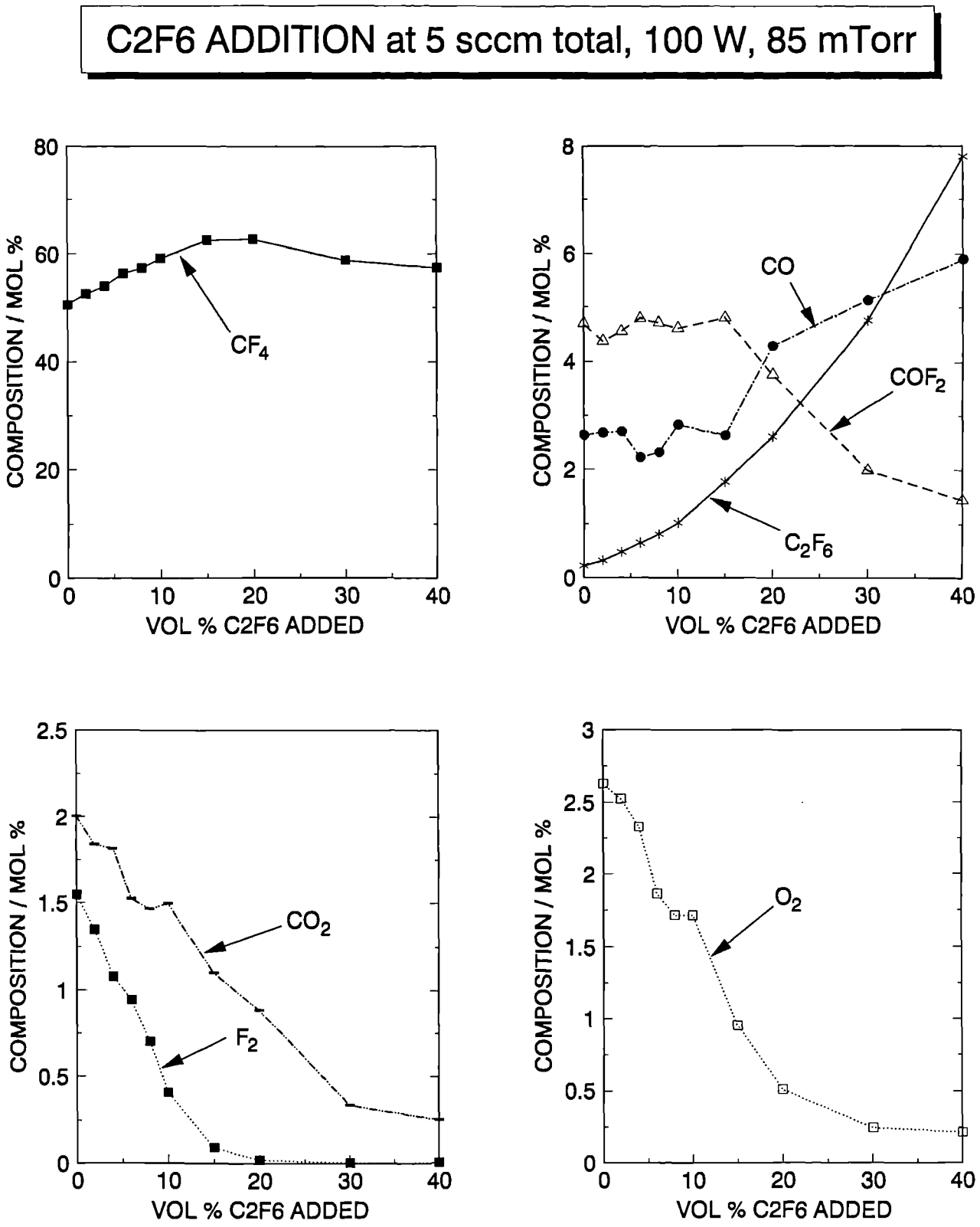

Figure 4.8. Graphs showing the Mass Spectrometry results for variation of the volume percentage of C_2F_6 added to CF_4 + 8 vol % O_2 process gas, at conditions of 5 sccm, 100 W and 85 mTorr with no wafer present.

Laser Induced Fluorescence measurements of $[CF_2]$ and [O] to be adopted from the literature [46]. The concentrations of species measured by QMS at these conditions, which are used for those kinetic calculations, are given below in table 4.1. Since data points were not taken at exactly 40 sccm, the concentrations were obtained from figure 4.1 by linear interpolation of the adjacent two points.

Species	Composition \ mol %
C_2F_6	0.14
CF_4	52
O_2	4.5
CO	0.94
COF_2	2.7
CO_2	0.87
F_2	0.46

Table 4.1. The concentrations of species measured by QMS expressed as mol % compositions at conditions of 40 sccm, 100 W and 85 mTorr for CF_4 + 8 vol % O_2 process gas with no wafer present.

At this point, it is appropriate to add a note concerning the gas addition experiments. Due to the low total flow rate of 5 sccm, the lowest vol % additions of the added gas required flow rates which were at the lower limit of the effective operating range of the MFC. This resulted in the true flow rate being slightly greater than the indicated flow rate. This effect is illustrated most clearly in the results of the O_2 addition experiment (figure 4.5), where it can be seen that there is $\approx$ 1 mol % O_2 present in the plasma even when there was nominally 0 vol % O_2 added to the CF_4 feed gas. However, this does not affect the interpretation of the results for the following reasons. Firstly, the observed trends in species concentrations are not affected, so the results do show the true effect that the added gas has on the plasma. Secondly, the concentration calculations performed using these results (presented later in this chapter) use the *measured* species concentrations and not the nominal vol % additions as calculation inputs, and are therefore also unaffected.

4.3 ARE WALL REACTIONS IMPORTANT?

The total carbon, fluorine and oxygen atom budgets must remain constant in the chamber. In this section, we apply this conservation principle to the QMS results, and show that reactions at the walls of the plasma chamber are important in controlling the overall plasma chemistry.

4.3.1 ATOM BUDGET RESULTS; THE INFLUENCE OF THE REACTOR WALLS

The total C, O and F atom budgets are fixed by the feed gas composition and the total gas pressure, and must remain constant. The total amount of C, O and F atoms present as unreactive molecules can be found easily from the QMS results. If these two quantities are not equal, i.e. if the total budgets of C, O and F atoms are not accounted for by the atoms which comprise unreactive molecules alone, then the difference must be due to gaseous radicals in the plasma which could not be detected by the QMS, or alternatively it may indicate that processes which result in a loss of C, O or F atoms to the chamber walls are occurring.

The calculation of the percentage of C, O and F not accounted for by the QMS results, the "budget deficit", is presented below in figure 4.9 for the flow rate variation experiment at 100 W and 85 mTorr.

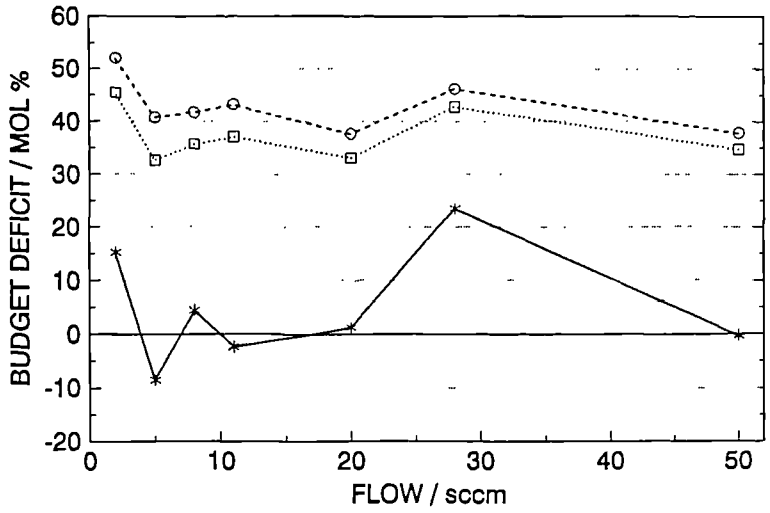

Figure 4.9. Graph showing the % budget deficit of carbon, oxygen and fluorine for the flow rate variation experiment, at conditions of 100 W and 85 mTorr with no wafer present.

From these results, several observations can be made.

a) It is clear from figure 4.9 that the O present in the feed gas is all accounted for by unreactive molecules in the discharge (O_2, CO, CO_2 and COF_2). This indicates that very little oxygen is present as gaseous radical species, in accordance with results presented later in this chapter which show that less than 2 % of the oxygen in the feed gas initially is present in the plasma as radical species (O and COF) at conditions of 40 sccm, 100 W and 85 mTorr. The results also indicate that there is no net loss of oxygen to the walls once a steady state is reached. Clearly O-containing molecules which collide with the walls return very rapidly to the gas phase. Note however that this does not exclude the possibility of reactions at the walls. We show later that reactions involving O-containing molecules do indeed occur at the walls.

b) The results for C and F indicate that around 35 % of the C atoms and 40 % of the F atoms present in the feed gas initially are not present in the plasma as unreactive

molecules. Calculations later in this chapter indicate that, at conditions of 40 sccm, 100 W and 85 mTorr, only 0.6 % of the C atoms and 5 % of the F atoms in the feed gas initially are present in the plasma as radical species. It is clear therefore that not all the C and F is accounted for by gas phase species alone. The explanation for this is that the remaining C and F is adsorbed at the chamber walls. This view is supported by observations in section 4.5.4.3 where we show that CF_2 is removed very rapidly from the gas phase by adsorption at the chamber walls.

c) The results in figure 4.9 show that the budget deficits of C and F remain constant while the flow rate, and hence the time for which molecules remain in the chamber before being pumped away (the residence time), changes by a factor of 25. If net deposition was occurring, then more C and F would be lost to the walls at long residence times than at short residence times, contrary to these results. This indicates that C and F atoms are released from the walls as well as deposited, and that a steady state surface coverage of these species is reached such that the rates of adsorption of C and F equals the rates of desorption.

In order to explain these observations, the reaction scheme below is proposed.

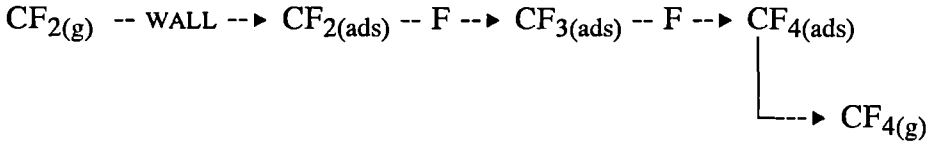

This reaction is assumed to take place over the entire internal surface area of the reaction chamber which contains the plasma. In this scheme, CF_2 adsorbs onto the reactor walls and is sequentially fluorinated at the wall by F atoms to produce CF_4, which then desorbs into the gas phase. This provides the necessary adsorption and desorption processes to explain the observations outlined above. Direct adsorption of CF_3 is regarded as minimal because firstly, the flux of CF_3 to the wall will be lower than CF_2 due to its lower concentration

(see table 4.5 on p.112 later), and secondly, the sticking coefficient for CF_3 is expected to be lower than for CF_2 because it only has 1 available bond with which to chemisorb at the wall. We assume also that fluorination of $CF_{3(ads)}$ is the rate limiting step. We make this assumption because CF_2 will have a dangling bond for F atoms to attack even when chemisorbed to the surface, whereas CF_3 will use the only available bond to chemisorb at the wall. This means that the above reaction will show effective first-order kinetics with respect to F, and the overall reaction scheme may be written

$$CF_{2(ads)} \text{ -- } 2F \text{ --▸ } CF_{4(g)} \,. \qquad \text{Rate} = k^{1st}[F]$$

The rate expression assumes for simplicity that the surface coverage of CF_3 available for reaction is constant regardless of the experimental conditions. Thus the surface coverage of CF_3 is included in k^{1st}. Later, in section 4.5.1.2, we show that the reaction is inhibited by O atoms, which causes k^{1st} to be dependant on [O].

We now estimate the importance of this wall reaction by deriving steady state equations for the adsorption and desorption of carbon and fluorine at the chamber walls. We consider only conditions of 40 sccm, 100 W and 85 mTorr for this purpose in order to allow a comparison with the results of calculations presented later in this chapter which were performed at those conditions.

4.3.2 WALL PROCESSES INVOLVING CARBON

In this section, we estimate the volume production rate of CF_4 at the walls, and show that this process is likely have important influences on the plasma composition.

We assume that the carbon-containing species (CCS) are adsorbed at the wall exclusively as CF_2 and removed exclusively as CF_4. At steady state, the flux of CCS adsorbing at the walls must equal the flux of carbon-containing species released from the walls, as indicated by the results of the previous section (point c). The rate of CCS adsorption is therefore given by

CCS adsorption rate = $\phi(CF_2)\ s(CF_2)$

where $\phi(CF_2) = \frac{1}{4}\ v(CF_2)\ [CF_2]$.

Here, $\phi(CF_2)$ is the flux of CF_2 to the wall, $s(CF_2)$ is the sticking coefficient for CF_2 and $v(CF_2)$ is the thermal velocity of CF_2. Taking 0.34 % of the species in the chamber to be CF_2, as calculated in section 4.5.4.3, with $s(CF_2) = 0.3$ (section 4.5.4.3) and $v(CF_2) = 35400\ cm\ s^{-1}$ (at 295 K), a value for the CCS adsorption rate of $2.5 \times 10^{16}\ cm^{-2}\ s^{-1}$ is obtained. At steady state, this is equal to the CCS flux from the walls, and hence also the flux of CF_4 from the walls. The volume production rate of CF_4 is therefore given by 2.5×10^{16} (A / V), where A is the internal surface area of the chamber and V is the chamber volume. Using values for $A = 1840\ cm^2$ and $V = 4860\ cm^3$, an estimate for the CF_4 production rate of $9 \times 10^{15}\ cm^{-3}\ s^{-1}$ is obtained. In section 4.5.1.2 later, we find that a wall production rate of $5 \times 10^{15}\ cm^{-3}\ s^{-1}$ is necessary to explain our observations. This value accords well with the value estimated above, lending support to the CF_4 wall production model.

4.3.3 WALL PROCESSES INVOLVING FLUORINE

In this section, we use arguments similar to those used in the previous section to calculate a value for the loss rate of F atoms at the chamber walls.

We assume that fluorine is adsorbed at the reactor walls only as CF_2 and as F atoms, and is desorbed only as CF_4. In this case, the loss rate of F atoms at the chamber walls is given by

Wall loss rate = Wall production rate

$$2\ \phi(CF_2)\ s(CF_2) + \phi(F)\ s(F) = 4\ \phi(CF_4)$$

yielding

$$\phi(F)\ s(F) = 4\ \phi(CF_4) - 2\ \phi(CF_2)$$

where $\phi(F) = \frac{1}{4}\ v(F)\ [F]$

Here $\phi(F)$ is the flux of F atoms to the chamber walls, s(F) is the sticking coefficient for F and $\phi(CF_4)$ is the flux of CF_4 from the walls. Using the values for the fluxes of CF_2 and CF_4 to and from the chamber walls given in the previous section, then a value for the loss rate of F atoms at the wall (at 40 sccm, 100 W and 85 mTorr) of around 5 x 10^{16} cm^{-2} s^{-1} is obtained. Taking 18 % of the species in the chamber to be F atoms, as calculated in section 4.5.1.2, a value for s(F) of around 0.004 is obtained. This agrees well with the value of 0.004 calculated in section 4.5.4.1 using the steady state equation for F atoms.

It is also possible to estimate the relative adsorbed amounts of F and CF_x by considering the ratio of the C and F budget deficits. For the conditions mentioned above, the ratio of the absolute F budget deficit to the absolute C budget deficit is around 4 (see figure 4.9, noting that for CF_4 feed gas the total F budget is 4 times the total C budget). This shows that F is not present at the walls exclusively as CF_2 and CF_3, since that would produce a value for this ratio of between 2 and 3, depending on the relative adsorbed amounts of these two species (CF_4 is not expected to adsorb to any significant extent [53]). The value of 4 indicates that the adsorbed amount of F atoms exceeds that of CF_x by a factor of between 1.3 and 2.

4.4 THE KINETIC MODEL

In this section, we describe all the processes which are included in the kinetic model of CF_4 + O_2 plasmas. (The modelling of etching plasmas was discussed briefly in section 1.8).

1) **The gas flow production rate and the pumping speed.** In order to calculate these parameters it is first necessary to determine the plasma volume. The plasma is assumed to occupy the entire chamber lid volume but not to extend into the dead space region below, giving a value for the volume, V, of 4860 cm^3. The flow rate is expressed as a volume production rate, and denoted R_{flow}. R_{flow} (in molecules

cm^{-3} s^{-1}), and the first-order pumping rate coefficient, k_{pump} (in s^{-1}) can then be calculated as below

$$R_{flow} = Q / V = 9.24 \times 10^{13} q \qquad (4.1)$$

$$k_{pump} = Q / (V n_i) = 9.24 \times 10^{13} q / n_i \qquad (4.2)$$

where Q is the flow rate in molecules s^{-1}, q is the flow rate in sccm (and $Q = 4.48 \times 10^{17} q$), V is the plasma volume in cm^3 and n_i is the total gas concentration (pressure) in molecules cm^{-3}. The calculated values of k_{pump} were verified experimentally by observing by QMS the fall-off in concentration of species which are produced by the action of the plasma, immediately after the plasma is extinguished. A first-order decay in concentration is observed with a fall-off rate consistent with equation (4.2) above. The residence time, k_{pump}^{-1}, is the mean time that molecules remain in the chamber before being pumped away, and spans the range 0.6 to 15 s in this work. (Note that the residence time used here is not the same as the residence time used in surface science to refer to the length of time that molecules remain adsorbed at surfaces).

2) **Diffusion effects.** At the pressures involved in this work, the rates of diffusion are very rapid. Given also the long residence times, it is expected that the plasma will be well mixed, so that the concentrations of species will be uniform throughout the plasma region.

There are, however, differences in concentration of some species between the plasma and the dead space region, as we saw in section 3.3.4 when sampling gas from within the effluent. This will cause some non uniformity in the concentrations of species at the edge of the plasma in the vicinity of the pumping holes. However, we assume for simplicity that this effect is localised, and does not affect the concentrations of species in the bulk of the plasma.

3) **Dissociation rates.** Plumb and Ryan [42] estimate the dissociation rates of molecules in the plasma using the Mass Spectrometry results of Smolinsky and Flamm [100]. This was done by considering the percentage conversion of CF_4 in an oxygen-rich $CF_4 + O_2$ plasma at short residence times of < 0.1 s. Under such conditions it is expected that reactions between O and CF_2 and O and CF_3 would dominate, and that reactions between CF_3 or CF_2 and F to reform CF_4 would become unimportant. Using this approach, a phenomenological first order dissociation rate coefficient, k_{diss}, of the order of 20 s^{-1} was obtained for CF_4. A similar argument was used for O_2, again yielding a value of around 20 s^{-1}.

In principle, dissociation rates can also be derived by estimating the electron concentration and the electron energy distribution, and combining these estimates with what is known of electron impact dissociation cross-sections of the species concerned. Plumb and Ryan used this approach as well as that outlined above for comparison. They calculate an electron concentration of 6×10^{10} cm^{-3} with mean energy 5.9 eV for the system which they modelled, which yielded a value for k_{diss} of 27 s^{-1} for CF_4. The close agreement of this calculation with their above estimate of 20 s^{-1} led Plumb and Ryan to make the simplifying assumption that the dissociation rate for all species was 20 s^{-1}, except where more quantitative information was available. For CO_2, reaction cross section data [94] indicated a dissociation rate of around twice as fast as that for CF_4, so a value of $k_{diss} = 40$ s^{-1} was used. For CO, no dissociation pathway was included in their model because CO dissociates only slowly at the electron energies encountered in this work [36] due to the strength of the C-O bond. These values of dissociation rate coefficients were used throughout the entire range of conditions considered in that study (variation of flow rate and percentage O_2 added to CF_4 at constant power and pressure).

We adopt a similar simplifying approach in this study, but make adjustments to account for the different conditions found in our reaction chamber. Welch [37]

has made Langmuir Probe measurements (see section 1.9.4) on CF_4 plasmas in a reactor similar to the one used in the present work. At conditions of 85 mTorr and 100 W, values for the electron concentration and mean electron energy of around 2.5×10^{10} cm^{-3} and 3.7 eV respectively were obtained; these values are consistent with the measurements of Steinbruchel [103]. In the absence of more quantitative information, we therefore assume values for the effective first order dissociation rate coefficients to be half those used by Plumb and Ryan, resulting in a value for k_{diss} of 10 s^{-1} for all monitored species except for CO_2 (k_{diss} = 20 s^{-1}) and CO (k_{diss} insignificant), as discussed above. The plasma density is thought to be fairly uniform across the chamber at low pressures [29], therefore we make the additional assumption that dissociation rates do not change across the plasma region.

Following Plumb and Ryan, variations in flow rate and feed gas composition were assumed not to alter the dissociation rates. Due to the uncertainties in the behaviour of the electron density and energy distribution with varying power and pressure, kinetic calculations at powers and pressures other than 100 W and 85 mTorr were not attempted.

4) **The branching ratio for CF_4 dissociation.** Plumb and Ryan [42] present evidence that CF_4 can dissociate to produce both (CF_3 + F) and (CF_2 + 2F) directly by two independent pathways, each involving a single electron impact with CF_4. Both CF_2 and CF_3 can therefore be considered as direct products of the dissociation of CF_4. Plumb and Ryan also show that the ratio of the primary dissociation rate for CF_2 production relative to that for CF_3 production is 2.5 $\pm$ 1. We adopt this value for the branching ratio of CF_4 in this work.

5) **Chemical kinetics.** The chemical reactions and rate coefficients used in our kinetic model are taken from Plumb and Ryan [42] and are presented in table 4.2 for conditions of 100 W and 85 mTorr. (Note that by convention kineticists omit

"molecules^{-1}" from the units. Thus second order rate coefficients, which have units of molecules^{-1} cm^3 s^{-1}, are written with units of cm^3 s^{-1}. Similarly, third order rate coefficients are written cm^6 s^{-1}). The quoted rate coefficients assume a temperature of 295 K. This should be similar to the temperature found in our water-cooled reaction chamber, so the quoted values are expected to be valid for our experimental conditions. The rate coefficients for three body reactions in the fall-off region (between second and third order kinetic behaviour) are expressed as effective second order rate coefficients. They are corrected for the different pressure used in the present work (85 mTorr) by employing the method of Troe [41], using parameters given in table 4.3. Reactions marked with an asterisk in table 4.2 form the reduced set which were found by Plumb and Ryan to be sufficient to model the experimental results for [CF_4], [O_2], [COF_2], [CO], [CO_2] and [F].

6) **Wall reactions.** In the model used by Plumb and Ryan [42], wall reactions were neglected in order to assess the extent to which gas-phase free radical reactions alone could explain product distributions. In the present work, it was found necessary to include wall reactions in order to explain the experimental observations, (see for example section 4.3). These reactions are given in table 4.4 for conditions of 40 sccm, 100 W and 85 mTorr. The reactions and the values for the quoted rate coefficients are discussed in later sections.

In some cases, values for reaction probabilities, r, or effective sticking coefficients, s, can be calculated. For a first-order heterogeneous process, s and r are both given by

$$4\, k^{1st}\, (V / A)\, (1 / v) \qquad (4.3)$$

where k^{1st} is the first-order rate coefficient, V is the chamber volume (= 4860 cm^3), A_{is} the chamber internal surface area (= 1840 cm^2) and v is the mean speed

	Reaction	Rate coefficient at 85 mTorr [a]	
1)*	CF_4 -- e --▸ CF_3 + F	3	
2)*	CF_4 -- e --▸ CF_2 + 2F	7	
3)	CF_3 -- e --▸ CF_2 + F	10	
4)	CF_2 -- e --▸ CF + F	10	
5)	CF_3 + CF_3 -- M --▸ C_2F_6	8×10^{-12}	b
6)*	CF_3 + F -- M --▸ CF_4	6.5×10^{-12}	b
7)	CF_2 + CF_2 ------▸ C_2F_4	5×10^{-14}	
8)*	CF_2 + F -- M --▸ CF_3	8.6×10^{-14}	b
9)	CF + F -- M --▸ CF_2	9×10^{-16}	b
10)	C_2F_6 -- e --▸ CF_3 + CF_3	10	
11)	C_2F_4 -- e --▸ CF_2 + CF_2	10	
12)	F + C_2F_4 ------▸ CF_3 + CF_2	4×10^{-11}	
13)	CF_2 + CF_3 -- M --▸ C_2F_5	7.9×10^{-13}	b
14)	C_2F_5 + F ------▸ CF_3 + CF_3	1×10^{-11}	
15)	CF + CF_2 ------▸ C_2F_3	1×10^{-12}	
16)	C_2F_3 + F ------▸ C_2F_4	1×10^{-12}	
17)*	O_2 -- e --▸ O + O	3.25	
18)	O_2 -- e --▸ O + $O(^1D)$	3.75	
19)	O_2 -- e --▸ O^- + O	3	
20)	$O(^1D)$ + O_2 ------▸ O + O_2	4×10^{-11}	
21)	$O(^1D)$ + CF_4 ------▸ O + CF_4	1.8×10^{-13}	
22)	$O(^1D)$ + COF_2 ------▸ O + COF_2	5.3×10^{-11}	
23)	$O(^1D)$ + COF_2 ------▸ F_2 + CO_2	2.1×10^{-11}	
24)	$O(^1D)$ -- WALL --▸ O	300	c
25)	O^- + O ------▸ O_2 (+e)	3×10^{-10}	
26)	O^- -- e --▸ O (+e)	2500	
27)*	CF_3 + O ------▸ COF_2 + F	3.1×10^{-11}	
28)*	CF_2 + O ------▸ COF + F	1.4×10^{-11}	
29)*	CF_2 + O ------▸ CO + 2F	4×10^{-12}	
30)*	COF + O ------▸ CO_2 + F	9.3×10^{-11}	
31)*	COF + F -- M --▸ COF_2	1.6×10^{-13}	b
32)	CF_3 + O_2 -- M --▸ CF_3O_2	8.1×10^{-14}	b
33)	CF_3O_2 + O ------▸ COF_2 + F + O_2	1×10^{-11}	
34)	CF_3O_2 -- e --▸ CF_3 + O_2	10	
35)	F_2 -- e --▸ F + F	10	
36)*	COF_2 -- e --▸ COF + F	10	
37)*	CO_2 -- e --▸ CO + O	20	
38)*	F + CO -- M --▸ COF	2.2×10^{-16}	b
39)	F + O_2 -- M --▸ FO_2	4.3×10^{-17}	b
40)	F + FO_2 ------▸ O_2 + F_2	5×10^{-11}	
41)	O + FO_2 ------▸ FO + O_2	5×10^{-11}	
42)	O + FO ------▸ O_2 + F	5×10^{-11}	
43)	COF + CF_2 ------▸ CF_3 + CO	3×10^{-13}	
44)	COF + CF_2 ------▸ COF_2 + CF	3×10^{-13}	
45)	COF + CF_3 ------▸ CF_4 + CO	1×10^{-11}	
46)	COF + CF_3 ------▸ COF_2 + CF_2	1×10^{-11}	
47)	COF + COF ------▸ COF_2 + CO	1×10^{-11}	
48)	C_2F_5 + O ------▸ CF_3COF + F	3×10^{-11}	
49)	CF + O ------▸ CO + F	2×10^{-11}	

Notes: a) Units of s^{-1} for first order reactions and $cm^3\ s^{-1}$ for second order reactions.
b) Reaction in fall-off region. See table 4.3 for parameters used to calculate the rate.
c) Calculated on the basis of collision efficiency = 0.05 (following Plumb and Ryan).

Table 4.2. The set of gas phase reactions considered for the calculations. For further notes on quoted rate coefficients, see reference [42]. Reactions marked with an asterisk form the reduced set of reactions found by Plumb and Ryan to be sufficient to explain product distributions. Taken from Plumb and Ryan [42].

	Reaction	k_o / cm^6 s^{-1}	k_∞ / cm^3 s^{-1}	F_c	k_{2nd} / cm^3 s^{-1} [a]
5)	$CF_3 + CF_3 -- M \rightarrow C_2F_6$	2.8×10^{-23}	8.3×10^{-12}	0.32	8×10^{-12}
6)	$CF_3 + F -- M \rightarrow CF_4$	7.7×10^{-27}	2×10^{-11}	0.63	6.5×10^{-12}
8)	$CF_2 + F -- M \rightarrow CF_3$	3.0×10^{-29}	1.3×10^{-11}	0.73	8.6×10^{-14}
9)	$CF_2 + F -- M \rightarrow CF_3$	3.2×10^{-29}	1×10^{-11}	0.72	9×10^{-16}
13)	$CF_2 + CF_3 -- M \rightarrow C_2F_5$	2.3×10^{-26}	1×10^{-12}	0.39	7.9×10^{-13}
31)	$COF + F -- M \rightarrow COF_2$	6.5×10^{-29}	1.4×10^{-11}	0.68	1.6×10^{-13}
32)	$COF + F -- M \rightarrow COF_2$	3.5×10^{-29}	8×10^{-12}	0.49	8.1×10^{-14}
38)	$F + CO -- M \rightarrow COF$	8.1×10^{-32}	9.4×10^{-11}	0.73	2.2×10^{-16}
39)	$F + O_2 -- M \rightarrow FO_2$	1.6×10^{-32}	3×10^{-11}	0.70	4.3×10^{-17}

Notes: a) The effective second order rate coefficient, k_{2nd}, is calculated for our conditions of 85 mTorr using [42]

$$k_{2nd} = \frac{k_o [M]}{1 + k_o [M] / k_\infty} F_c^{(1 + \{\log_{10} k_o [M] / k_\infty\}^2)^{-1}}$$

where [M] is the total gas concentration (= 85 mTorr) and k_∞ and k_o are the low and high pressure limits of the reaction rate respectively. F_c is a broadening factor to account for departure from simple Lindeman theory.

Table 4.3. Parameters for the calculation of effective second order rate coefficients for three body association reactions in the fall-off region. For further notes on the quoted values of F_c, k_∞, and k_o, see reference 42. Taken from Plumb and Ryan [42].

	Reaction	Rate coefficient at 40 sccm, 100 W and 85 mTorr [a]
50)	$CF_{2(ads)} -- 2F \rightarrow CF_4$	10.2
51)	$O -- WALL \rightarrow \frac{1}{2} O_2$	412
52)	$O + CO -- WALL \rightarrow CO_2$	4.9×10^{-12}
53)	$CF_2 -- WALL \rightarrow CF_{2(ads)}$	1070

Notes. a) Units of s^{-1} for first order reactions and cm^3 s^{-1} for second order reactions.

Table 4.4. Wall reactions included in the kinetic model. These reactions are discussed in more detail in the text.

of the impinging molecules (in cm s^{-1}). Where possible, estimates for s and r have been made using this equation.

4.5 THE STEADY STATE EQUATION CALCULATIONS

The ideal way to proceed would be to use numerical methods to simultaneously solve a set of non-linear differential equations, comprising steady state equations for each species present in the plasma and three conservation equations (for C, O and F), in order to calculate species concentrations. This represents a very complex numerical problem which is beyond the scope of this work. However, steady state equations can still be used to yield useful information concerning the important processes occurring in the plasma. In the following sections, we derive steady state equations for each species present, and use them to calculate species concentrations and to determine the important chemical pathways which occur in the plasma. All the kinetic calculations were performed using the spread-sheet software package LOTUS 123.

We now explain how the steady state equations are derived and presented. Firstly, all of the processes which produce or remove each species are presented in a table, along with the reaction rate coefficients. The units for rate coefficients are s^{-1} for first order reactions and $cm^3\ s^{-1}$ for second order reactions. Effective second order rate coefficients are used for three body reactions, and effective first order rate coefficients are used for dissociation reactions (see section 4.4). The reaction rate for species production or removal has been calculated for each reaction using rate coefficients from tables 4.2 and 4.4, with species concentrations from tables 4.1 and 4.5. The calculated reaction rates are presented as a percentage contribution to the total production or removal rate, allowing the relative importance of contributing reactions to be easily recognised. (Note that, due to rounding errors, the sum of these percentage contributions does not always add up to exactly 100 %). Reactions with overall contributions of greater than 10 % are considered to be important processes in controlling the concentration of the species of interest, unless otherwise mentioned in the text. The percentage contributions of the important reactions are

shown in bold typeface for emphasis. Steady state equations are then derived using only these important contributions.

4.5.1 DETERMINATION OF THE CONCENTRATIONS OF IMPORTANT RADICAL SPECIES

In this section, we determine the concentrations of CF_3, F, CF_2, O and COF. $[CF_3]$ and [F] are calculated for a wide range of experimental conditions, using the steady state equations for C_2F_6 and CF_4. For [F], it was found necessary to include wall reactions (see section 4.3) in order to make the calculations of [F] agree with the F atom OES results. $[CF_2]$, [O] and [COF] could not be calculated directly from our QMS results. For $[CF_2]$ and [O], values are adopted from the literature for CF_4 + 8 vol % O_2 process gas at conditions which correspond to our own results at 40 sccm, 100 W and 85 mTorr. We then use values for $[CF_3]$ and [F] calculated at 40 sccm, 100 W and 85 mTorr along with the literature values for $[CF_2]$ and [O] to calculate [COF] under these conditions, using the steady state equation for COF. In this way, we calculate values for the concentrations of all the important radical species present in the plasma at conditions of 40 sccm, 100 W and 85 mTorr. These concentrations are collected together in table 4.5 below.

Radical	composition / mol %
CF_3	0.088
F	18
CF_2	0.34
O	0.20
COF	0.09

Table 4.5. The concentrations of important radical species expressed as mole percentage compositions at conditions of 40 sccm, 100 W and 85 mTorr with no wafer present.

We now present the calculations which were used to obtain these values.

4.5.1.1 THE CALCULATION OF [CF_3] USING THE STEADY STATE EQUATION FOR C_2F_6

The production and loss processes considered for C_2F_6 are given below.

Reaction	Rate coefficient	percentage contribution
Production processes:		
5) $CF_3 + CF_3$ -- M --▸ C_2F_6	8×10^{-12}	**100**
Removal processes:		
10) C_2F_6 -- e --▸ $CF_3 + CF_3$	10	**88**
PUMP (40 sccm)	1.35	**12**

Table 4.6. The reactions which produce and remove C_2F_6 in the plasma, along with reaction rate coefficients (s^{-1} for first order and $cm^3\ s^{-1}$ for second order reactions) and the percentage contributions of each reaction to the overall production or removal rate.

Note that wall production of C_2F_6 by reaction of gaseous CF_3 with adsorbed CF_3 is not considered to be an important production mechanism for C_2F_6. Although there is no direct evidence to support or contradict this view, we note that the present results can be adequately explained without the need to include wall production of C_2F_6.

The only important production process is reaction 5, and the main removal process at 40 sccm is dissociation via reaction 10, with a small contribution from pumping.

We now derive the steady state equation for C_2F_6. Equating production and loss rates yields

$$k_5 [CF_3]^2 = k_{pump} [C_2F_6] + k_{10} [C_2F_6]$$

yielding

$$[C_2F_6] = k_5 [CF_3]^2 / (k_{pump} + k_{10})$$

and

$$[CF_3] = ([C_2F_6]\ \{k_{pump} + k_{10}\} / k_5)^{1/2} \qquad (4.4).$$

$[C_2F_6]$ has been measured by QMS (section 4.2), and $[CF_3]$ may be calculated using the values for rate coefficients given in table 4.2. Values for the concentration of CF_3 in the plasma are presented in figure 4.10 for the experiments of flow rate variation and volume percentage addition of O_2, CO, CO_2, and C_2F_6. Note that, even in the C_2F_6 addition experiment, flow production of C_2F_6 does not compete significantly with reaction 5 due to the low total flow rate of 5 sccm used in that experiment, so it is still valid to use equation 4.4 to calculate $[CF_3]$. Typical values for the concentration of CF_3 are $\approx$ 0.1 mol %. The trends observed will be discussed in section 4.6.3 later.

4.5.1.2 THE CALCULATION OF [F] USING THE STEADY STATE EQUATION FOR CF_4

In this section we calculate the mole percentage composition of F using the steady state equation for CF_4 and compare the calculations with some of the results of the F atom OES study. This comparison indicates that production of CF_4 at the walls is an important process, in accordance with the results of section 4.3. It is also found that wall production of CF_4 is inhibited by O atoms because O atoms compete with F atoms for surface sites.

The relative concentration of F atoms is given by the OES measurements of the emission intensity from excited F atoms, allowing a cross-check for our calculations. The intensity of the emitted light is proportional to the concentration of ground state F atoms provided that (a) the main production mechanism for excited F atoms is excitation from the ground state by electron impact, and (b) the electron density and energy distribution function are constant with varying conditions. Evidence from the literature indicates that the first assumption is valid [46]. The second assumption is also expected to be valid in all the experiments except where power and pressure are varied, as mentioned in section 4.4.

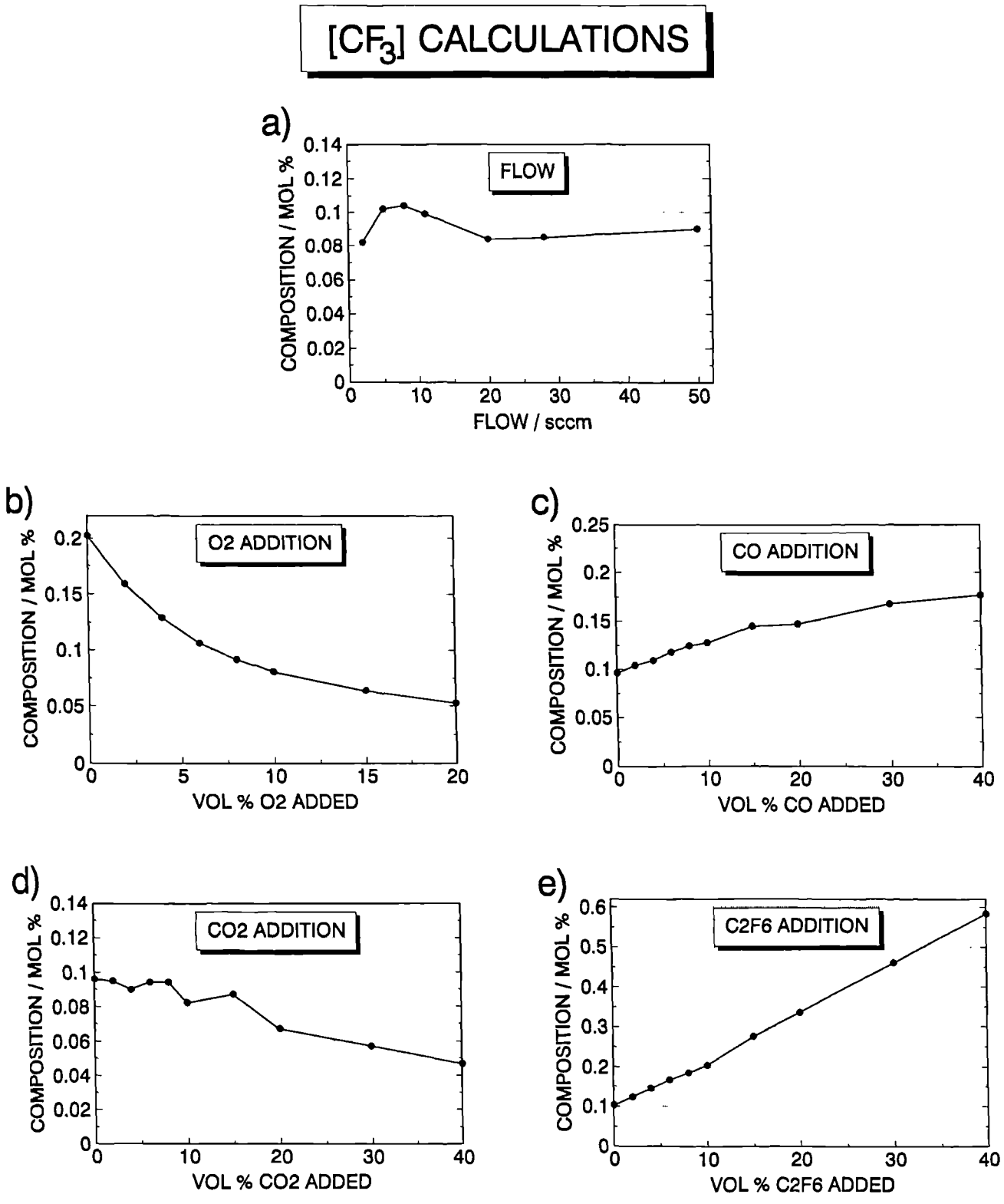

Figure 4.10. Graphs showing the results of the calculations of $[CF_3]$ for various experimental conditions (see section 4.2 for more details of exact conditions).

Thus for the present purposes, we assume that the intensity of F atom emission is proportional to the ground state F atom concentration.

[F] was first calculated using the steady state equation for CF_4, including only the gas phase reactions listed in table 4.2. This yielded

$$[F] = (\{k_{pump} + k_1 + k_2\} [CF_4] - R_{flow}) / (k_6 [CF_3]) \qquad (4.5)$$

where R_{flow} is the rate at which CF_4 is gained by flow into the chamber. Although the calculations of [F] using equation 4.5 were able to reproduce some of the trends observed by OES, the agreement was in general rather poor. In particular, the well-known increase in [F] on addition of O_2 to the discharge [46], [56], [57], [63], [65] was not reproduced.

Calculations of [F] using the steady state equation for CF_4 were therefore performed which included the wall production mechanism of CF_4 which was discussed in section 4.3 (with rate = k^{1st} [F]). The steady state equation this time yielded

$$[F] = (\{k_{pump} + k_1 + k_2\} [CF_4] - R_{flow}) / (k_6 [CF_3] + k^{1st}) \qquad (4.6)$$

where k^{1st} is the rate coefficient for wall production of CF_4. However, equation 4.6, with the inclusion of the wall production process which is simply first-order in F, was similarly unable to reproduce the OES results.

The reason for these discrepancies is indicated by the work of Hancock et al [46], who measured surface loss rates of F atoms at the chamber walls. They found that the surface loss rate decreased markedly on addition of O_2 to the discharge, due to O atoms competing with F atoms for surface sites. We propose that O inhibits the reaction of adsorbed CF_2 and CF_3 with F atoms, so that the rate of CF_4 at the chamber walls depends on the surface coverage of O atoms. By including this effect, using the approach described below, the OES results can be reproduced as we show later in this section.

In section 4.5.3.1 we show that, to a first approximation, [O] α [O_2]. We then make the assumption that the [O]-dependent rate coefficient for wall production of CF_4, k_{50}, depends on [O], as shown by the expression below.

50) $CF_{2(ads)}$ -- 2F --▸ $CF_{4(g)}$ Rate = k_{50} [F]

where $k_{50} = k_{wall} \exp(-B [O_2])$

(k_{50} has replaced k^{1st} from the discussions above). The parameter k_{wall} is the first-order rate coefficient for this process if there were no O present (i.e. the maximum value of k_{50}), and B is a scaling factor which affects the magnitude of the inhibiting effect of O atoms. There is no *a priori* justification for the above form of k_{50}, but we note that the OES results can now be reproduced if k_{50} is included in the calculation of [F] using B and k_{wall} as fitting parameters.

The production and loss processes considered for CF_4 are given below.

Reaction	Rate coefficient	percentage contribution
Production processes:		
6) CF_3 + F -- M --▸ CF_4	6.5×10^{-12}	**47**
45) COF + CF_3 -- M --▸ CF_4 + CO	1×10^{-11}	0.4
50) $CF_{2(ads)}$ -- 2F --▸ CF_4	10.2	**31**
FLOW (40 sccm)		**21**
Removal processes:		
1) CF_4 -- e --▸ CF_3 + F	3	**26**
2) CF_4 -- e --▸ CF_2 + 2F	7	**62**
PUMP (40 sccm)	1.35	**12**

Table 4.7. The reactions which produce and remove CF_4 in the plasma, along with reaction rate coefficients (s^{-1} for first order and $cm^3\ s^{-1}$ for second order reactions) and the percentage contributions of each reaction to the overall production or removal rate.

The main production processes for CF_4 are reaction 6 and reaction 50, with a smaller contribution from feed gas flow. (The values for B and k_{wall} which have been used to calculate the rate of reaction 50 are explained later). Reaction 45 is unimportant at 40 sccm, 100 W and 85 mTorr. As with C_2F_6 earlier, the main removal process is dissociation, with a small contribution from pumping.

The importance of reactions 6 and 50 indicate that CF_4 is rapidly recycled in the discharge. This effect can be seen clearly in the results of the flow rate variation experiments (figure 4.1). If CF_4 were not reformed in the discharge, the gas flow of CF_4 into the chamber would be the main production process. The removal rate by dissociation is constant with flow rate, so $[CF_4]$ would therefore be expected to rise with flow rate. However, $[CF_4]$ remains relatively constant with flow showing that CF_4 is indeed reformed in the discharge. The behaviour of $[CF_4]$ with increasing power further supports this view. If CF_4 were not reformed in the discharge then $[CF_4]$ would fall with increasing power due to the increase in the dissociation rate. However, $[CF_4]$ falls only slightly with increasing power (figures 4.2 and 4.3), again indicating that CF_4 is reformed in the discharge.

We now derive the steady state equation for CF_4. Equating production and loss rates (neglecting reaction 45) yields

$$R_{flow} + k_6 [CF_3] [F] + k_{wall} \exp(-B [O_2]) [F] = k_1[CF_4] + k_2[CF_4] + k_{pump} [CF_4]$$

yielding

$$[CF_4] = (R_{flow} + k_6 [CF_3] [F] + k_{wall} \exp(-B [O_2]) [F]) / (k_1 + k_2 + k_{pump})$$

and

$$[F] = (\{k_{pump} + k_1 + k_2\} [CF_4] - R_{flow}) / \{k_6 [CF_3] + k_{wall} \exp(-B [O_2])\} \quad (4.7)$$

$[CF_4]$ has been measured by QMS (section 4.2) and $[CF_3]$ was calculated in the previous section. Values for the percentage composition of F in the plasma can therefore be calculated using k_{wall} and B as adjustable parameters. k_{wall} and B were used to fit the trends shown by the [F] calculations using equation 4.7 to the trends observed by OES.

This was done for the results of the experiments with varying flow rate and varying volume percentage addition of O_2, CO, CO_2 and C_2F_6 (figures 4.1 and 4.5 to 4.8). The fitting procedure used a combination of least squares and visual comparison to assess the fit. The best data fit was obtained using values of $k_{wall} = 120\ s^{-1}$ and $B = 0.55$. It is interesting to note that using these values, the calculated rate of wall reaction 50 at 40 sccm, 100 W and 85 mTorr is $5 \times 10^{15}\ cm^{-3}\ s^{-1}$. This accords well with the estimate for this value of $9 \times 10^{15}\ cm^{-3}\ s^{-1}$ given in section 4.3.2 earlier. The results of the F atom concentration calculations using equation 4.7 are presented in figure 4.11 for various experimental conditions. Also plotted for comparison are the normalised F atom emission intensity results at 6856 Å, which correctly indicate [F] (see section 6.3.1).

We now discuss the degree of fit between the F atom concentration calculations and the OES results shown in figure 4.11. The agreement is very close for the CO, C_2F_6 and CO_2 addition experiments (figures 4.11c to e). The increase in the F atom concentration with increasing volume additions of O_2 is now reproduced (figure 11b), although there is some deviation above $\approx$ 10 vol % O_2 addition. This perhaps indicates that the inhibiting effect of O atoms reaches a saturation value for high [O], noting that Hancock [46] found that F atoms were no longer removed significantly by the walls above $\approx$ 10 vol % O_2. This generally good agreement is strong evidence in support of a mechanism in which O atoms inhibit wall production of CF_4 via reaction 50. We show later in section 4.5.4.1 that the increase in [F] as O_2 is added to the plasma is due largely to the inhibiting effect of O an the removal of F atoms at the walls via reaction 50.

For the flow rate experiment (figure 11a), the emission results indicate very little change in [F], while the calculation shows a small increase in [F] with flow. The reason for the discrepancy is not clear, although we note that the assumption that $[O] \alpha [O_2]$ becomes less accurate at higher flow rates, due to the associated increase of the relative importance gas flow to the overall volume production rate of O_2 (see section 4.5.3.1). This error would tend to cause the observed increase in the calculated concentration of F.

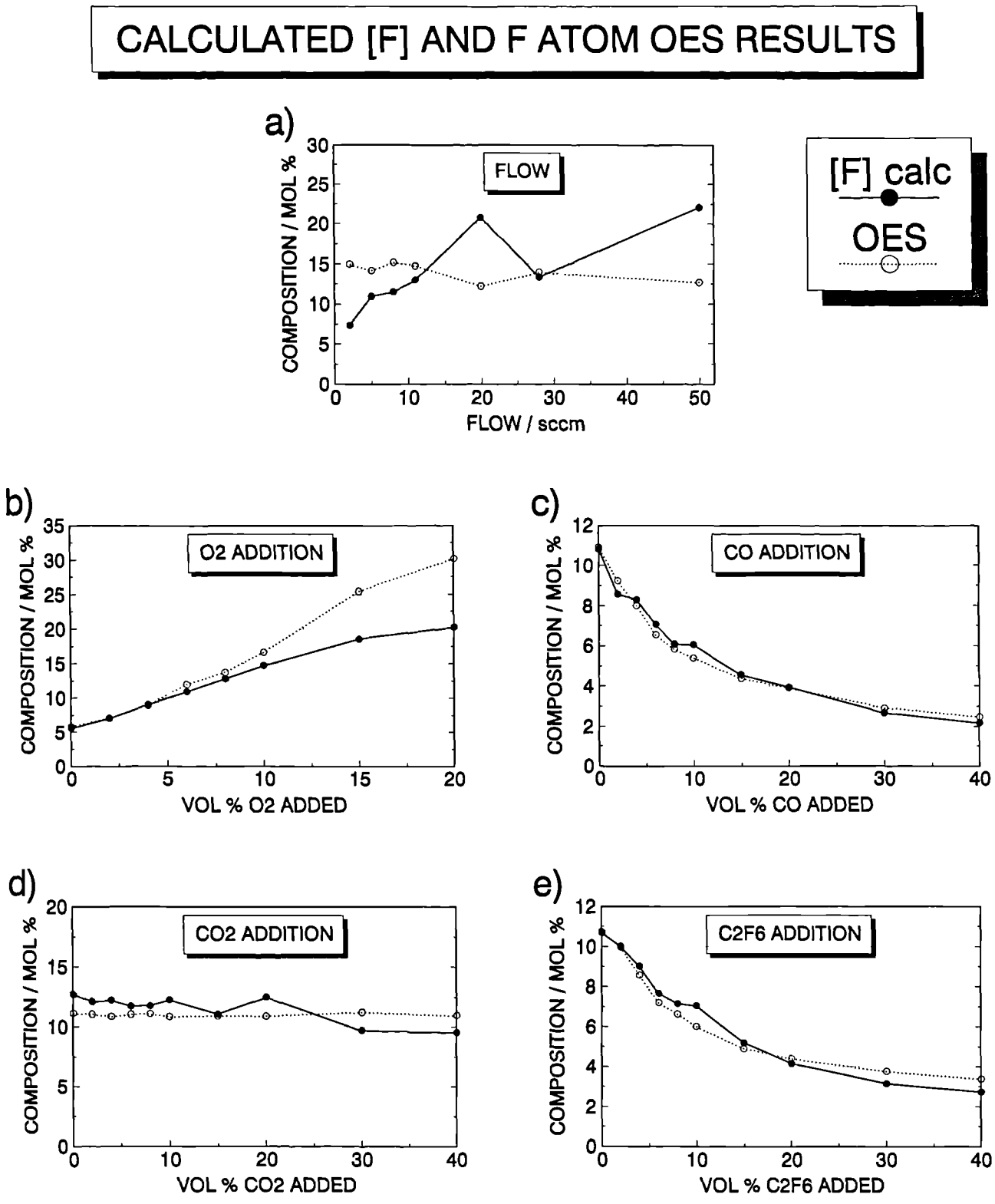

Figure 4.11. Graphs showing the results of the calculations of [F], plotted with normalised F atom optical emission results for comparison, for various experimental conditions (see section 4.2 for more details of exact conditions).

Having shown that the experimental trends are reproduced by the calculations, we now consider the size of the values calculated for the concentration of F atoms. Typical values of up to 20 mol % are obtained (see figure 4.11). Unfortunately, few absolute measurements of [F] appear in the literature to compare with these calculations. Direct measurement of [F] is difficult because F atoms cannot be observed by Laser Induced Fluorescence [46], which is generally the technique best suited to measuring ground-state concentrations of reactive species. However, Mogab et al [65] have used a method of gas phase titration to measure [F] downstream from a parallel plate rf reactor. Their measurements indicated concentrations of up to $\approx$ 15 mol % in plasmas of CF_4 + O_2 with no wafer present, for conditions of 350 mTorr, 200 sccm and 200 W. Clearly large concentrations of F are possible in CF_4 + O_2 plasmas, further supporting the [F] calculations presented in figure 4.11.

4.5.1.3 THE CONCENTRATIONS OF CF_2 AND O

It was not possible to calculate [CF_2] and [O] directly from our QMS results. Consequently it was necessary to adopt values from the literature.

Hancock [46] has measured the concentrations of CF_2 and O by Laser Induced Fluorescence (LIF) using a similar reactor to the one used in the present work. Those measurements were made as a function of the vol % of O_2 in CF_4 feed gas for conditions of 40 sccm total flow rate, 100 W and 50 mTorr. At 8 vol % O_2 addition, these conditions correspond reasonably well to the those used in the present work during the flow rate variation experiments (2 - 50 sccm, 100 W and 85 mTorr). We then make the assumptions that, firstly, the concentrations measured by Hancock are relevant to our own system, and secondly, that the proportion of CF_2 and O in the discharge does not alter significantly between 50 and 85 mTorr. The values for the concentrations of CF_2 and O at 8 vol % O_2 addition from that work are thus assumed to be applicable to our own results in the flow rate variation experiment at 40 sccm. The errors in this approximation are uncertain, but we would not expect them to be greater than a factor of 2. The LIF measurements of

Hancock gave concentrations for CF_2 = 0.34 mol % and for O = 0.20 mol % at 8 vol % O_2 addition. Linear interpolation using figures 4.10a and 4.11a give values for CF_3 = 0.088 mol % and F = 18 mol %. The concentrations of species measured by QMS at 40 sccm were given earlier in table 4.1 on p.100. These values can now be used to calculate [COF] at 40 sccm, 100 W and 85 mTorr using the steady state equation for COF. All subsequent calculations are also performed at these conditions.

4.5.1.4 THE STEADY STATE EQUATION FOR COF AND THE CALCULATION OF [COF]

The production and loss processes considered for COF are given below.

	Reaction	Rate coefficient	percentage contribution
Production processes:			
28)	$CF_2 + O \text{-----▸} COF + F$	1.4×10^{-11}	**49**
36)	$COF_2 \text{ -- e --▸} COF + F$	10	**51**
38	$F + CO \text{ -- M --▸} COF$	2.2×10^{-16}	0.2
Removal processes:			
30)	$COF + O \text{-----▸} CO_2 + F$	9.3×10^{-11}	**73**
31)	$COF + F \text{ -- M --▸} COF_2$	1.6×10^{-13}	**12**
43)	$COF + CF_2 \text{-----▸} CF_3 + CO$	3×10^{-13}	0.4
44)	$COF + CF_2 \text{-----▸} COF_2 + CF$	3×10^{-13}	0.4
45)	$COF + CF_3 \text{-----▸} CF_4 + CO$	1×10^{-11}	4
46)	$COF + CF_3 \text{-----▸} COF_2 + CF_2$	1×10^{-11}	4
47)	$COF + COF \text{-----▸} COF_2 + CO$	1×10^{-11}	7
	PUMP (40 sccm)	1.35	0.2

Table 4.8. The reactions which produce and remove COF in the plasma, along with reaction rate coefficients (s^{-1} for first order and $cm^3\ s^{-1}$ for second order reactions) and the percentage contributions of each reaction to the overall production or removal rate.

The main production processes for COF are reactions 28 and 36. At conditions of 40 sccm, 100 W and 85 mTorr, reaction 38 is unimportant. The main removal process for COF is reaction 30, with a small contribution from reaction 31. Reactions 43 to 47 and

removal by the pump are unimportant under these conditions. (Note that the percentage contribution from reaction 47 was arrived at by using a value for [COF] which was calculated with reaction 47 removed from the scheme. This is valid because the contribution of reaction 47 to the overall COF loss rate turns out to be small.)

The steady state equation for COF is

$$k_{28}\,[CF_2]\,[O] + k_{36}\,[COF_2] = k_{30}\,[COF]\,[O] + k_{31}\,[COF]\,[F]$$

yielding

$$[COF] = (k_{28}\,[CF_2]\,[O] + k_{36}\,[COF_2]) / (k_{30}\,[O] + k_{31}\,[F]) \qquad (4.8)$$

Using values of $[CF_2]$, [O] and [F] from table 4.5 on p.112, and $[COF_2]$ from table 4.1 on p.100, this yields a value of 0.09 mol % for the concentration of COF in the plasma at 40 sccm, 100 W and 85 mTorr.

4.5.2 CALCULATIONS OF THE CONCENTRATIONS OF OTHER SPECIES NOT DETECTED BY QMS

Using values of concentrations from tables 4.1 on p.100 and 4.5 on p.112, steady state equations have been derived for FO_2, FO, CF_3O_2, O^-, $O(^1D)$, CF, C_2F_3, C_2F_5 and C_2F_4, allowing the concentrations of these species to be calculated for conditions of 40 sccm, 100 W and 85 mTorr. The resulting values are given in table 4.9 below.

Species	Composition / mol %
FO_2	4×10^{-6}
FO	4×10^{-6}
CF_3O_2	6×10^{-4}
O^-	3×10^{-3}
$O(^1D)$	2×10^{-3}
CF	0.032
C_2F_3	6×10^{-4}
C_2F_5	1×10^{-4}
C_2F_4	2×10^{-5}

Table 4.9. The concentrations of species not observed by QMS expressed as mole percentage compositions at conditions of 40 sccm, 100 W and 85 mTorr with no wafer present.

All of these species are present at concentrations which are too low to be important in the plasma. This means that reactions involving these species do not contribute significantly to the production or removal of any other species, as will become clear later.

It is interesting to note that the value for the concentration of CF of 0.032 mol % agrees well with the value of $\approx$ 0.04 mol % indicated by the LIF measurements of Hancock et al [46], [104], lending support to the validity of the kinetic model.

4.5.3 STEADY STATE CALCULATIONS FOR SPECIES MEASURED BY QMS

In this section we derive the steady state equations for the species whose concentrations were measured by QMS (i.e. O_2, CO, COF_2, CO_2 and F_2), again for conditions of 40 sccm, 100 W and 85 mTorr. The concentrations of these species are then calculated using the steady state equations and compared with the experimental measurements, allowing the validity of the kinetic model to be tested directly. This test shows that for O_2 and CO, the gas phase reaction set used by Plumb and Ryan [42] (table 4.2) is not sufficient to explain the experimental results. In these cases, wall reactions are introduced (see table 4.4 on p.110b). With these wall reactions included in the model, the

calculated concentrations for all the species listed above are within a factor of three of the experimental measurements, lending further support to the kinetic model. In addition, the reactions which are important in controlling the concentrations of these species are highlighted, as before.

4.5.3.1 THE STEADY STATE EQUATION FOR O_2

The model used by Plumb and Ryan [42] suggests that the only significant source of O_2 in their system is gas flow. In this work, however, the QMS results for $[O_2]$ indicate strongly that O_2 is reformed in the discharge, as we now show using similar arguments to those used for CF_4 in section 4.5.1.2.

The dissociation rate of O_2 is sufficiently high that if no O_2 is reformed in the plasma, very little O_2 would remain in the chamber after the residence time had passed. However, the results indicate that there is more than 2 mol % O_2 remaining in the chamber from the original 8 vol % in the feed gas, even at the longest residence time of 15 s ($\equiv$ 2 sccm) (figure 4.1). In addition, if gas flow were the only source of O_2 in the discharge, then it would be expected that $[O_2]$ would be proportional to the gas flow rate. From figure 4.1 it can be seen that $[O_2]$ rises by a factor of just $\approx$ 3 while the flow rate rises by a factor of 25. Clearly there is another production mechanism for O_2 in our system.

One possible mechanism for O_2 production is reaction 25:

25) $O^- + O \text{-----}\blacktriangleright O_2 (+ e)$ $\qquad k_{25} = 3 \times 10^{-10}\ cm^3\ s^{-1}$

However, this reaction proceeds at a rate which is more than an order of magnitude too slow to explain the $[O_2]$ results. We propose that the major pathway for the production of O_2 in the plasma is recombination of O atoms at the chamber walls.

Greaves and Linnett [45] have studied the recombination of O atoms on a variety of different surfaces. They found that the recombination reaction followed first order kinetics, and that the reaction probability, r, was in the range 10^{-4} to 2×10^{-1} for all the materials tested. Other workers have measured values for r of 0.005 to 0.009 [105] and 0.09 [106], both within the range indicated by Greaves and Linnett. We propose that O_2 molecules are produced in the discharge by the wall reaction written below.

51) $O \text{ -- WALL --} \blacktriangleright \frac{1}{2} O_2$ $\qquad k_{51} = 412\ s^{-1}$

The value of the first-order rate coefficient k_{51} has been set to fit the results of the calculation of $[O_2]$ (given below) to the QMS measurements. Using equation 4.3 from section 4.4, a value for the reaction probability, r, of 0.06 is obtained for conditions of 40 sccm, 100 W and 85 mTorr, consistent with Greaves and Linnett [45].

We now derive the steady state equation for O_2. The production and loss mechanisms considered for O_2 are given below.

	Reaction	Rate coefficient	percentage contribution
Production processes:			
25)	$O^- + O \text{ -----▸ } O_2 (+ e)$	3×10^{-10}	9
33)	$CF_3O_2 + O \text{ -----▸ } COF_2 + F + O_2$	1×10^{-11}	0.06
34)	$CF_3O_2 \text{ -- e --▸ } CF_3 + O_2$	10	0.01
40)	$F + FO_2 \text{ -----▸ } O_2 + F_2$	5×10^{-11}	0.2
41)	$O + FO_2 \text{ -----▸ } FO + O_2$	5×10^{-11}	0.002
42)	$O + FO \text{ -----▸ } O_2 + F$	5×10^{-11}	0.002
51)	$O \text{ -- WALL --▸ } ½\ O_2$	412	**71**
	FLOW		**19**
Removal processes:			
17)	$O_2 \text{ -- e --▸ } O + O$	3.25	**28**
18)	$O_2 \text{ -- e --▸ } O + O(^1D)$	3.75	**32**
19)	$O_2 \text{ -- e --▸ } O^- + O$	3	**26**
32)	$CF_3 + O_2 \text{ -- M --▸ } CF_3O_2$	8.1×10^{-14}	2
39)	$F + O_2 \text{ -- M --▸ } FO_2$	4.3×10^{-17}	0.3
	PUMP	1.35	**12**

Table 4.10. The reactions which produce and remove O_2 in the plasma, along with reaction rate coefficients (s^{-1} for first order and $cm^3\ s^{-1}$ for second order reactions) and the percentage contributions of each reaction to the overall production or removal rate.

As explained above, the main production mechanism for O_2 is wall recombination, with some contribution from gas flow. The main removal processes for O_2 are dissociative (reactions 17 to 19), with a small contribution from pumping removal at higher flow rates.

The steady state equation for O_2 including only the important reactions is

$$R_{flow} + k_{51}[O] = k_{17}[O_2] + k_{18}[O_2] + k_{19}[O_2] + k_{pump}[O_2]$$

yielding

$$[O_2] = (R_{flow} + k_{51}[O]) / (k_{17} + k_{18} + k_{19} + k_{pump}) \qquad (4.9)$$

It is clear from equation 4.9 that if k_{51} (and hence the reaction probability for O recombination) is independent of the experimental conditions, then to a first approximation, $[O_2] \propto [O]$ (for constant power and pressure), since flow and pumping have relatively small

contributions to the overall production and removal rate (see table 4.10). This approximation is of course better at low flow rates where flow and pumping become less important. $[O_2]$ can therefore be used to indicate [O], as it was in section 4.5.1.2 earlier. This fact is also very useful for the interpretation of the QMS results (section 4.6.3) because [O] is otherwise difficult to determine.

4.5.3.2 THE STEADY STATE EQUATION FOR CO

As with the case of O_2 above, the gas phase reaction set used by Plumb and Ryan [42] is not sufficient to explain the results for CO. Using that reaction set, the calculated value for [CO] is too high by a factor of more than 20. The calculations of Plumb and Ryan indicate that the main removal processes of CO in their system were pumping and three-body reaction 38 (table 4.2). However, the pumping speeds encountered in this work are much lower than those of Plumb and Ryan, and our lower pressure of 85 mTorr means that the rate of reaction 38 becomes insignificant. Clearly there must be another removal mechanism operating.

The identity of the required removal mechanism for CO is indicated by the results of the CO addition experiment (figure 4.6). Those results show that as CO is added to the discharge, the concentration of O_2 falls despite the increase in the total oxygen budget. Noting that $[O_2] \alpha [O]$ (section 4.5.3.1), it appears that a reaction is occurring which removes O from the gas phase. We propose that the reaction which explains the above observations is the wall reaction of CO with O atoms to produce CO_2. This reaction is expected to exhibit second order kinetics, noting that the related reaction between CO and O atoms (produced from dissociative adsorption of O_2) proceeds by a Langmuir-Hinshelwood mechanism [107].

52) $CO + O \text{ -- WALL --} \blacktriangleright CO_2$ $\qquad k_{52} = 4.8 \times 10^{-12} \text{ cm}^3 \text{ s}^{-1}$

The value of the second-order rate coefficient, k_{52}, has been set to fit the results of the calculation of [CO] (given below) to the QMS measurements, and should not be confused with a gas phase two-body reaction rate coefficient.

We now derive the steady state equation for CO. The production and loss mechanisms considered for CO are given below.

	Reaction	Rate coefficient	percentage contribution
Production processes:			
29)	$CF_2 + O \text{ -----▸ } CO + 2F$	4×10^{-12}	**23**
37)	$CO_2 \text{ -- e --▸ } CO + O$	20	**54**
43)	$COF + CF_2 \text{ -----▸ } CF_3 + CO$	3×10^{-13}	1
45)	$COF + CF_3 \text{ -----▸ } CF_4 + CO$	1×10^{-11}	6
47)	$COF + COF \text{ -----▸ } COF_2 + CO$	1×10^{-11}	6
49)	$CF + O \text{ -----▸ } CO + F$	2×10^{-11}	10
Removal processes:			
38)	$F + CO \text{ -- M --▸ } COF$	2.2×10^{-16}	1
52)	$CO + O \text{ -- WALL --▸ } CO_2$	4.9×10^{-12}	**94**
	PUMP	1.35	5

Table 4.11. The reactions which produce and remove CO in the plasma, along with reaction rate coefficients (s^{-1} for first order and $cm^3\ s^{-1}$ for second order reactions) and the percentage contributions of each reaction to the overall production or removal rate.

The main production process for CO is dissociation of CO_2, with a smaller contribution from reaction 29. Reaction 49 may also make a contribution to the production of CO. However, it appears that in general, [CF] α $[CF_2]$ [104], which suggests that the percentage contributions of reactions 29 and 49 will always be in the same ratio. Since [CF] « $[CF_2]$, reaction 29 will always make a larger contribution to CO production than reaction 49, and the behaviour of the two reactions with varying conditions will be the same. For these reasons it was decided not to include reaction 49, and hence CF, in the overall reaction scheme in order to keep the number of species in the model to a minimum.

The main removal process for CO in the plasma is reaction 52. We now derive the steady state equation for CO.

The steady state equation for CO including only the important reactions is

$$k_{29}\,[CF_2]\,[O] + k_{37}\,[CO_2] = k_{52}\,[CO]\,[O]$$

yielding

$$[CO] = (k_{29}\,[CF_2]\,[O] + k_{37}\,[CO_2]) \,/\, k_{52}\,[O] \qquad (4.10)$$

The value for k_{52} was set to fit [CO] calculated by this equation to the QMS measurements given in table 4.1 on p.100 earlier, so equation 4.10 cannot be used to test the kinetic model.

4.5.3.3 THE STEADY STATE EQUATION FOR COF_2

The production and loss processes considered for COF_2 are given below.

Reaction	Rate coefficient	percentage contribution
Production processes:		
27) $CF_3 + O \text{ -----▸ } COF_2 + F$	3.1×10^{-11}	**55**
31) $COF + F \text{ -- M --▸ } COF_2$	1.6×10^{-13}	**27**
33) $CF_3O_2 + O \text{ -----▸ } COF_2 + F\,O_2$	1×10^{-11}	0.1
44) $COF + CF_2 \text{ -----▸ } COF_2 + CF$	3×10^{-13}	1
46) $COF + CF_3 \text{ -----▸ } COF_2 + CF_2$	1×10^{-11}	8
47) $COF + COF \text{ -----▸ } COF_2 + CO$	1×10^{-11}	8
Removal processes:		
23) $O(^1D) + COF_2 \text{ -----▸ } F_2 + CO_2$	2.1×10^{-11}	14
36) $COF_2 \text{ -- e --▸ } COF + F$	10	**80**
PUMP	1.35	**10**

Table 4.12. The reactions which produce and remove COF_2 in the plasma, along with reaction rate coefficients (s^{-1} for first order and $cm^3\ s^{-1}$ for second order reactions) and the percentage contributions of each reaction to the overall production or removal rate.

The main production processes for COF_2 are reactions 27 and 31. The main removal process for COF_2 is dissociation reaction 36, with a small contribution from pumping at the highest pumping speeds. The small contribution from reaction 23 to the removal of COF_2 is neglected in order to simplify the overall kinetic model by allowing $O(^1D)$ to be removed from the reaction scheme. This has only a small effect on the predictions of the model because the contribution of reaction 23 to the overall removal rate is small (14 %) compared to that of reaction 36 (80 %).

The steady state equation for COF_2 including only the important reactions is given below.

$$k_{27}\,[CF_3]\,[O] + k_{31}\,[COF]\,[F] = k_{36}\,[COF_2] + k_{pump}\,[COF_2]$$

yielding

$$[COF_2] = (k_{27}\,[CF_3]\,[O] + k_{31}\,[COF]\,[F]) \,/\, (k_{36} + k_{pump}) \qquad (4.11)$$

Using this equation, the calculated concentration of COF_2 in the plasma is 1.9 mol %, which agrees very well with the value of 2.65 mol % measured by QMS (see table 4.1 on p.100). The closeness of this agreement provides evidence that the concentrations of reactive radical species given in table 4.5 on p.112 are close to the real concentrations, and also that the proposed mechanisms for production and removal of COF_2 are correct. Note also that equation 4.11 contains no adjustable parameters.

4.5.3.4 THE STEADY STATE EQUATION FOR CO_2

The production and loss processes considered for CO_2 are given below.

Reaction	Rate coefficient	percentage contribution
Production processes:		
23) $O(^1D) + COF_2 \text{-----} \blacktriangleright F_2 + CO_2$	2.1×10^{-11}	3
30) $COF + O \text{-----} \blacktriangleright CO_2 + F$	9.3×10^{-11}	**62**
52) $CO + O$ -- WALL --$\blacktriangleright CO_2$	4.9×10^{-12}	**34**
Removal processes:		
37) CO_2 -- e --$\blacktriangleright CO + O$	20	**94**
PUMP	1.35	6

Table 4.13. The reactions which produce and remove CO_2 in the plasma, along with reaction rate coefficients (s^{-1} for first order and $cm^3\ s^{-1}$ for second order reactions) and the percentage contributions of each reaction to the overall production or removal rate.

The main production process for CO_2 is reaction 30, with a smaller contribution from reaction 52. The main removal mechanism is dissociation reaction 37.

The steady state equation for CO_2 including only the important reactions is given below.

$$k_{30}\,[COF]\,[O] + k_{52}\,[CO]\,[O] = k_{37}\,[CO_2]$$

yielding

$$[CO_2] = (k_{30}\,[COF]\,[O] + k_{52}\,[CO]\,[O]) / k_{37} \qquad (4.12)$$

Using this equation, the calculated concentration of CO_2 is 3.5 mol %, compared with the value of 0.86 mol % measured by QMS. We note that the error could be reduced by adjustment of the value of k_{52}. The value of k_{52} was set to fit the calculation of [CO] to the QMS measurements (section 4.5.3.2). A smaller value for k_{52} would bring calculations of both [CO] and $[CO_2]$ within a factor of three of the QMS measurements. This generally good agreement lends support to the validity of the proposed mechanisms for CO_2 production and removal.

4.5.3.5 THE STEADY STATE EQUATION FOR F_2

The production and loss processes considered for F_2 are given below.

Reaction	Rate coefficient	percentage contribution
Production processes:		
23) $O(^1D) + COF_2 \text{-----▸} F_2 + CO_2$	2.1×10^{-11}	**96**
40) $F + FO_2 \text{-----▸} O_2 + F_2$	5×10^{-11}	4
Removal processes:		
35) $F_2 \text{-- e --▸} F + F$	10	**88**
PUMP	1.35	**12**

Table 4.14. The reactions which produce and remove F_2 in the plasma, along with reaction rate coefficients (s^{-1} for first order and $cm^3\ s^{-1}$ for second order reactions) and the percentage contributions of each reaction to the overall production or removal rate.

The main production process for F_2 is reaction 23. F_2 is removed mainly by dissociation reaction 35, with some contribution from pumping at high pumping speeds.

The steady state equation for F_2 including only the important reactions is given below.

$$k_{23}\,[O(^1D)]\,[COF_2] = k_{35}\,[F_2] + k_{pump}\,[F_2]$$

yielding

$$[F_2] = k_{23}\,[O(^1D)]\,[COF_2] \,/\, (k_{35} + k_{pump}) \qquad (4.13)$$

Using this equation, the calculated concentration of F_2 in the plasma is 0.21 mol %, compared to the measured value of 0.46 mol %. (But note that, as we explained in section 3.3.3, the QMS measurement of $[F_2]$ is subject to errors). Although the agreement is good, there is evidence that F_2 is also produced by another mechanism, as we discuss below.

Firstly, we note that the F_2 dissociation rate may be faster than expected [108], which would result in a lower calculated value for $[F_2]$. In addition, the QMS results obtained when sampling downstream of the discharge show that $[F_2]$ is more than twice that within the plasma, which shows that F_2 continues to be produced downstream (see table 3.3 on p.93). It is very unlikely that reaction 23 produces F_2 downstream due to the very rapid quenching of $O(^1D)$ by reactions 20 to 24 (table 4.2 on p. 110a). We propose that F_2 is also formed by the recombination of F atoms at the chamber walls. Assuming this process is first order [109], a value for the wall reaction probability of around 3×10^{-5} is necessary to make the calculation of $[F_2]$ agree with the QMS measurements. Values for r have been measured [109] using a discharge through F_2 as the source of F atoms. The quoted values for r are 6.4×10^{-5} for an alumina surface and 1.8×10^{-3} for aluminium, although it is noted that the copper alloyed in the aluminium (0.25 %) may be responsible for the higher recombination efficiency on aluminium (copper was shown to be very active for F atom recombination). In reference 108, a value of $r = 2 \pm 2 \times 10^{-4}$ is quoted. In the RIE plasma environment, these values for r are expected to be lower because there are other reactive species present, especially O atoms, which compete for surface sites (see section 4.5.1.2 and reference 47) thus reducing the effective surface area available for reaction. Although the surfaces in contact with the plasma are in an unknown state of passivation, it appears that the calculated value for r of 3×10^{-5} is not in conflict with the values reported in the literature, and we conclude that F_2 is indeed produced at the walls.

We now consider the importance of F_2 in the plasma. The only reaction of F_2 which could be important in the plasma is dissociation to give F atoms (see table 4.14). However, we show later in section 4.5.4.1 that this process does not represent a significant production mechanism for F atoms. It is clear that F_2 does not affect the concentrations of any other species in the plasma, and is therefore not important in determining the overall chemistry of $CF_4 + O_2$ discharges. It is also unlikely that F_2 is important in the etching of Si, Ge or SiGe wafers. It has been shown that on exposure of Si wafers to F and F_2, F atoms penetrate deep into the surface, ultimately forming SiF_4, whereas F_2 adsorbs to form just a single monolayer [110]. This shows clearly that F_2 is much less active than F towards

the Si surface and it is therefore expected that F_2 does not contribute significantly to the etching process, especially since $[F_2] \ll [F]$ for all conditions considered in this work. For these reasons, F_2 is not included in the overall reaction scheme.

4.5.4 CALCULATIONS FOR RADICAL SPECIES

In this section, we derive the steady state equations for CF_3, F, CF_2 and O in order to discover which are the important production and loss mechanisms for these species. In addition, the concentrations of these species are calculated at 40 sccm, 100 W and 85 mTorr using the steady state equations, in order to compare them with the values determined independently in sections 4.5.1.1 to 4.5.1.3. This test reveals the extent to which the calculations presented in this work are mutually self-consistent, and also gives a further indication of whether or not the proposed reaction schemes are valid. For [F], $[CF_3]$ and [O] (sections 4.5.4.1, 4.5.4.2 and 4.5.4.4), the agreement is found to be within a factor of two. For CF_2 (section 4.5.4.3), the results indicate that an additional loss mechanism is occurring, which we propose is due to adsorption of CF_2 at the reactor walls, as indicated by the results of section 4.3.1. We also show in section 4.5.4.1 below that competition for surface sites between O and F is the reason for the increase in [F] as O_2 is added to the plasma.

4.5.4.1 THE STEADY STATE EQUATION FOR F

The production and loss mechanisms considered for F are given below.

	Reaction	Rate coefficient	percentage contribution
Production processes:			
1)	CF_4 -- e --▸ CF_3 + F	3	**15**
2)	CF_4 -- e --▸ CF_2 + 2F	7	**71**
3)	CF_3 -- e --▸ CF_2 + F	10	0.1
4)	CF_2 -- e --▸ CF + F	10	0.3
27)	CF_3 + O -----▸ COF_2 + F	3.1×10^{-11}	1
28)	CF_2 + O -----▸ COF + F	1.4×10^{-11}	2
29)	CF_2 + O -----▸ CO + 2F	4×10^{-12}	1
30)	COF + O -----▸ CO_2 + F	9.3×10^{-11}	4
33)	CF_3O_2 + O -----▸ COF_2 + F + O_2	1×10^{-11}	0.003
35)	F_2 -- e --▸ F + F	10	1
36)	COF_2 -- e --▸ COF + F	10	3
42)	O + FO -----▸ O_2 + F	5×10^{-11}	0.0001
48)	C_2F_5 + O -----▸ CF_3COF + F	3×10^{-11}	0.002
49)	CF + O -----▸ CO + F	2×10^{-11}	0.3
Removal processes:			
6)	CF_3 + F -- M --▸ CF_4	6.5×10^{-12}	**40**
8)	CF_2 + F -- M --▸ CF_3	7.8×10^{-15}	2
9)	CF + F -- M --▸ CF_2	8.6×10^{-16}	0.002
12)	F + C_2F_4 -----▸ CF_3 + CF_2	4×10^{-11}	0.06
14)	C_2F_5 + F -----▸ CF_3 + CF_3	1×10^{-11}	0.1
16)	C_2F_3 + F -----▸ C_2F_4	1×10^{-12}	0.04
31)	COF + F -- M --▸ COF_2	1.6×10^{-13}	1
38)	F + CO -- M --▸ COF	2.2×10^{-16}	0.01
39)	F + O_2 -- M --▸ FO_2	4.3×10^{-17}	0.01
40)	F + FO_2 -----▸ O_2 + F_2	5×10^{-11}	0.01
50)	$CF_{2(ads)}$ -- 2F --▸ CF_4	10.2	**53**
	PUMP	1.35	4

Table 4.15. The reactions which produce and remove F in the plasma, along with reaction rate coefficients (s^{-1} for first order and $cm^3\ s^{-1}$ for second order reactions) and the percentage contributions of each reaction to the overall production or removal rate.

The main production mechanism for F atoms is dissociation of CF_4. The main removal processes for F atoms involve reforming CF_4 via reactions 6 and 50.

It is interesting to note that reactions 27 to 30 make insignificant contributions to the production of F. These reactions are therefore not responsible for the observed increase in [F] as O_2 is added to the plasma (section 4.5.1.2). There is a reduction in the rate of F removal via reaction 6 when O_2 is added, due to the associated decrease in [CF_3] (see figure 4.10), which will tend to cause an increase in [F]. However, this effect is offset

by a decrease in the rate of F atom production by reactions 1 and 2, due to the decrease in $[CF_4]$ as O_2 is added (see figure 4.5). The increase in [F] as O_2 is added to the plasma is instead caused by a reduction in the rate of removal of F atoms via reaction 50, due to the inhibiting effect of O atoms on that reaction (see section 4.5.1.2). This accords with the recent findings of Hancock et al 46.

The steady state equation for F including only the important reactions is given below.

$$k_1 [CF_4] + 2 k_2 [CF_4] = k_6 [CF_3] [F] + 2 k_{50} [F]$$

yielding

$$[F] = (k_1 + 2 k_2) [CF_4] / (k_6 [CF_3] + 2 k_{50}) \qquad (4.14)$$

Using this equation, with k_{50} calculated as in section 4.5.1.2, the calculated concentration of F in the plasma is 25 mol %. This accords well with the value of 18 mol % calculated in section 4.5.1.2. We note also that the F atom wall loss rate by reaction 50 leads to a value of 0.004 for the sticking coefficient of F at the walls, calculated using equation 4.3 (p.110). This shows excellent agreement with the earlier independent estimate of this value (section 4.3.3), which also yielded a value of 0.004.

4.5.4.2 THE STEADY STATE EQUATION FOR CF_3

The production and loss mechanisms considered for CF_3 are given below.

Reaction	Rate coefficient	percentage contribution
Production processes:		
1) CF_4 -- e --▸ CF_3 + F	3	**90**
8) CF_2 + F -- M --▸ CF_3	7.8×10^{-14}	8
10) C_2F_6 -- e --▸ CF_3 + CF_3	10	2
12) F + C_2F_4 -----▸ CF_3 + CF_2	4×10^{-11}	0.3
14) C_2F_5 + F -----▸ CF_3 + CF_3	1×10^{-11}	0.4
43) COF + CF_2 -----▸ CF_3 + CO	3×10^{-13}	0.2
Removal processes:		
3) CF_3 -- e --▸ CF_2 + F	10	0.3
5) CF_3 + CF_3 -- M --▸ C_2F_6	7.8×10^{-12}	1
6) CF_3 + F -- M --▸ CF_4	6.5×10^{-12}	**92**
13) CF_2 + CF_3 -- M --▸ C_2F_5	7.9×10^{-13}	0.2
27) CF_3 + O -----▸ COF_2 + F	3.1×10^{-11}	5
32) CF_3 + O_2 -- M --▸ CF_3O_2	8.1×10^{-14}	0.3
45) COF + CF_3 -----▸ CF_4 + CO	1×10^{-11}	0.7
46) COF + CF_3 -----▸ COF_2 + CF_2	1×10^{-11}	0.7
PUMP	1.35	0.04

Table 4.16. The reactions which produce and remove CF_3 in the plasma, along with reaction rate coefficients (s^{-1} for first order and $cm^3\ s^{-1}$ for second order reactions) and the percentage contributions of each reaction to the overall production or removal rate.

The main production process for CF_3 is dissociation of CF_4 via reaction 1, and the main removal process is reaction 6.

The steady state equation for CF_3 including only the important reactions is given below.

$$k_1\,[CF_4] = k_6\,[F]\,[CF_3]$$

yielding

$$[CF_3] = k_1\,[CF_4] \,/\, (k_6\,[F]) \qquad (4.15)$$

Clearly the concentration of CF_3 is strongly dependent on [F].

Using this equation, the calculated concentration of CF_3 in the plasma is 0.049 mol %, in good agreement with the value of 0.088 mol % calculated earlier in section 4.5.1.1, providing further evidence for the self consistency of the kinetic model.

4.5.4.3 THE STEADY STATE EQUATION FOR CF_2

If gas phase reactions alone are used to calculate $[CF_2]$, a value which is more than a factor of 7 too large is obtained. This indicates that a surface process is occurring which removes CF_2, in accordance with our earlier atom budget results (section 4.3.1). CF_2 has been shown to be responsible for the deposition of polymeric species in CF_4 plasmas [111], indicating that CF_2 adsorbs at the walls. In addition, Hancock et al [46] have measured wall loss rates for CF_2 in pure CF_4 plasmas (see later), again showing that CF_2 adsorbs at the walls. We include this adsorption process according to the reaction below.

53) CF_2 -- WALL --▸ $CF_{2(ads)}$ $\qquad k_{53} = 1070\ s^{-1}$

The value of k_{53} is set to fit the results of the calculation of $[CF_2]$ (given below) to the measurements of Hancock et al discussed earlier in section 4.5.1.3.

The production and loss mechanisms considered for CF_2 are given below.

	Reaction	Rate coefficient	percentage contribution
Production processes:			
2)	CF_4 -- e --▸ CF_2 + 2F	7	**99**
3)	CF_3 -- e --▸ CF_2 + F	10	0.2
9)	CF + F -- M --▸ CF_2	8.6×10^{-16}	0.004
11)	C_2F_4 -- e --▸ CF_2 + CF_2	10	0.00006
12)	F + C_2F_4 -----▸ CF_3 + CF_2	4×10^{-11}	0.1
46)	COF + CF_3 -----▸ COF_2 + CF_2	1×10^{-11}	0.6
Removal processes:			
4)	CF_2 -- e --▸ CF + F	10	1
7)	CF_2 + CF_2 -- M --▸ C_2F_4	5×10^{-14}	0.1
8)	CF_2 + F -- M --▸ CF_3	7.7×10^{-14}	3
13)	CF_2 + CF_3 -- M --▸ C_2F_5	7.9×10^{-13}	0.2
15)	CF + CF_2 -----▸ C_2F_3	1×10^{-12}	0.1
28)	CF_2 + O -----▸ COF + F	1.4×10^{-11}	6
29)	CF_2 + O -----▸ CO + 2F	4×10^{-12}	2
43)	COF + CF_2 -----▸ CF_3 + CO	3×10^{-13}	0.06
44)	COF + CF_2 -----▸ COF_2 + CF	3×10^{-13}	0.06
53)	CF_2 -- WALL --▸ $CF_{2(ads)}$	1070	**88**
	PUMP	1.35	0.1

Table 4.17. The reactions which produce and remove CF_2 in the plasma, along with reaction rate coefficients (s^{-1} for first order and $cm^3\ s^{-1}$ for second order reactions) and the percentage contributions of each reaction to the overall production or removal rate.

The main production process for CF_2 is dissociation of CF_4 via reaction 2, and the main removal process is adsorption at the walls via reaction 53.

The steady state equation for CF_2 including only the important reactions is given below.

$$k_2\,[CF_4] = k_{53}\,[CF_2]$$

yielding

$$[CF_2] = k_2\,[CF_4] / k_{53} \qquad (4.16)$$

As noted above, the value for k_{53} was set to fit the calculation of $[CF_2]$ by the above equation to the measurements of Hancock et al. This results in a value for $s(CF_2)$ of around

0.3, which is a factor of 4 larger than the value of 0.07 indicated by the results of Hancock et al [46]. The reason for this discrepancy is not clear. However, we note that the value of $s(CF_2) = 0.3$ was used to estimate the volume production rate of CF_4 by wall reaction 50 (section 4.3.2), yielding a value which was consistent with the value calculated later by an independent method in section 4.5.1.2. The value for $s(CF_2)$ determined above is therefore consistent with other aspects of the kinetic model.

4.5.4.4 THE STEADY STATE EQUATION FOR O

The production and loss mechanisms considered for O are given below.

	Reaction	Rate coefficient	percentage contribution
Production processes:			
17)	O_2 -- e --▸ O + O	3.25	**29**
18)	O_2 -- e --▸ O + $O(^1D)$	3.75	**17**
19)	O_2 -- e --▸ O + O^-	3	**14**
20)	$O(^1D)$ + O_2 -----▸ O + O_2	4×10^{-11}	8
21)	$O(^1D)$ + CF_4 -----▸ O + CF_4	1.8×10^{-13}	0.4
22)	$O(^1D)$ + COF_2 -----▸ O + COF_2	5.3×10^{-11}	6
24)	$O(^1D)$ -- WALL --▸ O	300	0.5
26)	O^- -- e --▸ O	2500	8
37)	CO_2 -- e --▸ CO + O	20	**17**
Removal processes:			
25)	O^- + O -----▸ O_2 (+ e)	3×10^{-10}	3
27)	CF_3 + O -----▸ COF_2 + F	3.1×10^{-11}	**7**
28)	CF_2 + O -----▸ COF + F	1.4×10^{-11}	**12**
29)	CF_2 + O -----▸ CO + 2F	4×10^{-12}	**4**
30)	COF + O -----▸ CO_2 + F	9.3×10^{-11}	**22**
33)	CF_3O_2 + O -----▸ COF_2 + F + O_2	1×10^{-11}	0.02
41)	O + FO_2 -----▸ FO + O_2	5×10^{-11}	0.0005
42)	O + FO -----▸ FO_2	5×10^{-11}	0.0005
48)	C_2F_5 + O -----▸ CF_3COF + F	3×10^{-11}	0.01
49)	CF + O -----▸ CO + F	2×10^{-11}	2
51)	O -- WALL --▸ ½ O_2	412	**39**
52)	CO + O -- WALL --▸ CO_2	4.9×10^{-12}	**12**
	PUMP	1.35	0.1

Table 4.18. The reactions which produce and remove O in the plasma, along with reaction rate coefficients (s^{-1} for first order and $cm^3\ s^{-1}$ for second order reactions) and the percentage contributions of each reaction to the overall production or removal rate.

The main production process for O is by dissociation of O_2 via reactions 17, 18 and 19, with a smaller contribution from dissociation of CO_2 by reaction 37. We note that dissociation of O_2 yields $O(^1D)$ and O^- aswell as O atoms. However, the main role of these species is to return O atoms to the gas phase via reactions 20, 21, 22, 24 and 26. In order to simplify the model, we use the approximation that O_2 dissociates exclusively via reaction 17, and we set the rate coefficient for that reaction equal to ($k_{17} + k_{18} + k_{19}$), following Plumb and Ryan [42]. This has only a small effect on the calculation of [O] given below.

There are several processes which are found to be important removal mechanisms for O. The main removal process is reaction 51, with significant contributions

from reaction 30, reaction 52 and from reactions with CF_x (x = 2-3) (reactions 27, 28 and 29). All the reactions of O with CF_x have been included in the calculations because their collective effect is significant.

The steady state equation for O including only the important reactions is given below.

$$2\,(k_{17} + k_{18} + k_{19})\,[O_2] + k_{37}\,[CO_2] = k_{27}\,[CF_3]\,[O] + (k_{28} + k_{29})\,[CF_2]\,[O] + k_{30}\,[COF]\,[O] + k_{51}\,[O] + k_{52}\,[O]\,[CO]$$

yielding

$$[O] = \{2\,(k_{17} + k_{18} + k_{19})\,[O_2] + k_{37}\,[CO_2]\} / \{k_{27}\,[CF_3] + (k_{28} + k_{29})\,[CF_2] + k_{30}\,[COF] + k_{51} + k_{52}\,[CO]\} \quad (4.17)$$

Using this equation, the calculated concentration of O in the plasma is 0.11 mol %, which agrees well with the value of 0.20 mol % measured by Hancock et al (see section 4.5.1.3), lending further support to the kinetic model.

4.6 THE OVERALL REACTION SCHEME

In this section, we collect together all the reactions and species which have been shown to have important influence in the plasma. An overall reaction scheme is produced, and the role played by each species in the plasma is discussed. We outline in general terms the main consequences of the proposed reaction scheme, and then use it to explain the trends observed in the QMS results (section 4.2).

In the steady state equation calculations described in the previous sections, many reactions were shown to have a negligible influence in the plasma. Out of the initial 53 reactions in tables 4.2 and 4.4, only 17 have been shown to have significant effects on composition of the plasma. These 17 reactions are listed in table 4.19. Also given, in table 4.20, are the concentrations of the species which have been shown to be important in the

plasma (i.e. having high concentration or being important in determining the concentrations of other species), reproduced from tables 4.1 and 4.5 here for convenience.

In order to illustrate more clearly the important pathways which occur in the plasma, a diagrammatic reaction scheme has been produced, shown in figure 4.12. Also given are the relative reaction rates for each reaction, with the rate for the fastest reactions (reactions 2 and 53, with reaction rates of 1 x 10^{16} cm^{-3} s^{-1}) set equal to 1000. Reaction rates are calculated for the reactions as expressed in table 4.19, for conditions of 40 sccm, 100 W and 85 mTorr. This is done in order to give an indication of the relative importance of each reaction. Pumping is not included in figure 4.12, for clarity, noting that it is not a major removal process at 40 sccm due to the fast dissociation and chemical removal rates. Pumping is only found to have a significant contribution to the removal rate of CF_4, O_2, COF_2 and C_2F_6 where it contributes just 12 % to the overall removal rate, so the general predictions of the reaction scheme are not affected by this omission.

It is interesting at this point to compare the findings of this study with those of Plumb and Ryan [42]. In the work of Plumb and Ryan, only gas phase reactions were considered. They found that a reduced set of 13 of the initial 49 reactions considered in that study were just as satisfactory as the full set for calculating [F] and unreactive product distributions (excluding C_2F_6). In this work we find that all of those 13 reactions are important except for two;

8) $CF_2 + F \text{ -- M --▸ } CF_3$ $\qquad k_8 = 8.6 \times 10^{-14}\ cm^3\ s^{-1}$

38) $F + CO \text{ -- M --▸ } COF$ $\qquad k_{38} = 2.2 \times 10^{-16}\ cm^3\ s^{-1}$

both of which are three-body reactions which are too slow to be important at the lower pressures encountered in this work. The 11 remaining gas phase reactions in the reduced set used by Plumb and Ryan are marked with an asterisk in table 4.19. Two further gas phase reactions which produce and remove C_2F_6 have been added in this work. While these reactions do not affect the concentration of any species other than C_2F_6, they are included explicitly in table 4.19 because they are important in controlling $[C_2F_6]$, which was used in

	Reaction	Rate coefficient at 40 sccm, 100 W and 85 mTorr [a]
1)*	CF_4 -- e --▸ CF_3 + F	3
2)*	CF_4 -- e --▸ CF_2 + 2F	7
5)	CF_3 + CF_3 -- M --▸ C_2F_6	8×10^{-12}
6)*	CF_3 + F -- M --▸ CF_4	6.5×10^{-12}
10)	C_2F_6 -- e --▸ CF_3 + CF_3	10
17)*	O_2 -- e --▸ O + O	10 [b]
27)*	CF_3 + O ------▸ COF_2 + F	3.1×10^{-11}
28)*	CF_2 + O ------▸ COF + F	1.4×10^{-11}
29)*	CF_2 + O ------▸ CO + 2F	4×10^{-12}
30)*	COF + O ------▸ CO_2 + F	9.3×10^{-11}
31)*	COF + F -- M --▸ COF_2	1.6×10^{-13}
36)*	COF_2 -- e --▸ COF + F	10
37)*	CO_2 -- e --▸ CO + O	20
50)	$CF_{2(ads)}$ -- 2F --▸ CF_4	10.2
51)	O -- WALL --▸ ½ O_2	412
52)	O + CO -- WALL --▸ CO_2	4.9×10^{-12}
53)	CF_2 -- WALL --▸ $CF_{2(ads)}$	1070

Notes. a) Units of s^{-1} for first order reactions and $cm^3\ s^{-1}$ for second order reactions.
b) The quoted rate coefficient is set equal to (k_{17} + k_{18} + k_{19}) - see section 4.5.4.4

Table 4.19. Reactions which have important consequences on the chemistry of the plasma. Rate constants are quoted for conditions of 40 sccm, 100 W and 85 mTorr. Reactions marked with an asterisk form part of the reduced set of reactions, found by Plumb and Ryan to be sufficient to explain product distributions (see text for further explanation).

Species	Composition / mol %
C_2F_6	0.14
CF_4	52
O_2	4.5
CO	0.94
COF_2	2.7
CO_2	0.87
CF_3	0.088
F	18
CF_2	0.34
O	0.20
COF	0.090

Table 4.20. The concentrations of important species present in the plasma expressed as mole percentage compositions at conditions of 40 sccm, 100 W and 85 mTorr.

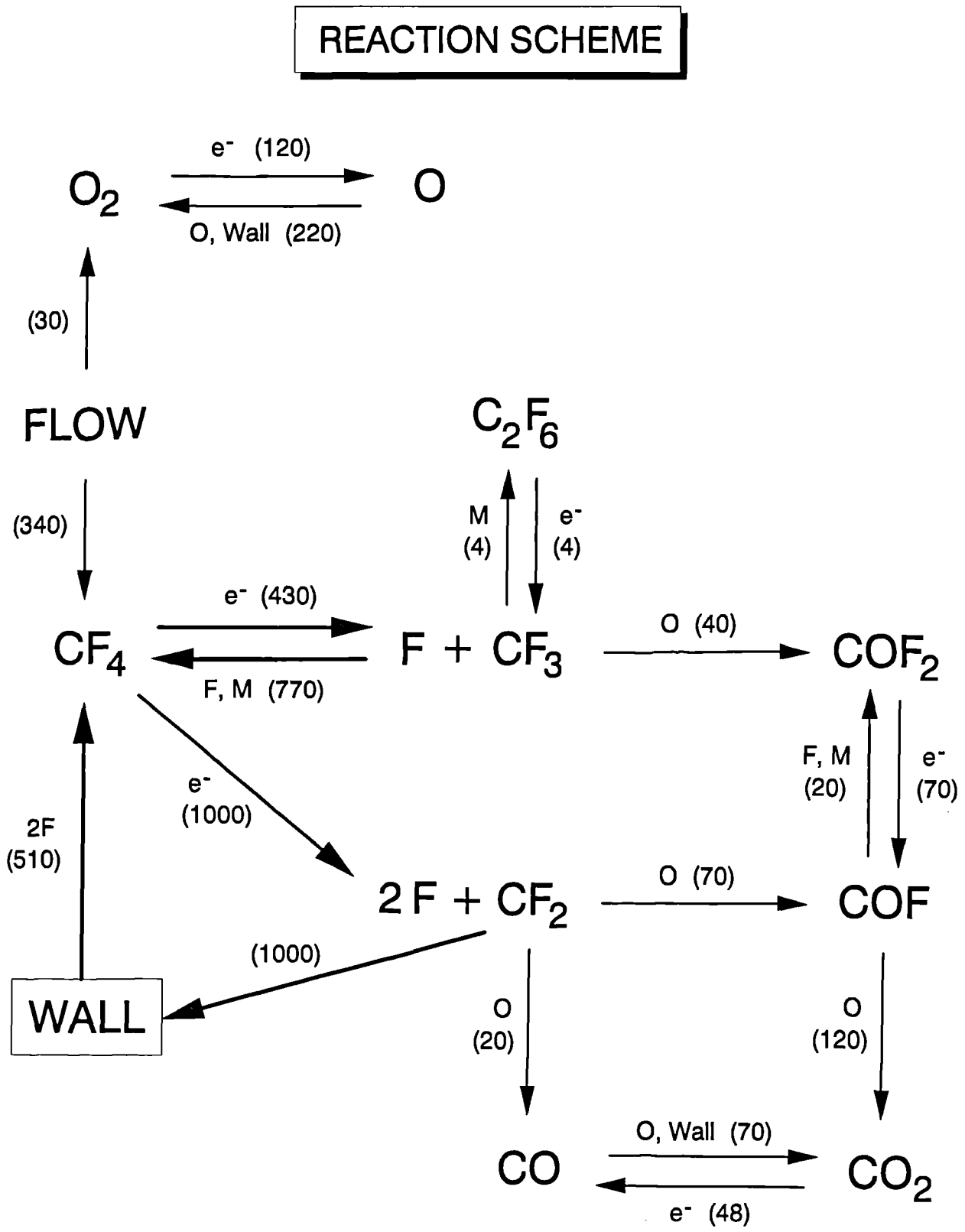

Figure 4.12. The overall reaction scheme for CF_4 + O_2 process gas showing all the reactions found to be important in the steady state equation calculations. Bracketed numbers represent relative reaction rates for CF_4 + 8 vol % O_2 process gas at conditions of 40 sccm, 100 W and 85 mTorr with no wafer present.

this work to calculate [CF_3]. Plumb and Ryan did not attempt to calculate [C_2F_6] using their reduced set, and so did not include these reactions.

The main difference between our model and that of Plumb and Ryan is in the inclusion of wall reactions 50 to 53. In our work, wall reactions were found to be essential for understanding our results. We note that the physical conditions used in the work modelled by Plumb and Ryan were very different to our own. It is therefore possible that wall reactions were indeed not important processes in that work. However, in the low-pressure, long residence time environment usually encountered in industrial etching processes, it is very likely that wall reactions are important.

4.6.1 THE ROLE OF EACH SPECIES PRESENT IN THE PLASMA

We now discuss each species present in the plasma in turn, explaining the role that each has in influencing the overall plasma chemistry.

CF_4 The role of CF_4 is to provide the main source of F, CF_2 and CF_3 via dissociation reactions 1 and 2.

O_2 The role of O_2 in the plasma is to provide a source of O atoms. Thus the effect of adding O_2 to the plasma is simply to add O atoms to the plasma because O_2 molecules do not take part in any fast chemical reactions.

F The main role of F atoms is to recycle CF_2 and CF_3 back to CF_4 via reactions 6 and 50. F atoms also make a significant contribution to the production of COF_2 by reacting with COF via reaction 31.

CF_3 CF_3 serves to reform CF_4 in the plasma by reacting with F atoms via reaction 6. CF_3 also reacts via reaction 27, forming the main production process for COF_2 and

also removing O atoms. In addition, CF_3 provides the only source of C_2F_6 in the plasma via reaction 5.

CF_2 The role of CF_2 is to reform CF_4 by adsorbing at the chamber walls and reacting there with F atoms. CF_2 is also the main precursor for production of CO and CO_2 via reaction 29 and reaction 28 followed by reaction 30.

O The role of O atoms is the most difficult to establish because it is involved in many processes. Perhaps the most important influence of O atoms on the overall plasma chemistry is the inhibiting effect it has on wall reaction 50, discussed in sections 4.5.1.2 and 4.5.4.1. This means that O has an important effect in controlling [F]. [O] is limited by wall recombination via reaction 51, which also forms the main production process for O_2. Wall reaction 52 forms the main removal mechanism for CO, and contributes to CO_2 production. O also reacts with CF_3 to produce COF_2 via reaction 27, and with CF_2 to produce CO via reaction 29 and also CO_2 via reaction 28 followed by reaction 30 (which has a limiting effect on [COF]).

COF COF reacts with O to produce CO_2 via the fast reaction 30, and with F to produce COF_2 via reaction 31.

CO The main role of CO in the plasma is to remove O and produce CO_2 via reaction 52.

CO_2 The role of CO_2 is to dissociate in the plasma, providing a source of CO and O.

COF_2 The role of COF_2 is to dissociate, providing a source of COF.

C_2F_6 C_2F_6 plays no active role in the plasma, except where $[C_2F_6]$ is artificially high in the C_2F_6 addition experiment, where it becomes a significant source of CF_3.

F_2 As we discussed in section 4.5.3.5 earlier, F_2 does not play an important role in the plasma.

Walls The role of the walls is to provide a reaction surface for association reactions which would otherwise be too slow to be important in the gas phase. The aluminium from which the walls are constructed will be covered by an oxide layer due to exposure to O atoms in the plasma and exposure to air when the chamber is opened. This oxide layer is likely to be covered by a layer of adsorbed species, consisting mainly of adsorbed CF_2, CF_3, F, O and as adsorbed polymer of the form $(CF_2)_n$. At the steady state, the surface coverage of these species will be constant, but the surface species will be exchanging rapidly with species in the gas phase.

4.6.2 THE MAIN CONSEQUENCES OF THE REACTION SCHEME

We now highlight the main consequences of the reaction scheme. The best way to discover how the model behaves with changing conditions would be to perform mutually self-consistent calculations including all the reactions listed in table 4.19 and shown in figure 4.12; ideally, all the reactions listed in table 4.2 would also be included in the calculations. As we discussed earlier (section 4.5), such calculations were not possible in this work. However, it is still possible to recognise some important consequences of the reaction scheme shown in figure 4.12. These are discussed below.

a) The rate of removal of reaction products by the pump is always slow compared with the rate of removal by chemical reactions. This means that an atom entering the plasma will be part of many different molecules before it is pumped away. Similarly, gas flow of CF_4 and O_2 is slow compared to the production of these molecules by chemical reactions, thus flow is not the main production process for CF_4 and O_2 in the plasma.

b) It is clear from figure 4.12 that dissociation and production of CF_4 are the fastest processes which occur in the plasma. This means that when CF_4 dissociates to form CF_2 and CF_3, the majority of these species are recycled back to CF_4 again. This effect is illustrated clearly by the fact that only around 5 % of the carbon budget in the plasma is removed from the rapid recycling process to form CO, CO_2, COF_2 and C_2F_6 (at 40 sccm, 100 W and 85 mTorr).

c) The recycling of CF_4 in the plasma is disrupted by the presence of O atoms, which are formed mainly by dissociation of O_2. O atoms compete with F atoms for surface sites at the chamber wall and inhibit the production of CF_4 via reaction 50. This also has the effect of increasing [F]. Reactions of CF_x and COF with O atoms to produce F atoms, and removal of F atoms by reaction with CF_3, do not contribute significantly to this increase in [F].

d) Once the carbon budget in the plasma is removed from the CF_4 recycling process by reaction of CF_x with O atoms to give CO, CO_2 and COF_2, it can not reform CF_4. Once carbon atoms are converted to CO and CO_2, they are exchanged between these two molecules, but do not return to other parts of the reaction scheme, thus forming a sink for carbon atoms. It is therefore expected that, given sufficient time in the plasma, the main carbon containing oxidation products would be CO and CO_2.

4.6.3 USING THE REACTION SCHEME TO UNDERSTAND THE QMS RESULTS

In this section, we use the reaction scheme shown in figure 4.12 to explain qualitatively the experimental trends observed in the QMS results, which were presented in section 4.2 p.99a ff earlier. This is best done for the experiments of varying flow and vol % gas additions, where the reaction scheme proves very effective at explaining the observed experimental trends. (Note that the relative reaction rates given in figure 4.12 are

relevant to conditions of 40 sccm, 100 W and 85 mTorr, and can therefore only be used as a rough guide at other conditions). The reactions which are referred to by number are listed in table 4.19 on p.142a.

Flow variation at 100 W and 85 mTorr - see figures 4.1, 4.9a and 4.10a.

In the flow rate variation experiment, the flow rate of CF_4 + O_2 process gas was varied along with the pumping speed to keep the total pressure constant. This has the effect of changing the production rates of CF_4 and O_2, and also changing the residence time which molecules spend in the chamber. The main observed effects as flow rate increases are an increase in $[O_2]$ and a decrease in [CO], $[CO_2]$ and $[COF_2]$ (figure 4.1). This is explained in terms of the change in the residence time during which chemical reactions can occur, noting that the contributions from flow and pumping to the overall production and loss processes are always small compared to the important chemical production and loss processes. As the residence time falls, there is less time for CF_2 and CF_3 to react with O to produce CO, CO_2 and COF_2. This causes the observed rise in $[O_2]$ and the observed fall in [CO], $[CO_2]$ and $[COF_2]$ as the flow rate increases. This effect is also reflected in the observed rise in $[CF_4]$ as the flow rate increases, because there is less time for CF_4 to be converted to other products.

Power variation at 85 mTorr for 5 and 50 sccm - see figures 4.2 and 4.3.

The results of the power variation experiment are difficult to interpret. This is because varying the power changes the electron density and energy distribution, which leads to a change in dissociation rates. We have no quantitative information concerning this effect, so the details are impossible to establish. However, some of the broader experimental trends can still be understood, as we explain below.

Firstly, the results for power variation at 5 and 50 sccm are consistent with the flow rate results, in that the concentrations of O_2, CO, CO_2 and COF_2 are all lower at 50 sccm than at 5 sccm. The observed experimental trends as the power varies are broadly

similar at both 5 and 50 sccm. The main changes observed as the power is increased are that [CF_4] falls, due to increased dissociation, while [C_2F_6] and [COF_2] rise. From the reaction scheme in figure 4.12 it is expected that as power increases, then [CO] and [CO_2] will increase also, because they form a sink for C in the plasma, and should be produced faster at higher powers. However, the results show that this is not the case. At 5 sccm, [CO] and [CO_2] fall with increasing power, and at 50 sccm [CO] remains fairly constant while [CO_2] appears to show a peak in concentration at around 80 W. The reasons for this unexpected behaviour are not immediately evident. Nevertheless, an explanation is to be sought in the ratio of [CF_3] / [CF_2], which may change with power. For example, if [CF_3] / [CF_2] increases with power, then oxygen will be converted to COF_2 via reaction 27 in favour of reactions with CF_2 to form CO and CO_2, explaining the decrease in [CO] and [CO_2] observed at 5 sccm. This also explains the observed increases in [C_2F_6] and [COF_2] which are both formed from CF_3. Perhaps the branching ratio of CF_4 (section 4.4) shifts in favour of CF_3 at higher powers, or alternatively the wall loss rate of CF_2 is increased as power increases. At all events, further work is necessary to understand fully the effect of changing the discharge power.

Pressure variation at 5 sccm and 100 W - see figure 4.4.

The results of the pressure variation experiment are more difficult to interpret than the power experiment. As the pressure is changed, several effects are expected. Firstly, the dissociation rates will change because the same amount of power is applied to a different amount of gas. Secondly, species concentrations, and hence reaction rates will be strongly influenced by the pressure, especially for the three body reactions in the fall-off region. In addition, the pumping speed, and hence the residence time will also be affected. It is therefore impossible to interpret the pressure variation results adequately using the reaction scheme.

O_2 addition at 5 sccm, 100 W and 85 mTorr - see figures 4.5, 4.10b and 4.11b.

The gas addition experiments are more readily explained using the reaction scheme in figure 4.12. This is because the flow rate, power and pressure are constant, so avoiding the problems encountered above. Here, gas molecules are added at a specific point in the reaction scheme, allowing the effects on other parts of the scheme to be determined. The O_2 addition results can be understood as follows.

As we noted earlier, the only role of O_2 is to add O atoms to the plasma. As O_2 is added, [F] increases due to the reduced rate of wall reaction 50, caused by O atoms competing with F atoms for surface sites. $[CF_3]$ falls due to increased removal by F atoms via reaction 6, which in turn causes the observed fall in $[C_2F_6]$. As [O] increases, reactions 27 to 31 result in an increase in [CO], $[CO_2]$ and $[COF_2]$. As [O] increases more, the initially rapid rise in $[COF_2]$ tails off in favour of CO and CO_2, which continue to rise. This results because at low [O], reaction 27 dominates the O atom reactions, producing COF_2, but as [O] increases, more COF is produced and the very fast reaction 31 takes over, producing CO_2 and also therefore CO by dissociation of CO_2. The fall in $[CF_4]$ as $[O_2]$ increases results because reactions of CF_x with O convert more of the carbon in the plasma to CO, CO_2 and COF_2.

CO addition at 5 sccm, 100 W and 85 mTorr - see figures 4.6, 4.10c and 4.11c.

As CO is added to the plasma, [O] falls due to wall reaction 52, resulting in the observed fall in $[O_2]$ and the rise in $[CO_2]$. The fall in [O] causes an increase in the rate of wall reaction 50 due to reduced competition with F for surface sites, resulting in the observed fall in [F] (figure 4.11c). As [F] falls, $[CF_3]$ rises due to reduced CF_3 removal via reaction 6.

The unusual behaviour of $[COF_2]$ is more difficult to understand. $[COF_2]$ shows an increase until around 15 vol % CO addition, above which it falls off. The initial increase in $[COF_2]$ as CO is added is surprising because [O] and [F], which are precursors

for COF_2, both fall in concentration. The reason may be that at lower [O], reaction 27 dominates the O atom reactions, as found in the O_2 addition results above. This would tend to produce relatively more COF_2, and would also be enhanced by the increase in $[CF_3]$. This would explain why $[CO_2]$ rises only slightly as CO is added, because the increase in the production rate of CO_2 via reaction 52 is offset by a decrease in production via reaction 31. As [O] falls further with increasing CO addition, $[COF_2]$ falls as expected. This demonstrates the complex interplay of plasma reactions!

CO_2 addition at 5 sccm, 100 W and 85 mTorr - see figures 4.7, 4.10d and 4.11d.

As CO_2 is added to the plasma, CO is produced by dissociation of CO_2 via reaction 37, giving the observed rise in [CO]. O atoms are also produced by this dissociation, but due to the rise in [CO], many are removed by reaction to reform CO_2 via reaction 52, as we saw above. Thus, although the production rate of O is increased, only a small resultant increase in $[O_2]$ is observed because of the increased rate of O atom removal via reaction 37. $[CF_3]$, and hence $[C_2F_6]$, falls as CO_2 is added due to the decrease in $[CF_4]$, which results mainly from the reduced flow rate of CF_4. [F] remains fairly constant because although F atoms are produced more slowly by reaction 1 due to the fall in $[CF_4]$, they are also removed more slowly. This is because removal by reaction with CF_3 via reaction 6 is slower due to the fall in $[CF_3]$, and in addition, the rate of removal by wall reaction 50 is reduced due to the small increase in [O] causing an increased inhibiting effect on this reaction. The behaviour of $[COF_2]$ is again more difficult to understand. Production of COF_2 via reaction 27 is not expected to increase because the rise in [O] is offset by the fall in $[CF_3]$. The increase must be due to an increase in the production rate via reaction 31. This would indicate that an increase in [COF], and therefore its $[CF_2]$ precursor, has occurred, but we have no information on the trends in concentration of these species in this experiment.

C_2F_6 addition at 5 sccm, 100 W and 85 mTorr - see figures 4.8, 4.10e and 4.11e.

The main effect of the addition of C_2F_6 to the plasma is an increase in $[CF_3]$ due to the increased production rate of CF_3 by dissociation of C_2F_6 via reaction 10. It is interesting to note that the increase in $[C_2F_6]$ is due to an increased production rate by recombination of CF_3 via reaction 8, and not due to introduction by the gas flow of C_2F_6. The increase in $[CF_3]$ (figure 4.10e) results in an increased removal rate of F via reaction 6, causing the observed fall in [F] (figure 4.11e). Under these conditions the removal of F is dominated by reaction 6; wall reaction 50 does not contribute significantly to the reduction in [F] despite the reduced inhibiting effect of O atoms caused by the fall in [O]. The increased rate of reaction 6 also causes the initial rise in $[CF_4]$, until around 15 vol % addition of C_2F_6, when the reduction in [F] (figure 4.11e) overtakes the increase in $[CF_3]$.

The increase in $[CF_3]$ also causes a reduction in [O] due to increased O removal via reaction 27, giving rise to the observed fall in $[O_2]$. The fall in [O] results in a reduced rate of CO_2 production from CO via reaction 52, causing the observed decrease in $[CO_2]$ and the increase in [CO]. The behaviour of $[COF_2]$ is explained as follows. As $[CF_3]$ increases, reaction 27 dominates production of COF_2 because the fall in [F] and expected fall in [COF] will reduce production of COF_2 via reaction 31. Initially, the fall in [O] is balanced by the rise in $[CF_3]$ resulting in $[COF_2]$ remaining constant. As more C_2F_6 is added, the fall in [O] dominates, causing the observed fall in $[COF_2]$ above 15 vol % addition of C_2F_6.

4.7 SUMMARY OF THE MAIN CONCLUSIONS

In this section we summarise the main conclusions which have been drawn in this chapter.

a) Wall reactions have been shown to be important in plasmas of $CF_4 + O_2$ under the conditions studied in this work. Of greatest importance is the production of CF_4 by the reaction of adsorbed CF_2 with impinging F atoms (reaction 50). This reaction is

inhibited by O atoms which compete with F atoms for surface sites, with the result that [O] has a strong influence on [F]. Indeed, this is the main cause of the well-known increase in [F] when O_2 is added to the plasma. Wall reactions involving O atoms have also been shown to be important in the plasma.

b) Of the 53 reactions considered in the model initially, only 17 were found to have important influences on the chemistry of the plasma, allowing a tractable reaction scheme to be produced (figure 4.12). These 17 reactions comprise 7 gas phase chemical reactions, 6 dissociation processes and 4 surface reactions. Of the 7 gas phase reactions, the rate coefficients for all but 1 are well established. Dissociation rates and the branching ratio for CF_4 have been adopted from the measurements and calculations of Plumb and Ryan [42], with a correction for the lower electron density and energy found in our reactor. Obviously there is some uncertainty in these dissociation rates. The rate coefficients for the wall reactions have been used as fitting parameters to fit the calculations of concentrations to experimental measurements. Improvements in the model can therefore be made if better values for dissociation rate coefficients were to become available, together with a greater understanding of wall processes.

c) Using the simplified kinetic model, the concentrations of [CF_3] and [F] have been calculated (using the steady state equations for C_2F_6 and CF_4 respectively) for a wide range of experimental conditions. For [F], good agreement with OES measurements is obtained. Concentrations were then calculated for all species present in the plasma using the steady state equation for each species in turn for one set of conditions (40 sccm, 100 W and 85 mTorr). These calculations show agreement of better than a factor of three with experimental measurements and with our earlier calculations of [CF_3] and [F].

d) Using the reaction scheme shown in figure 4.12, the role of every species present in the plasma has been identified. In addition, the major trends observed in the QMS results have been qualitatively explained.

CHAPTER 5

THE ETCHING OF Si AND Ge WAFERS USING CF_4 + 8 VOL % O_2 PROCESS GAS

5 THE ETCHING OF Si AND Ge WAFERS USING CF_4 + 8 VOL % O_2 PROCESS GAS

5.1 INTRODUCTION

This chapter is concerned with understanding the processes which occur during the etching of Si and Ge wafers. We present the results and discussion of the experiments performed during the study of the etching of Si and Ge wafers in CF_4 + 8 vol % O_2 process gas.

Six sets of experiments were performed in which one process parameter was varied (flow rate, rf power, pressure or area of exposed wafer) while all other parameters remained constant. The experimental conditions which were used are listed in table 2.4, reproduced as table 5.1 below for convenience.

Experiment name	Variable parameter	Fixed parameters
FLOW RATE	2 - 50 sccm	100 W, 85 mTorr, Const. area
PRESSURE	10 - 85 mTorr	5 sccm, 100 W, Const. area
AREA AT 5 sccm	0 to 1 wafer	5 sccm, 100 W, 85 mTorr
AREA AT 50 sccm	0 to 1 wafer	50 sccm, 100 W, 85 mTorr
POWER AT 5 sccm	10 - 200 W	5 sccm, 85 mTorr, Const. area
POWER AT 50 sccm	10 - 200 W	50 sccm, 85 mTorr, Const. area

Table 5.1. Table showing the experimental conditions used for the etching experiments.

For each set of conditions, experiments were performed with no wafer (NW), Si and Ge present. Three-inch diameter Si(100) and Ge(100) were used for all etching experiments (area 45.45 cm^2) except where the exposed wafer area was varied, in which case the whole three-inch wafers were cleaved to obtain smaller substrate areas. During each experimental run, simultaneous measurements were made by QMS and OES after the plasma had reached a steady state, and the etch rates of Si and Ge wafers were made by the method of weight loss.

The time required to reach a steady state, which we refer to as the weathering time, was sometimes up to an hour or even longer. This was mainly due to the need to remove adsorbed water molecules which enter the vacuum chamber from the air when the wafers are introduced to the chamber. This poses no problem in the Si and Ge etching experiments discussed in this chapter because the wafers are very thick compared with the amount of material etched from the surface during the experiment. However, when etching thin SiGe alloy layers (chapter 7) there is the possibility that the SiGe alloy layer may be removed before the steady state is reached, making it necessary to reduce the weathering time. In section 7.2, the weathering process is discussed in more detail, along with the procedures adopted in order to reduce the weathering time in the SiGe etching experiments.

The etch rate results for Si and Ge are presented in section 5.2.1. In all cases, Ge etches faster than Si. However, the trends in the etching behaviour with changing experimental conditions are found to be similar for Si and Ge, indicating that Si and Ge most likely etch by a similar chemical mechanism. This view is further supported by the OES and QMS results. The differences in etching behaviour which do occur are attributed to the fact that the etching of Si relies more on ion bombardment than does the etching of Ge. The etch rate data are then used to calculate utilisation factors, which are defined as the fraction of the CF_4 feed gas molecules which are converted to etch products. Utilisation factors are useful in understanding the changes in the gas phase composition on introducing a wafer into the plasma.

OES spectra were recorded in the range 6200 - 7400 Å in order to measure the intensity of emission from F atoms in a variety of electronically excited states. The OES results are presented in section 5.2.2. F atom emission is found to reduce on introducing a wafer into the plasma. The reduction is larger over Ge, reflecting the larger etch rate. Emission from the 3p $^2P^\circ$ states of F shows different behaviour to emission from all other observed states of F. This effect is discussed in detail in chapter 6, where we propose that the 3p $^2P^\circ$ states are populated by resonant energy transfer during collisions with excited O_2 molecules in the $^1\Phi_u$ state as well as by electron impact with ground state F atoms. The

6856 Å emission line is a reliable indicator of [F] in the area and flow variation experiments, where power and pressure are constant. Emission at 6856 Å tracks the etch rate of both Si and Ge, confirming that F atoms are the main etchant species of both substrate materials.

Using QMS, concentrations of CF_4, C_2F_6, O_2, COF_2, CO, CO_2 and F_2 were measured, along with SiF_4 and GeF_4 when etching Si and Ge wafers. The QMS results are presented in section 5.2.3. When the process conditions are changed, we observe very similar changes in concentration whilst etching Si and Ge, but exaggerated when etching Ge reflecting the faster etch rate. This confirms that the chemical processes occurring during etching are similar in each case. Furthermore, on first introducing a Si or Ge wafer into the plasma, the concentration changes we observe are in general in the same direction, varying only in magnitude, regardless of the specific experimental conditions.

The SiF_4 and GeF_4 products of the etching reaction observed by QMS are discussed separately in section 5.2.3.1. For Si etching, it is shown that the Si budget is present almost exclusively as SiF_4 because lower fluorides of Si are rapidly converted to SiF_4 at the walls. For Ge etching, the Ge atom budget is present mainly as GeF_4 with the remainder adsorbed at the chamber walls. It appears that GeF_2 from the plasma adsorbs at the chamber walls and is fluorinated only slowly by F atoms to produce GeF_4, which is then released into the gas phase. At steady state, up to $\approx$ 40 % of the Ge atom budget is present at the walls as fluorinated Ge-containing species.

In sections 5.3.1 and 5.3.2, calculations of $[CF_3]$ and [F] are presented for the flow rate and area variation experiments. These calculations show that the reduction in [F] on introducing a wafer into the plasma is not due to direct removal of F by the etching process. Instead, we show that the reduction in [F] is due to an increased removal rate of F atoms by gas phase and wall reactions, caused by changes in the gas composition induced by the presence of the wafer. Then in section 5.4 we propose that the changes in the gas composition observed by OES and QMS on introducing a wafer into the plasma are brought about by a reduction in the fluorine-to-carbon ratio (F / C). This occurs because the etching

process causes F atoms to be "trapped" as fluorides of Si and Ge rather than being recycled in the plasma. The utilisation factor, U, is shown to be a measure of the magnitude of the reduction in F / C. The observed changes in the gas phase composition of the plasma on introducing a wafer into the plasma are then qualitatively explained.

5.2 THE RESULTS OF THE Si AND Ge ETCHING STUDIES

5.2.1 THE ETCH RATE RESULTS

The etch rate results are presented in figure 5.1. The etching behaviour is broadly similar for Si and Ge, with Ge etching faster than Si in all cases, i.e. there is selectivity towards Ge. These findings are in agreement with earlier work [112], [78]. It has been long established that F atoms are the principle etchant species for Si [56], [65], [113]. The general similarity in etching characteristics, confirmed also by our OES and QMS results (sections 5.2.2 and 5.2.3), suggests that the chemical etching mechanisms are similar, and therefore that F atoms are also the principle etchants of Ge. In all subsequent discussions, reference to "with a wafer present" refers to both Si and Ge wafers, unless stated otherwise.

Oehrlein et al [78] have proposed that the etching of Ge induced by plasma-generated F atoms relies much less on ion bombardment than does the etching of Si by considering the etching behaviour of these materials with increasing pressure. Oehrlein et al found that the etch rate of Ge increases with increasing pressure while the etch rate of Si reaches a maximum and eventually falls. They argue as follows. As the pressure increases, the arrival rate of radicals increases while the ion flux to the surface remains roughly constant, but with lower energy ions. Thus as the pressure increases, the Ge etch rate benefits from the higher radical flux more than does the Si etch rate, which is limited by the reduced ion bombardment. This result is reproduced in our work in figure 5.1 b, where the etch rate of Ge rises above $\approx$ 60 mTorr while the etch rate of Si tails off.

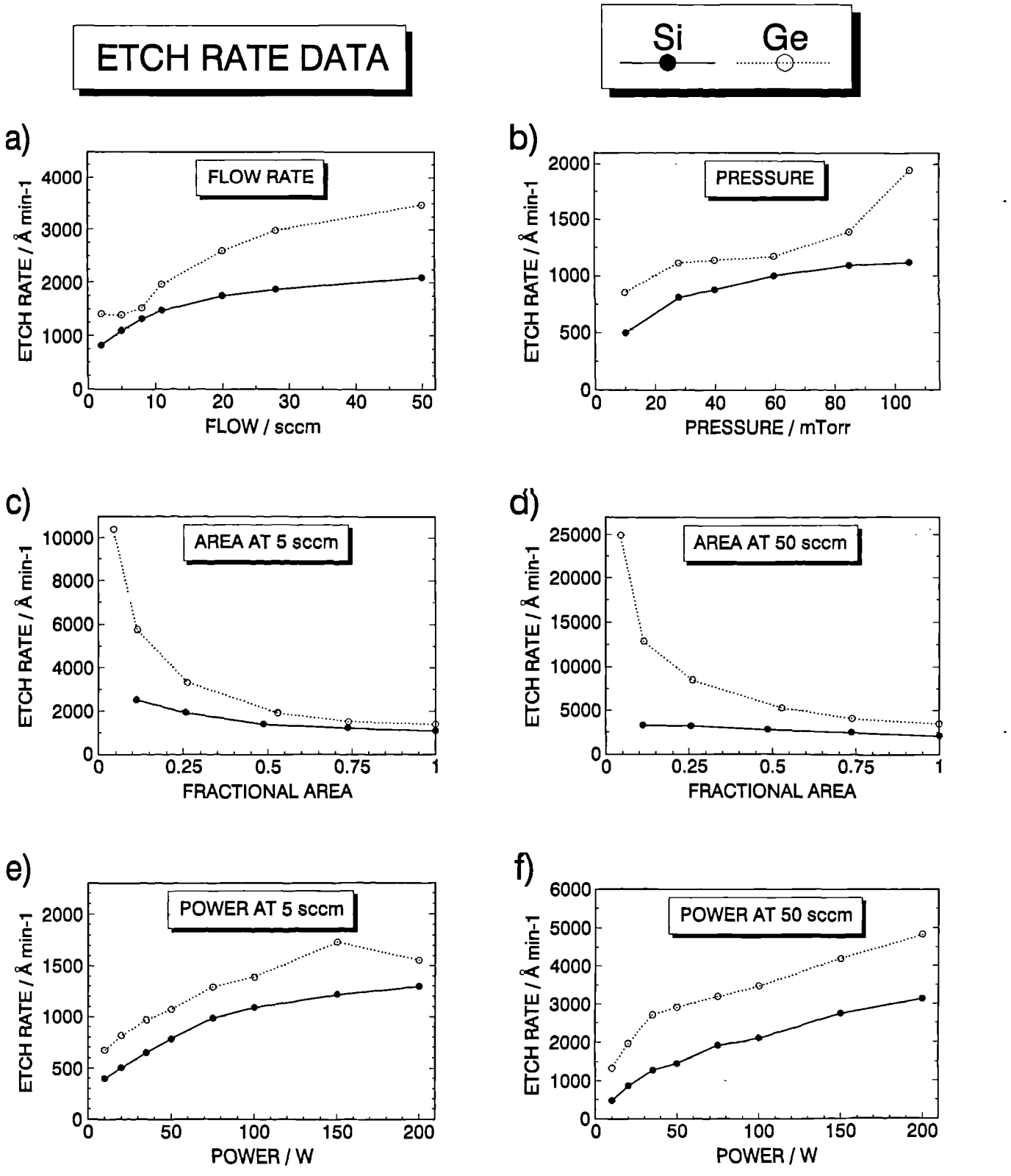

Figure 5.1. Graphs showing the etch rates of Si and Ge under a wide range of experimental conditions (see table 5.1).

The results of the area variation experiments (figures 5.1c and d show that the etch rates of both Si and Ge decrease as the exposed area increases. This is referred to as the *loading effect*, and is well known for Si etching in fluorine-based plasmas [28], [114], [115]. We will discuss this effect further in the light of the OES results presented in section 5.2.2. There, we also explain the observed increase in the selectivity towards Ge as wafer area decreases (see figures 5.1c and d), showing that it is due to the differences in the importance of ion bombardment in Si and Ge etching, discussed above.

We now calculate values for the *utilisation factor*, U, which is defined [28] as

$$U = \frac{\text{Removal rate of Si or Ge atoms}}{\text{Input flux of } CF_4 \text{ molecules}}$$

$$U = 3.72 \times 10^{-28} R_{etch} N A_s / q \qquad (5.1)$$

where R_{etch} is the etch rate (Å min^{-1}), N is the wafer density (atoms cm^{-3}) (4.96×10^{22} atoms cm^{-3} for Si and 4.05×10^{22} atoms cm^{-3} for Ge), A_s is the substrate area (cm^2) and q is the flow rate of CF_4 (sccm). U gives the fraction of CF_4 molecules converted to SiF_4 or GeF_4 product molecules, assuming these to be the only etch products (it is assumed that O_2 plays no direct role in etching). The calculations of U are presented in figure 5.2. It is clear that a significant proportion of CF_4 process gas can be converted to etch products, especially at low flow rates (e.g. $U \approx 0.2$ for the etching of 3" Si and Ge wafers at conditions of 5 sccm, 100 W and 85 mTorr). In section 5.4 later we show that U is a very useful parameter for understanding the changes in the gas phase composition when etching Si and Ge wafers.

5.2.2 THE RESULTS OF THE OES STUDIES OF F ATOM EMISSION

OES spectra were recorded in the range 6200 - 7400 Å to observe F atom emission lines. Typical spectra are shown in figure 5.3, from which line emission

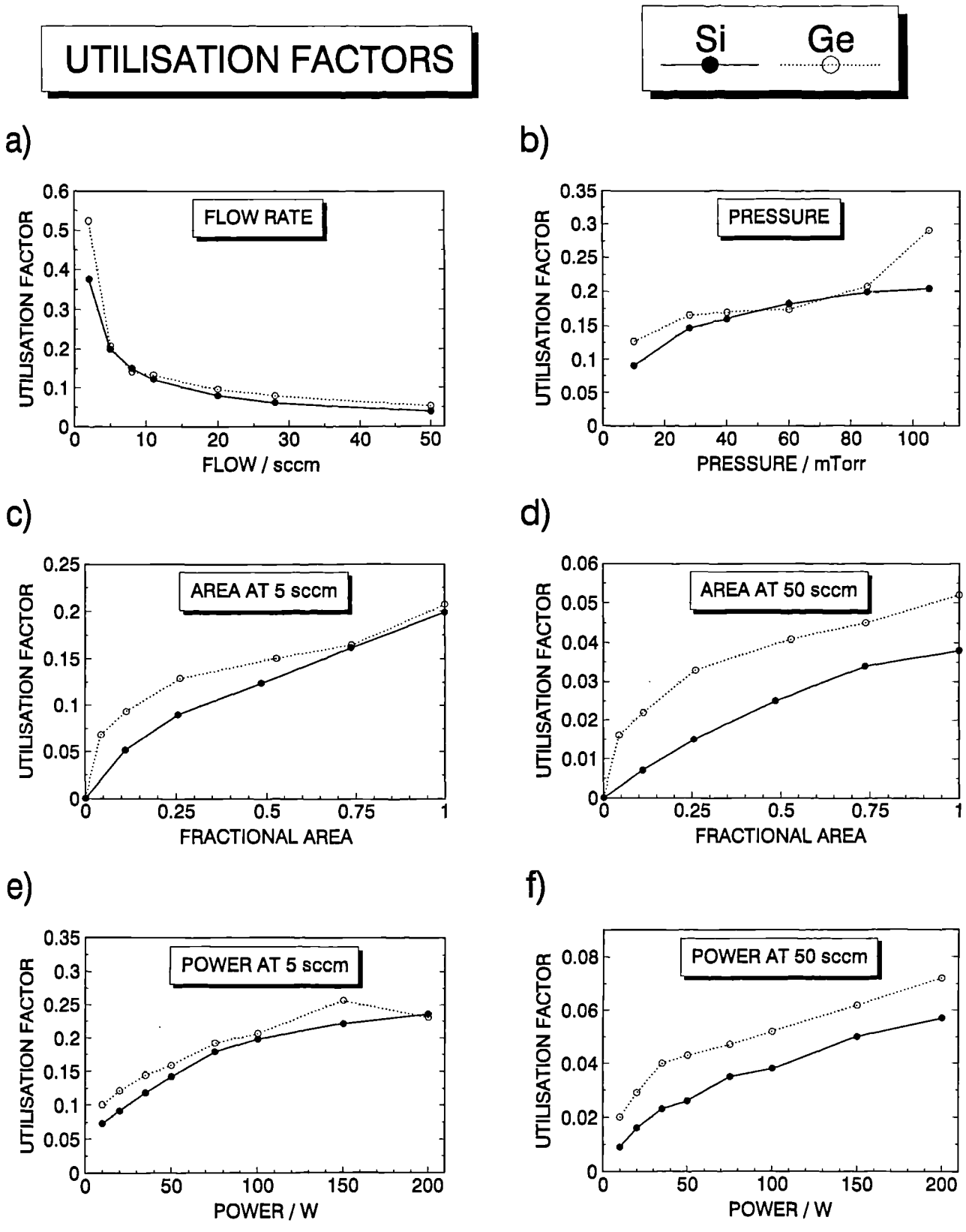

Figure 5.2. Graphs showing utilisation factors, U, calculated using equation 5.1 for the etching of Si and Ge under a wide range of experimental conditions (see table 5.1).

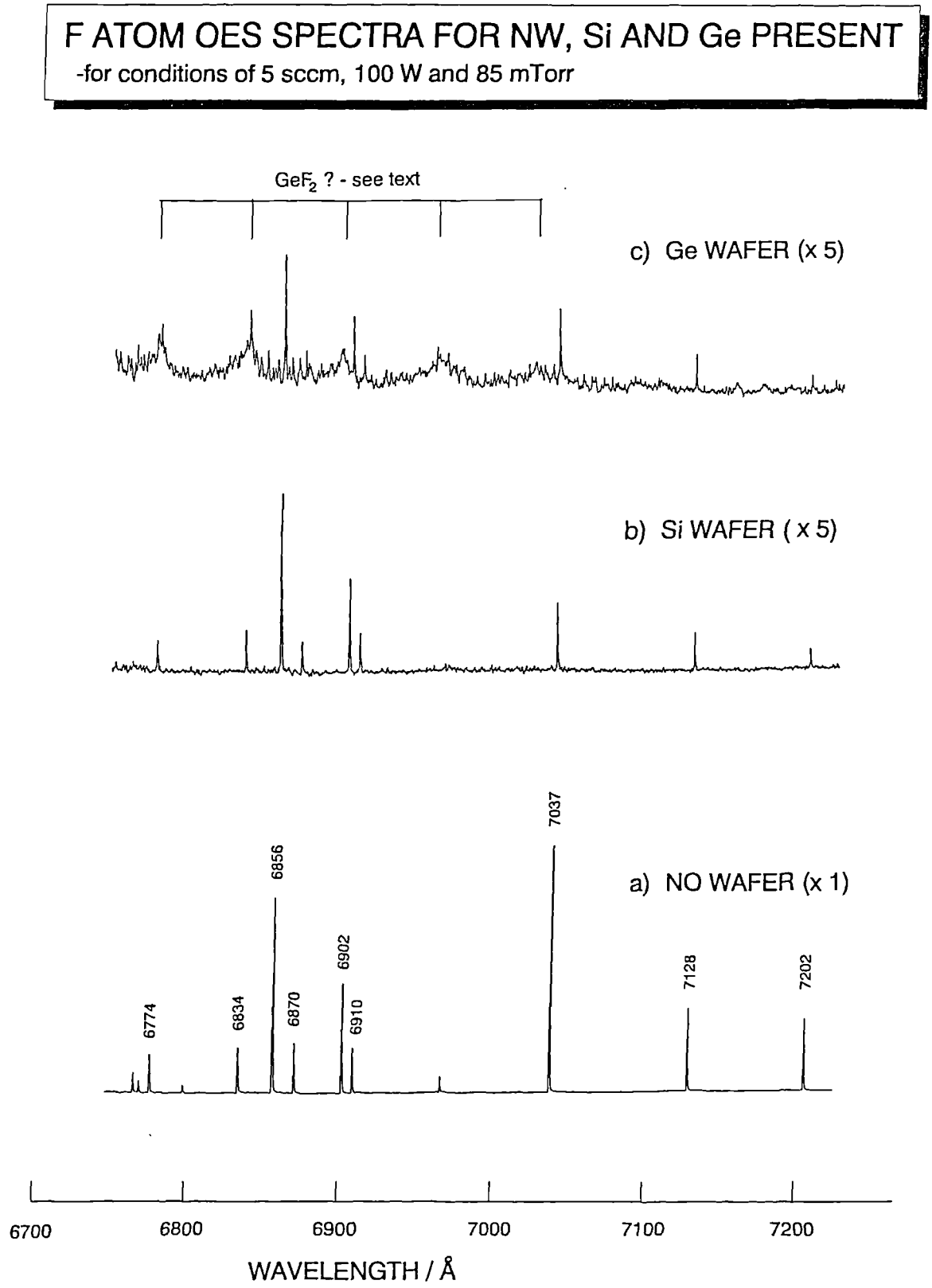

Figure 5.3. OES spectra in the range 6750 Å to 7250 Å showing emission lines from excited F atoms for a) no wafer, b) Si wafer and c) Ge wafer present. Also shown in c) are emission bands attributed to GeF_2.

intensities can be measured. Before we discuss the F atom emission results, we first discuss the emission bands shown in figure 5.3c, marked as "GeF_2 ?".

The unknown emission bands in figure 5.3c show a clear progression, very regularly spaced, with a energy difference of $\approx$ 125 cm^{-1}. They do not correspond to any known transitions of molecules likely to be present in the plasma, and are not assigned at present. However, since the emission is only observed over Ge, it seems likely that the molecule is a Ge-containing etch product, probably GeF, GeF_2 or GeF_3. The fact that the bands are evenly spaced and with a very small energy gap suggests that the progression is due to a bending transition of either GeF_2 or GeF_3. No information concerning GeF_3 is available, but it would not be expected to show such a clearly defined progression of bands. For GeF_2, information is available only for the ground ($X\ ^1A_1$) and first excited ($A\ ^1B_1$) states [116]. Transitions between these levels give bands around 2200 Å [117] and are therefore not the cause of our observed transitions. However, we note that the bending frequency of the $A\ ^1B_1$ state of GeF_2 is 165 cm^{-1}, reasonably close to the spacing observed here (125 cm^{-1}), showing that GeF_2 could give closely spaced bands. It therefore seems likely that the unknown bands are due to GeF_2 transitions between energy levels higher than the first excited state. We note also that GeF_2 is relatively unreactive in the gas phase [118], making it likely that significant concentrations of GeF_2 will be present.

We now return to the discussion of the F atom OES results. In table 5.2 below are presented the OES results for conditions of 5 sccm, 100 W and 85 mTorr, expressed as the ratio of line intensities with and without a wafer present, denoted I (NW / Si) and I (NW / Ge). The wavelength and relevant transition are also shown for all the F emission lines studied in this work.

Wavelength / Å	Transition Lower - Upper	I (NW / Si) errors ± ≈ 10 %	I (NW / Ge) errors ± ≈ 15 %
6240	$3s\ ^4P_{5/2}$ - $3p\ ^4S°_{3/2}$	5.3	9.4
6774	$3s\ ^4P_{5/2}$ - $3p\ ^4D°_{3/2}$	5.7	8.1
6856	$3s\ ^4P_{5/2}$ - $3p\ ^4D°_{7/2}$	5.3	9.0
6870	$3s\ ^4P_{1/2}$ - $3p\ ^4D°_{7/2}$	5.1	8.2
6902	$3s\ ^4P_{3/2}$ - $3p\ ^4D°_{5/2}$	5.5	8.3
6910	$3s\ ^4P_{1/2}$ - $3p\ ^4D°_{3/2}$	5.3	7.3
7037	$3s\ ^2P_{3/2}$ - $3p\ ^2P°_{3/2}$	18	19
7128	$3s\ ^2P_{1/2}$ - $3p\ ^2P°_{1/2}$	10.5	13
7202	$3s\ ^2P_{1/2}$ - $3p\ ^2P°_{3/2}$	16	18
7309	$3s'\ ^2D_{5/2}$ - $3p'\ ^2F°_{7/2}$	6.1	9.5
7311	$3s\ ^2P_{3/2}$ - $3p\ ^2S°_{1/2}$	6.0	8.7
7332	$3s\ ^4P_{5/2}$ - $3p\ ^4P°_{3/2}$	5.9	8.4
7399	$3s\ ^4P_{5/2}$ - $3p\ ^4P°_{5/2}$	5.8	9.1

Table 5.2. The F atom emission lines observed in this work with relevant transitions. Also shown are the measured emission intensities expressed as intensity ratios I (NW / Si) and I (NW / Ge), for conditions of 5 sccm, 100 W and 85 mTorr.

The errors in the intensity ratio data are larger for Ge than for Si because of difficulties in subtracting the background emission observed over Ge (discussed above) from the F atom emission. Note that intensity ratios must be the same for lines which share a common upper level (e.g. 6856 Å and 6870 Å). Considerations of this kind allow the accuracy of a proportion of the intensity ratio values to be checked. A subset of the energy level diagram for F atoms is given in figure 5.4, showing the transitions observed in this work (spin orbit splitting is omitted for simplicity). Note that the use of intensity ratios ensures that any effects on emission intensities brought about by changes in the process conditions (especially power and pressure) which may affect the electron density and energy distribution function cancel out. Intensity ratios therefore represent genuine changes in [F] provided that the electron density and energy distribution function are not altered by the presence of the wafer. In this regard, we note that on inserting a wafer into the plasma after a NW run, the reflected power was typically < 10 % of the forward power (for the same process conditions), before adjustment of the matching network. This shows that the electrical properties of the plasma do not change greatly on introducing a wafer into the plasma, and we therefore conclude that the intensity ratios do indeed represent genuine

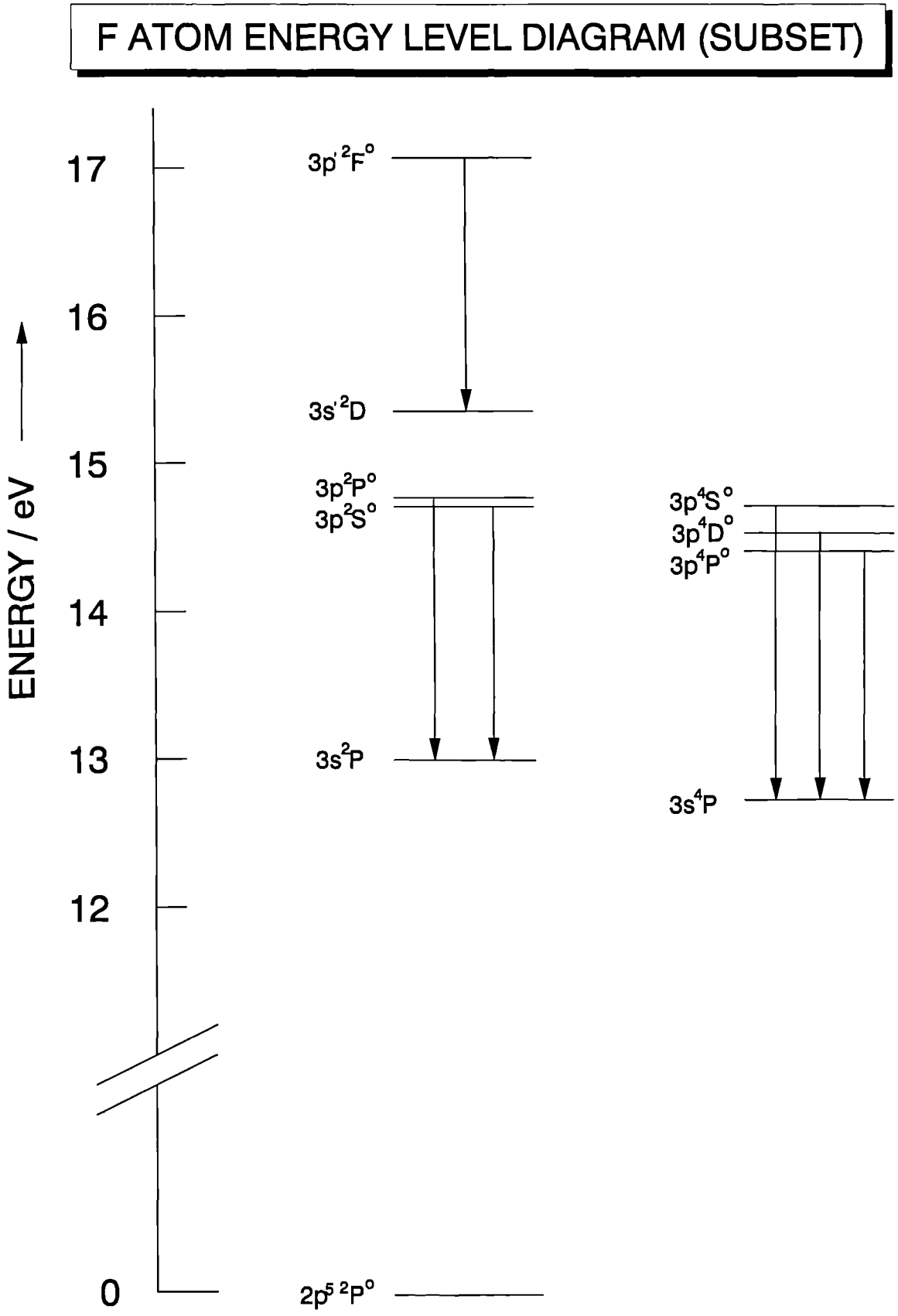

Figure 5.4. A subset of the energy levels of F atoms, showing all the transitions observed in this work. J levels are omitted for simplicity.

changes in [F]. We now discuss some of the effects which are clear from the intensity ratio results of table 5.2.

(a) Firstly, the emission from F atoms is greatly reduced over both Si and Ge, showing that [F] is reduced as a result of the etching process. In addition, the reduction of emission intensity over Ge is greater than that over Si, reflecting the faster etch rate of Ge found in section 5.2.1. The cause of the reduction in [F] is discussed later in sections 5.3.2 and 5.4, but it is worth noting here that this reduction cannot be taken as direct evidence that F atoms etch Si and Ge (see section 5.3.2).

(b) It is also clear from table 5.2 that the reduction in emission intensity on introducing a wafer into the plasma is equal (within experimental error) for all observed transitions except those originating from the $3p\ ^2P^\circ$ levels (lines at 7037 Å, 7128 Å and 7202 Å), where the intensity over a wafer falls by a larger factor. Interestingly, emission originating from $3p\ ^2P^\circ_{3/2}$ falls in intensity by a larger factor than emission from the $3p\ ^2P^\circ_{1/2}$ level. In chapter 6 we discuss this effect in detail. We show that the effect not confined only to the etching of a wafer, and that it is dependent on $[O_2]$ in the plasma. We propose that these levels are populated by collisional energy transfer from excited O_2 molecules in the $^1\Phi_u$ state. Emission from these two levels cannot therefore be used as an indicator of [F] in the presence of O_2 because it is populated by other mechanisms in addition electron impact with ground state F atoms (section 6.3.1). However, the intensity ratio results show that emission from all other observed levels of F is free from this effect, and therefore does give a reliable indication [F]. For this reason, the strong 6856 Å emission line has been used to indicate [F] due to the better signal to noise ratio which is achieved (see section 6.3.1).

The OES intensity ratio results using the 6856 Å line are presented in figure 5.5 for all the etching experiments listed in table 5.1. The trends observed in these results can

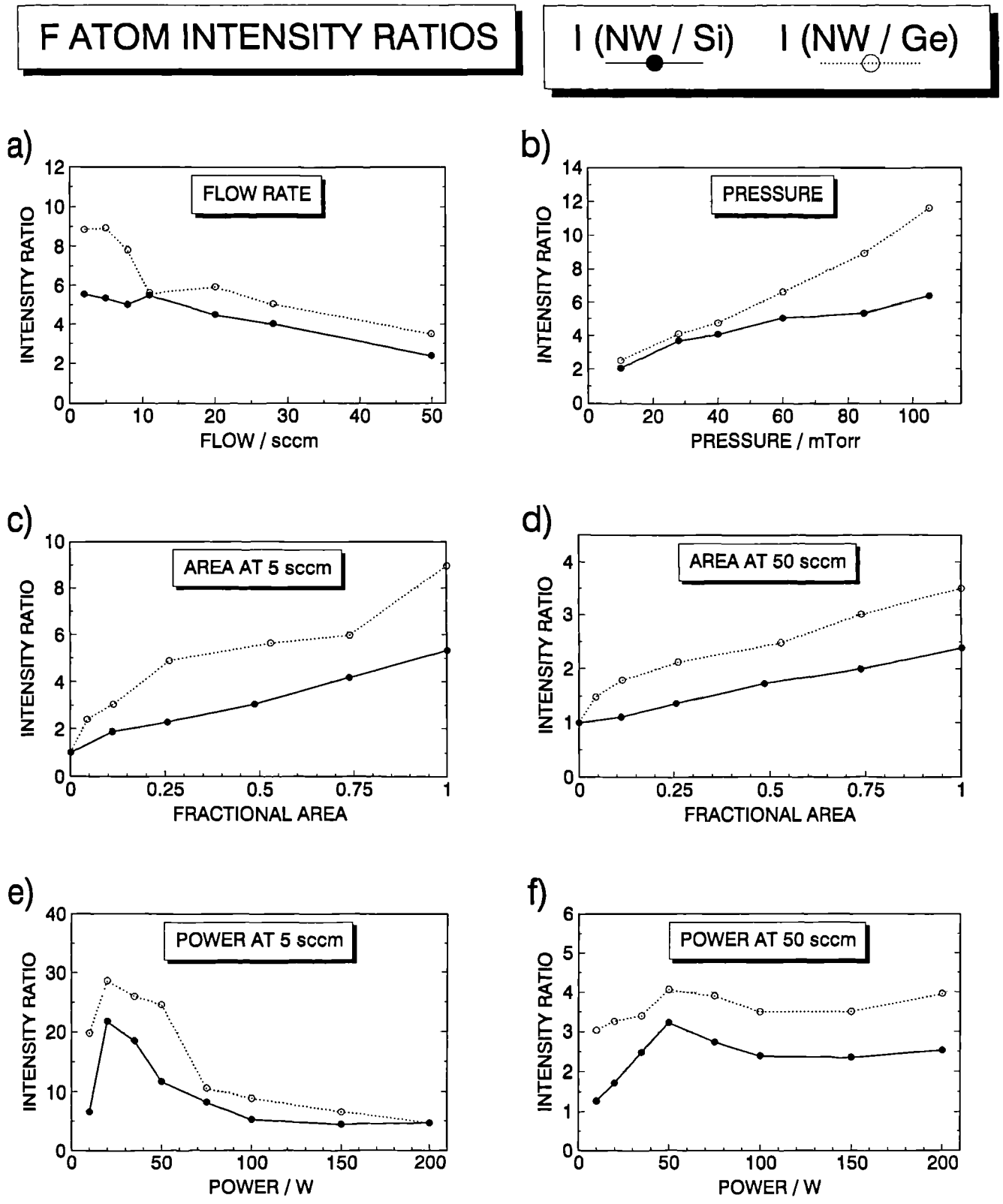

Figure 5.5. Graphs showing F atom emission intensities expressed as intensity ratios, using the 6856 Å line, for a wide range of experimental conditions (see table 5.1).

be more easily understood after the QMS results have been presented, and will be discussed further in section 5.3.2. However, some useful conclusions can be drawn here.

(i) Firstly, the trends in the behaviour of the F atom emission is similar for Si and Ge. This confirms the earlier proposal made in section 5.2.1, that Si and Ge etch by a similar mechanism.

(ii) During the flow rate and area variation experiments, the electron density and energy distribution are expected to remain constant because the power and pressure are constant (see section 4.4). Under these conditions, the intensity of F atom emission at 6856 Å will be proportional to [F]. In addition, the ion bombardment will also be constant. Since F atoms are the main etchant species, the etch rate is expected to be strongly dependent on [F]. In figure 5.6, we present the absolute emission intensity results for the flow rate and area variation experiments, along with the relevant etch rate results of figure 5.1 for comparison, reproduced here for convenience. In general, the trends shown by the absolute OES results match those shown by the etch rate results, as predicted. We note, however, that simple proportionality between etch rate and [F] is not expected because the etch rate may depend on other factors which themselves depend on experimental conditions, such as competition for wafer surface adsorption sites between O atoms and F atoms [46], or the thickness and composition of the fluorinated surface layers [84].

(iii) We now return to the loading effect observed in the area variation experiments, mentioned earlier in section 5.2.1. The loading effect is attributed to the reduction in concentration of etchant species (F atoms in this case) caused by the etching process; [F] therefore decreases as the exposed wafer area increases [28], [114], [115]. This effect is shown clearly in the results of figures 5.6d and f, where F atom emission falls strongly as the exposed wafer area increases. In section 5.3.2 we show that the reduction in [F] is not due directly to removal of F by the etching process, as was previously thought [28], [114], [115]. Instead, we will show that the

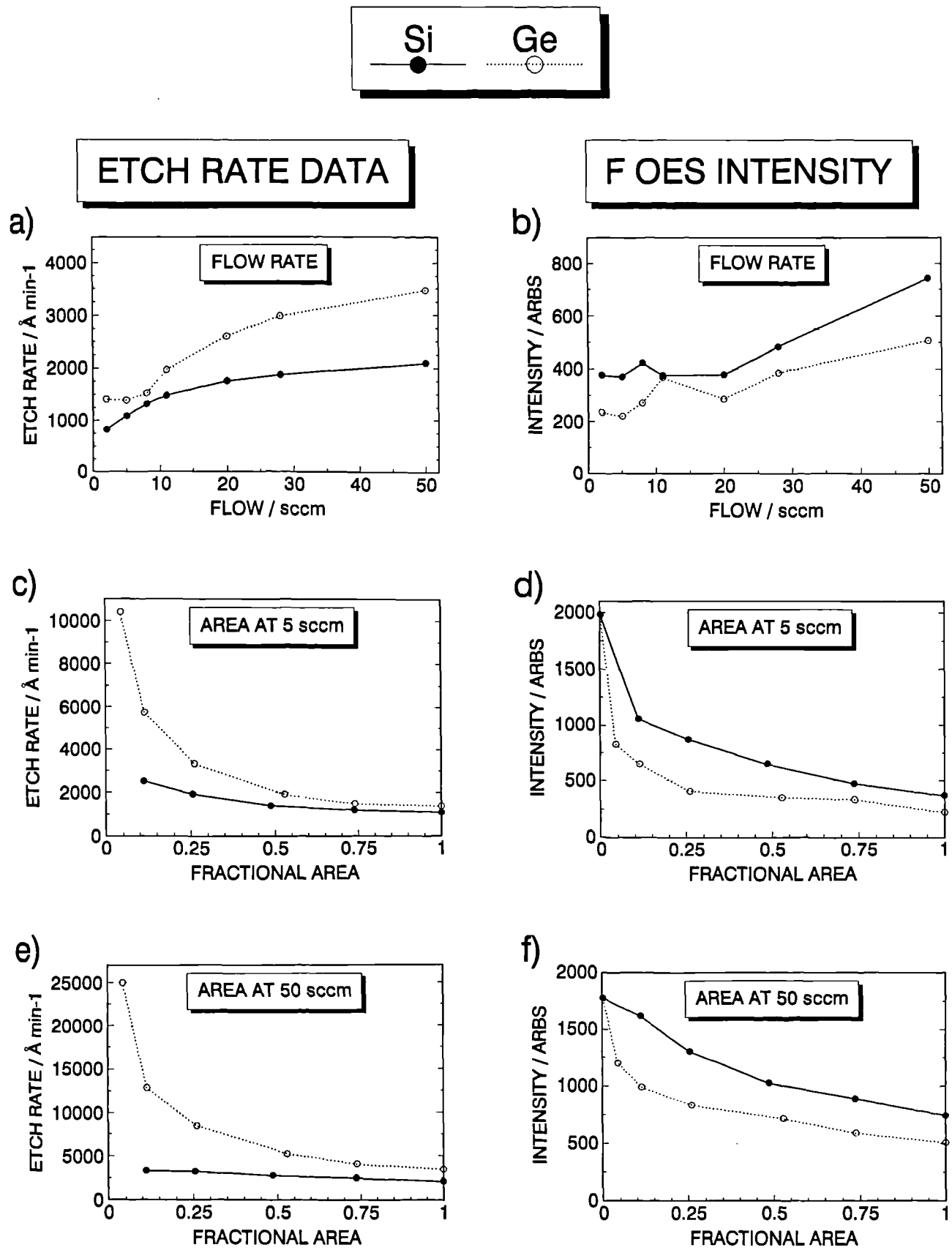

Figure 5.6. Graphs to allow a comparison of etch rate data with absolute emission intensities of the 6856 Å line of F atoms in arbitrary units (arbs), for the flow rate and area variation experiments (see table 5.1). Graphs a), c) and e) show the etch rate data (reproduced from figure 5.1) and graphs b), d) and f) show the OES data.

reduction in [F] is due to an increased loss rate of F atoms via reactions in the gas phase and at the chamber walls, caused by changes in gas phase species concentration which are induced by the presence of the wafer.

We can now understand the observation that the selectivity towards Ge increases at low exposed wafer area. We stated in section 5.2.1 that the etching of Ge relies much less on ion bombardment than does the etching of Si. As mentioned above, when the wafer area decreases, [F] increases while the ion bombardment remains constant. Ge etching will therefore benefit more from the increase in [F] than Si etching which is limited by the ion bombardment, explaining the observed selectivity behaviour.

5.2.3 THE QMS RESULTS

The results of the QMS study are presented in figures 5.7 to 5.12 for NW, Si and Ge present, giving mole percentage compositions (marked as "% composition" on the ordinates of these figures) of CF_4, C_2F_6, O_2, COF_2, CO and CO_2, along with SiF_4 and GeF_4 when etching Si and Ge wafers. Data for F_2 is not presented. This is due to errors in $[F_2]$ caused by background F_2^+ signals produced in the QMS ion source from CF_4 parent molecules. These background signals are up to an order of magnitude larger than the signal from F_2 parent molecules themselves, resulting in large errors in the calculated $[F_2]$. However, it is clear from the results that $[F_2]$ falls very strongly in the presence of a wafer by typically around an order of magnitude. (Note that with no wafer present, $[F_2]$ in the chamber was high enough to successfully subtract the contribution from CF_4 without incurring intolerable errors). The QMS results with NW present have already been discussed in chapter 4, so we confine our discussion to the changes observed on introducing a wafer substrate to the plasma.

An interesting feature of all the QMS results is that when the process conditions are changed, we observe very similar changes in concentration whilst etching Si and Ge, but exaggerated when etching Ge, reflecting the faster etch rate. This accords with the etch

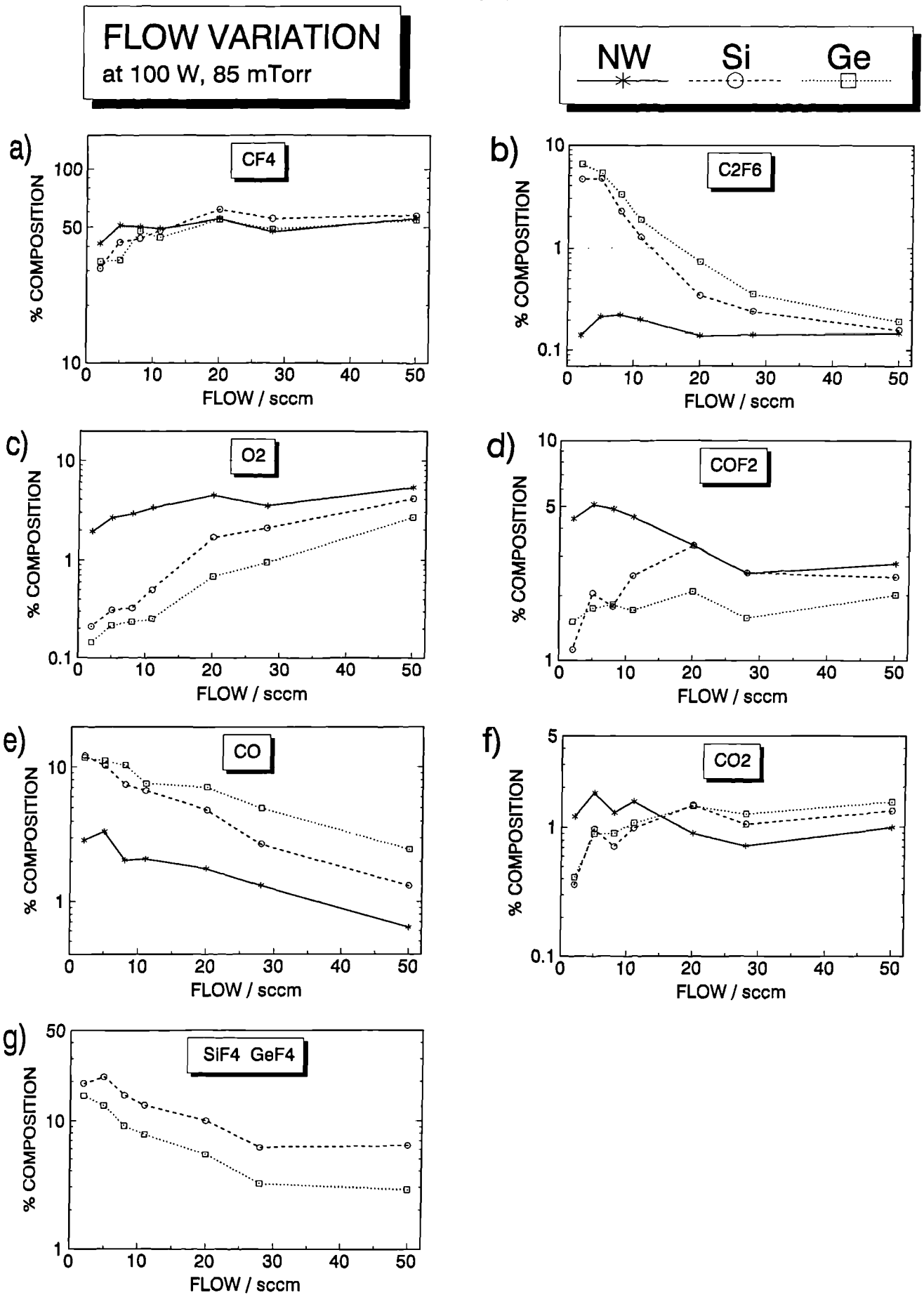

Figure 5.7. Graphs showing the mol % composition of gas phase species measured by QMS as a function of flow rate at 100 W and 85 mTorr. Note the logarithmic y-axis scales.

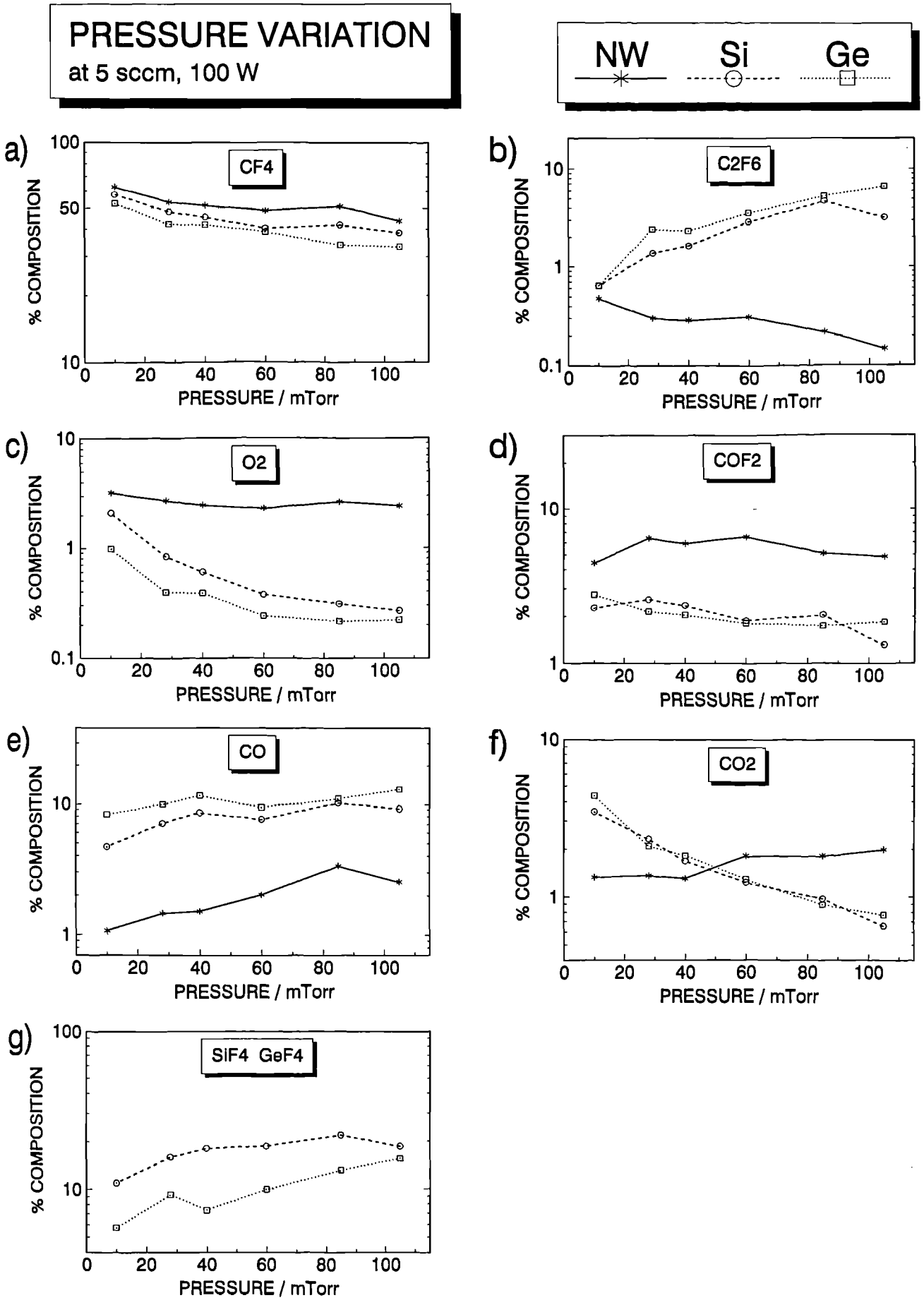

Figure 5.8. Graphs showing the mol % composition of gas phase species measured by QMS as a function of pressure at 5 sccm and 100 W. Note that the x-axes show mole the percentage compositions but not true concentrations because the pressure is changing. Note the logarithmic y-axis scales.

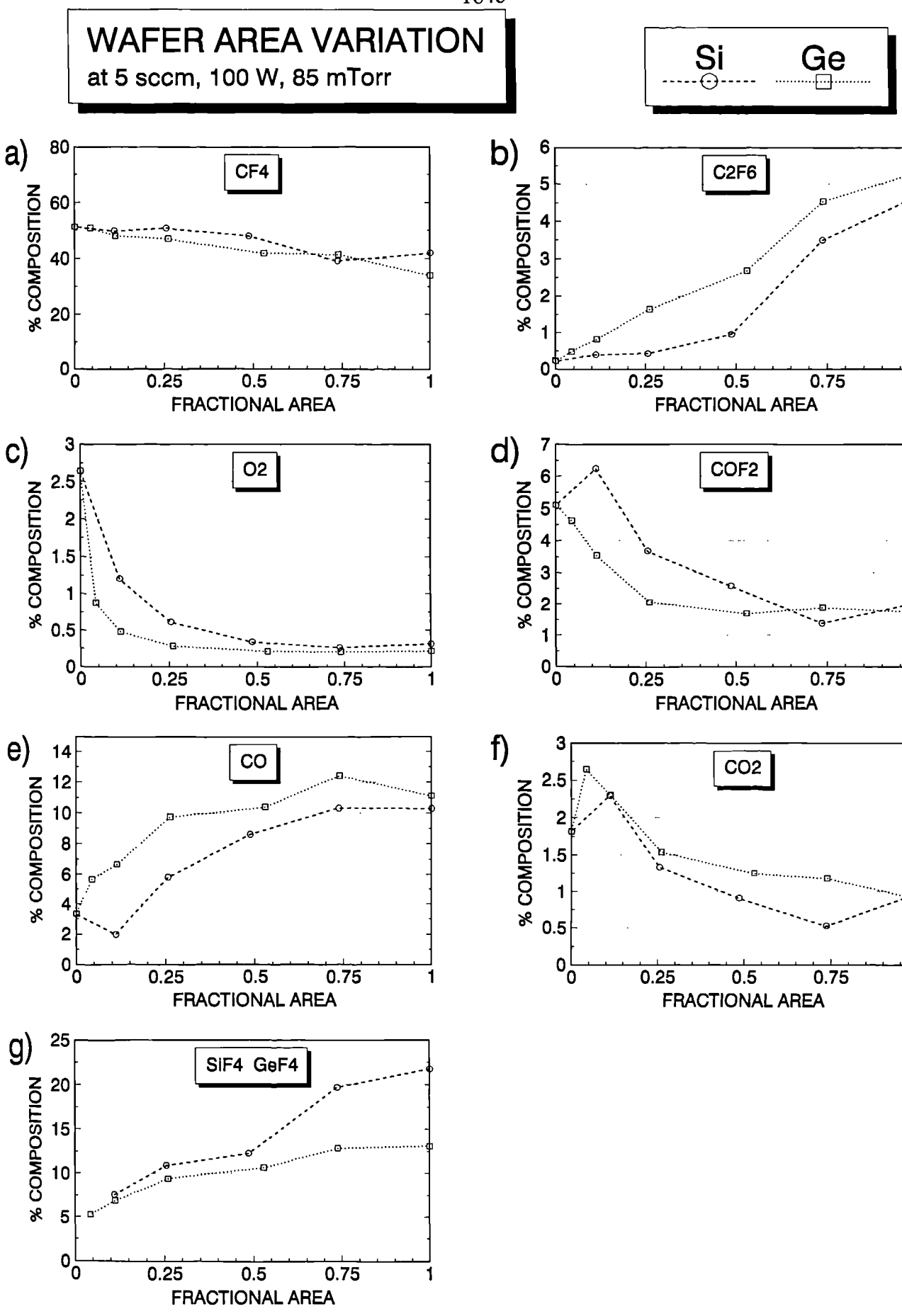

Figure 5.9. Graphs showing the mol % composition of species measured by QMS as a function of exposed wafer area (0 to 1 three inch wafers) at 5 sccm, 100 W and 85 mTorr. Note that the y-axis scales here are linear.

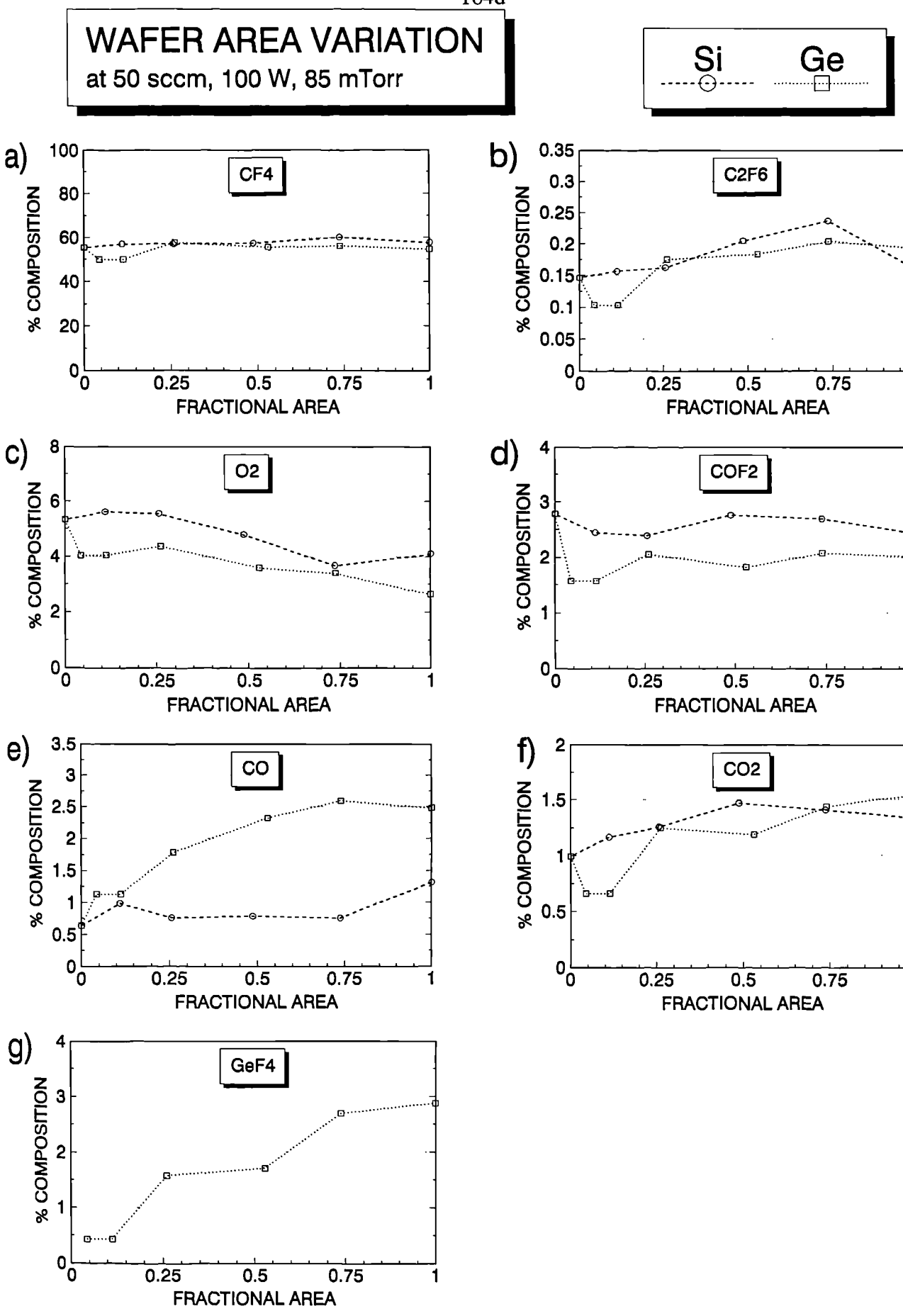

Figure 5.10. Graphs showing the mol % composition of gas phase species measured by QMS as a function of exposed wafer area (0 to 1 three inch wafers) at 50 sccm, 100 W and 85 mTorr. SiF_4 data is not presented (see text). Note that the y-axis scales here are linear.

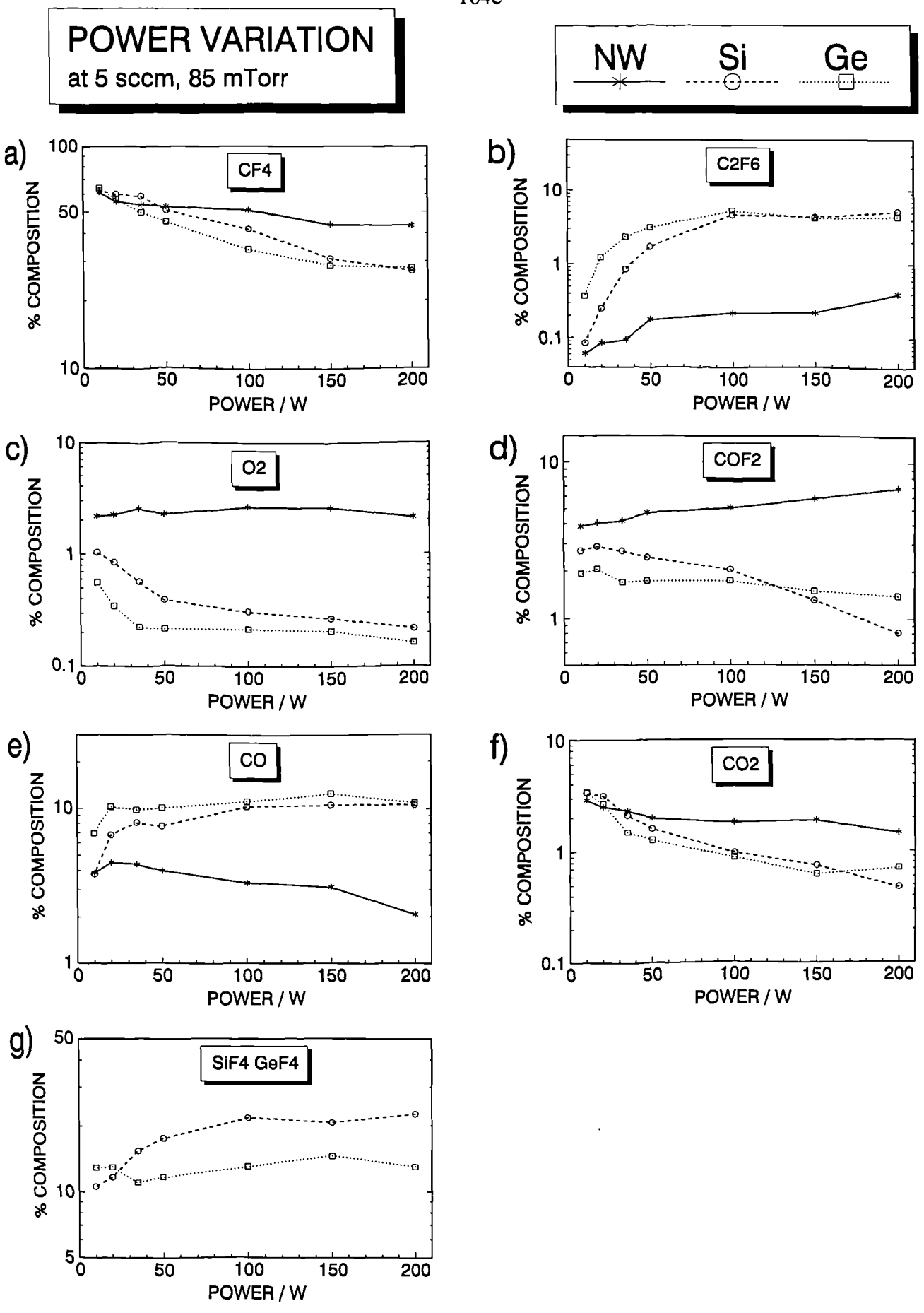

Figure 5.11. Graphs showing the mol % composition of gas phase species measured by QMS as a function of applied rf power at 5 sccm and 85 mTorr. F_2 was not monitored during this experiment. Note the logarithmic y-axis scales.

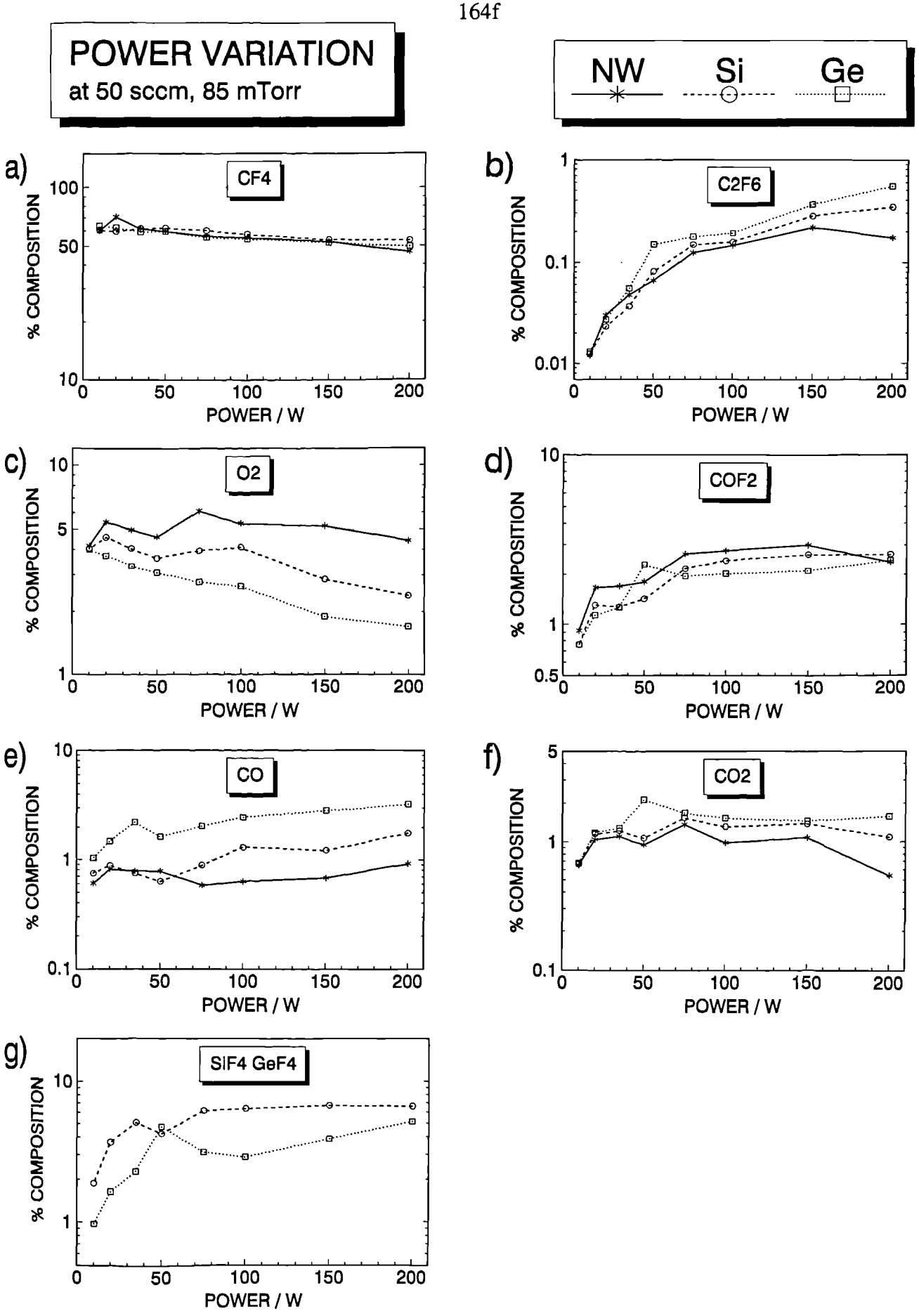

Figure 5.12. Graphs showing the mol % composition of gas phase species measured by QMS as a function of applied rf power at 50 sccm and 85 mTorr. Note the logarithmic y-axis scales.

rate and OES results, and adds further confirmation to the earlier proposal that the chemical etching mechanisms for Si and Ge are similar (sections 5.2.1 and 5.2.2).

On first introducing a Si or Ge wafer into the plasma, the concentration changes we observe are in general in the same direction, varying only in magnitude, regardless of the specific experimental conditions. We now summarise briefly these concentration changes, which can be most clearly recognised from the results of the area variation experiment at 5 sccm (figure 5.9) where the observed changes are large, and can be seen as a function of exposed wafer area.

Firstly, peaks due to SiF_4 and GeF_4 etch products appear in the mass spectrum. These etch products are discussed separately in the following section. The most apparent changes in the concentrations of other gas phase species are the large increase in $[C_2F_6]$ and the large reduction in $[O_2]$ and in $[F_2]$ (as mentioned above). The change in $[O_2]$ is especially sensitive to even a very small exposed area of wafer material (figure 5.9c). The concentrations of CO, CO_2 and COF_2 change by smaller factors, with [CO] increasing somewhat, while $[CO_2]$ and $[COF_2]$ generally fall slightly. The concentration of CF_4 in general remains constant, or falls slightly under some experimental conditions (e.g. at low flow rate and high power, figure 5.11a) when a wafer is introduced to the chamber. In section 5.4, we discuss these changes in the plasma composition in more detail, and propose a mechanism which may qualitatively explain them.

5.2.3.1 SiF_4 AND GeF_4 PRODUCT SPECIES

Before discussing these etch products, a point should be made concerning the use of the SiF_3^+ QMS signal to measure $[SiF_4]$ when etching Si wafers. As we noted in section 3.3.2, SiF_3^+ signals are also obtained in the QMS as products of the etching of the capillary probe, which can cause an artificial enhancement of the SiF_3^+ signal, thus introducing errors. However, these errors can be estimated realistically by considering the SiF_3^+ signal when etching Ge, because the reduction in [F] and hence the probe material etching rate is similar when etching Ge to that when etching Si. For the etching of whole

3" wafers, we estimate that the errors are $< \approx 5$ % at low flow rates ($\approx$ 5 sccm), rising as high as $\approx$ 30 % at higher flow rates ($\approx$ 50 sccm). When the wafer area is reduced, the errors in [SiF_4] are larger, but at 5 sccm remain $< \approx 20$ % even for the smallest wafers used. However, at 50 sccm, the errors approach 100 % for the smallest wafers used, so the [SiF_4] results are meaningless and are therefore not presented for that experiment (figure 5.10g). Clearly the [SiF_4] results must be interpreted carefully. We now return to the discussion of the SiF_4 and GeF_4 product species.

The only products of etching which have been detected by QMS are SiF_4 and GeF_4. No etch product molecules containing C or O atoms, or any Si_2F_y or Ge_2F_y type species were detected. (No attempt was made to measure lower fluorides due to uncertainties inherent in the detection of radical species (see section 3.2.1)). This further confirms that F atoms are the main etchant species in Si and Ge etching, since only fluorinated product molecules are detected.

For all the conditions studied, it is found that [SiF_4] > [GeF_4] despite the faster etching of Ge. In order to explain this effect, we now estimate the proportion of the total Si and Ge atom budget which is present as SiF_4 and GeF_4 respectively. Using Z to denote Si or Ge, and curly brackets { } to denote concentrations expressed as fractions the total gas present, the total Z budget is given by

$$\Sigma \{ZF_y\ (y = 0 - 4)\} = \frac{\text{Removal rate of Z from the wafer surface}}{\text{Input flux of } CF_4 + O_2}$$

$$= 0.92\ U$$

(The factor of 0.92 appears because U is defined in equation 5.1 using the input flux of CF_4 only, but here we need the total input flux of CF_4 + 8 vol % O_2 process gas). The fraction of products observed as ZF_4 is therefore given by

$$\frac{\{ZF_4\}}{\Sigma\{ZF_y\ (y = 0 - 4)\}} = \frac{\{ZF_4\}}{0.92\ U} \qquad (5.2)$$

The results of calculations using equation 5.2 are presented below in figure 5.13 for the power variation experiment at 5 sccm (where the errors in $[SiF_4]$ due to probe etching are < 5 %). We note that the product fraction should be $\leqslant 1$, so the fact that values slightly greater than 1 are obtained for both Si and Ge suggests that there is a systematic error, probably due to inaccurate calibration of the MFC, but this does not affect the observed trends. The results of figure 5.13 reflect the general result that the Si budget is present almost exclusively as SiF_4, but that only $\approx$ 60 % of the Ge atom budget is present as GeF_4 except at low power where the proportion as GeF_4 rises towards 100 %. We now discuss the reasons behind these observations, beginning with the case of Ge wafers.

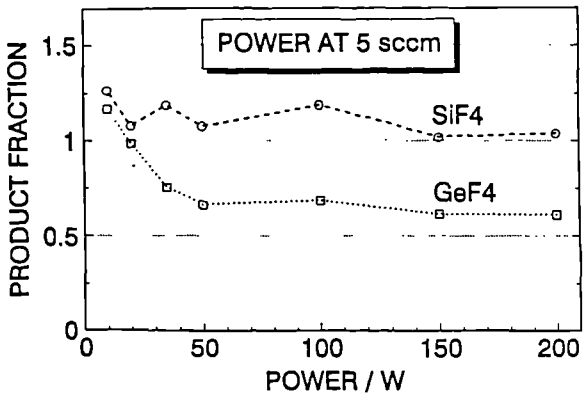

Figure 5.13. Graph showing the proportion of the total Si and Ge atom budget present as SiF_4 and GeF_4 respectively as a function of rf power at 5 sccm and 85 mTorr.

In chapter 4 we showed that C-containing species are present at the chamber walls in $CF_4 + O_2$ plasmas (section 4.3). This was due to CF_2 radicals adsorbing at the chamber walls and subsequently being removed as CF_4, so that at the steady state around 30 % of the C atom budget was present at the walls. We propose that a similar effect is occurring here with Ge-containing species. Earlier, in section 5.2.2, we presented evidence for significant concentrations of GeF_2 in the plasma during the etching of Ge. GeF_2 is involatile (m.p. 110 °C [119]) and will therefore readily adsorb at the chamber walls. We

propose that the adsorbed GeF_2 is then fluorinated by F atoms to gain GeF_4 in the gas phase, such that at the steady state, $\approx$ 40 % of the Ge atom budget is present at the walls, as indicated in figure 5.13. Evidence for this may be found as follows.

We have found that when a plasma is struck over Ge wafers, $[GeF_4]$ is initially quite low, and may take several minutes to increase to its steady state concentration. This could be attributed to a delay in the onset of etching caused, for example, by the need to first remove an etch resistant oxide layer from the wafer surface. However, in section 7.4.1 we demonstrate that this is not the case by considering the etching of SiGe alloys. In this case, $[GeF_4]$ initially rises slowly as with Ge etching, whereas $[SiF_4]$ is seen to rise rapidly indicating that etching begins immediately. A similar effect to the low initial $[GeF_4]$ seen in the present work has been observed by Takeo et al [120] who measured the microwave spectrum of GeF_2. They found that the signal intensity increased with time as their reaction cell was used, and concluded that a reaction may be taking place initially at the cell walls. We therefore attribute the slow rise of $[GeF_4]$ in our system to the adsorption of GeF_2 at the walls, and explain this behaviour as follows. When the plasma is first switched on with a Ge wafer present, there is no Ge present at the chamber walls and so GeF_2 adsorption is more rapid than the removal of GeF_2 as GeF_4. This results in the observed low initial concentration of GeF_4. The surface coverage of Ge-containing species then increases so that after several minutes of etching, a steady state coverage is reached such that the rate of adsorption of GeF_2 is balanced by the rate of desorption of GeF_4, and so $[GeF_4]$ reaches a steady state value.

Direct evidence to show that Ge-containing species are present at the walls was obtained by running a plasma with no wafer present immediately after Ge has been etched in the chamber. A signal due to $[GeF_4]$ is observed when the plasma is switched on, rising to maximum after a few minutes, after which it falls off slowly to zero, as the Ge-containing layer is removed.

It is now possible to understand the results of Figure 5.13 earlier, which show that at low power, a higher proportion of the Ge atom budget is present as GeF_4. At low

powers, GeF_4 produced by the etching process is dissociated more slowly to lower fluorides. This will result in lower [GeF_2] and hence a lower proportion of the Ge atom budget being present at the walls.

In the case of Si etching, molecular beam studies have shown that the major products initially desorbed from the Si surface during etching by F atoms, both with and without ion bombardment, are SiF_2, SiF_4 and Si_2F_6 [84]. We mentioned earlier that Si_2F_6 was not detected in the present work: presumably it rapidly dissociates in the plasma. It has also been shown that SiF_2 radicals are rapidly converted to SiF_4 by reactions at the chamber walls [121]. In addition, Tu et al [122] have proposed that the reason they detect no SiF_x (x = 1-3) in their system is that these species are rapidly fluorinated by collisions with F and F_2 at the walls. The finding in the present work that the Si budget is present almost exclusively as SiF_4 is therefore consistent with other results in the literature. Clearly fluorination of SiF_x at the chamber walls to gain $SiF_{4(g)}$ is so rapid that at the steady state, very little of the Si budget is present at the walls as adsorbed molecules. We note that the bond energies of Si-F and Ge-F are 565 kJ mol^{-1} and 452 kJ mol^{-1} in SiF_4 and GeF_4 respectively [123]. The greater exothermicity of the Si-F bond supports slower dissociation of SiF_4 than GeF_4, and also the rapid fluorination of SiF_x at the walls.

5.3 STEADY STATE EQUATION CALCULATIONS OF [CF_3] AND [F]

In chapter 4, the [CF_3] and [F] in the plasma were calculated with no wafer present, for conditions of 100 W and 85 mTorr (sections 4.5.1.1 and 4.5.1.2). The concentrations of these important species may also be calculated with a wafer present provided that dissociation rates in the plasma do not change on introduction if a wafer into the plasma. As we mentioned earlier in section 5.2.2, the electron density and energy distribution are not affected significantly by the presence of wafer material in the plasma, so dissociation rates are not expected to change on introducing a wafer into the plasma. This allows [CF_3] and [F] to be calculated for conditions of 100 W and 85 mTorr (i.e. in the flow rate and area variation experiments) using similar methods to those used in chapter

4. These calculations also allow the reasons for reduction in [F] on introducing a wafer to the plasma to be identified.

5.3.1 CALCULATION OF [CF_3] USING THE STEADY STATE EQUATION FOR C_2F_6

Since C_2F_6 is only formed by gas phase recombination of CF_3 radicals in the plasma and is removed only by dissociation and pumping (section 4.5.4.2), it is very unlikely that the presence of the wafer affects the production or removal rates of C_2F_6. This makes it possible to calculate [CF_3] using the steady state equation for C_2F_6, derived in section 4.5.1.1, which yielded (equation 4.4)

$$[CF_3] = ([C_2F_6] \{k_{pump} + k_{10}\} / k_5)^{½} .$$

The [CF_3] calculations are presented in figure 5.14 for the flow rate and area variation experiments. They show an increase in [CF_3] on introducing a wafer into the plasma, especially at large exposed wafer area and at low flow rates. These results will be discussed in section 5.4 later.

5.3.2 CALCULATION OF [F] USING THE STEADY STATE EQUATION FOR F

We now derive the steady state equation for F with a wafer present, making it possible to calculate [F]. This is done in order to understand which reactions are responsible for the large reduction in [F] observed on introducing a wafer into the plasma.

The important production and loss processes for F are the same as those determined in section 4.5.4.1, with additional processes due to the presence of the wafer. We introduce a term R_{wafer}, to denote the overall removal rate of F atoms (in $cm^{-3}\ s^{-1}$) from the plasma by adsorption and reaction of F at the wafer surface and by reactions of F

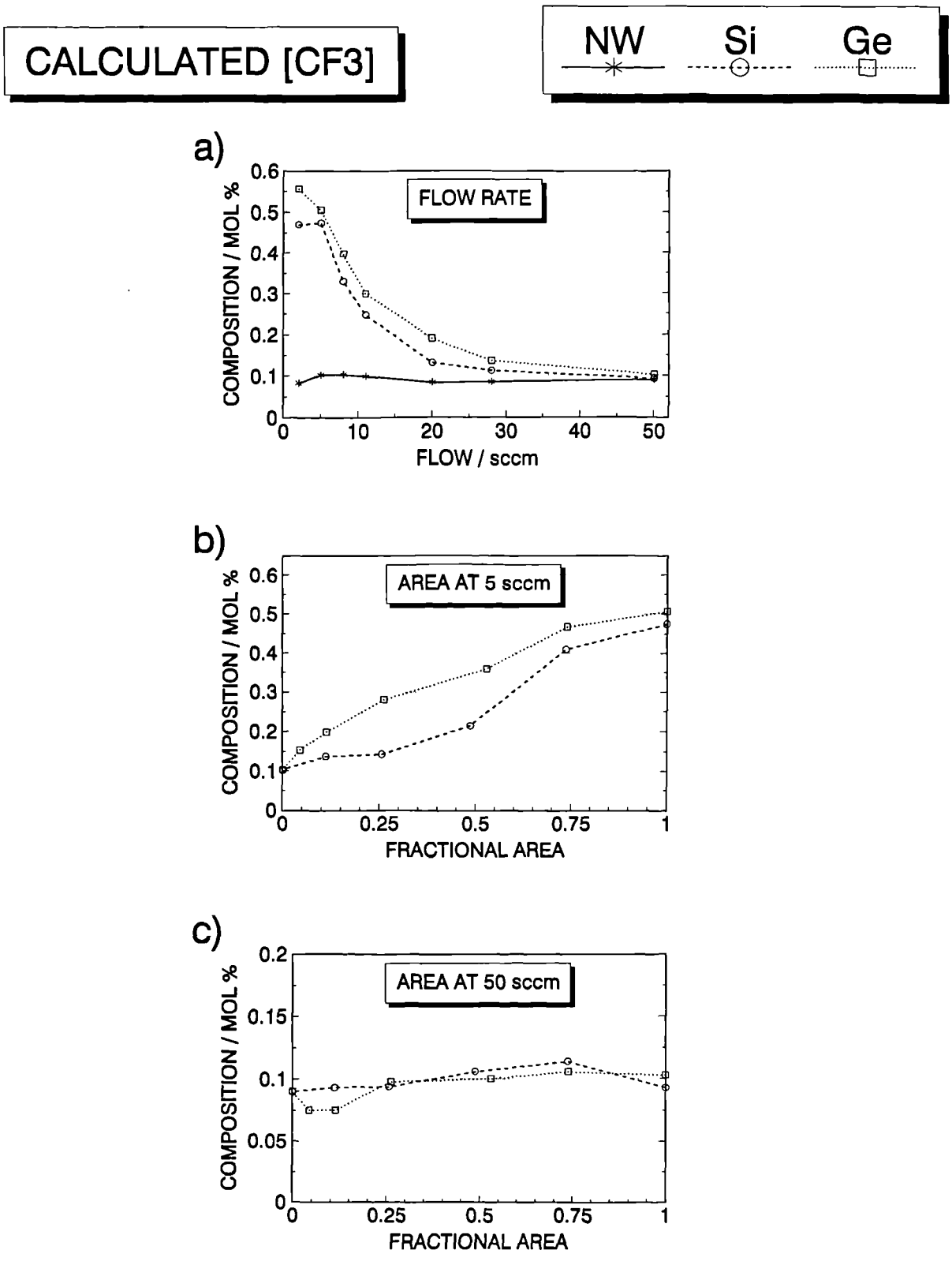

Figure 5.14. Graphs showing the mol % composition of CF_3, calculated using equation, as a function of flow rate and area (see table 5.1 for exact conditions).

with SiF_y and GeF_y ($y < 4$) in the gas phase and at the walls. The steady state equation for F is therefore

$$(k_1 + 2\,k_2)[CF_4] = k_6\,[CF_3]\,[F] + 2\,k_{50}\,[F] + R_{wafer}$$

yielding

$$[F] = \frac{(k_1 + 2\,k_2)\,[CF_4] - R_{wafer}}{k_6\,[CF_3] + 2\,k_{50}} \qquad (5.3)$$

where

$$k_{50} = k_{wall} \exp(-B\,[O_2])\,.$$

We assume for simplicity that k_{50} and the kinetics of wall reaction 50 (discussed in sections 4.3.1 and 4.5.1.2) are unaffected by the presence of the wafer. In order to simplify equation 5.3 further, production of F atoms by dissociation of SiF_4 and GeF_4 is not included. Such processes can only cause an increase in [F], and are therefore not the cause of the observed reduction in [F] on introducing a wafer into the plasma which we seek to understand.

From equation 5.3, it is clear that the reduction in [F] due to the etching process is explained if R_{wafer} is comparable to $(k_1 + 2\,k_2)\,[CF_4]$. The maximum possible value for R_{wafer} for a given set of experimental conditions is where each Si or Ge atom is removed from the wafer surface along with 4 F atoms, thus

$$R_{wafer}(max) = 4 \times (\text{Removal rate of Si or Ge / atoms cm}^{-2}\,\text{s}^{-1})\;A_s / V \;\; \text{cm}^{-3}\,\text{s}^{-1}$$

$$= 6.67 \times 10^{-10}\,R_{etch}\,A_s\,N / V \qquad (5.4)$$

Taking the case where $R_{wafer}(max)$ is largest (for etching a whole Ge wafer at conditions of 50 sccm, 100 W and 85 mTorr) then the values below are obtained

$$R_{wafer}(max) = 8.8 \times 10^{14}\ cm^{-3}\ s^{-1}$$

and

$$(k_1 + 2\ k_2)\ [CF_4] = 2.1 \times 10^{16}\ cm^{-3}\ s^{-1}.$$

Thus even for conditions where $R_{wafer}(max)$ is largest, its value is still only $\approx$ 4 % of the value of $(k_1 + 2\ k_2)\ [CF_4]$. This means that direct removal of F atoms by adsorption and reaction at the wafer surface is not responsible for the reduction in [F] observed on introducing a wafer into the plasma. Equation 5.3 can therefore be simplified to

$$[F] = \frac{(k_1 + 2\ k_2)\ [CF_4]}{k_6\ [CF_3] + 2\ k_{50}}. \qquad (5.5)$$

Note that equation 5.5 contains no terms resulting directly from the etching process. It is now possible to calculate [F] for the flow rate and area variation experiments using this equation. The results of the calculations are shown in figure 5.15. They are presented as a ratio of [F] with no wafer to [F] with a wafer present, in order to allow a comparison with the OES emission intensity ratio results from figure 5.5 earlier (reproduced in figure 5.15 here for convenience), and also to emphasise the reduction in [F]. It is clear that the reduction in [F] observed by OES is predicted by the calculations, and also that the trends in behaviour are reproduced quite well. This confirms that direct removal of F by the wafer is not responsible for the reduction in [F]. Instead, the reduction in [F] arises from the associated increase in $[CF_3]$ and the decrease in $[O_2]$, which causes an increase in the terms in the denominator of equation 5.5 when a wafer is introduced into the chamber. Thus the reduction in [F] during etching, which gives rise to the loading effect mentioned earlier (sections 5.2.1 and 5.2.2), is due to faster removal of F atoms via reactions in the gas phase and at the chamber walls, and not due directly to removal of F atoms at the surface of the wafer, in contrast to the conclusions of Mogab [114]. This also shows that the reduction in [F] over a wafer can not be taken as evidence that F atom etch Si and Ge, as mentioned earlier in section 5.2.2.

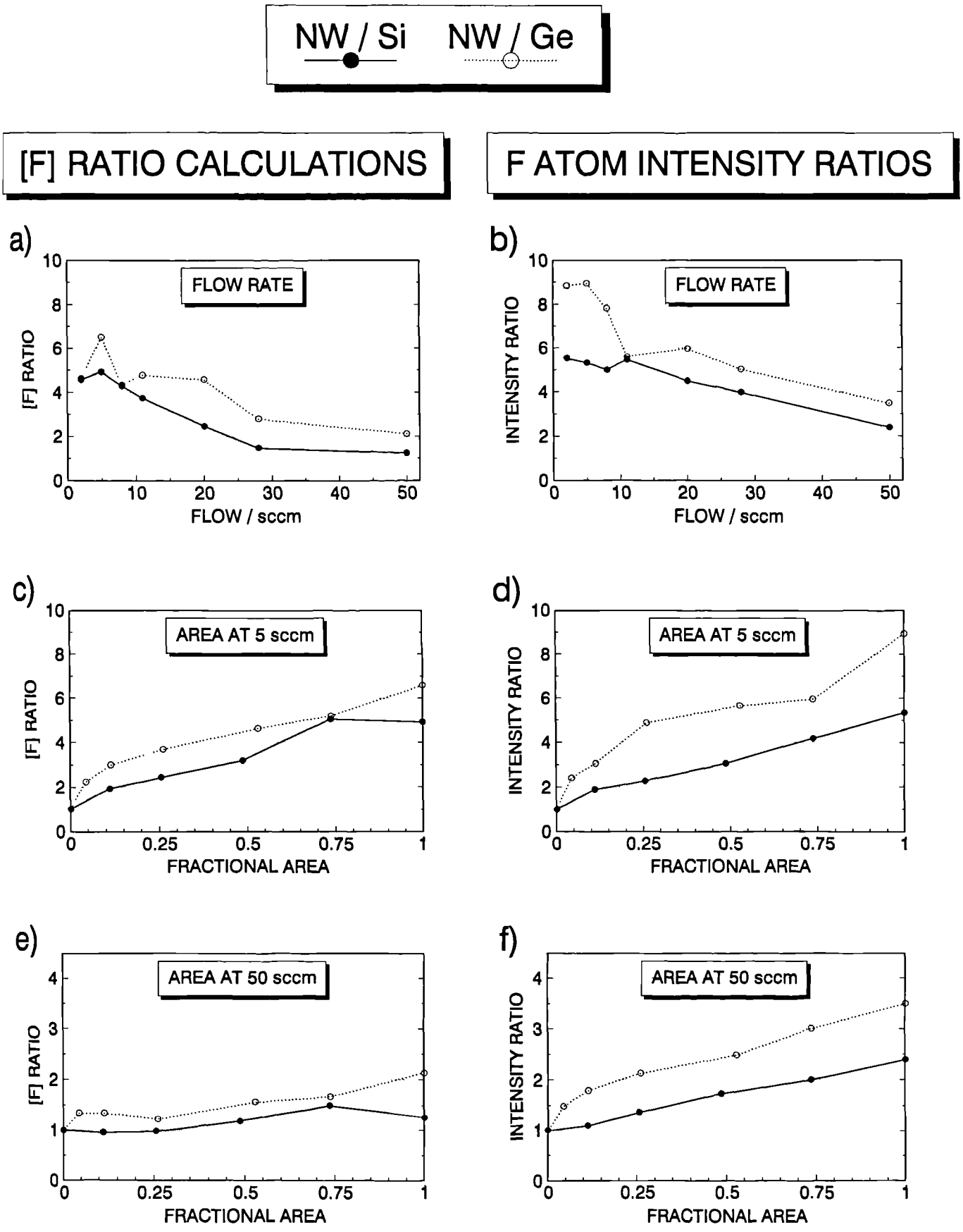

Figure 5.15. Graphs showing the ratio of [F] without to with a wafer present, calculated using equation 5.5, along with OES intensity ratio data reproduced from figure 5.5 for comparison. Results are shown as a function of flow rate and exposed wafer area (see table 5.1 for exact conditions).

5.4 DISCUSSION OF THE Si AND Ge ETCHING RESULTS

In section 5.3.2 we showed that F atoms are not removed directly by the etching process because the removal rate of F atoms at the wafer surface is much less than the removal rate of F by gas phase and wall reactions. However, there is an important difference between the removal of F atoms by the wafer and by other processes. The gas phase and wall reactions all cause F atoms to be rapidly cycled between different molecules in the plasma, whereas the etching reactions "trap" F atoms as SiF_4 and GeF_4 (or lower fluorides) so that they are effectively removed from the system. Thus although the removal rate of F atoms by the wafer is slow, the residence time is sufficiently long (up to 15 s) for a significant amount of the F atom budget to be incorporated into fluorides of Si or Ge. This has the effect of reducing the effective fluorine-to-carbon ration (F / C) in the plasma. This effect has been noted by other workers [124], [125], and is known to lead to an increase in the concentrations of CF_3 and CF_2. We now discuss qualitatively how the reduction in F / C affects the overall chemistry of the plasma, making use of the reaction scheme which was determined in chapter 4 (figure 4.12). That reaction scheme is reproduced here as figure 5.16 for convenience, but is modified to show the number of each reaction to assist in the following discussion.

The main effects which are expected to be caused by the introduction of a wafer into the plasma are given below.

(a) The wafer causes a reduction in F / C, and so $[CF_2]$ and $[CF_3]$ increase as mentioned above.

(b) The increase in $[CF_2]$ and $[CF_3]$ results in an increase in the removal rate of O atoms via reactions 27, 28 and 29, leading to a reduction in [O].

(c) The increase in $[CF_3]$ results in an increase in the removal rate of F atoms via reaction 6, causing a reduction in [F]. In addition, the reduction in [O] mentioned

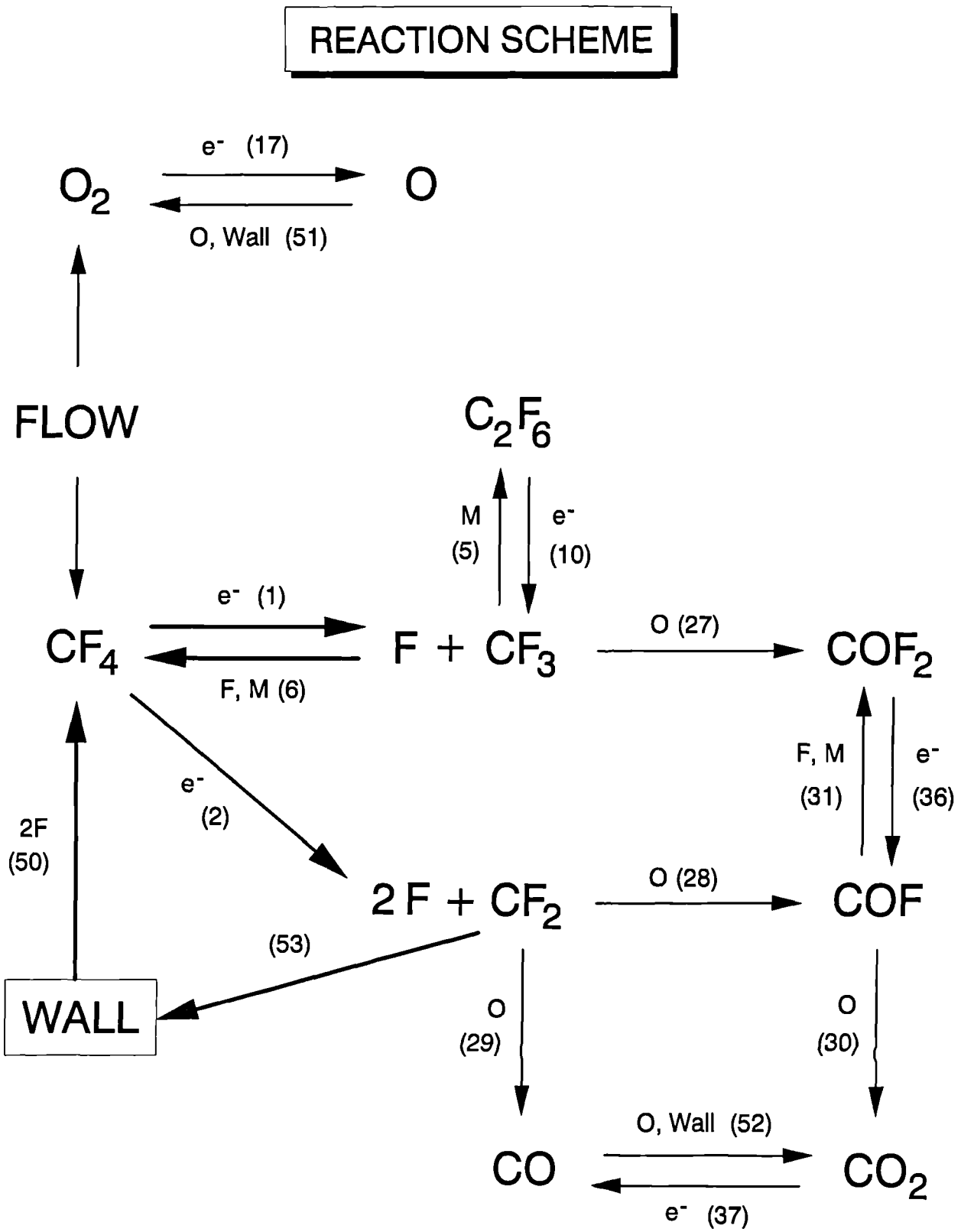

Figure 5.16. The overall reaction scheme for $CF_4 + O_2$ process gas showing the important reaction pathways, from figure 4.12. Bracketed numbers give the reaction numbers (see table 4.19).

in (b) above results in a reduction in the inhibiting effect which O atoms have on reaction 50. This causes an increase in the removal rate of F atoms at the walls via reaction 50, giving a further reduction in [F].

The overall effect of (a) to (c) is to cause an increase in $[CF_3]$ (and hence $[C_2F_6]$) and $[CF_2]$, and a decrease in [F] and [O]. We have not measured $[CF_2]$, but our results show that $[CF_3]$, [F] and [O] do show the predicted behaviour when a wafer is introduced to the plasma system. This can be seen most easily from the results of the area variation experiment at 5 sccm (see figure 5.9c, noting that [O] α $[O_2]$ (section 4.5.3.1), figure 5.5c and figure 5.14b). Note also that the strongly coupled nature of (a) to (c) leads to the possibility of positive feedback. This is illustrated as follows. The initial increase in $[CF_2]$ causes a reduction of [O]. This in turn leads to a reduced loss rate of CF_2 by reactions with O atoms (reactions 28 and 29), which has the effect of reinforcing the initial increase in $[CF_2]$. Similar arguments also apply to $[CF_3]$ and [F]. This means that the plasma system is very sensitive changes in F / C, as we show later. We now discuss how the magnitude of the reduction in F / C may be determined, and then return to discuss the results for the remaining gas phase species.

The size of the reduction in F / C is indicated by the values of U calculated in section 5.2.1. U gives the fraction of CF_4 feed gas molecules which is converted to SiF_4 and GeF_4 product molecules, and can therefore be used to indicate the magnitude of the reduction in F / C. We note however that U and F / C are not simply proportional for the following reasons. Firstly, not all of the Ge atom budget is present as GeF_4 (section 5.2.3.1), so U may overestimate the effect of Ge wafers on F / C. Secondly, the presence of oxygen also affects the F / C ratio by trapping C atoms as unreactive molecules such as CO and CO_2 [124]. Clearly this effect is characterised by [CO] and $[CO_2]$, and so it will depend on the experimental conditions. In addition, F / C may be influenced by other processes such as adsorption of C and F-containing species at the walls. However, U still appears to be a useful parameter for indicating the magnitude of the changes to the plasma composition on introducing a wafer into the plasma. This is confirmed by a comparison of

the U results (figure 5.2) with the OES (figure 5.5) and QMS (figures 5.7 to 5.12) results. This comparison makes clear the following points:

(1) As expected, the biggest changes to the gas phase composition on introducing a wafer into the plasma occur where U is large ($> \approx 0.1$), and increase in magnitude as U increases (compare for example the flow rate variation results presented in figures 5.2a, 5.5a, 5.7 and 5.14a).

(2) It is also clear from the flow rate results that the plasma composition is very sensitive to U as U increases above ≈ 0.1. This sensitivity to changes in U and hence F / C was predicted earlier in this section.

We have already explained earlier in this section the behaviour of [O_2], [F] and [CF_3]. We now discuss the behaviour of [CO], [CO_2] and [COF_2].

The reduction in F / C caused by the etching of the wafer results in an increase in [CF_2] and [CF_3]. CF_2 and CF_3 react with O atoms to produce CO, CO_2 and COF_2 (reactions 27, 28 and 29), so it is expected that the sum of the concentrations of these species will increase. This is indeed what is observed; for example, at 5 sccm, 100 W and 85 mTorr, the sum of the mole percentage compositions of these species is $\approx$ 11 mol % with no wafer present, and rises to $\approx$ 18 mol % with a 3" Si wafer present. It is difficult to predict the relative distributions of [CO], [COF_2] and [CO_2] without knowledge of [COF] because COF is important in determining the concentrations of these species as can be seen from figure 5.16. We can, however, explain some of the observed behaviour as follows.

The QMS results show that in general CO is the favoured oxygen containing product on introducing a wafer into the plasma (see for example the area variation results of figure 5.9, where [CO] rises while [CO_2] and [COF_2] fall as the exposed wafer area increases). This is to be expected under conditions of reduced [O] (as with a wafer

present), because once CO is formed it is converted more slowly to CO_2 by reaction with O at the walls (reaction 52), which is the main removal mechanism for CO. Thus a greater proportion of the O budget is present as CO with a wafer present. It is interesting to note that the increase in [CO] will give rise to an increase in the removal rate of O atoms via reaction 52, causing a decrease in [O] as we saw from the results of the CO addition experiments (section 4.2). This will serve to reinforce the reduction of [O] caused by the increase in $[CF_2]$ and $[CF_3]$ discussed earlier, illustrating the complex interplay of the chemical processes which occur in plasma systems.

We now explain the fall in $[F_2]$ on introducing a wafer into the plasma mentioned in section 5.2.3 earlier. The main production processes for F_2 are via reaction 23 ($O(^1D) + COF_2 \dashrightarrow F_2 + CO_2$) and via recombination of F atoms at the chamber walls (section 4.5.3.5). $O(^1D)$ is produced by dissociation of O_2 (see table 4.2 on p. 110a), so the fall in $[O_2]$ means that $[O(^1D)]$ will also be lower. Thus all the species involved in the production of F_2 are reduced in concentration over a wafer, explaining the observed fall in $[F_2]$. We note that F_2 is not expected to be important in the etching process because it has lower activity towards the wafer surface than F atoms and is present in smaller concentrations (see section 4.5.3.5).

5.5 SUMMARY OF THE MAIN CONCLUSIONS

We now summarise the main conclusions drawn from the etching studies of Si and Ge wafers in CF_4 + 8 % O_2 plasmas.

1) Si and Ge wafers etch by a similar chemical mechanism, although the etching of Si relies more on ion bombardment than does the etching of Ge. F atoms are the main etchant species in both cases.

2) For Si etching, the Si budget is present almost exclusively as SiF_4. For Ge etching, the Ge atom budget is present mainly as GeF_4 with the remainder (up to 40 %) present in Ge-containing species adsorbed at the chamber walls.

3) Emission from the 3p $^2P°$ levels of F atoms behaves differently from emission from all other observed states of F. This result is discussed in chapter 6, where we propose that the 3p $^2P°$ levels are populated by resonant energy transfer during collisions with excited O_2 molecules in the $^1\Phi_u$ state as well as by electron impact excitation.

4) It is well known that the loading effect is caused by a reduction in [F] on introducing a wafer into the plasma. However, contrary to previous thought, the reduction in [F] is not caused directly by the removal of F atoms by adsorption and reaction at the wafer surface. Instead it is caused by an increased loss rate of F atoms by reactions in the gas phase and at the chamber walls.

5) The changes in the gas composition on introducing a wafer into the plasma result from a reduction in the fluorine-to-carbon ratio, F / C, which occurs because the etching process causes F atoms to be "trapped" as fluorides of Si and Ge. The utilisation factor, U, is a measure of the magnitude of the reduction in F / C. The observed changes in the gas phase composition of the plasma on introducing a wafer into the plasma can be qualitatively explained.

CHAPTER 6

WHY DOES OPTICAL EMISSION FROM THE 3p ^{2}P° STATES OF F ATOMS BEHAVE DIFFERENTLY FROM THAT OF ALL OTHER OBSERVED STATES OF F ?

6 WHY DOES OPTICAL EMISSION FROM THE 3p $^2P^\circ$ STATES OF F ATOMS BEHAVE DIFFERENTLY FROM THAT OF ALL OTHER OBSERVED STATES OF F ?

6.1 INTRODUCTION

In section 5.2.2 we mentioned briefly that when a wafer is added to the plasma, optical emission from the 3p $^2P^\circ$ states of F behaves differently from that of all the other states of F which we have observed in this work. In addition, emission from the two states of the 3p $^2P^\circ$ spin-orbit doublet also show different behaviour from each other. In this chapter we investigate these effects further.

In section 6.2, we present more detailed results of the OES study into this effect than those presented in chapter 5. Section 6.2.1 gives the results of the Si and Ge etching experiments which illustrate further the anomalous behaviour of emission from the 3p $^2P^\circ_{1/2}$ and 3p $^2P^\circ_{3/2}$ states of F. Then in section 6.2.2 we present the results from the gas addition experiments, which show that the effect is dependent on $[O_2]$ or [O] in the plasma, and that it is not confined only to the etching of a wafer substrate.

We have shown earlier that adding O_2 to the plasma affects strongly the concentration of F atoms, because O atoms compete with F atoms for surface sites (see section 4.5.1.2). In section 6.3.1 we use a simple model in which excited F atoms are produced only by an electron excitation mechanism, in order to ascertain if this surface effect is also responsible for the anomalous behaviour of emission from the 3p $^2P^\circ$ states of F. The model suggests that all the observed states of F are formed exclusively by a single electron collision with ground state F atoms, except for the 3p $^2P^\circ$ states. These states appear to be formed by another process in addition to electron excitation, and this other process selectively populates just those two states. We then propose in section 6.3.2 that this additional process involves near resonant energy transfer in collisions between ground state $2p^5\ ^2P_{3/2}$ F atoms and O_2 molecules in the $^1\Phi_u$ state, which lies close in energy to the

3p $^2P°$ states of F. This mechanism can explain qualitatively the differences in behaviour between the two states of the 3p $^2P°$ spin-orbit doublet.

6.2 THE OES RESULTS; A COMPARATIVE STUDY OF THE BEHAVIOUR OF EMISSION FROM DIFFERENT ELECTRONIC STATES OF F ATOMS

6.2.1 THE RESULTS OF THE ETCHING STUDIES

We now present the OES results which allow comparison of the behaviour of the emission from different excited states of F atoms. Presented below in table 5.2 (reproduced from section 5.2.2) are the OES results for conditions of 5 sccm, 100 W and 85 mTorr, expressed as the ratio of line intensities with and without a wafer present (denoted I (NW / Si) and I (NW / Ge)).

Wavelength / Å	Transition Lower - Upper	I (NW / Si) errors ± ≈ 10 %	I (NW / Ge) errors ± ≈ 15 %
6240	$3s\ ^4P_{5/2}$ - $3p\ ^4S°_{3/2}$	5.3	9.4
6774	$3s\ ^4P_{5/2}$ - $3p\ ^4D°_{3/2}$	5.7	8.1
6856	$3s\ ^4P_{5/2}$ - $3p\ ^4D°_{7/2}$	5.3	9.0
6870	$3s\ ^4P_{1/2}$ - $3p\ ^4D°_{7/2}$	5.1	8.2
6902	$3s\ ^4P_{3/2}$ - $3p\ ^4D°_{5/2}$	5.5	8.3
6910	$3s\ ^4P_{1/2}$ - $3p\ ^4D°_{3/2}$	5.3	7.3
7037	$3s\ ^2P_{3/2}$ - $3p\ ^2P°_{3/2}$	18	19
7128	$3s\ ^2P_{1/2}$ - $3p\ ^2P°_{1/2}$	10.5	13
7202	$3s\ ^2P_{1/2}$ - $3p\ ^2P°_{3/2}$	16	18
7309	$3s'\ ^2D_{5/2}$ - $3p'\ ^2F°_{7/2}$	6.1	9.5
7311	$3s\ ^2P_{3/2}$ - $3p\ ^2S°_{1/2}$	6.0	8.7
7332	$3s\ ^4P_{5/2}$ - $3p\ ^4P°_{3/2}$	5.9	8.4
7399	$3s\ ^4P_{5/2}$ - $3p\ ^4P°_{5/2}$	5.8	9.1

Table 5.2. The F atom emission lines observed in this work with relevant transitions, along with measured emission intensities expressed as intensity ratios I (NW / Si) and I (NW / Ge), for conditions of 5 sccm, 100 W and 85 mTorr.

From this table can be drawn the following conclusions which are of interest in this chapter.

1) The emission from all observed states of F is similarly reduced with a wafer present except that originating from the $3p\,^2P^\circ$ states (7037 Å, 7128 Å and 7202 Å lines), which is reduced in intensity by a larger factor.

2) Emission originating from the $3p\,^2P^\circ_{3/2}$ state (7037 Å and 7202 Å lines) is reduced in intensity by a larger factor than emission from the $3p\,^2P^\circ_{1/2}$ state (7128 Å line).

In all the following results and discussions, we use the 7037 Å line to monitor the behaviour of $3p\,^2P^\circ_{3/2}$ F atoms and the 7128 Å line to monitor the behaviour of $3p\,^2P^\circ_{1/2}$ F atoms. The 6856 Å line is used to indicate the behaviour of all the other emission lines, which all show the same behaviour for all the experimental conditions used during the etching study. The anomalous behaviour of emission from $3p\,^2P^\circ$ F atoms is further highlighted in figures 6.1 and 6.2 (for Si and Ge etching respectively), where intensity ratios are presented for the 7037 Å, 7128 Å and 6856 Å lines for the experiments in which the flow rate, power, pressure and exposed wafer area were varied while all other parameters remained constant (the exact conditions are listed in table 5.1). In each case, the emission from the $3p\,^2P^\circ$ states is more strongly reduced than emission from all other observed states of F. In addition, the reduction is larger for the $3p\,^2P^\circ_{3/2}$ level than for the $3p\,^2P^\circ_{1/2}$ level in all cases.

Similar anomalous behaviour of the emission from $3p\,^2P^\circ$ F atoms has been observed in a previous study performed in this laboratory by Field et al [126] for Si etching, with CF_4 + 8 vol % O_2 process gas as in the present work, but using a plasma etching system. That study contained emission intensity results for doublet and quartet F atoms, and also for singlet, triplet and quintet F^+ ions. Strong differences were found in the behaviour emission from excited singlet, triplet and quintet F^+ ions when a Si wafer was introduced to the chamber. The concept of conservation of spin angular momentum in gas-

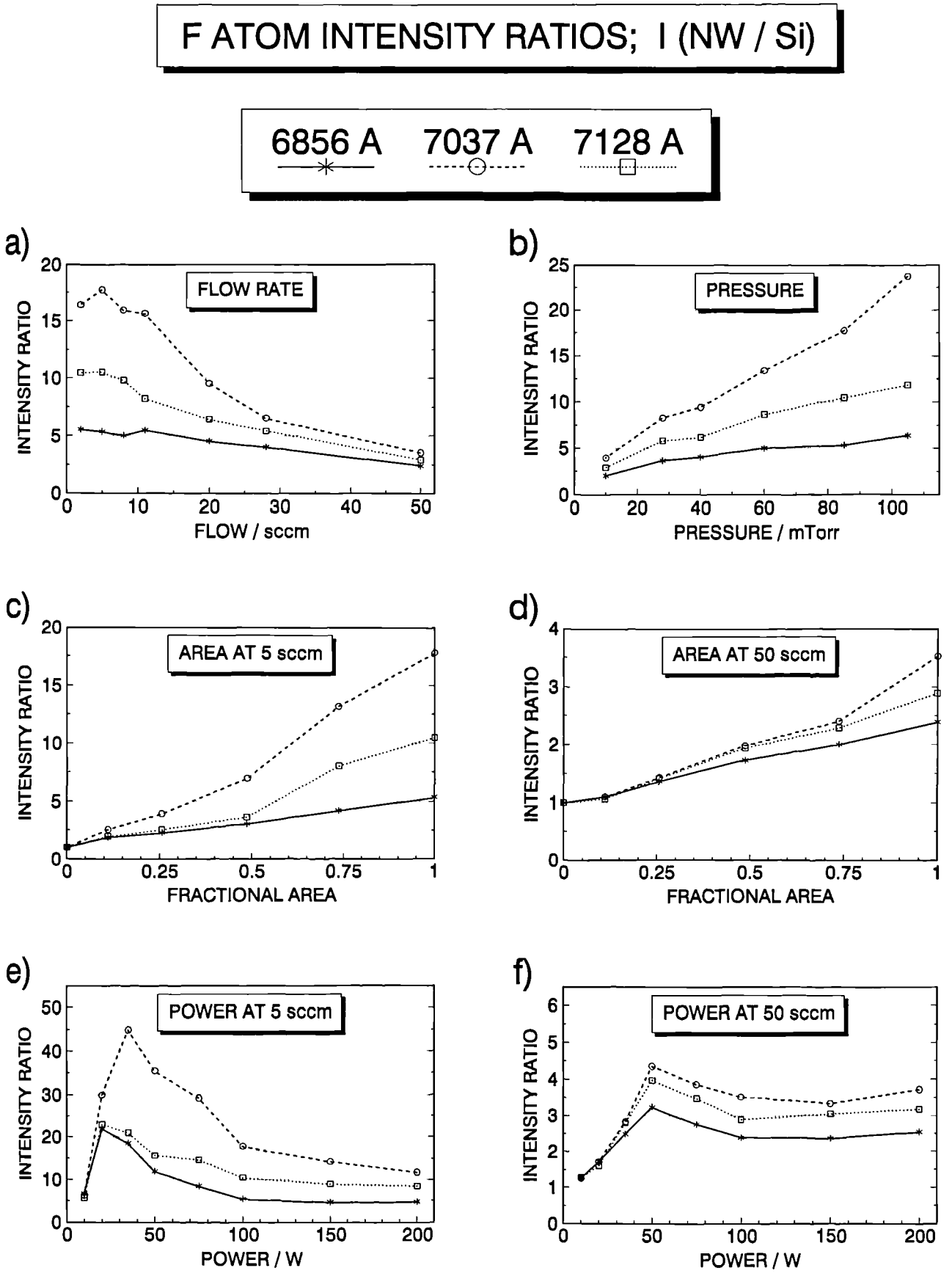

Figure 6.1. Graphs showing intensity ratios I (NW / Si) for the 7037, 7128 and 6856 Å emission lines of F under a wide range of experimental conditions (see table 5.1).

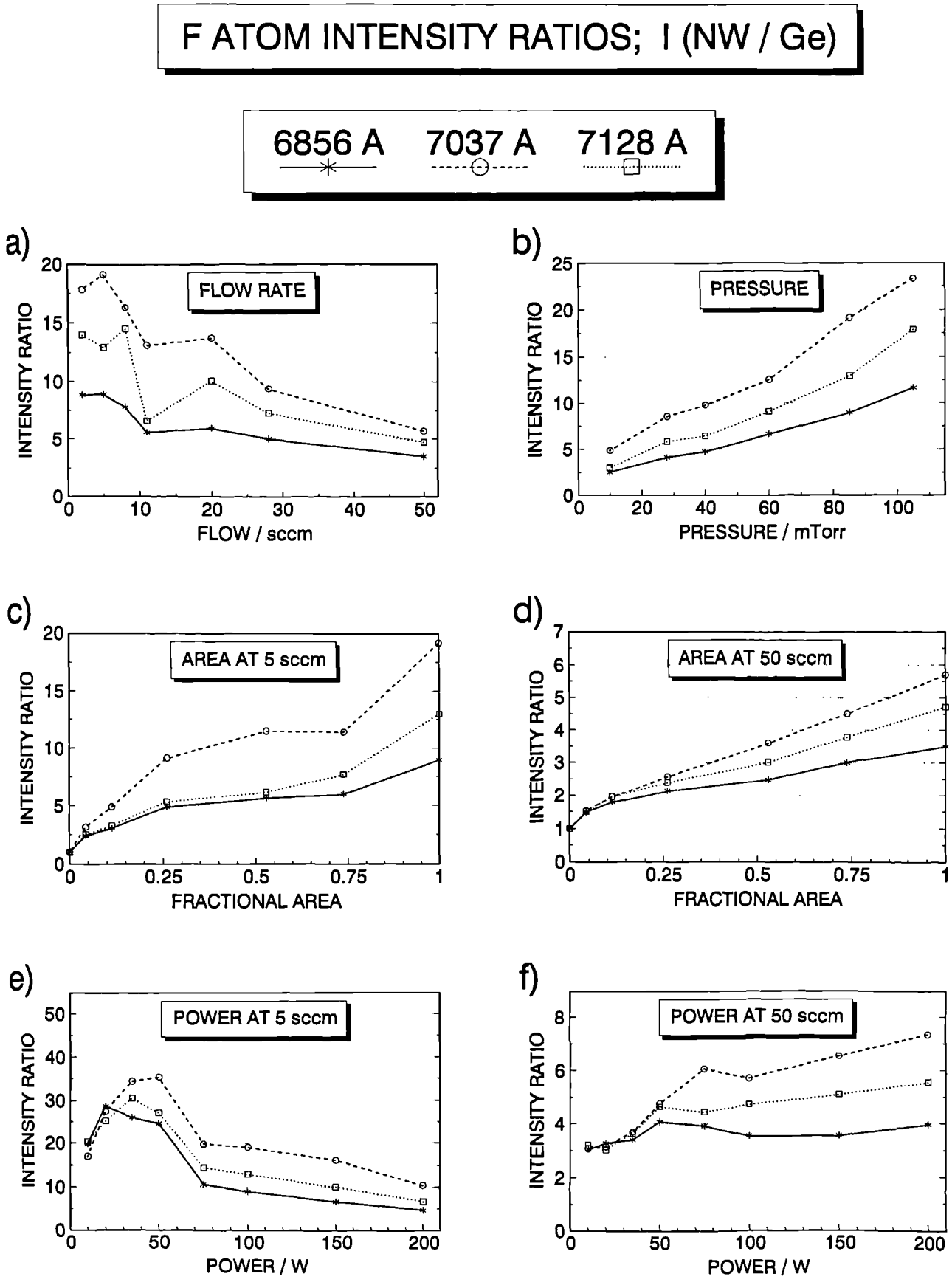

Figure 6.2. Graphs showing intensity ratios I (NW / Ge) for the 7037, 7128 and 6856 Å emission lines of F under a wide range of experimental conditions (see table 5.1).

surface interactions was introduced, and used to explain those results. The anomalous behaviour of the $3p\ ^2P^\circ$ states of F atoms was also interpreted using this concept. However, in the RIE system used in the present work, anomalous behaviour of the $3p\ ^2P^\circ$ states of F is also found to occur with no wafer present when the composition of the feed gas mixture is altered. Those results (given in the following section) indicate that the effect is linked to the concentration of O_2 in the plasma, rather than resulting from direct interactions of F with the wafer surface. Clearly the concept spin angular momentum conservation can not be used to explain the results in the present work.

6.2.2 THE RESULTS OF THE GAS ADDITION EXPERIMENTS

In the gas addition experiments, the effects of varying the percentage of O_2 in CF_4, and the effects of adding CO, CO_2 and C_2F_6 to CF_4 + 8 vol % O_2 feed gas were studied, all with no wafer present at conditions of 5 sccm, 100 W and 85 mTorr. The QMS measurements of the gas composition and OES emission intensity measurements of the 6856 Å line were presented earlier in sections 4.2 and 4.5.1.2 respectively. We now present the OES emission intensity measurements of the 7037 Å and 7128 Å emission lines of F atoms to allow comparison with the earlier 6856 Å emission line results, and so to highlight the differences in the behaviour of these emission lines.

The differences in the behaviour of the 7037 Å, 7128 Å and 6856 Å lines can be demonstrated by the use of the emission line intensity ratios given below

$$\frac{I\ (7037\ Å)}{I\ (6856\ Å)} \quad \text{and} \quad \frac{I\ (7128\ Å)}{I\ (6856\ Å)}.$$

These emission line intensity ratios (normalised to equal 1 for a feed gas mixture of CF_4 + 8 vol % O_2) are presented in figure 6.3, plotted as a function of feed gas composition. If the 7037 Å, 7128 Å and 6856 Å emission lines were all to exhibit the same behaviour when the gas composition is changed, then the normalised line emission intensity ratios would of course equal 1 for all feed gas compositions. This is clearly not the case, as can

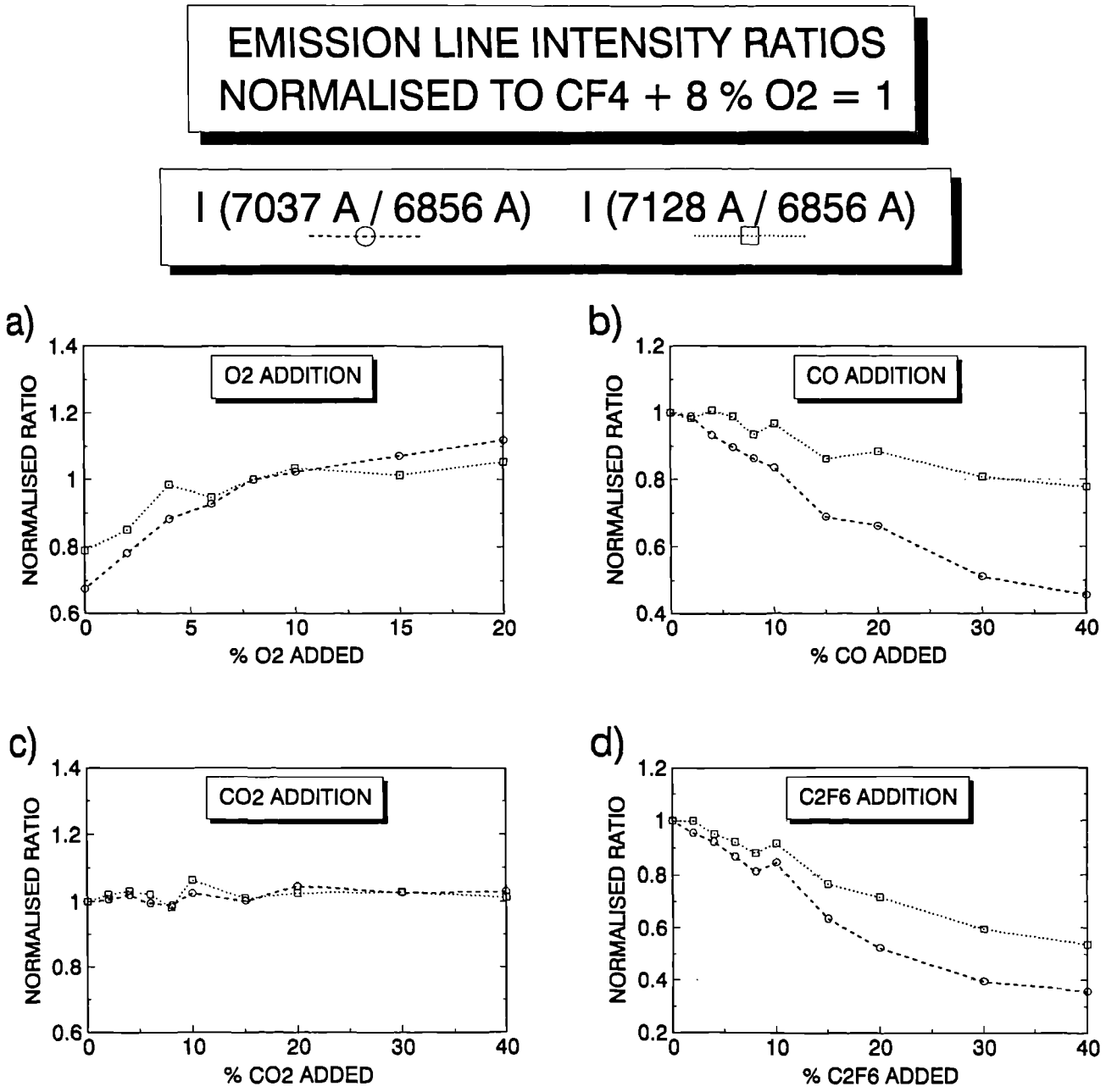

Figure 6.3. Graphs showing emission line intensity ratios I (7037 Å / 6856 Å) and I (7128 Å / 6856 Å) normalised to CF_4 + 8 vol % O_2 = 1 versus a) vol % O_2 added to CF_4 feed gas, and b), c) and d) vol % CO, CO_2 and C_2F_6 added to CF_4 + 8 vol % O_2 feed gas, all at 5 sccm, 100 W and 85 mTorr.

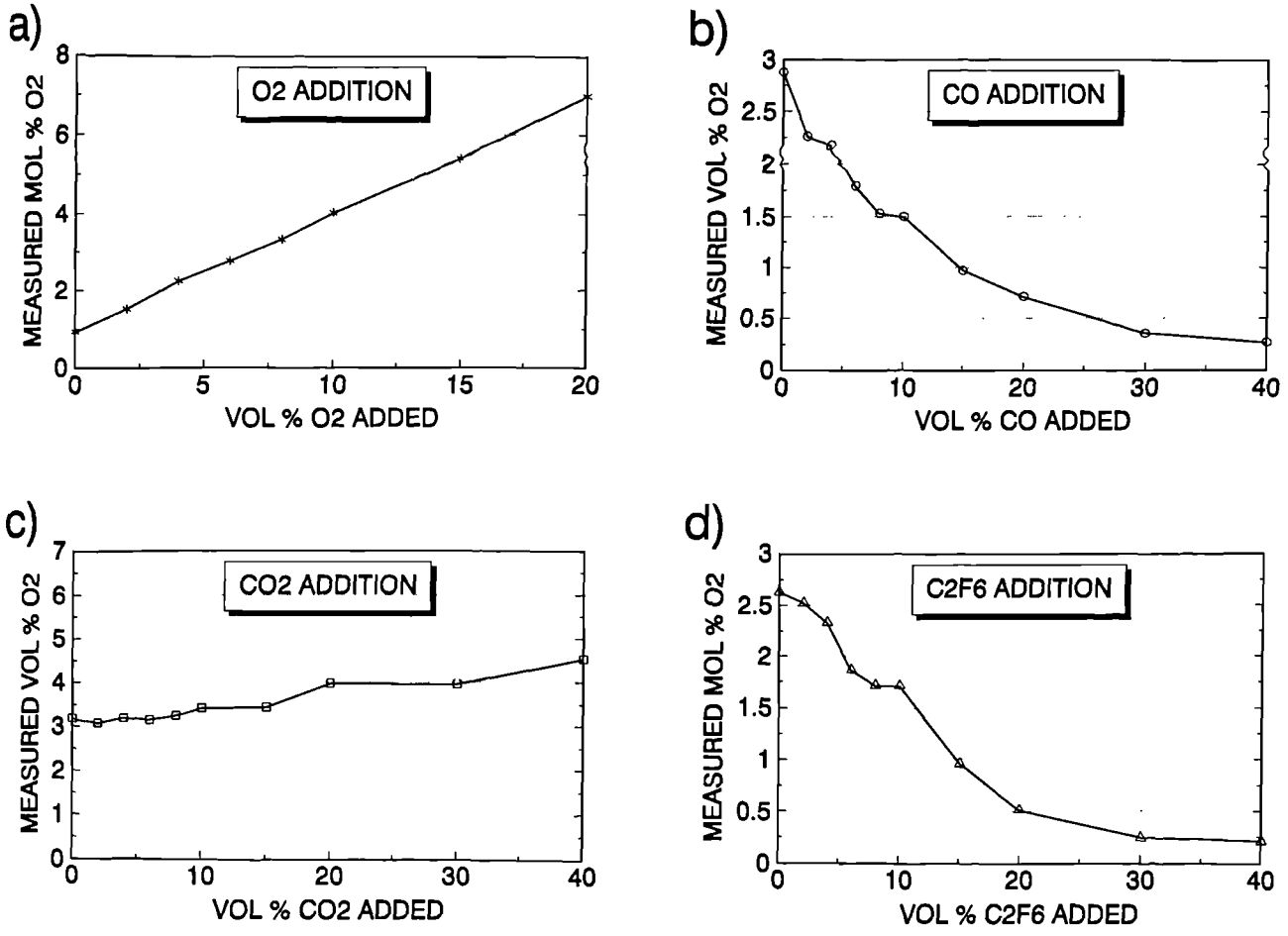

Figure 6.4. Graphs showing the mole percentage composition of O_2 measured by QMS versus; a) vol % O_2 added to CF_4 feed gas, and b), c) and d) vol % CO, CO_2 and C_2F_6 added to CF_4 + 8 vol % O_2 feed gas, all at 5 sccm, 100 W and 85 mTorr with no wafer present.

be recognised most easily from figures 6.3a, b and d. It is now apparent that changes in the gas composition can cause differences in the behaviour of these emission lines, so the effects are not confined only to the etching of a wafer substrate. They appear to be dependent on the concentration of O_2 or O in the plasma, as we now show.

In figure 6.4 is presented the percentage composition of O_2 as a function of feed gas composition (taken from the QMS data of figures 4.5 to 4.8 in section 4.2). The emission line intensity ratios for the 7037 Å, 7128 Å and 6856 Å emission lines (figure 6.3) can be seen to follow the trends shown by the concentration of O_2 (figure 6.4). This suggests that the effect is somehow linked to O_2 (or [O], noting that $[O_2] \alpha [O]$ as shown in section 4.5.3.1). In figure 6.5, the normalised line emission intensity ratios from figures 6.3a to d are plotted together on the same axes against the measured $[O_2]$ (from figure 6.4). The data points from all the gas addition experiments lie on a single curve, showing that the differences in the behaviour of the 7037 Å, 7128 Å and 6856 Å lines are indeed dependent on $[O_2]$ or [O]. (The greater scatter in the data in figure 6.5b occurs because the 7128 Å line is much weaker in intensity than the 7037 Å and 6856 Å lines). Figure 6.5 shows that as $[O_2]$ increases, the 7037 Å and 7128 Å lines are increased in intensity by a larger factor than the 6856 Å line. This effect is stronger with the 7037 Å line than the 7128 Å line.

It is interesting to note at this point that Coburn and Chen [63] found that the 6856 Å and 7037 Å lines observed in that work each show essentially the same functional dependence on the percentage of O_2 in CF_4 feed gas, in contrast to the present work (results for the 7128 Å line were not presented). It therefore appears that the effect is dependent upon the system used.

We can now understand the anomalous behaviour of emission from the $3p\ ^2P^\circ$ states of F atoms observed when etching Si and Ge wafers (section 6.2.1). We showed in section 5.2.3 that $[O_2]$ is reduced in the presence of Si or Ge wafers. It is therefore expected from the results of figure 6.5 that the 7037 Å and 7128 Å lines will be reduced in intensity by a larger factor than the 6856 Å line in the presence of a wafer, and that this

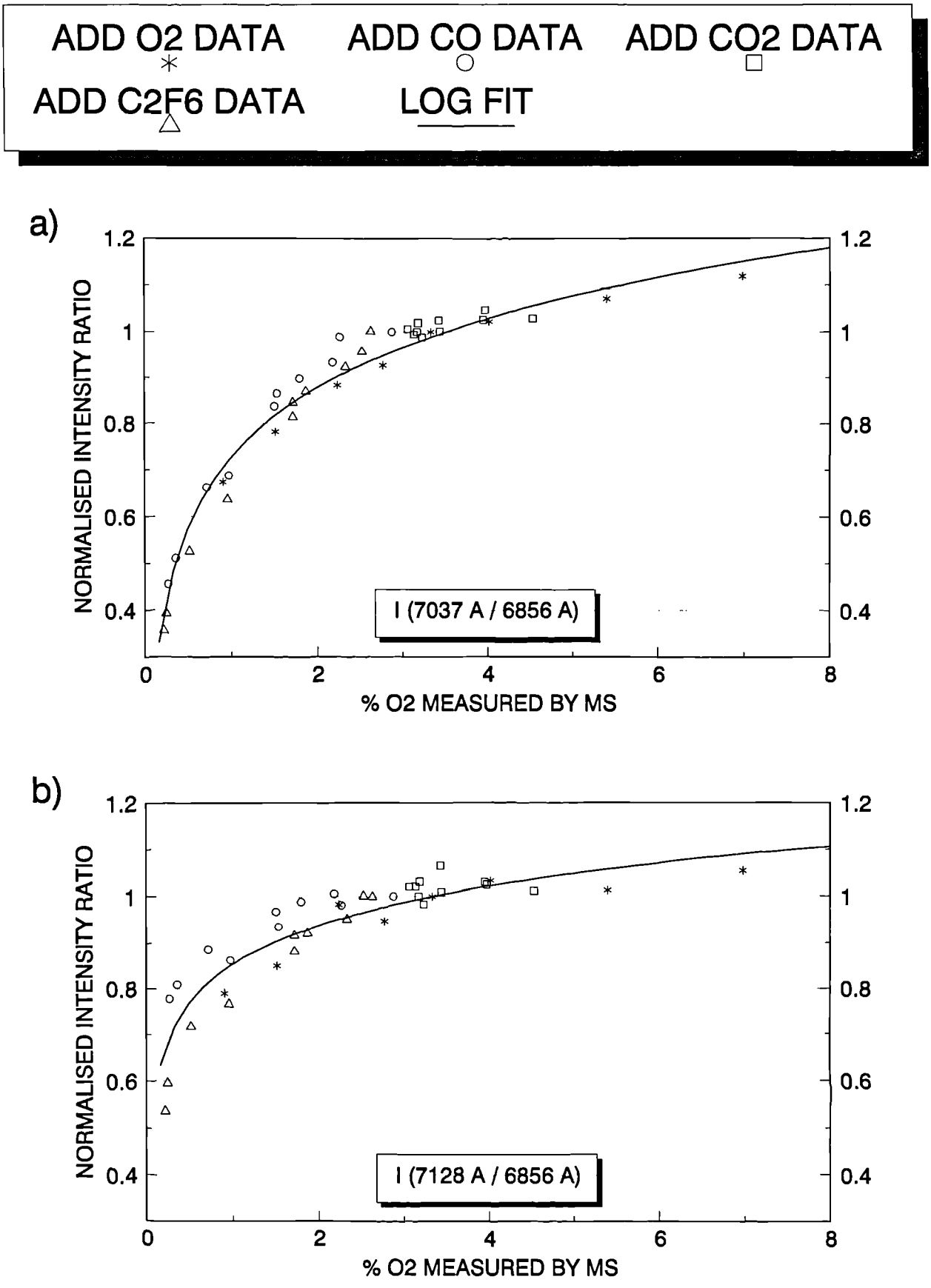

Figure 6.5. Graphs showing emission line intensity ratios I (7037 Å / 6856 Å) and I (7128 Å / 6856 Å) normalised to CF_4 + 8 vol % O_2 = 1 versus mol % composition of O_2 measured by QMS in the gas addition experiments using experimental data from figures 6.3 and 6.4.

reduction will be greater with the 7037 Å line than with the 7128 Å line. This is indeed the result observed in figures 6.1 and 6.2 (see section 6.2.1). Further, the observed differences in the behaviour of these emission lines are larger where $[O_2]$ is reduced more strongly in the presence of a wafer (compare figures 6.1 and 6.2 with the $[O_2]$ results of figures 5.7c to 5.12c on p.164a ff). This shows clearly that the anomalous behaviour of emission from the 3p $^2P°$ states of F atoms is linked to O_2 or O, and is not due to direct interactions with the wafer surface. It appears that *the 3p $^2P°$ states are caused to have a greater population in the presence of O_2*. Relevantly, we recall from section 5.3.2 that the wafer is found not to be directly responsible for the reduction in [F] in the presence of a wafer, rather that it is due to reactions in the gas phase and at the chamber walls. It might therefore be expected that the wafer is similarly not directly responsible for the anomalous F atom emission behaviour.

6.3 MECHANISMS TO EXPLAIN THE ANOMALOUS BEHAVIOUR OF THE 3p $^2P°$ STATES OF F

We have shown that the 3p $^2P°$ states are caused to have a greater population in the presence of O_2. The fluorescent lifetimes of excited F atoms are very short (typically $\approx$ 10 ns [127]) compared with the time between collisions in the plasma (of the order of 1 μs at 85 mTorr and 298 K). Thus once formed, the observed excited states of F atoms will emit a photon before being quenched by collisions, so gas molecules do not interact directly with the excited F atoms. The effect of O_2 (or O) must therefore be to increase the rate at which 3p $^2P°$ F atoms are formed, while leaving all other states unaffected. We now consider some mechanisms which could explain how this may come about.

6.3.1 MECHANISM INVOLVING INELASTIC ELECTRON COLLISIONS ALONE

We have shown in previous sections (4.5.1.2 and 5.3.2) that the concentration of F is affected by $[O_2]$ because O atoms compete with F atoms for surface sites. We

showed that a change in $[O_2]$ also leads to a change in [F]. We now explore the possibility that this effect is also responsible for the anomalous behaviour of the emission from the $3p\ ^2P°$ states of F atoms when $[O_2]$ changes. In order to test this hypothesis, we use the same model of the excitation processes for the production of excited F atoms as that used by Field et al [126], in which inelastic collisions with electrons are the only production mechanism for excited F atoms. We show that our experimental results cannot be explained by this simple model.

We now describe briefly the model used by Field et al [126]. It is assumed that excited F atoms are formed only by excitation through inelastic collision of electrons with the reservoir of ground state ($2p^5\ ^2P°$) or lowest metastable ($3s\ ^4P$) F atoms in the plasma. Because excitation processes involving electrons do not follow simple dipole selection rules, spin changing excitation may occur with significant cross section (as in the well-known electron impact excitation of triplet states of N_2 in the earth's atmosphere [128]). Thus $3p\ ^2P°_{1/2}$ and $3p\ ^2P°_{3/2}$ states of F may be populated from both $2p^5\ ^2P°$ and $3s\ ^4P$ reservoirs of F atoms. This is illustrated schematically in figure 6.6 below.

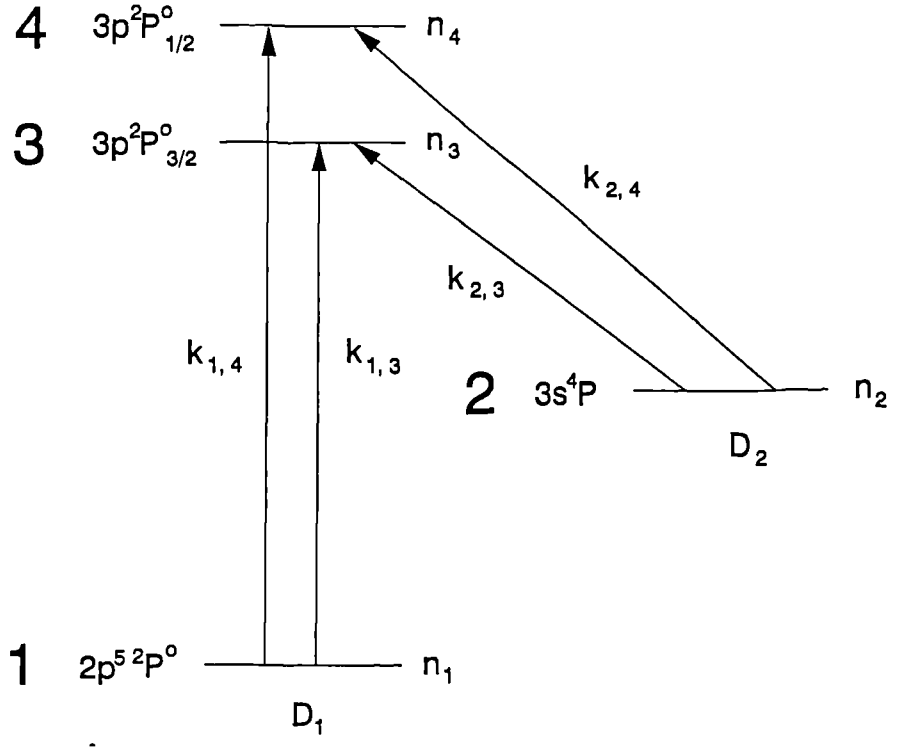

Figure 6.6. Excitation processes in electron + F collisions. See text for an explanation of the symbols used. (Adapted from reference 126).

The simplifying assumptions are made firstly that it is not necessary to take into account the multiplet character of the $2p^5\ ^2P°$ and $3s\ ^4P$ reservoirs of population, and secondly that rate coefficients rather than cross-sections for excitation are appropriate to this analysis (cp the dissociation rate constants described in section 4.4). Effective first order rate coefficients for electrons to excite an atom from level i to level j are written as $k_{i,j}\ s^{-1}$. The initial populations of $2p^5\ ^2P°$, $3s\ ^4P$, $3p\ ^2P°_{1/2}$ and $3p\ ^2P°_{3/2}$ are n_1, n_2, n_3 and n_4 respectively. D_1 and D_2 are the factors by which the populations of $2p^5\ ^2P°$ and $3s\ ^4P$ change when $[O_2]$ changes. It can readily be shown that the ratio of the $3p\ ^2P°_{1/2}$ emission intensity before and after a change in $[O_2]$ is given in the steady state by

$$(k_{1,4}\, n_1 + k_{2,4}\, n_2) / (k_{1,4}\, D_1\, n_1 + k_{2,4}\, D_2\, n_2) \qquad (1)$$

and that of $3p\ ^2P°_{3/2}$ by

$$(k_{1,3}\, n_1 + k_{2,3}\, n_2) / (k_{1,3}\, D_1\, n_1 + k_{2,3}\, D_2\, n_2) \qquad (2)$$

As we showed experimentally in section 6.2.2 earlier, the emission intensity from the $3p\ ^2P°_{1/2}$ and $3p\ ^2P°_{3/2}$ change by different factors when $[O_2]$ changes, i.e. the values of (1) and (2) are not equal (see figure 6.5). Using the above model, the only general grounds for the difference in the values of (1) and (2) is that D_1 and D_2 are not equal, or in other words that the populations of $2p^5\ ^2P°$ and $3s\ ^4P$ are affected to a different extent by a change in $[O_2]$. Similar arguments can be used to explain the difference in behaviour of emission from the $3p\ ^2P°$ states from that of all the other observed states of F, again with the conclusion that D_1 and D_2 are not equal. However, questions about the validity of the above model arise when it is applied to levels which exhibit the same behaviour, as we now discuss.

Expressions (1) and (2) can be applied to any pair of levels 3 and 4. We now apply the model to the case where levels 3 and 4 exhibit the same behaviour as $[O_2]$ changes, i.e. where (1) and (2) are equal (true for all observed levels of F except for

$3p\ ^2P°$, as we showed earlier in section 6.2.1). Simple algebra shows that if D_1 and D_2 are not equal, as was concluded above, then (1) and (2) can be equal only if one of (a), (b) or (c) below are true.

(a) $k_{1,4} = k_{1,3}$ and $k_{2,4} = k_{2,3}$,

(b) $k_{2,4}\, n_2 \ll k_{1,4}\, n_1$ and $k_{2,3}\, n_2 \ll k_{1,3}\, n_1$

(c) $k_{2,4}\, n_2 \gg k_{1,4}\, n_1$ and $k_{2,3}\, n_2 \gg k_{1,3}\, n_1$

Point (a) states that electron excitation rates from $2p^5\ ^2P°$ and $3s\ ^4P$ to any pair of levels 3 and 4 (i.e. all levels which show the same behaviour) are equal. Processes of electronic excitation tend to occur through resonances at specific electron energies. Given the range of different energies of the observed states of F, it would therefore seem unlikely that the emission lines would show the same behaviour if the electron energy distribution function were to change (if, for example, the power were altered). However, as mentioned already, our results have shown clearly that all levels except the $3p\ ^2P°$ levels behave the same for all the conditions studied in this work. Point (a) must therefore be rejected as untenable.

Points (b) and (c) state that excited states of F are populated from just one of the $2p^5\ ^2P°$ or $3s\ ^4P$ reservoirs but not from the other. It seems unlikely that the metastable $3s\ ^4P$ level could be the main source of excited atoms since it too must initially be populated from the ground state $2p^5\ ^2P°$ level. The most likely explanation for the similar behaviour of most states of F is therefore that they are formed exclusively by inelastic electron collisions with ground state $2p^5\ ^2P°$ F atoms (point (c)), and not from metastable $3s\ ^4P$ F atoms (point (b)). This also suggests therefore that the steady state population of the $3s\ ^4P$ level, n_2, is small, in which case, expressions (1) and (2) become

$$(k_{1,4}\, n_1) / (k_{1,4}\, D_1\, n_1) \qquad (1a)$$

$$(k_{1,3}\, n_1) / (k_{1,3}\, D_1\, n_1)\ . \qquad (2a)$$

Thus the change in F atom emission when $[O_2]$ changes depends only on the value of D_1 (D_2 is now irrelevant since n_2 is small). This explains the similar behaviour of most states of F.

The arguments used earlier to explain the anomalous behaviour of the $3p\ ^2P°$ states of F are now no longer valid. Clearly there is an additional process which can selectively populate the $3p\ ^2P°$ level in the presence of O_2 while leaving all the other observed states of F unchanged. One possible mechanism which could cause this effect is discussed in section 6.3.2 below.

At this point, we note that the above findings mean that the emission intensity from any state of F except that of the $3p\ ^2P°$ states will be proportional to the concentration of ground state F atoms when the experimental conditions change, provided that the electron density and energy distribution remain constant. This is likely to be true if the power and pressure remain constant (see section 4.4). This justifies the use throughout this work of the 6856 Å emission line (from the $3p\ ^4D°_{7/2}$ state) to monitor [F] (sections 4.5.1.2, 5.2.2 and 7.4.3).

6.3.2 MECHANISM INVOLVING NEAR RESONANT ENERGY TRANSFER

As stated above, an additional excitation process is required which can selectively populate the $3p\ ^2P°$ states of F in the presence of O_2, while leaving all other states unaffected. One process which may produce this effect is near resonant energy transfer. This is a process whereby an excited state of one species may transfer the excitation to another species. This can occur provided both species possess an energy level of almost the same energy. The process can be expressed as

$$A^* + B \longrightarrow A + B^* .$$

The probability of such a transition is given by [129]

$$\text{Transition probability} \propto \exp(-\delta E / kT) \qquad 6.1$$

where δE is the energy difference between the two levels. At perfect resonance (i.e. where $\delta E = 0$) the rates of such processes are very fast, and are typically two orders of magnitude faster than "gas kinetic" [130]. The anomalous behaviour of emission from the $3p\ ^2P^\circ$ states of F can therefore be explained if there exists an excited state of O_2 or O at an appropriate energy to excite F atoms to the $3p\ ^2P^\circ$ states. We now construct a simple model for this process, and then show that an excited state of O_2 exists which can be used to explain the anomalous behaviour of emission from the $3p\ ^2P^\circ$ states. We also present calculations which correctly predict the relative magnitude of the effect for the $3p\ ^2P^\circ_{1/2}$ and $3p\ ^2P^\circ_{3/2}$ states.

We assume that the $3p\ ^2P^\circ$ levels can be populated from either the $2p^5\ ^2P^\circ$ and $3s\ ^4P$ reservoirs of F atoms by collisional energy transfer from excited O or O_2 (although we note that excitation from the $2p^5\ ^2P^\circ$ ground state is more likely since the results of section 6.3.1 indicated that the population of $3s\ ^4P$ is very small). For the O atom, no suitable state exists which can excite F atoms to either of these states. However, for the O_2 molecule, there exists an excited electronic state which lies very close in energy to the $3p\ ^2P^\circ$ states of F [131], [36]. This state of O_2 has been designated $^1\Phi_u$ [132]. Although there remains some doubt about this assignment, we will adopt it here. O_2 molecules in this $^1\Phi_u$ state can therefore excite F atoms from the $2p^5\ ^2P^\circ_{3/2}$ ground state to both the $3p\ ^2P^\circ_{3/2}$ and $3p\ ^2P^\circ_{1/2}$ states. The relevant levels of F and O_2 are shown below in figure 6.7, and the proposed resonant energy transfer processes are marked by dotted arrows. The rate coefficients for these processes are k_1 for excitation of the $3p\ ^2P^\circ_{3/2}$ level of F, and k_2 for excitation of the $3p\ ^2P^\circ_{1/2}$ level of F.

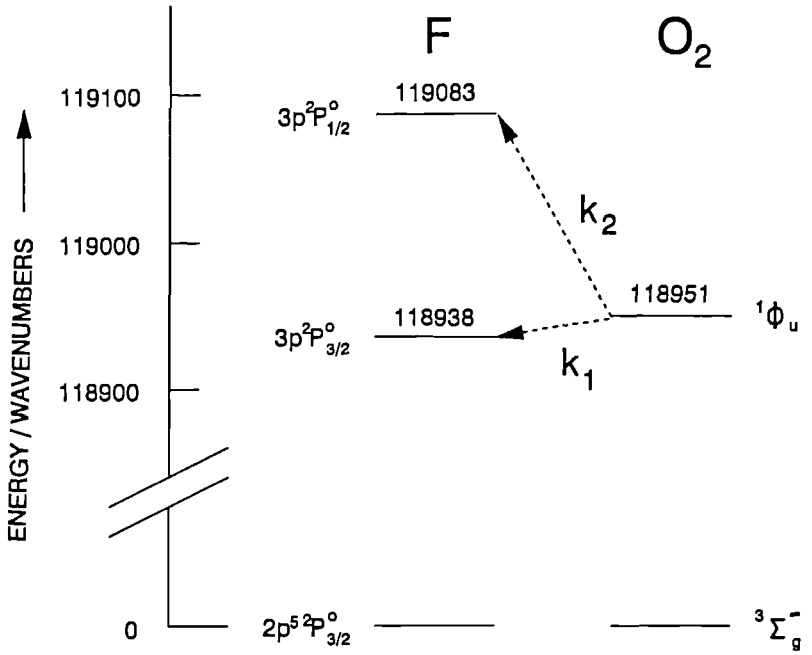

Figure 6.7. Energy levels of F and O_2 relevant to the process of resonant energy transfer from $(^1\Phi_u)$ O_2 to $(2p^5\ ^2P_{3/2})$ F, causing population of the $3p\ ^2P^\circ_{3/2}$ and $3p\ ^2P^\circ_{1/2}$ levels of F atoms. These processes are shown by dotted arrows, and have rate coefficients k_1 and k_2 respectively.

These resonant energy transfer processes can be written as below.

$$(^1\Phi_u)\ O_2\ (v = 0)\ +\ (2p^5\ ^2P_{3/2})\ F \longrightarrow (^3\Sigma^-_g)\ O_2\ (v = 0)\ +\ (3p\ ^2P^\circ_{(1/2\ \&\ 3/2)})\ F$$

The rotational levels of the $^3\Sigma_u$ and $^1\Phi_u$ states of O_2 mean that there are many possible rotational transitions which O_2 may undergo within this electronic transition. This results in a closely-spaced manifold of possible transition energies, centred on 118951 cm^{-1}, for the quenching of the $(^1\Phi_u)$ O_2 by collision with $(2p^5\ ^2P_{3/2})$ F atoms. The energy differences δE_1 and δE_2 associated with k_1 and k_2 will therefore also have a spread of energies, centred on 13 cm^{-1} and 132 cm^{-1} respectively. Taking δE_1 = 13 cm^{-1} and δE_2 = 132 cm^{-1}, we can estimate the relative values of k_1 and k_2 using values for the respective transition probabilities calculated from equation 6.1

$$k_1 = k_{max} \exp(-\delta E_1 / kT) \approx 0.9\ k_{max}$$

$$k_2 = k_{max} \exp(-\delta E_2 / kT) \approx 0.5\ k_{max}$$

where k_{max} is the maximum rate for these processes, i.e. where $\delta E = 0$. It is clear that these energy transfer processes occur at close to perfect resonance. Assuming k_{max} is the same for both processes, then

$$(k_1 / k_2) \approx 1.8$$

and we see that excitation to $3p\ ^2P^\circ_{3/2}$ is predicted to be ≈ 1.8 times as efficient as excitation to $3p\ ^2P^\circ_{1/2}$. This number should also be independent of $[O_2]$. We can calculate an experimental value for this ratio using the results of figure 6.5 earlier. Using the equations determined by the logarithmic fit to the experimental data of figure 6.5, it can be shown that

$$(k_1 / k_2)_{expt} \approx 1.8 \pm 0.3$$

in agreement with the theoretical value above. The experimental value is also reasonably independent of $[O_2]$, as predicted. This agreement of theory and experiment lends support to the resonant energy transfer mechanism.

The lifetime of ($^1\Phi_u$) O_2. Although the $^1\Phi_u$ level of O_2 has the correct energy to explain the experimental observations, it must also have a sufficiently long lifetime in order to allow collisions with F before it decays or is quenched through other channels. The times between collisions in the plasma are of the order of 1 μs at 298 K and 85 mTorr, so the $^1\Phi_u$ level of O_2 must live for at least this length of time in order to undergo resonant energy transfer with F (although we note that cross sections for near resonant energy transfer are typical two orders of magnitude faster than "gas kinetic" [130], as mentioned earlier, so 1 μs is probably an overestimate of the necessary lifetime of ($^1\Phi_u$) O_2).

Unfortunately, very little information is available concerning the $^1\Phi_u$ state of O_2. As mentioned earlier, even the assignment is uncertain. There have been no measurements of the lifetime of this state reported in the literature. However, some

indication can be obtained, as follows. The $^1\Phi_u$ state of O_2 has been observed in absorption in a transition from the metastable $a^1\Delta_g$ level [132]-[134]. The observed absorption bands appear to be strong indicating an allowed transition. In this case, the radiative lifetime of ($^1\Phi_u$) O_2 would be expected to be short (probably $<$ 1 ns) because of the large energy of transition involved ($\approx$ 14 eV). The vibrational bands of the absorption spectra show alternate sharp and diffuse nature. This is unusual and cannot be explained, but the broadening mechanism is probably either autoionisation or predissociation [132], both of which would tend to shorten the lifetime of ($^1\Phi_u$) O_2. It appears from the available evidence that ($^1\Phi_u$) O_2 will decay rapidly before collisions can take place. However, there remains considerable uncertainty, and further work is necessary to determine the lifetime of this state.

6.4 SUMMARY OF THE MAIN CONCLUSIONS

(1) Optical emission from the 3p $^2P°$ states of F behaves differently from that of all the other states of F which we have observed in this work. Emissions from the two states of the 3p $^2P°$ spin-orbit doublet also show different behaviour from each other. This effect is shown to be dependent on [O_2] or [O] in the plasma.

(2) It appears that excited states of F are populated exclusively by a single inelastic electron collision with ground state 2p ^2P F atoms, except for the 3p $^2P°$ states which are also selectively populated by an additional process in the presence of O_2.

(3) It is proposed that the 3p $^2P°_{1/2}$ and 3p $^2P°_{3/2}$ states of F are populated by a process of resonant energy transfer during collisions between ground state 2p $^2P_{3/2}$ F atoms and O_2 molecules in the $^1\Phi_u$ state, in addition to population by electron collision processes.

CHAPTER 7

THE ETCHING OF SiGe ALLOY WAFERS USING CF_4 + 8 VOL % O_2 PROCESS GAS

7 THE ETCHING OF SiGe ALLOY WAFERS USING CF_4 + 8 VOL % O_2 PROCESS GAS

7.1 INTRODUCTION

Currently there is a great deal of interest in the study of the properties and processing characteristics of epitaxial SiGe alloys grown on silicon. This interest is based on the ability to tailor the band gap in these materials according to the requirements of a variety of novel electronic devices (see section 1.4). Dry etching of SiGe alloys will be required in the fabrication of such devices, so the study of the etching properties of SiGe alloys is of great importance.

At this time, very little is known about how the dry etching properties of SiGe alloys differ from the dry etching properties of Si and Ge. Oehrlein et al [135], [136] have recently presented results concerning the etching of SiGe alloy thin layers on Si(100) with a Ge content of up to $\approx$ mol 20 %, using fluorine-based chemistry (CF_4 and SF_6 process gas). They have demonstrated that the etch rate of SiGe alloy is greater than that expected from a simple model, in which Si and Ge atoms are removed independently from the surface at rates measured for the pure elements at the same plasma conditions. Even a model in which Ge atoms are removed infinitely quickly from the SiGe alloy surface significantly underestimated the etch rate of SiGe alloys. This novel fast etching behaviour was also found for chlorine- and bromine-based plasma etching (CF_2Cl_2 and HBr respectively) in that study, although the etch rate enhancement was less pronounced in these cases than for fluorine-based plasma etching. Using X-ray Photoelectron Spectroscopy (XPS) the post-etch SiGe alloy surface was studied. The SiGe surface was found to be enriched in Ge [135], [136] after etching in fluorine-based plasmas. This is contrary to expectation since Ge etches faster. In contrast, a Si-rich surface was found after etching in chlorine- and bromine-based plasmas. There are clearly some interesting effects occurring here.

In this work, we present the results of a combined QMS and OES study of the etching of SiGe alloy material using CF_4 + 8 vol % O_2 process gas. We have studied the etching of SiGe alloy layers with 33 and 67 mol % Ge content grown on Si(100), and we make a comparison with the Si and Ge wafer etching results of chapter 5. The purpose of this study is to understand better the etching properties of SiGe alloy material and how they differ from the etching properties of Si and Ge. We work initially on the basis that SiGe alloy material has the properties which are expected from a simple mixture of its Si and Ge component parts. By this we mean that Si and Ge atoms are removed from the SiGe alloy surface at the rates measured for the pure elements at the same conditions, and that the concentrations of gas phase species lie between those found over pure Si and Ge according to the proportions of Si and Ge in the SiGe alloy. We adopt this procedure in order to look for deviations which would indicate novel etching behaviour. Our results show that SiGe alloy material exhibits the expected etching behaviour within experimental error for all the conditions studied, except at conditions of low power, where novel fast etching behaviour is found.

Before we present the results, we first discuss the experimental difficulties which have been encountered in the study of SiGe etching properties, and then explain the choice of SiGe alloy layers studied and give details of the etching experiments performed.

7.2 EXPERIMENTAL DIFFICULTIES

During the study of the etching of Si and Ge wafers (chapter 5), the plasma was always allowed to reach the steady state before data were taken. This sometimes required etching for up to an hour or even longer (section 5.1). However, because the Si and Ge wafers used were very thick compared with the amount of material etched from the surface during each experiment, the nature of the substrate material did not change during etching and so the results were not affected. However, when etching thin SiGe alloy layers, there is the possibility that the SiGe alloy layer may be removed before the plasma has reached the steady state, thus distorting the results. SiGe alloy layers are expensive to grow, so it was

necessary to design the experiments so as to reduce the etching time required to reach the steady state and therefore to make more efficient use of the SiGe alloy material. For the purposes of the following discussions, we define the length of time before the steady state is reached, which we refer to as the weathering time, as the etching time necessary for the concentrations of all monitored species to approach to within 20 % of their steady state concentrations. We now discuss some of the factors which affect the weathering time and how the experiments were designed in order to reduce it.

In our experiments, the main cause of the long weathering time appears to be contamination by water vapour. This problem is well known in plasma systems and in vacuum systems in general [137]. Contamination occurs when vacuum systems are exposed to atmosphere because water vapour is present in the air at high partial pressures (typically 10 Torr). This means that each time a wafer is introduced to the plasma system for etching, water vapour is also admitted, despite the use of dry N_2 to vent the chamber. Water molecules adsorb strongly to surfaces because they are highly polar, and are therefore very persistent once present in the plasma chamber. The adsorbed water molecules are released slowly into the gas phase, assisted by the action of the plasma, and therefore affect the chemistry of the plasma system. Water contamination was minimised in our SiGe etching experiments by enclosing the entire plasma chamber inside a large polythene bag filled with dry N_2, which was flushed with a continuous fast flow of dry N_2 to exclude water vapour from the gas surrounding the chamber while the wafers were inserted. Wafers were then introduced into the chamber as quickly as possible through this N_2 jacket to minimise the time for which the chamber lid was raised. This expedient greatly reduced the problem of water contamination, although it could not eliminate it completely.

In order to recognise water contamination, the effect of water vapour on the composition of the plasma was characterised by deliberately leaving the chamber open to the air for longer than necessary when inserting a wafer. For Si etching under these circumstances, we typically observe high initial concentrations of CO, CO_2 and O_2, and low initial concentrations of C_2F_6, COF_2, CF_4 and SiF_4. In general CO, CO_2, C_2F_6 and

CF_4 are the slowest species to reach a steady concentration, and may continue to change in concentration for up to an hour or even more if care is not taken to exclude water. Some of this behaviour can be understood. CF_3 is known to react with adsorbed water molecules to produce CO [138], explaining the initially high [CO] and low [C_2F_6]. In addition, water is known to reduce the etch rate of Si [56], explaining the initially low [SiF_4]. The effects of water contamination have not however been studied in detail. For the purposes of this work, it was only necessary to characterise the effects it has on the plasma composition. This allowed water contamination to be recognised, making it possible to minimise those effects and hence reduce the weathering time. We now discuss some other factors which may affect the weathering time.

The gas phase reactions which are important in the plasma are very rapid and are therefore not likely to contribute significantly to the weathering time. However, it appears that changes in the nature of the surfaces of the chamber walls may have some influence in delaying the approach to the steady state. An example of this sort of behaviour was given in section 5.2.3.1, where we showed that [GeF_4] rises only slowly to the steady state value due to the need first to form a layer of Ge-containing species at the chamber walls. In addition, we showed in chapter 4 that wall processes have important influences in the plasma. Clearly when the plasma is first switched on, the steady state gas composition can not be reached until the species which adsorb at the chamber walls have adjusted to their steady state surface coverages. The following experimental procedure was therefore adopted in an attempt to speed up this process in order to further reduce the weathering time.

Having selected the experimental process conditions, a plasma was first run with NW present to begin the weathering process, and also to allow QMS and OES measurements to be made in order to check that the system was showing the same behaviour as in previous experiments which were performed under the same conditions. Then, half a Si wafer and half a Ge wafer were introduced into the chamber and etched together in the plasma until the steady state was reached. This was done to mimic as closely

as possible the chemical environment expected during the etching of SiGe alloy wafers to prepare the chamber for SiGe etching. Then the SiGe alloy etching experiments were performed.

By inserting wafers with minimum water contamination as described earlier, and using the experimental procedure described above, the weathering time was typically reduced to between 5 and 20 minutes depending on the process conditions (conditions of high flow rate and high power result in the shortest weathering times). The full experimental procedure is discussed in more detail in section 2.8.1.3.

7.3 THE CHOICE OF SiGe ALLOY MATERIAL AND THE ETCHING EXPERIMENTS PERFORMED

We now discuss the choice of SiGe alloy layer thickness and composition used for this etching study, and list the experiments which have been run. The rationale which we have applied was to cover the greatest possible parameter space, in terms of both the SiGe alloy layer composition and the plasma process conditions, This approach is adopted in order to characterise more fully this etching system, and to increase the chances of revealing any novel etching behaviour.

The thickness of the SiGe alloy layers was chosen to be thick enough to allow the plasma to reach the steady state before complete removal of the SiGe alloy layer. This choice was made with regard to the weathering time discussed above, and on the assumption that SiGe alloy etch rates would lie between those found for Si and Ge at the same process conditions. The conditions which result in the lowest etch rates also result in the longest weathering times (i.e. low flow rate and low power). Typical Si and Ge etch rates are between 500 and 3000 Å min^{-1} (figure 5.1 in section 5.2.1), and typical weathering times are between 5 and 20 minutes. A nominal SiGe alloy layer thickness of 2 μm was therefore chosen in order to allow the plasma to reach the steady state before the SiGe alloy layer is completely removed. These layers were grown by Molecular Beam Epitaxy (MBE, section 1.3.3.1) onto 3" Si(100) wafers by Dr. Chris Gibbings and Dr.

Chris Tuppen at British Telecom Laboratories, Martlesham Heath. During MBE layer growth, the wafer sample holder protects a $\approx$ 1 mm wide ring around the edge of the wafer from the molecular beam. This results in a small step which allowed the actual layer thickness to be measured later at Bristol using a surface profiler (see section 1.9.6) (see table 7.1).

SiGe alloy compositions with 33 and 67 mol % Ge content were chosen for study. Pure Si (0 mol % Ge) and pure Ge (100 mol % Ge) etching has already been discussed in chapter 5, so this choice of SiGe alloy compositions completes the study of the full composition range from 0 to 100 mol % Ge content. 7 wafers of each composition were grown. All 14 layers were thicker than the critical thickness for these compositions (see section 1.4), and therefore the SiGe alloy material comprising these layers is relaxed. We recognise that for many applications, e.g. for heterojunction bipolar transistors, SiGe alloy layers with low Ge content ($<$ 20 %) which are strained are of primary interest. However, strain has been shown to have no effect on the etching properties of SiGe alloys [136]. It was therefore considered to be of more interest to study the full range of SiGe alloy compositions rather than limit our investigations to a small range of compositions.

The experimental process conditions at which these SiGe alloy layers were etched are detailed in table 7.1, along with the composition and measured thickness of the SiGe alloy layers. Conditions of flow rate from 5 sccm to 50 sccm (experiment nos. 1, 2 and 3), pressure from 10 mTorr to 85 mTorr (experiment nos. 4, 5 and 1) and power from 20 W to 200 W (experiment nos. 6, 7 and 1) have been studied for both the 33 mol % Ge and the 67 mol % Ge content SiGe alloy layers. Pure Si and pure Ge wafers have previously been etched at each of these sets of conditions (chapter 5).

During each etching experiment, the plasma was monitored continuously by QMS in order to obtain species concentrations. In each case, the SiGe alloy layer was completely removed and etching was continued into the underlying Si substrate. This allowed the gas phase composition over SiGe alloy to be compared directly with that over Si by observing the changes in concentration of gas phase species as the substrate

no.	SiGe layer details		Experimental conditions	Results presented in figure
	mol % Ge content	Thickness / μm		
1	33 67	2.2 2.15	5 sccm, 100 W, 85 mTorr	7.1 7.2
2	33 67	2.35 2.2	20 sccm, 100 W, 85 mTorr	7.3 7.4
3	33 67	3.1 2.25	50 sccm, 100 W, 85 mTorr	7.5 7.6
4	33 67	2.2 2.1	5 sccm, 100 W, 10 mTorr	7.7 7.8
5	33 67	2.2 2.1	5 sccm, 100 W, 40 mTorr	7.9 7.10
6	33 67	2.1 2.1	5 sccm, 20 W, 85 mTorr	7.11 7.12
7	33 67	2.3 2.1	5 sccm, 200 W, 85 mTorr	7.13 7.14

Table 7.1. Details of the SiGe alloy layer thickness and composition. Also shown are the experimental conditions used to etch each layer.

composition changed from SiGe alloy to underlying Si. This also allowed the endpoint to be detected (i.e. when the SiGe / Si interface is reached), which was necessary in order to measure etch rates. SiGe alloy etch rates were found by dividing the layer thickness by the endpoint time determined by QMS. In addition, the sharpness of the changes in species concentration at the endpoint indicates the level of uniformity of the etching. By OES, the intensity of F atom emission at 6856 Å was measured before the endpoint was reached, as a measure of [F] over SiGe alloy. We now present the results of these studies.

7.4 THE RESULTS OF THE SiGe ALLOY ETCHING STUDIES

7.4.1 THE QMS RESULTS

The temporal QMS results are presented in figures 7.1 to 7.14, giving mole percentage compositions (marked as % composition on the ordinates of these figures) vs time for CF_4, O_2, C_2F_6, COF_2, CO_2, CO, SiF_4 and GeF_4. [F_2] is not presented because of unacceptable errors caused by a large background signal due to cracking of CF_4 parent molecules in the QMS ion source (see section 5.2.3). The time at which the plasma was switched on (at t = 0) and off is marked by arrows at the top of these figures, as is the endpoint time (see later). The method of converting raw QMS data to mole percentage compositions for these figures is described in section 2.9. We now discuss some qualitative features of these results. (A more detailed quantitative discussion will be given in section 7.5 later, after the etch rate, uniformity and OES results have been presented).

The problems of weathering discussed in section 7.2 earlier are illustrated clearly in figures 7.1 to 7.14 by the changes in species concentrations observed in the first few minutes as the steady state is approached. These changes are especially apparent from the [CO], [CO_2], [C_2F_6] and [CF_4] data, indicating contamination from adsorbed water molecules (section 7.2). The more abrupt changes in species concentration (especially in [SiF_4] and [GeF_4]) during etching indicate that the endpoint has been reached. In all cases, the concentration changes at the endpoint occur over several minutes, indicating non-

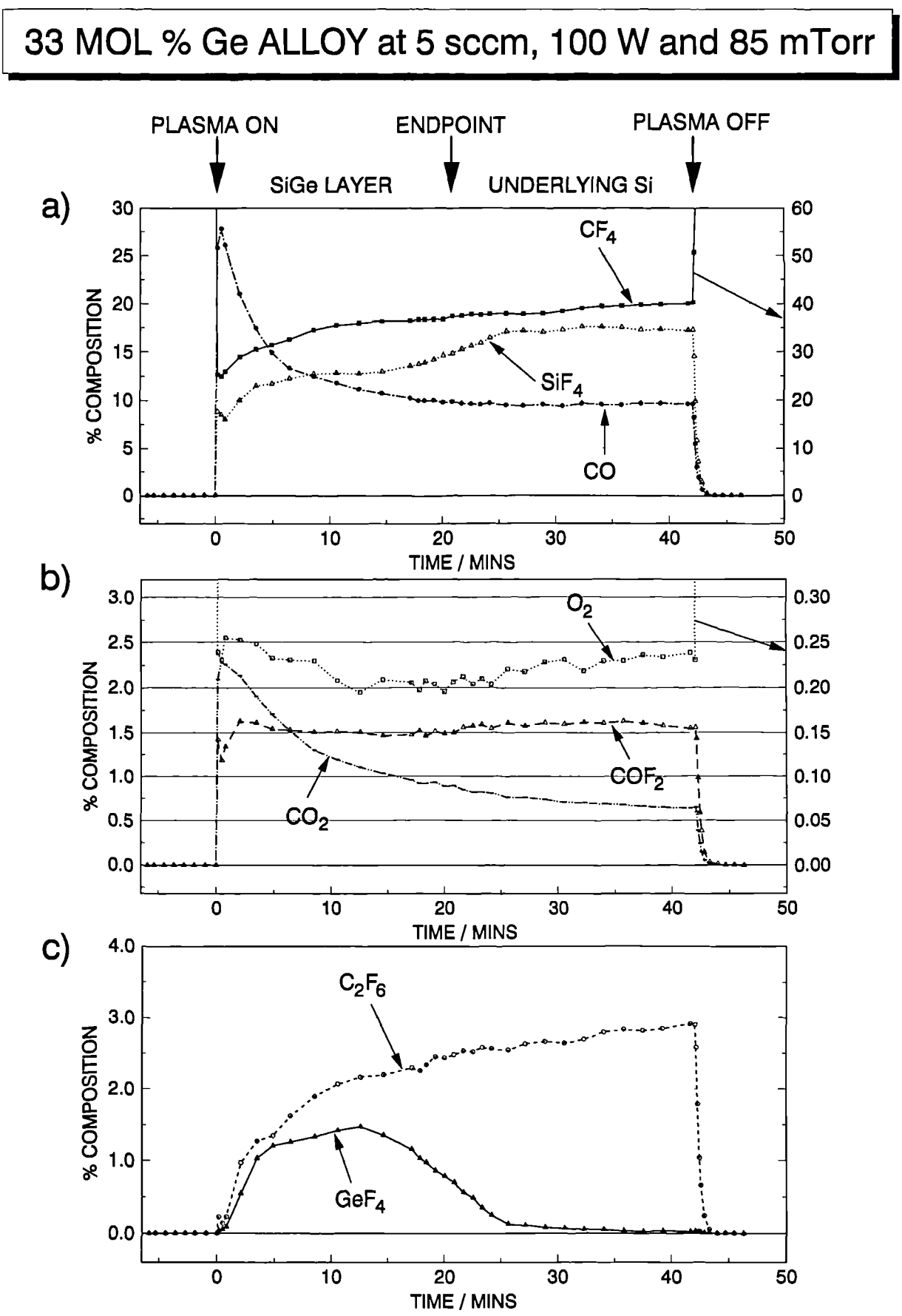

Figure 7.1. Graphs showing the temporal variation of species concentrations measured by QMS during the etching of a SiGe alloy layer with 33 mol % Ge content on Si using CF_4 + 8 vol % O_2 process gas at conditions of 5 sccm, 100 W and 85 mTorr.

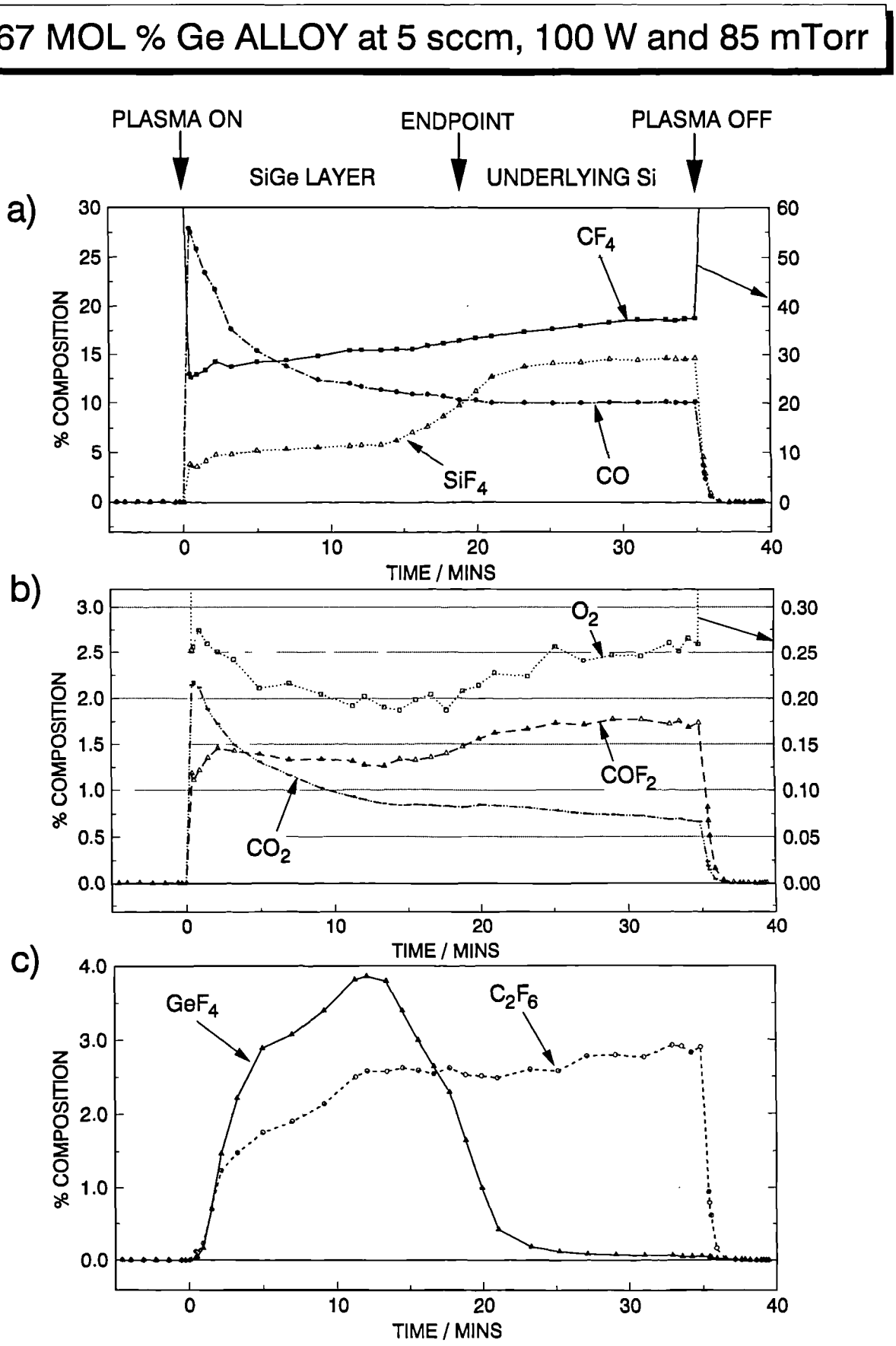

Figure 7.2. Graphs showing the temporal variation of species concentrations measured by QMS during the etching of a SiGe alloy layer with 67 mol % Ge content on Si using CF_4 + 8 vol % O_2 process gas at conditions of 5 sccm, 100 W and 85 mTorr.

33 MOL % Ge ALLOY at 20 sccm, 100 W and 85 mTorr

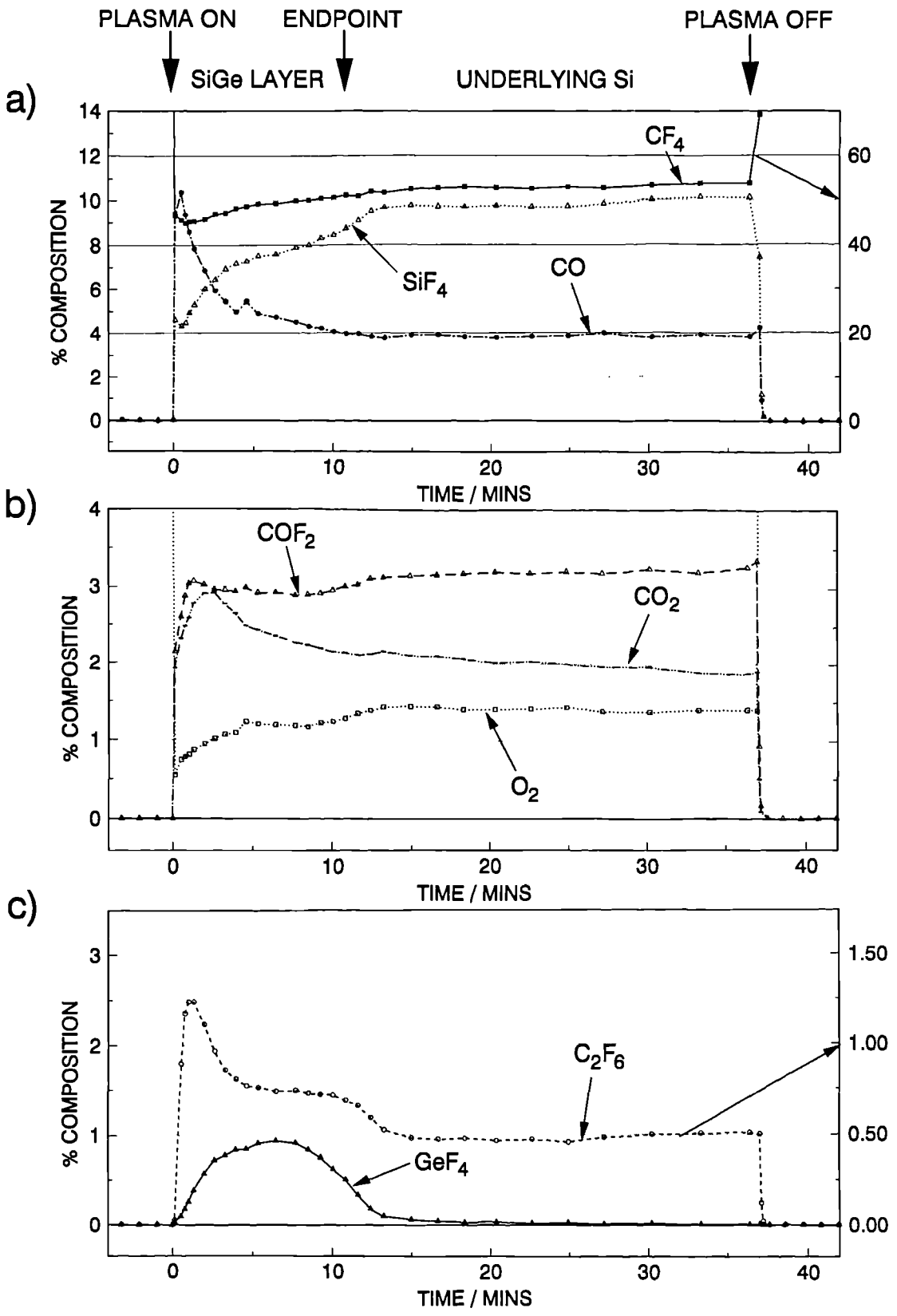

Figure 7.3. Graphs showing the temporal variation of species concentrations measured by QMS during the etching of a SiGe alloy layer with 33 mol % Ge content on Si using CF_4 + 8 vol % O_2 process gas at conditions of 20 sccm, 100 W and 85 mTorr.

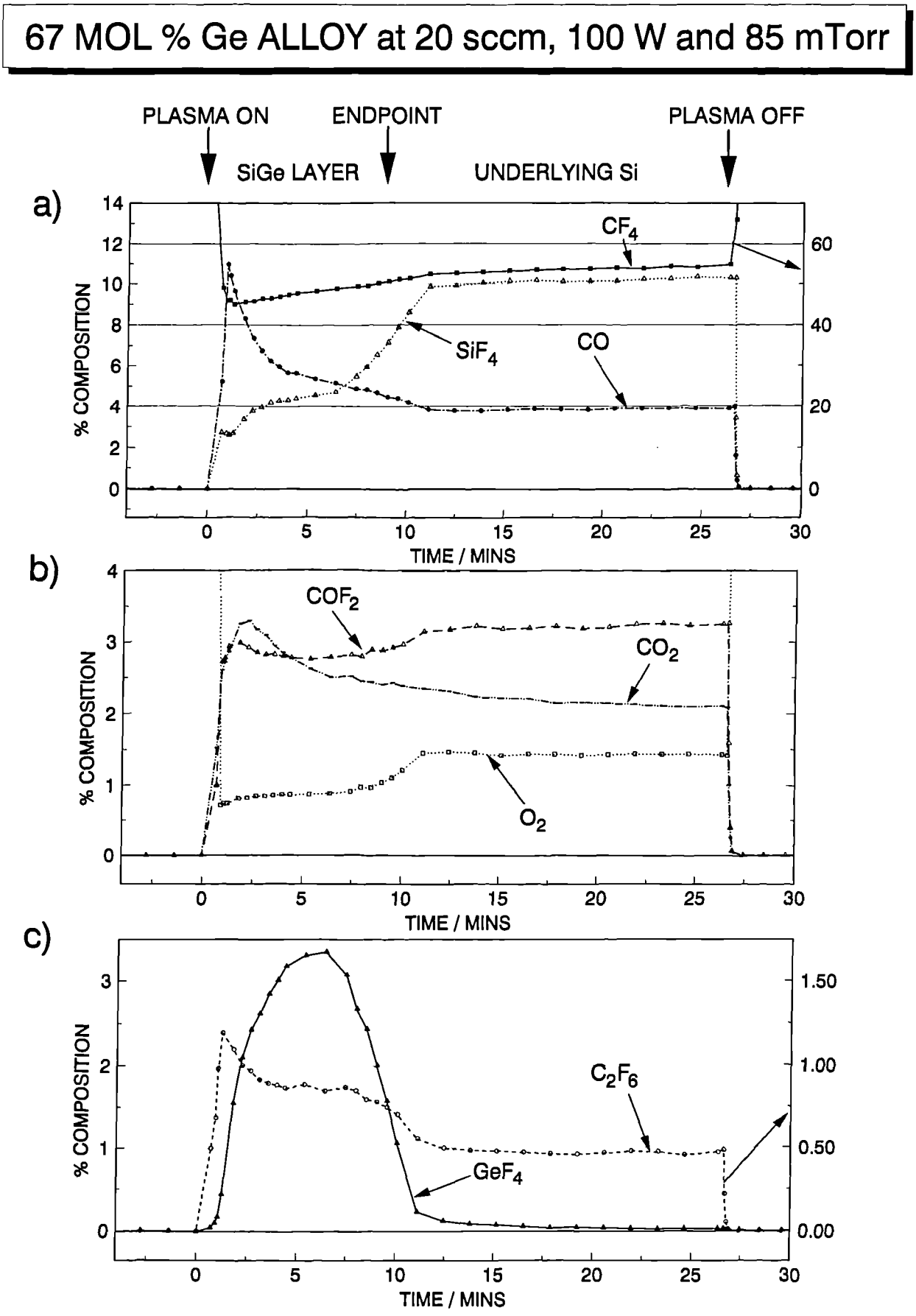

Figure 7.4. Graphs showing the temporal variation of species concentrations measured by QMS during the etching of a SiGe alloy layer with 67 mol % Ge content on Si using CF_4 + 8 vol % O_2 process gas at conditions of 20 sccm, 100 W and 85 mTorr.

33 MOL % Ge ALLOY at 50 sccm, 100 W and 85 mTorr

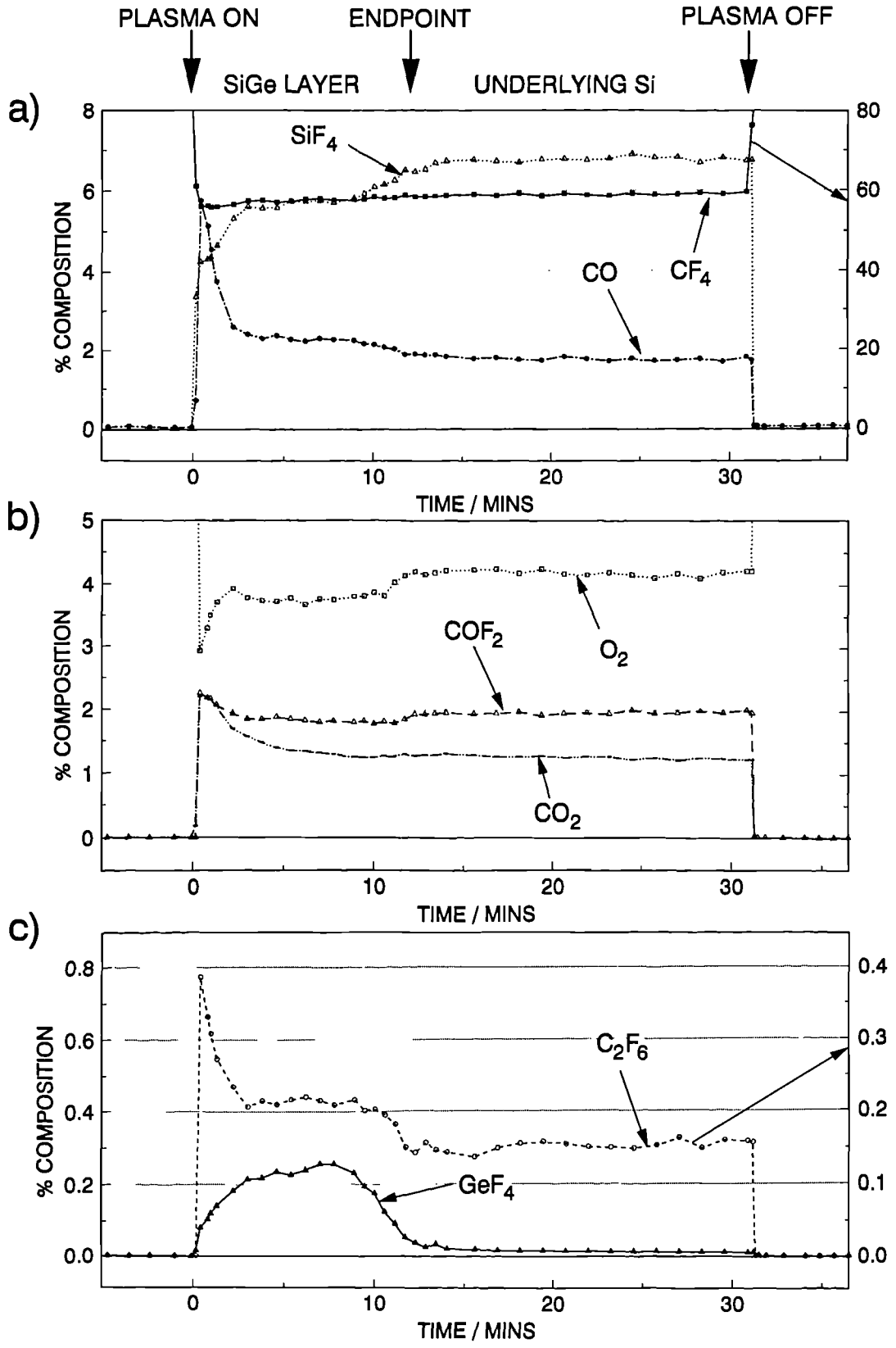

Figure 7.5. Graphs showing the temporal variation of species concentrations measured by QMS during the etching of a SiGe alloy layer with 33 mol % Ge content on Si using CF_4 + 8 vol % O_2 process gas at conditions of 50 sccm, 100 W and 85 mTorr.

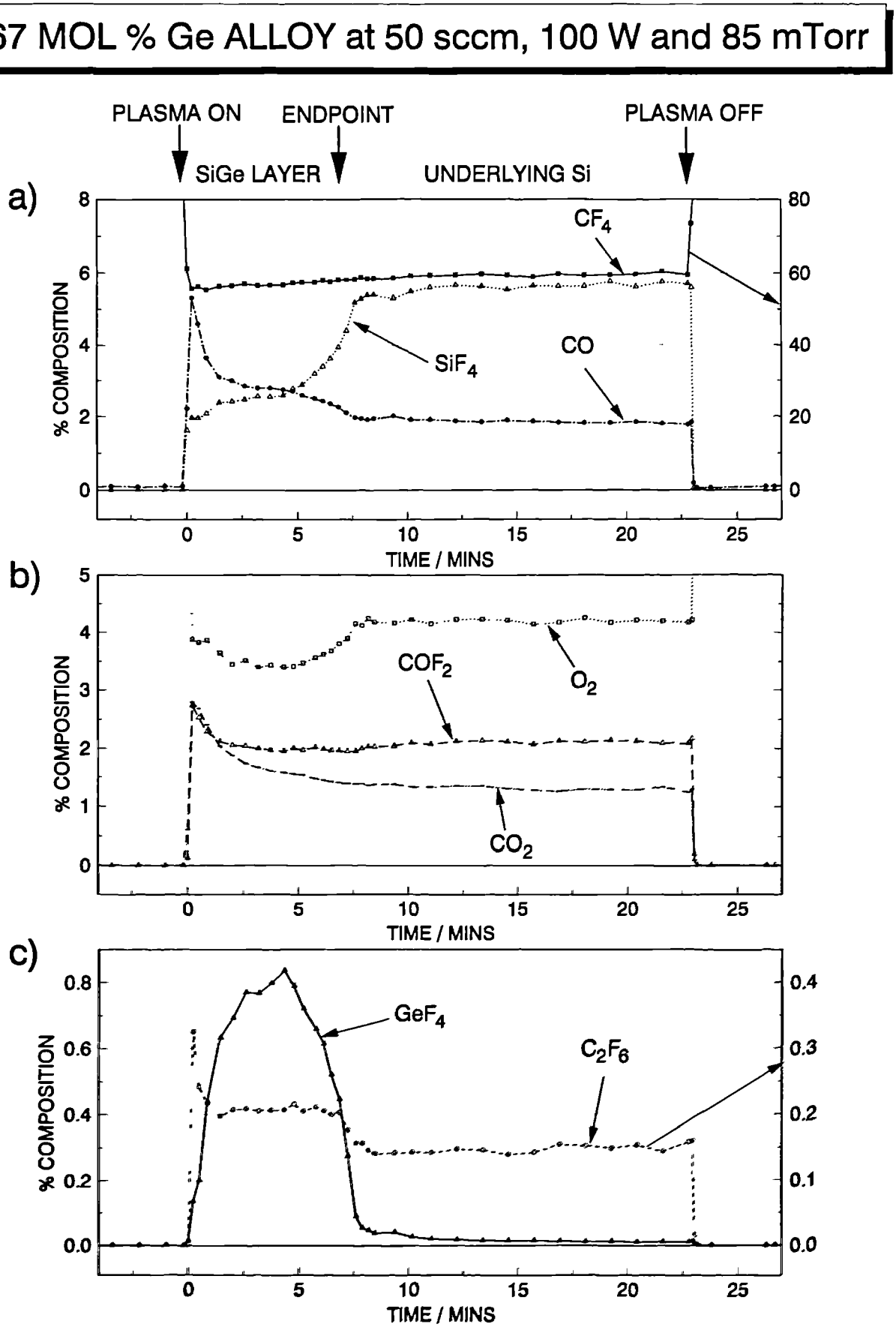

Figure 7.6. Graphs showing the temporal variation of species concentrations measured by QMS during the etching of a SiGe alloy layer with 67 mol % Ge content on Si using CF_4 + 8 vol % O_2 process gas at conditions of 50 sccm, 100 W and 85 mTorr.

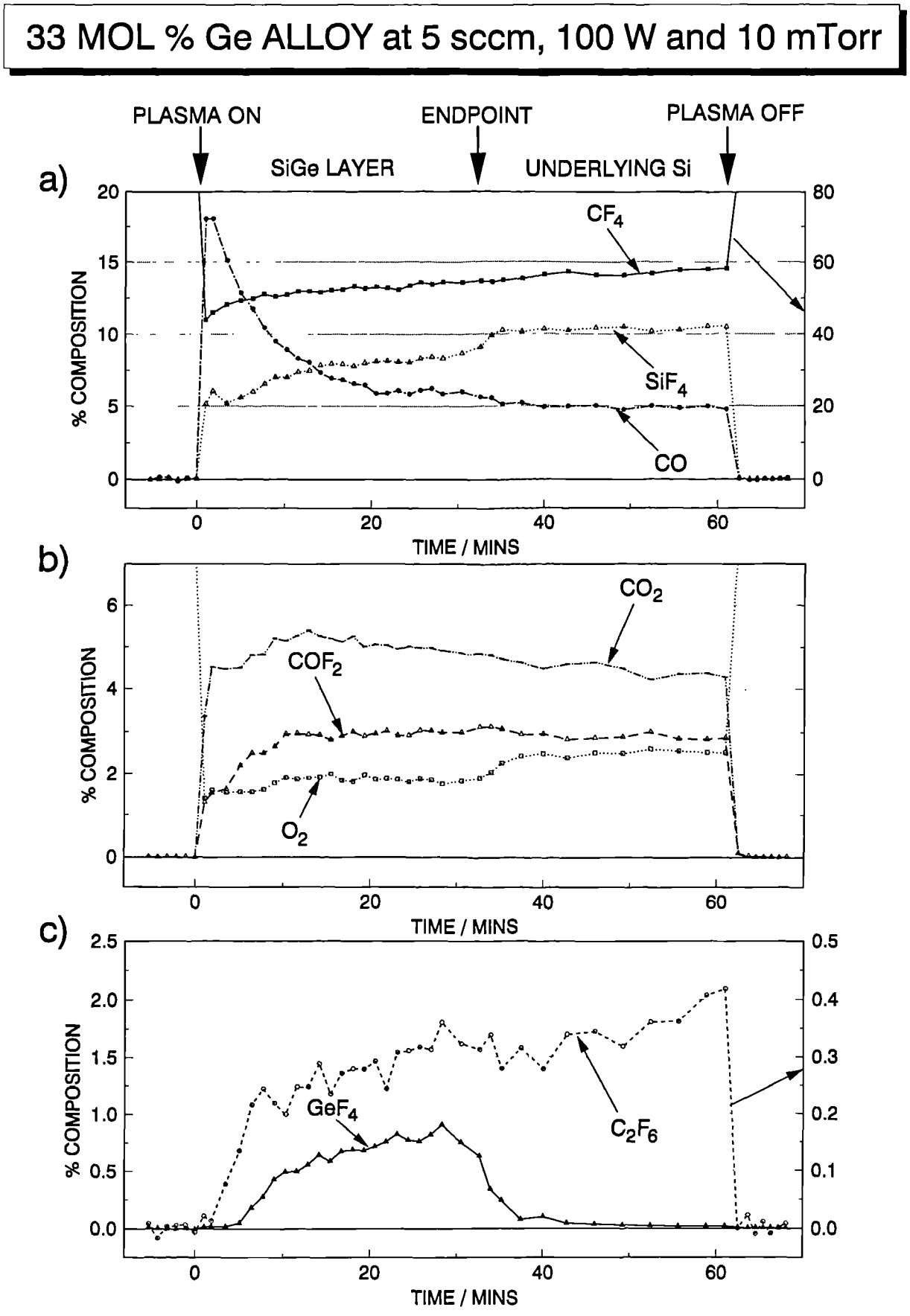

Figure 7.7. Graphs showing the temporal variation of species concentrations measured by QMS during the etching of a SiGe alloy layer with 33 mol % Ge content on Si using CF_4 + 8 vol % O_2 process gas at conditions of 5 sccm, 100 W and 10 mTorr.

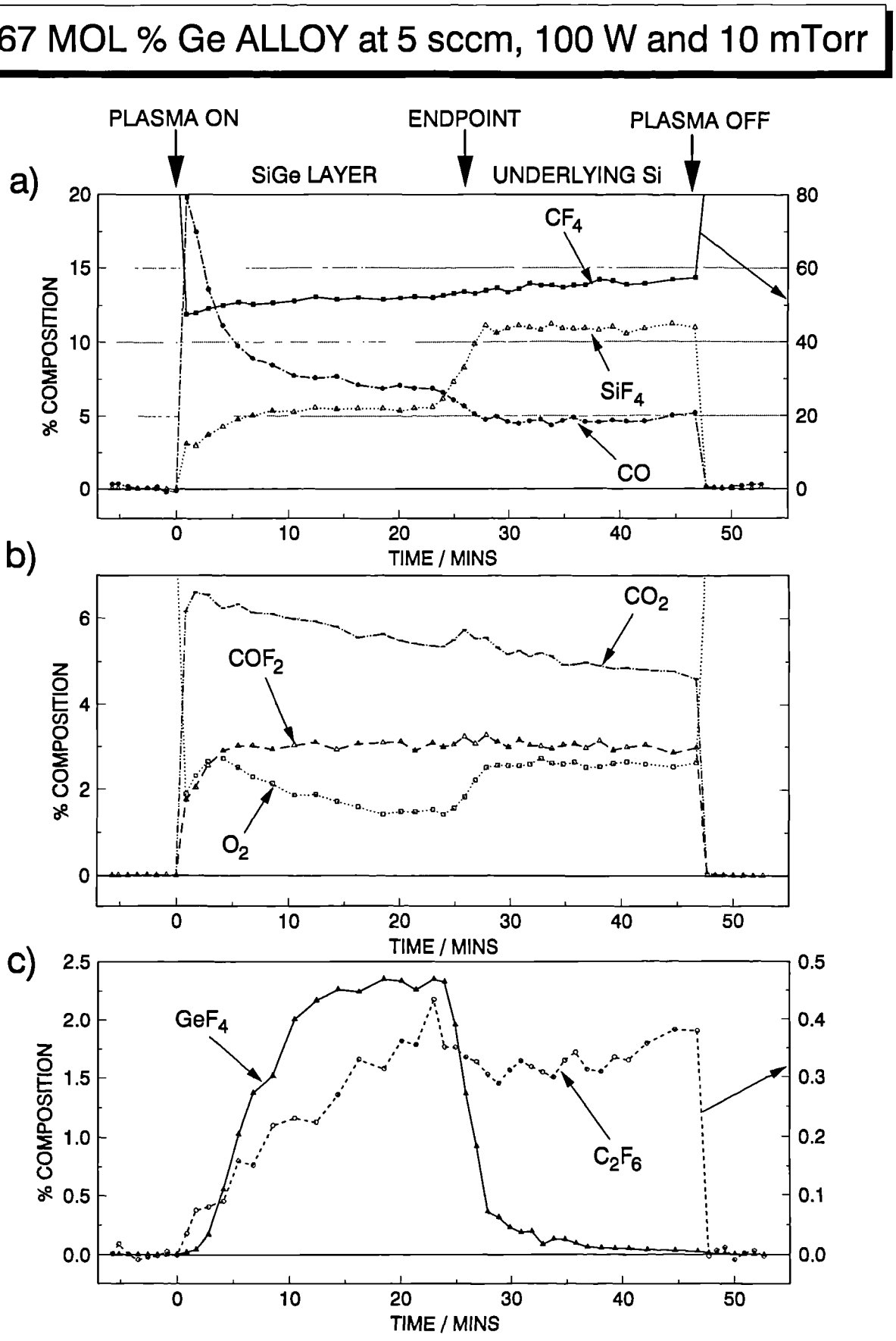

Figure 7.8. Graphs showing the temporal variation of species concentrations measured by QMS during the etching of a SiGe alloy layer with 67 mol % Ge content on Si using CF_4 + 8 vol % O_2 process gas at conditions of 5 sccm, 100 W and 10 mTorr.

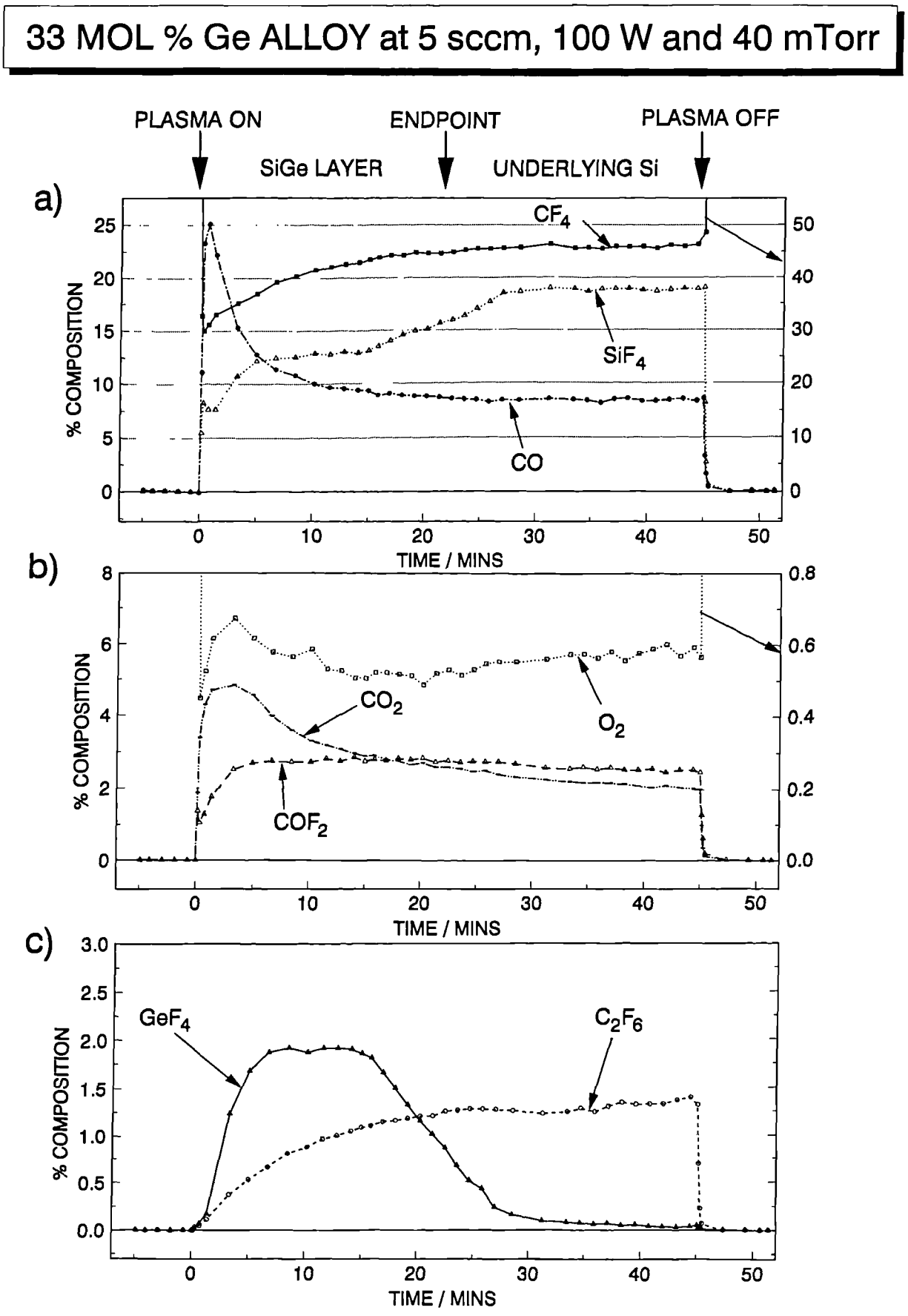

Figure 7.9. Graphs showing the temporal variation of species concentrations measured by QMS during the etching of a SiGe alloy layer with 33 mol % Ge content on Si using CF_4 + 8 vol % O_2 process gas at conditions of 5 sccm, 100 W and 40 mTorr.

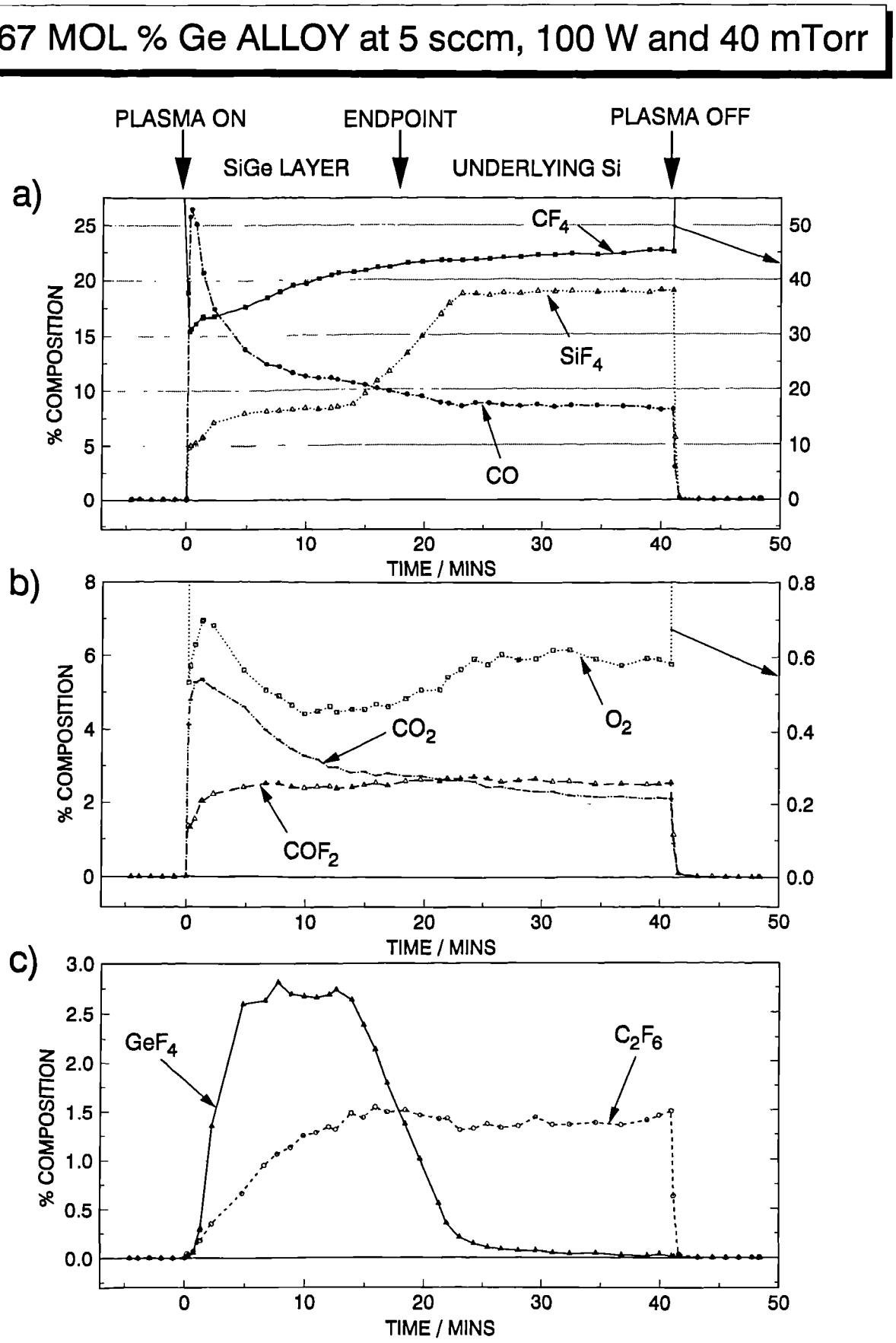

Figure 7.10. Graphs showing the temporal variation of species concentrations measured by QMS during the etching of a SiGe alloy layer with 67 mol % Ge content on Si using CF_4 + 8 vol % O_2 process gas at conditions of 5 sccm, 100 W and 40 mTorr.

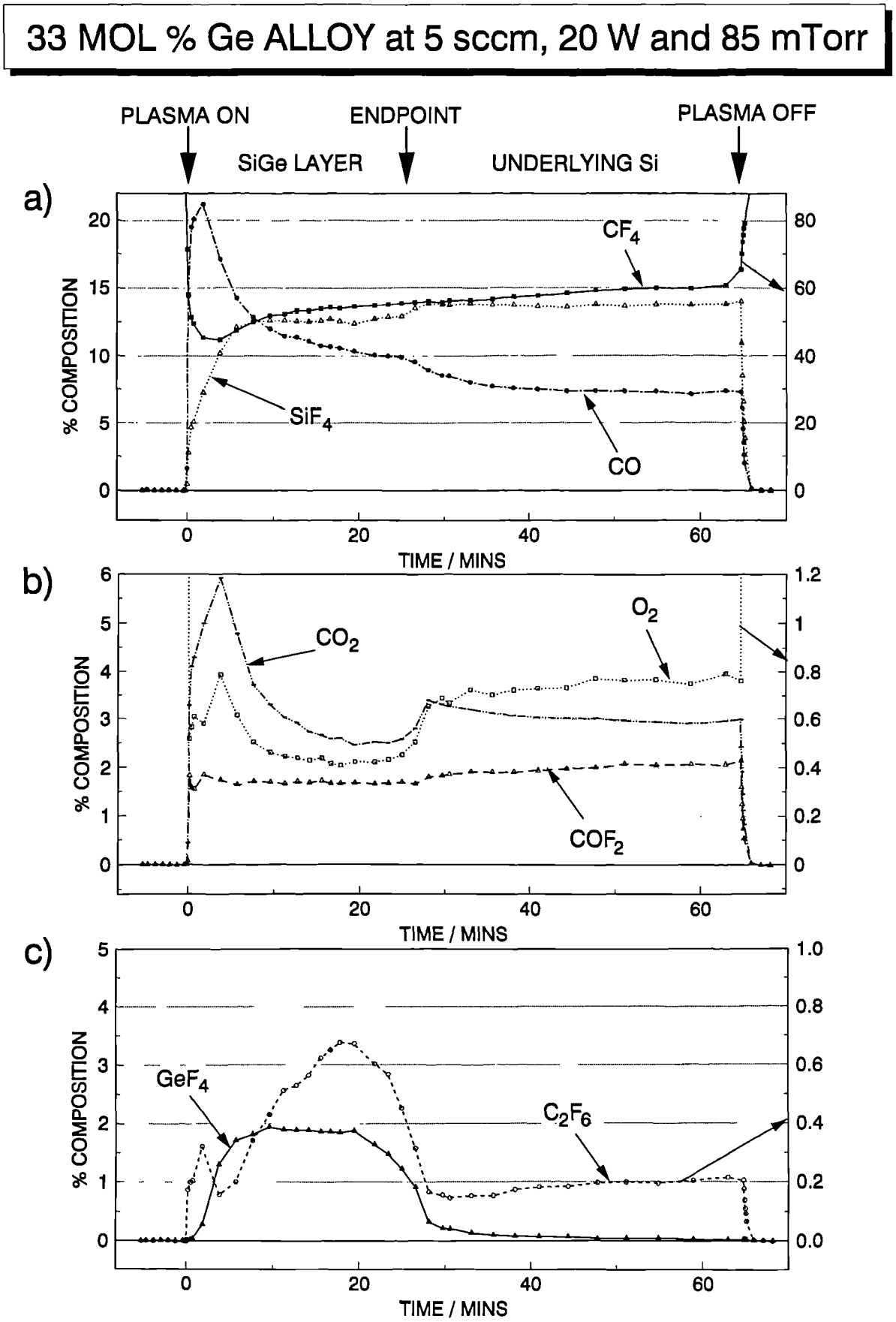

Figure 7.11. Graphs showing the temporal variation of species concentrations measured by QMS during the etching of a SiGe alloy layer with 33 mol % Ge content on Si using CF_4 + 8 vol % O_2 process gas at conditions of 5 sccm, 20 W and 85 mTorr.

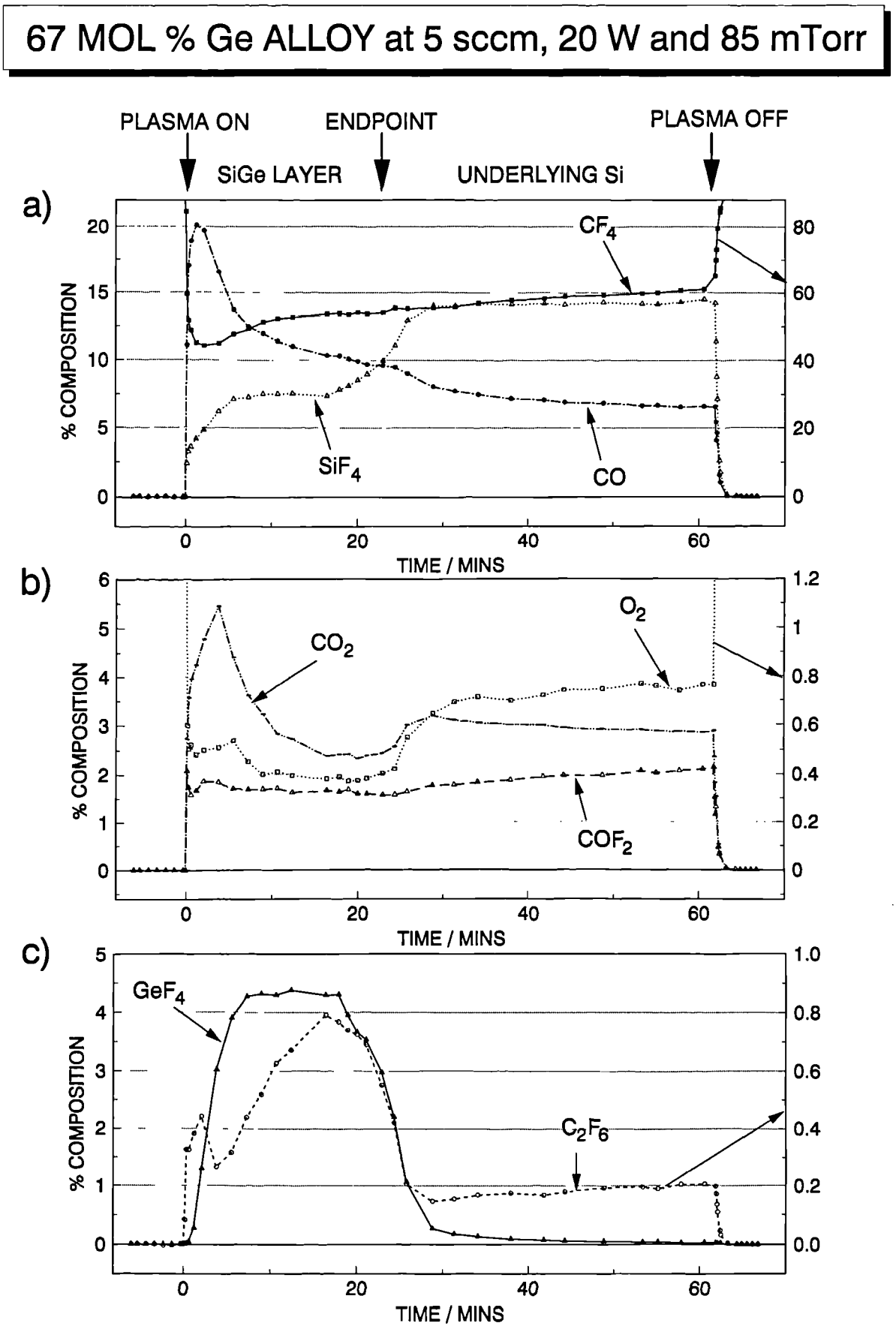

Figure 7.12. Graphs showing the temporal variation of species concentrations measured by QMS during the etching of a SiGe alloy layer with 67 mol % Ge content on Si using CF_4 + 8 vol % O_2 process gas at conditions of 5 sccm, 20 W and 85 mTorr.

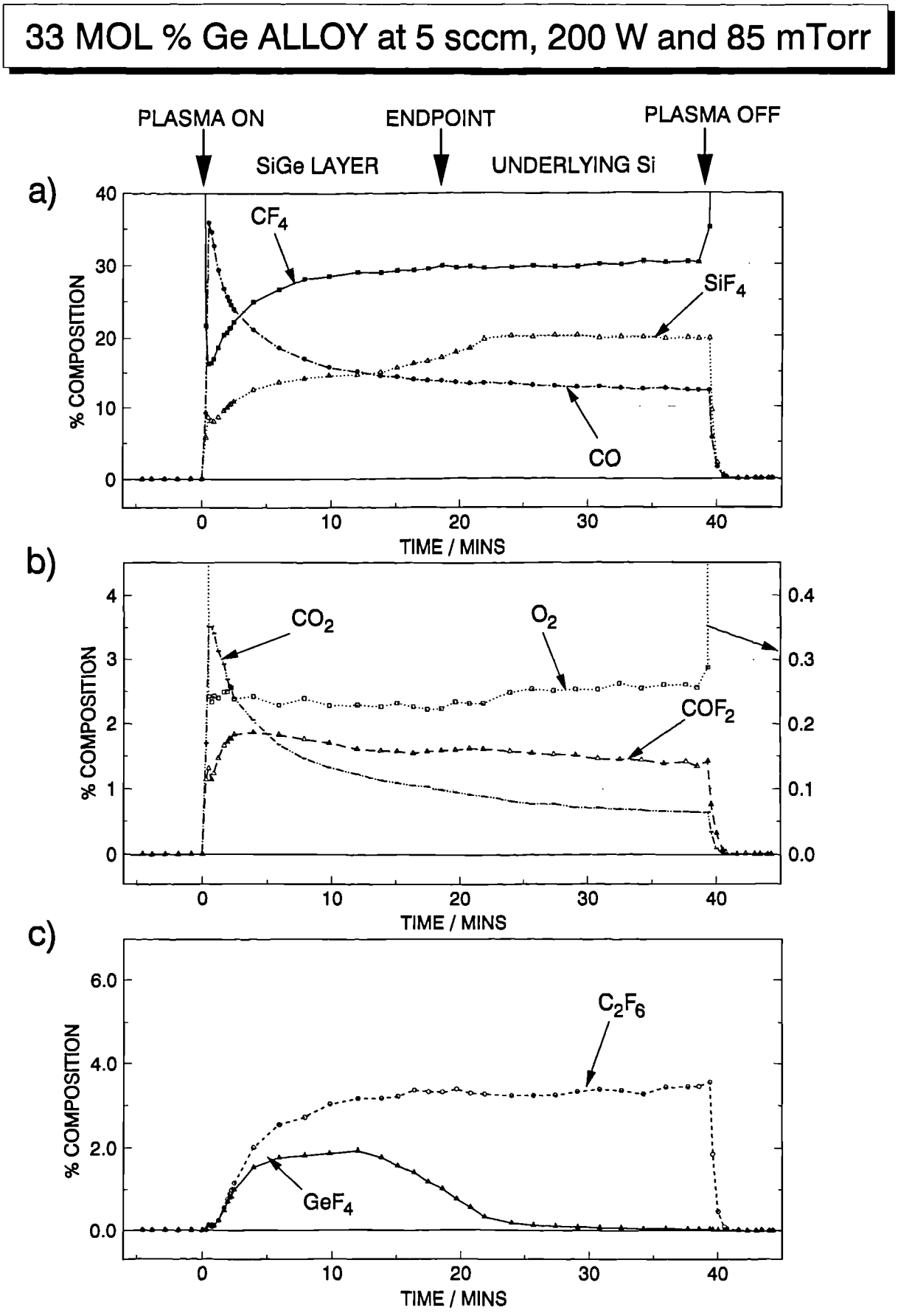

Figure 7.13. Graphs showing the temporal variation of species concentrations measured by QMS during the etching of a SiGe alloy layer with 33 mol % Ge content on Si using CF_4 + 8 vol % O_2 process gas at conditions of 5 sccm, 200 W and 85 mTorr.

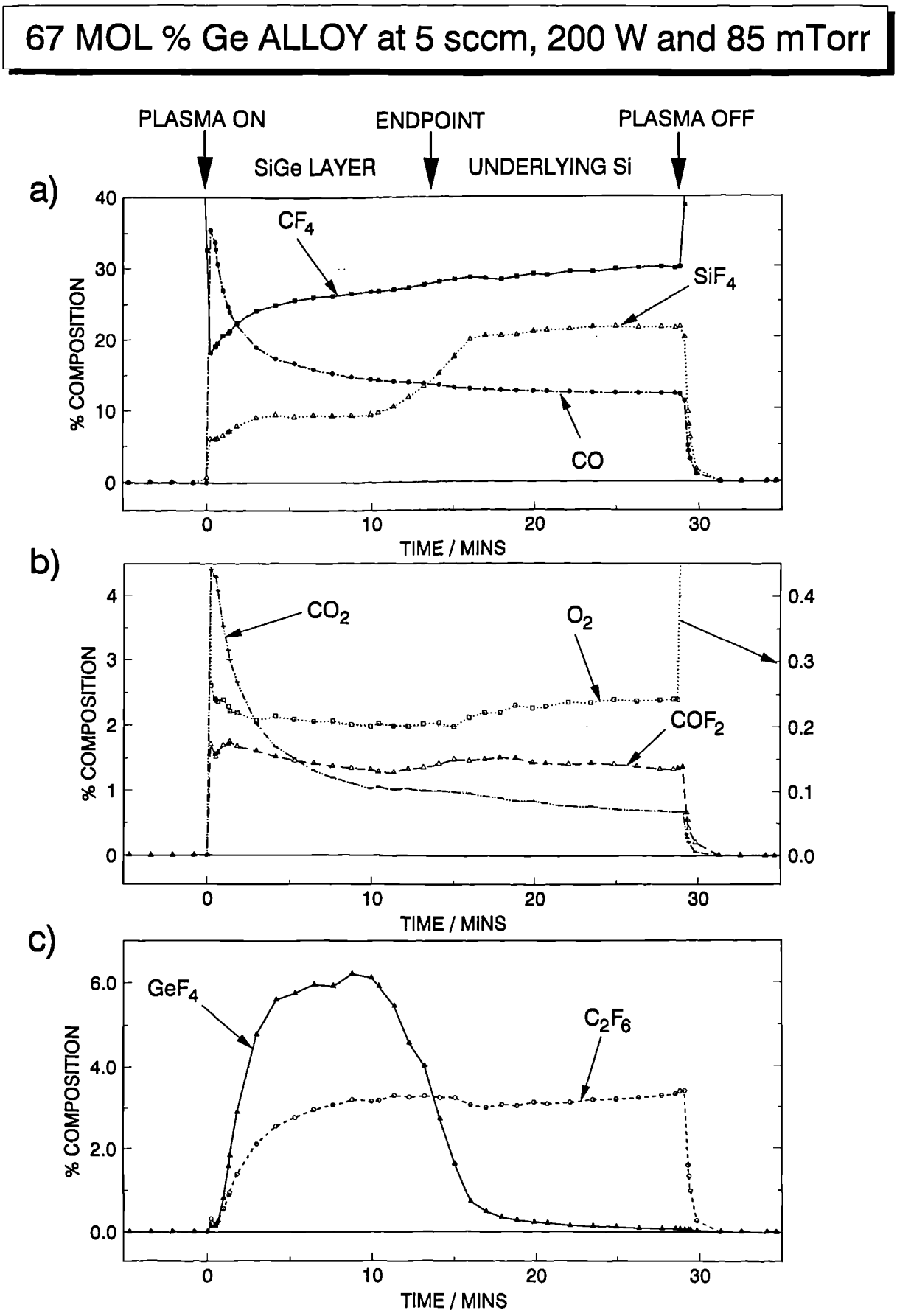

Figure 7.14. Graphs showing the temporal variation of species concentrations measured by QMS during the etching of a SiGe alloy layer with 67 mol % Ge content on Si using CF_4 + 8 vol % O_2 process gas at conditions of 5 sccm, 200 W and 85 mTorr.

uniform etching (see section 7.4.2). (Note that no process optimisation in order to achieve uniform etching was attempted in this work). In some cases it is clear that the plasma has not fully reached the steady state before the onset of the endpoint (meaning when $[SiF_4]$ and $[GeF_4]$ first begin to change as the underlying Si is exposed), despite the attempts to reduce the weathering time (see for example figure 7.1). In these cases, the measured concentrations of species over SiGe are not the true steady state concentrations in which we are interested. However, the changes in species concentration observed during the transition from SiGe to Si etching at the endpoint do allow a direct comparison of concentrations over SiGe with concentrations over Si to be made, so that even when weathering was incomplete, the data still convey useful information (see section 7.5).

An interesting feature of the results of figures 7.1 to 7.14 is that GeF_4 shows only a slow rise in concentration when the plasma is first switched on, whereas $[SiF_4]$ rises very quickly to $\approx$ 80 % of its steady state value. Clearly the slow rise of $[GeF_4]$ is not due to a delay in the onset of etching, because in that case, $[SiF_4]$ would show a similar slow rise. This phenomenon is attributed to the adsorption of GeF_2 at the walls, as described in section 5.2.3.1. This behaviour also results in a value for $[GeF_4]$ which is lower than expected over SiGe alloy because $[GeF_4]$ is still rising towards the steady state value at the endpoint (see section 7.5). After the endpoint is reached, the Ge-containing species present at the walls are removed as GeF_4. These adsorption phenomena may explain the Ge enrichment of the SiGe alloy surface after etching in fluorine-based plasmas which was observed by Oehrlein et al using XPS [135], [136]. Perhaps the adsorption of GeF_2 results in a steady state layer of fluorinated Ge-containing species adsorbed on the etching wafer surface which remains after the etching has stopped.

The endpoint time in the SiGe alloy etching experiments has been determined using the changes in $[GeF_4]$ and $[SiF_4]$ observed as the SiGe / Si interface is reached. The changes in $[SiF_4]$ and $[GeF_4]$ have been used in preference to other species because they are the only species which change consistently at the endpoint in all cases. Because of the poor etch uniformity, the endpoint time is not well defined. In order to avoid ambiguity,

we have arbitrarily chosen to define the endpoint time as the time after which the values for [SiF_4] and [GeF_4] over SiGe have undergone half the changes to their new values over the underlying Si. Values for endpoint times using [SiF_4] and [GeF_4] are obtained using the results of figures 7.1 to 7.14, and then averaged to obtain the final value. Endpoint times determined using [SiF_4] and [GeF_4] agree to within $\approx$ 4 %, indicating that the errors in the endpoint time are small.

The endpoint times have been used to calculate the etch rates of the SiGe alloy (section 7.4.2). In addition, the sharpness of the changes in [SiF_4] and [GeF_4] at the endpoint can be used to determine the level of uniformity of etching by calculating values for the uniformity factor (section 7.4.2). Endpoint detection is described in more detail in section 7.7 later.

Species concentrations over SiGe alloy have been obtained from the data of figures 7.1 to 7.14 using concentration readings which were taken just before the onset of the endpoint, as described in section 2.9.3. These concentrations are presented as a function of flow rate, pressure and power in figures 7.15 to 7.17, along with the results for pure Si and pure Ge taken from figures 5.7, 5.8 and 5.11 of section 5.2.3 for comparison. These results, and the temporal QMS data of figures 7.1 to 7.14 will be discussed in more detail in section 7.5 later, after we have first presented the etch rate, uniformity and OES results.

7.4.2 THE ETCH RATE AND UNIFORMITY RESULTS

The method of weight loss which was used in chapter 5 to measure etch rates of Si and Ge was not used for SiGe alloys because of errors introduced into the measurement by the etching of the underlying Si. Instead, the etch rates for SiGe alloys have been obtained by simply dividing the measured layer thickness by the endpoint time. The errors in the SiGe alloy layer thickness measurements are $\approx \pm$ 5 %, and the errors in the endpoint time are $\approx \pm$ 4 % resulting in overall calculation errors of $\approx \pm$ 7 %. We now discuss some other factors which affect the etch rates measured in this way.

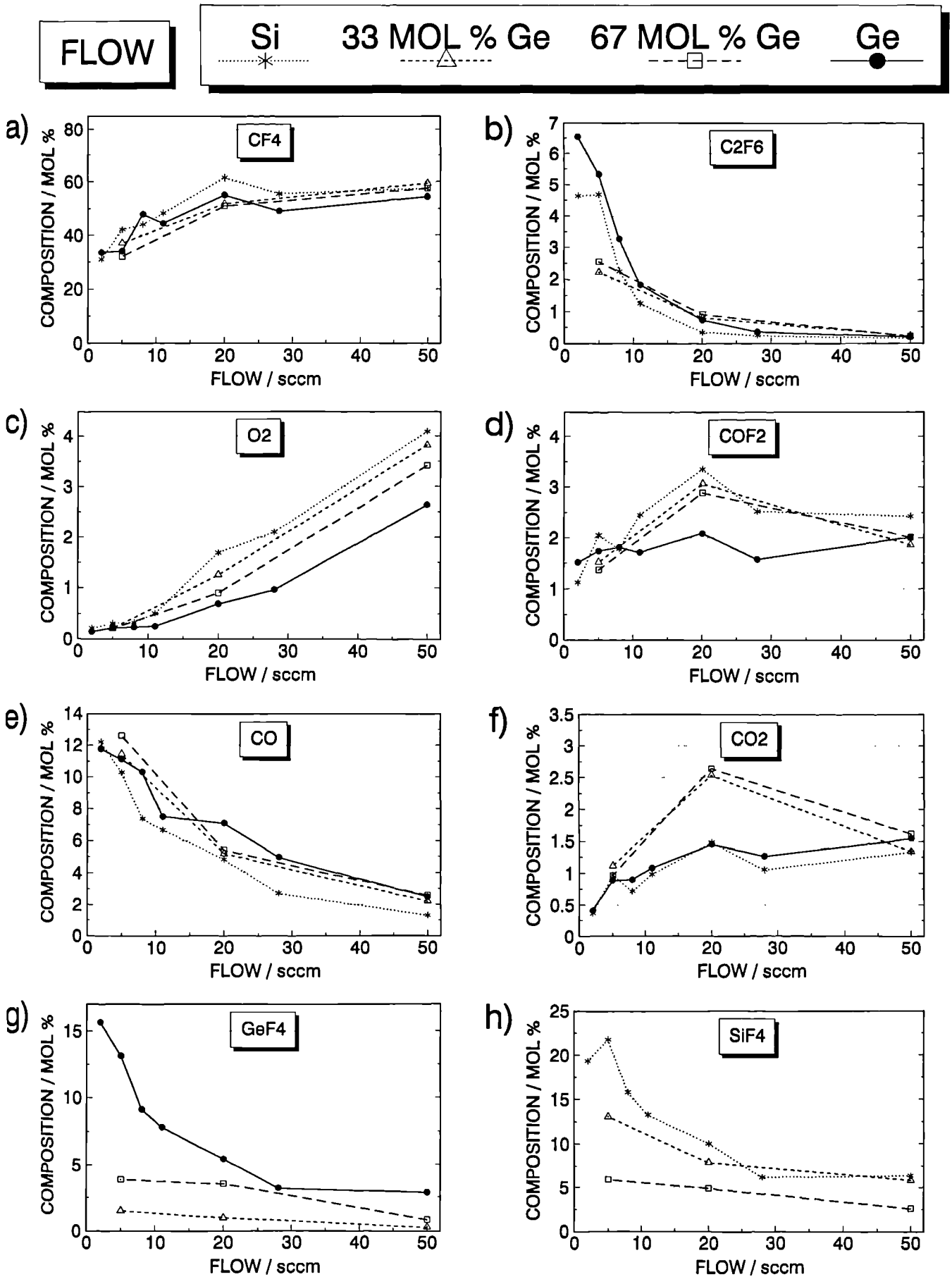

Figure 7.15. Graphs showing species concentrations measured by QMS during the etching of SiGe alloy layers with 33 mol % and 67 mol % Ge content on Si using CF_4 + 8 vol % O_2 process gas as a function of flow rate, with constant power and pressure (100 W and 85 mTorr). Also shown are species concentrations over pure Si and pure Ge taken from figure 5.7, for comparison.

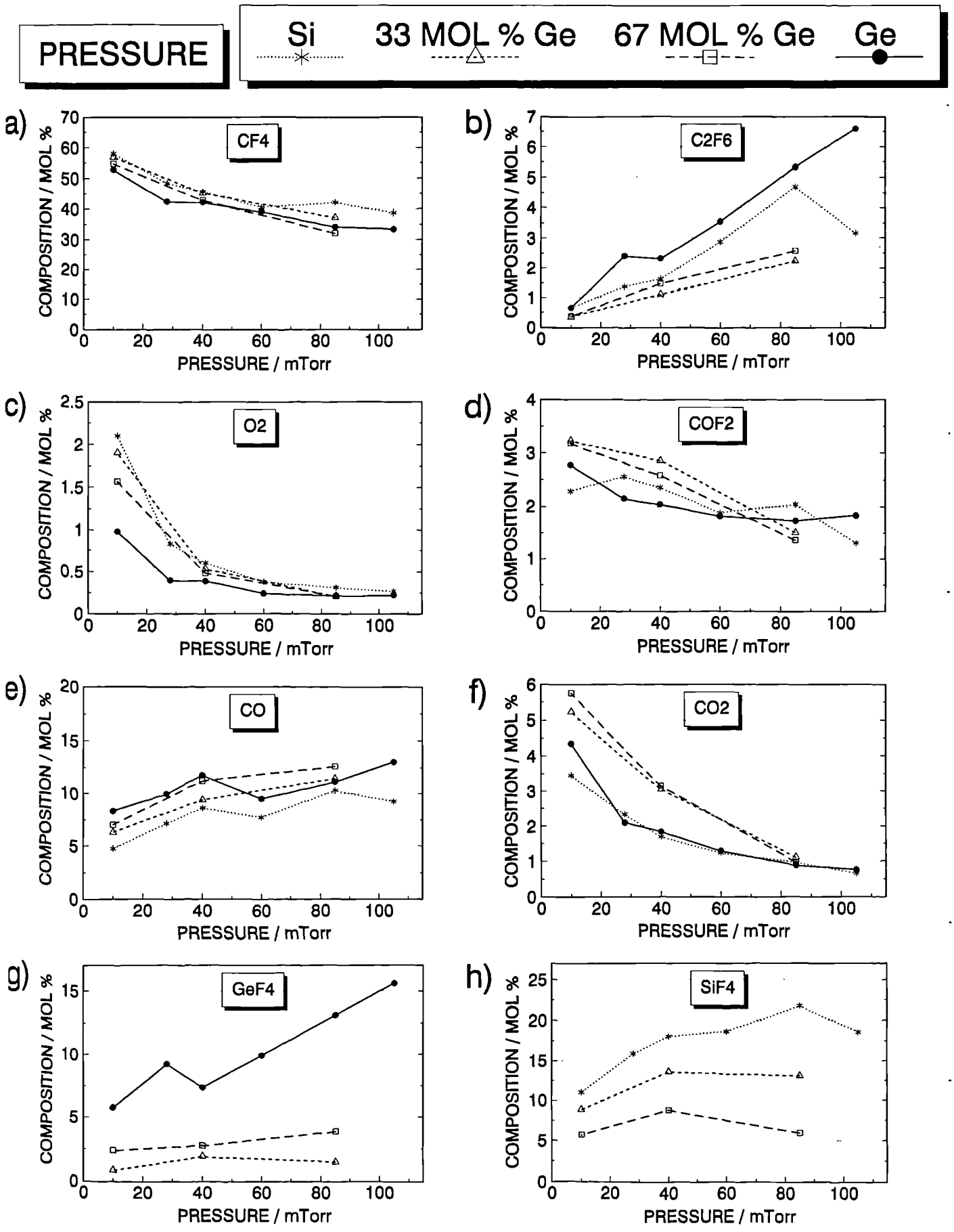

Figure 7.16. Graphs showing species concentrations measured by QMS during the etching of SiGe alloy layers with 33 mol % and 67 mol % Ge content on Si using CF_4 + 8 vol % O_2 process gas as a function of pressure, with constant flow rate and power (5 sccm and 100 W). Also shown are species concentrations over pure Si and pure Ge taken from figure 5.8, for comparison.

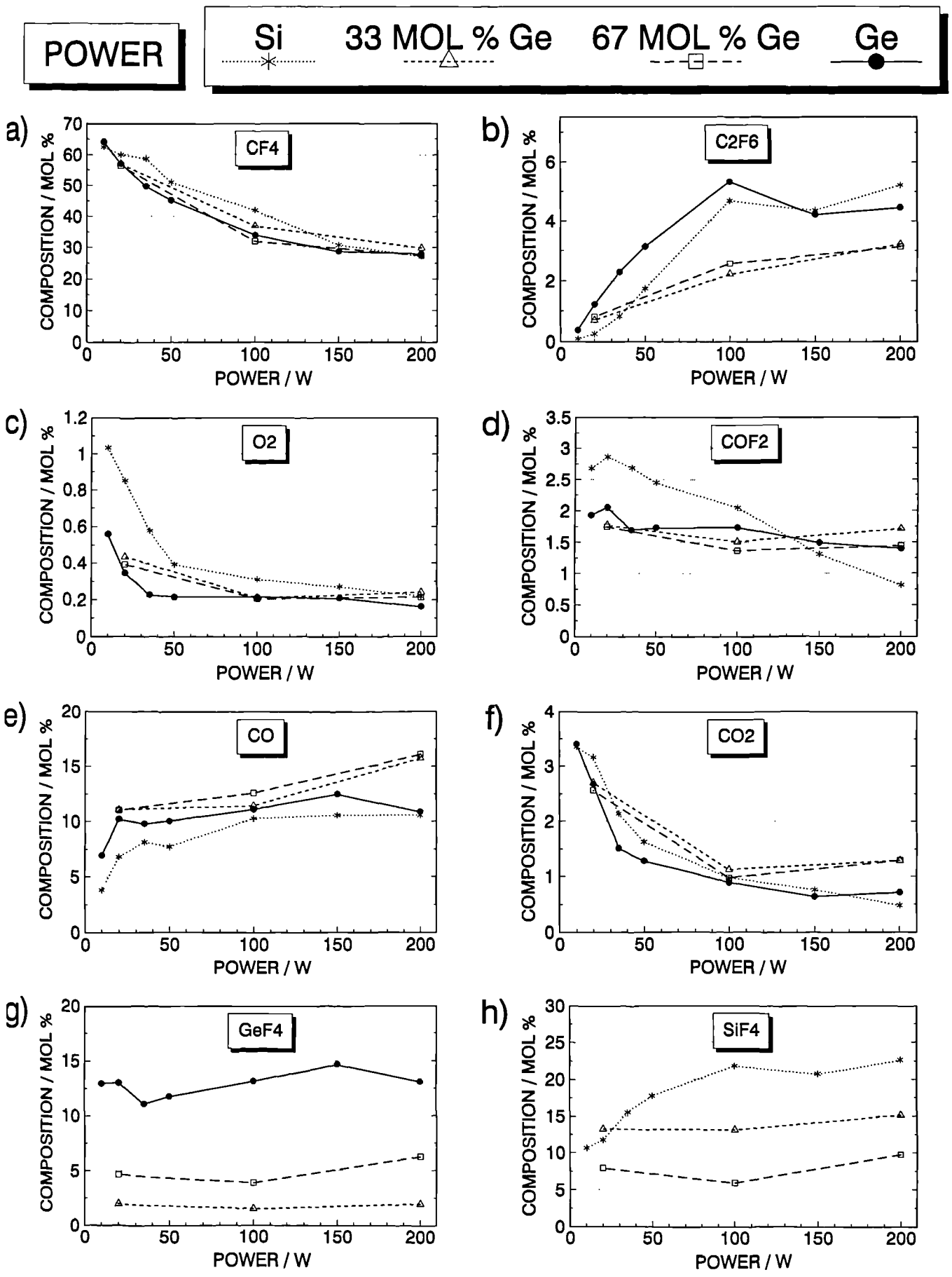

Figure 7.17. Graphs showing species concentrations measured by QMS during the etching of SiGe alloy layers with 33 mol % and 67 mol % Ge content on Si using CF_4 + 8 vol % O_2 process gas as a function of power, with constant flow rate and pressure (5 sccm and 100 W). Also shown are species concentrations over pure Si and pure Ge taken from figure 5.11, for comparison.

We mentioned in section 7.2 earlier that the effect of water is to reduce the etch rate of Si. It appears that this is also the case for SiGe etching. This is indicated by the behaviour of [SiF_4] when the plasma is switched on, where [SiF_4] rises rapidly to a value typically $\approx$ 80 % of the steady state value but then takes a few minutes to rise to the steady state value as the weathering process proceeds and the water is removed (see figures 7.1 to 7.14). This will cause the calculated etch rates for SiGe to be too low by a factor which is estimated to be up to $\approx$ 5 %. (Note that the slow rise of [GeF_4] observed in these figures is due mainly to adsorption of Ge-containing species initially at the walls, as discussed in section 5.2.3.1).

Another factor which affects the etch rate calculations is as follows. We require the average etch rate, which was measured by the method of weight loss for Si and Ge etching, because we wish to compare our SiGe alloy etch rate results with the earlier pure Si and pure Ge results. However, the poor etch uniformity means that the SiGe alloy material is etched at different rates at different points on the wafer surface. Clearly the calculated etch rates of SiGe alloy will depend on how we have defined the endpoint time (section 7.4.1). The results may therefore be subject to a systematic error, but this is not expected to exceed $\approx$ 10 %.

The etch rate results are presented in figures 7.18a, c and e, along with the etch rates for pure Si and pure Ge taken from figure 5.1 in section 5.2.1 for comparison. The etch rates of SiGe alloy with 67 mol % Ge content are always faster than the etch rates of the 33 mol % Ge layers, as expected. In order to assess whether or not the SiGe alloy shows novel etching behaviour, we have calculated the % deviation of the SiGe alloy etch rates from those expected from a simple mixture of Si and Ge. This analysis has revealed that the SiGe alloy etch rates are always within $\approx$ 10 % of the expected values except in the following cases.

1) The etch rate of SiGe alloy with 33 mol % Ge content at conditions of high flow rate (50 sccm, 100 W and 85 mTorr) etches at a rate which is 18 % faster than expected. However, we note that the SiGe alloy layer used for that experiment was

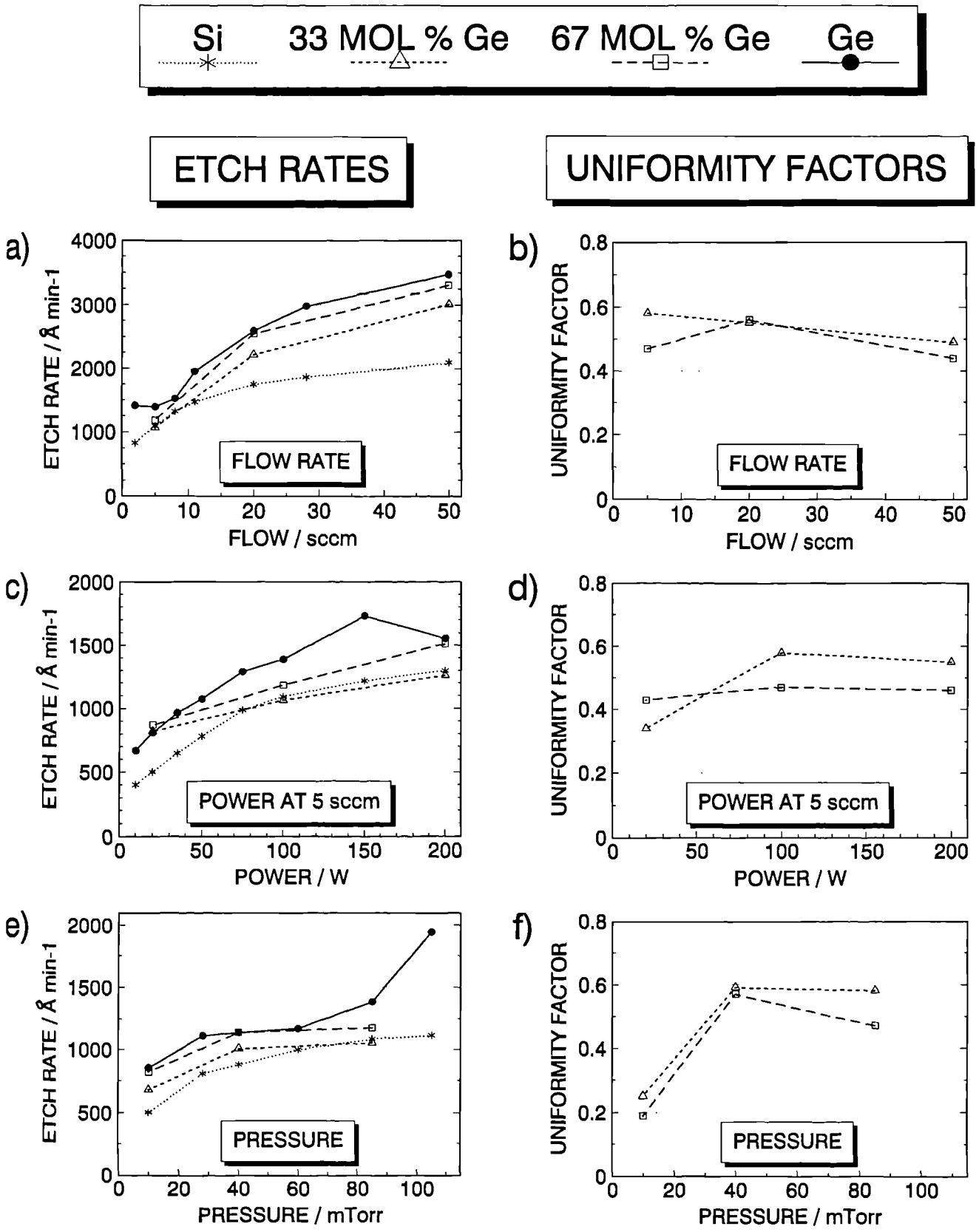

Figure 7.18. Graphs showing etch rates (a, c and e) and uniformity factors (b, d and f) for the etching of SiGe alloy layers with 33 mol % and 67 mol % Ge content on Si using CF_4 + 8 vol % O_2 process gas as a function of flow rate (at 100 W and 85 mTorr), pressure (at 5 sccm and 100 W) and power (at 5 sccm and 85 mTorr). Also shown in a, c and d are etch rates for pure Si and pure Ge taken from figure 5.1, for comparison.

3.1 μm thick compared with typically 2.2 μm thick in all other cases. The thicker layer will spend proportionately more of the etch time before the onset of the endpoint, than it will between the onset of the endpoint and the endpoint time where the etch rate reduces as the slower etching Si is exposed. In addition, proportionately less time is spent at reduced etch rates while water is initially removed from the system. Both these factors would tend to increase the calculated etch rate, as observed. We conclude that the apparently fast etch rate of SiGe alloy with 33 mol % Ge at 50 sccm is not evidence for novel etching behaviour, especially since the SiGe alloy with 67 mol % Ge content (2.25 μm thick) exhibited the expected etching behaviour within the 10 % experimental error when etched under the same conditions.

2) The etch rates of SiGe alloy at conditions of low power (5 sccm, 20 W and 85 mTorr) for 33 mol % and 67 mol % Ge material are 37 % and 25 % higher than expected respectively. This is significantly outside the 10 % error range within which the remaining data fall (except case 1 above). It appears that SiGe alloy material shows novel etching behaviour at conditions of low power. Interestingly, the effect appears to be stronger for the lower Ge content of 33 mol %. This novel behaviour is also confirmed later by the OES results and the QMS results, and will be discussed in section 7.6.

In summary, the etch rate results indicate that SiGe alloy shows the expected etching behaviour except at conditions of low power, where it etches significantly faster than expected. We now show that our etch rate measurements are consistent with the QMS measurements of [SiF_4].

Use of the [SiF_4] QMS measurements to check the etch rates. We showed in section 5.2.3.1 that the Si budget in the chamber is present almost exclusively as gaseous [SiF_4]. This means that [SiF_4] is proportional to the rate of evolution of Si from the etching wafer surface. It is therefore possible to calculate the etch rate of SiGe alloy material relative to

the etch rate of Si by using the [SiF_4] QMS data. The ratio of the Si etch rate to the SiGe etch rate is given by

$$\frac{\text{(Si etch rate)}}{\text{(SiGe etch rate)}} = \frac{\text{([SiF}_4\text{] over Si) x (Si atom density in SiGe)}}{\text{([SiF}_4\text{] over SiGe) x (Si atom density in Si)}} \qquad (7.1)$$

where the Si atom density in pure Si is 4.96×10^{22} atoms cm^{-3} and the Si atom density in SiGe is given by

$$\text{(Si atom density in SiGe)} = (D / m_{eff}) \text{ x (the fractional Si content in SiGe)} \qquad (7.2)$$

where D is the SiGe alloy density (3.43 g cm^{-3} for 33 mol % Ge and 4.44 g cm^{-3} for 67 mol % Ge [139]) and m_{eff} is the effective atomic mass of the SiGe alloy calculated from the atomic masses of Si and Ge and the relative proportions of each element in the SiGe alloy. Equation 7.2 yields the values given in table 7.2 below.

Ge content in SiGe alloy	Si atom density / 10^{22} atoms cm^{-3}
66 mol %	1.58
33 mol %	3.24
0 mol %	4.96

Table 7.2. The Si atom density in SiGe alloys, calculated using equation 7.2.

Using equation 7.1, we can calculate the ratio of the etch rate of Si to the etch rate of SiGe alloy from the [SiF_4] QMS data of figures 7.1 to 7.14. A comparison of this ratio calculated using [SiF_4] with that calculated using the etch rate data of figures 7.18a, c and e shows that the resultant values are equal within $\approx$ 15 % in all cases. This consistency indicates that both the etch rate measurements and the QMS results are reliable.

The uniformity results. The level of uniformity is indicated by the sharpness of the changes in $[SiF_4]$ and $[GeF_4]$ at the endpoint. It may be characterised by the uniformity factor, which we define as

$$\text{uniformity factor} = \frac{t_{cleared} - t_{onset}}{t_{endpoint}} \qquad (7.3)$$

where t_{onset} is the time at which $[SiF_4]$ and $[GeF_4]$ begin to change as the underlying Si is first exposed, $t_{cleared}$ is the time at which $[SiF_4]$ and $[GeF_4]$ level out when the SiGe alloy layer is completely removed and $t_{endpoint}$ is the endpoint time (all determined from figures 7.1 to 7.14). The uniformity factor results calculated using equation 7.3 are presented in figures 7.18b, d and f. Clearly a value of 0 indicates perfect uniformity; values of up to 0.6, as obtained in figures 7.18b, d and f indicate rather poor uniformity. The best uniformity is obtained at 10 mTorr (figure 7.18f). This may be understood as follows. At lower pressures, the relative chemical component of the etching is greatly reduced while the relative physical component is increased due to fewer ion collisions in the sheath. Physical etching effects are less likely to have a spatial dependence than chemical etching effects, hence the observed improved uniformity.

7.4.3 THE OES RESULTS

Using OES, the F atom emission intensity at 6856 Å, which indicates [F] (section 6.3.1), was measured whilst etching the SiGe alloy layer. These results, expressed as intensity ratios I (NW / Wafer) are presented in figure 7.19, along with data for pure Si and Ge from figures 5.5a, b and e in section 5.2.2. The errors in the intensity ratios for SiGe alloy material are greater than those for Si and Ge etching (10 % and 15 % respectively; see section 5.2.2), especially in cases where steady state etching was not achieved before the onset of the endpoint. As with the etch rate results earlier, we assess whether SiGe alloys show novel behaviour by comparing our measurements with the behaviour which is expected of a simple mixture of SiGe.

This analysis shows that in all cases, the F atom intensity ratios over SiGe alloys are within $\approx$ 20 % of the expected values, except in the case of the etching of SiGe alloy with 33 mol % Ge content at conditions of low power (5 sccm, 20 W and 85 mTorr), where the measured value is $\approx$ 40 % higher than expected. (For the etching of SiGe alloy with 67 mol % Ge content at low power, the intensity ratio was only 10 % higher than expected, and was therefore within the error limits). This provides further evidence for novel etching behaviour of SiGe alloy at low power with a stronger effect for lower Ge content, as found in the earlier etch rate results (section 7.4.2).

7.5 DISCUSSION OF THE QMS RESULTS

We now discuss the QMS results which were presented in section 7.4.1. The etch rate and OES results (sections 7.4.2 and 7.4.3) have shown that SiGe alloy in general shows no novel etching behaviour, except at conditions of low power. An examination of the QMS results provides further evidence to confirm these findings. We first discuss the results of figures 7.15 to 7.17, which show the mole percentage composition of the plasma vs changing process conditions. These results have errors which are larger than the errors of $\pm$ 20 % found in the earlier QMS results (see section 3.4) due to the problems of weathering discussed earlier in section 7.2. Nevertheless, they do allow broad conclusions to be drawn, as follows.

In the following analysis, we assume that the errors in the measured concentrations are $\approx \pm$ 30 %. From figures 7.15 to 7.17 it is clear that in most cases the composition of the plasma while etching SiGe alloy is within the range expected from the pure Si and pure Ge results, confirming the findings of the earlier etch rate and OES results. (Note that $[GeF_4]$ is lower than expected in figures 7.15 to 7.17 due to adsorption of GeF_2 at the chamber walls, as discussed in section 7.4.1). In cases where large deviations from the expected composition occur, it can be shown that these are artifacts of the weathering process by examining the temporal QMS results of figures 7.1 to 7.14 (from

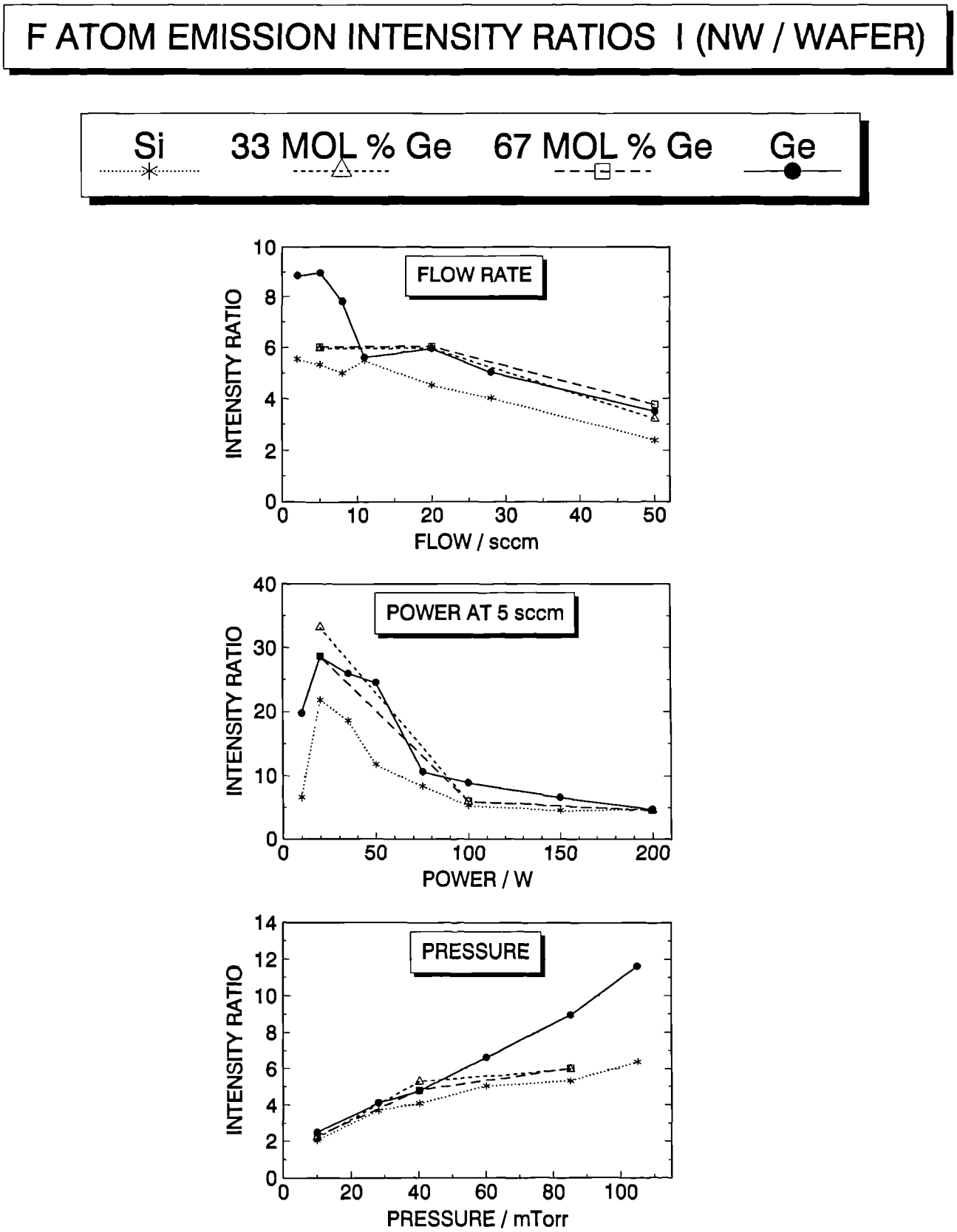

Figure 7.19. Graphs showing F atom emission intensity ratios using the 6856 Å line measured by OES during the etching of SiGe alloy layers with 33 mol % and 67 mol % Ge content on Si using CF_4 + 8 vol % O_2 process gas as a function of flow rate (at 100 W and 85 mTorr), pressure (at 5 sccm and 100 W) and power (at 5 sccm and 85 mTorr). Also shown are intensity ratios over pure Si and pure Ge taken from figure 5.5, for comparison.

which the plasma composition over the SiGe alloy was obtained for figures 7.15 to 7.17). This is best illustrated by some examples.

1) The results of figure 7.15f suggest that at 20 sccm, a large fall in $[CO_2]$ should occur at the endpoint because $[CO_2]$ is apparently much higher over SiGe than over Si. Inspection of figures 7.3b and 7.4b shows that no or very little endpoint change is observed. This is consistent with the very similar values for $[CO_2]$ obtained over pure Si and pure Ge, showing that the SiGe alloy etching is indeed behaving as expected. It is clear from figures 7.3b and 7.4b that at 20 sccm, $[CO_2]$ is still falling at the endpoint showing that the plasma had not reached the steady state (due to water contamination), explaining the high $[CO_2]$ obtained in figure 7.15f.

2) The results of figure 7.17b suggest that at 100 W, $[C_2F_6]$ should show a large rise at the endpoint because $[C_2F_6]$ is apparently much lower over SiGe than over Si. Inspection of figures 7.1c and 7.2c shows that this is not the case. Indeed, in figure 7.2c, a small fall in $[C_2F_6]$ at the endpoint is indicated by the abrupt reduction in the rise rate of $[C_2F_6]$ when the underlying Si is first exposed. This is consistent with the SiGe alloy etching behaviour which would be expected from a simple mixture of Si and Ge, because $[C_2F_6]$ is higher over Ge than over Si. Again, it is also clear that $[C_2F_6]$ is still rising at the endpoint towards the steady state value, explaining the low $[C_2F_6]$ obtained in figure 7.17b.

All the apparent deviations from the expected SiGe alloy etching behaviour observed in figures 7.15 to 7.17 can be understood in this way except in the cases of $[COF_2]$ at 200 W and $[C_2F_6]$ at 20 W. These two cases will be discussed separately later in this section.

We now take a more detailed look at the QMS results by considering more closely the changes in species concentration at the endpoint shown in the temporal QMS data (figures 7.1 to 7.14). This allows a direct comparison to be made between species concentrations over SiGe alloy and those over Si. It is also possible to predict the direction

and magnitude of the concentration changes, using the measured species concentrations over Si and Ge from figures 7.15 to 7.17. Thus novel behaviour is revealed by comparing the observed and predicted endpoint changes. We now consider some specific examples, which are interesting because the endpoint changes predicted from the Si and Ge results differ markedly when the process conditions are changed.

a) **The comparison of [CO] endpoint changes at 5 sccm and 50 sccm.** From figure 7.15e it is clear that at 5 sccm, [CO] is similar over both Si and Ge. We therefore expect little change in [CO] at the endpoint, as is indeed observed experimentally (figures 7.1a and 7.2a). At 50 sccm, however, [CO] is a factor of $\approx$ 1.9 higher over Ge than over Si. Therefore, for the etching of SiGe alloy material, we expect to observe a decrease in [CO] at the endpoint by factors of $\approx$ 1.3 and $\approx$ 1.6 for SiGe alloy with 33 mol % Ge and 67 mol % Ge content respectively. Inspection of figures 7.1a and 7.2a (5 sccm) and figures 7.5a and 7.6a (50 sccm) shows that the experimental values for these factors are $\approx$ 1.2 and $\approx$ 1.5, showing good agreement with predictions.

b) **The comparison of [O_2] endpoint changes at 10 mTorr and 85 mTorr.** From figure 7.16c it is clear that at 85 mTorr, [O_2] is similar over both Si and Ge, resulting in little change in [O_2] at the endpoint (figures 7.1b and 7.2b). At 10 mTorr, however, [O_2] is a factor of $\approx$ 2.2 lower over Ge than over Si. We therefore predict changes in [O_2] at the endpoint by factors of $\approx$ 1.4 and $\approx$ 1.8 for SiGe alloy with 33 mol % Ge and 67 mol % Ge content respectively. The experimental values from figures 7.7b and 7.8b are $\approx$ 1.3 and $\approx$ 1.7, again showing good agreement with predictions.

c) **The comparison of [O_2] endpoint changes at 20 W and 200 W.** Using similar arguments to those used for a) and b) above, we predict from figure 7.17c that at 200 W, [O_2] will increase at the endpoint by factors of just $\approx$ 1.1 and $\approx$ 1.2 for SiGe alloy with 33 mol % and 67 mol % Ge content, but at 20 W we expect

increases by factors of $\approx$ 1.5 and $\approx$ 2. The experimental values are $\approx$ 1.1 and $\approx$ 1.1 at 200 W (figures 7.13b and 7.14b), and 1.8 and 2.1 at 20 W (figures 7.11b and 7.12b), again showing agreement well within the $\pm$ 30 % errors set earlier.

The changes in species concentration which occur at the endpoint when etching SiGe alloy on Si can be predicted correctly using the Si and Ge etching data to within $\pm$ 30 % for all conditions, except in the two cases mentioned earlier, which we now discuss.

i) **[COF_2] at 200 W.** From the pure Si and pure Ge results at 200 W (figure 7.17d), a fall in [COF_2] at the endpoint is predicted, but the temporal data of figures 7.13 and 7.14 shows clearly that [COF_2] rises at the endpoint. The reason for this unexpected behaviour at high power is not clear at present. However, the behaviour of [COF_2] is the only anomaly at higher powers, and is not enough by itself to establish that novel etching behaviour is occurring.

ii) **[C_2F_6] at 20 W.** At conditions of 20 W, [C_2F_6] is a factor of $\approx$ 5 higher over Ge compared with [C_2F_6] over Si (see figure 7.17b). Therefore, for the etching of SiGe alloy material, we expect to observe an increase in [C_2F_6] at the endpoint by factors of $\approx$ 2.3 and $\approx$ 3.7 for SiGe alloy with 33 mol % Ge and 67 mol % Ge content respectively. Inspection of figures 7.11 and 7.12 shows that the experimental values for these increases are $\approx$ 4.2 and $\approx$ 5.0, which are $\approx$ 80 % and $\approx$ 40 % too high respectively. In addition, figures 7.11 and 7.12 show that [C_2F_6] is still rising at the endpoint, suggesting that the real endpoint changes are even larger. These values are well outside 30 % error limits set earlier. Recalling that the etch rate and OES data both indicated novel behaviour at 20 W, this is further evidence that SiGe alloys show novel etching behaviour at low power. In addition the deviation from the expected behaviour is greater for SiGe alloy with lower Ge content, also consistent with the earlier etch rate and OES results.

In summary, the QMS results show that within experimental error ($\approx \pm$ 30 %), the trends in the concentrations of gas phase species while etching SiGe alloy show behaviour which is consistent with a simple mixture of Si and Ge except at low power, where $[C_2F_6]$ is found to be higher than expected by $\approx$ 80 % and $\approx$ 40 % for SiGe alloy with 33 mol % and 67 mol % Ge content respectively. The deviation from the expected behaviour is greater for SiGe alloy with lower Ge content. These results are consistent with the earlier etch rate and OES results (section 7.4.2 and 7.4.3). In the following section, we discuss this novel fast etching behaviour of SiGe alloy material at low power in more detail.

7.6 THE NOVEL FAST ETCHING BEHAVIOUR OF SiGe ALLOYS AT LOW POWER

As mentioned earlier, novel fast etching behaviour has been reported by Oehrlein et al [135], [136] for SiGe alloy thin layers on Si(100) with a Ge content of up to $\approx$ 20 %. They have demonstrated that the etch rate enhancement can not be explained in terms of (a) the relative strengths of Si-Si and Si-Ge bonds (327 kJ mol^{-1} and 301 kJ mol^{-1} for Si_2 and Ge_2 [140], (b) surface modifications, for example Ge enrichment of the surface, (c) changes in the electronic properties of the film with Ge content, or (d) strain effects [135], [136]. While the details are not understood, Oehrlein et al conclude that the presence of Ge atoms significantly increases the rate of Si atom volatilisation by an (unknown) catalytic mechanism.

We also mentioned earlier that the less pronounced etch rate enhancement found for chlorine- and bromine-based chemistry found in the work of Oehrlein et al was attributed to the greater importance of ion bombardment in chlorine- and bromine-based chemistry compared with fluorine-based chemistry. They argued that an increase in the chemical reactivity of the substrate due to the replacement of Si atoms with Ge atoms will have less effect on the etch rate where ion bombardment is of greater importance [135], [136]. This suggests a reason why we have found novel fast etching behaviour at low

power only. At low power, the energy and flux of ions striking the substrate surface will be lower than at higher power. For example, Bisschops [102] has shown that the energies of ions striking the anode in an equal area electrode reactor fall by a factor around 1.6 when the power is reduced from 50 W to 20 W, while the ion flux falls by around an order of magnitude. Any effects due to changes in the chemical reactivity of the substrate are therefore more likely to be revealed at low power.

We now explain qualitatively the OES and QMS results of the present work. SiGe alloy etches faster than expected, therefore the effective F / C will be smaller than expected because more F atoms will be "trapped" as fluorides of Si and Ge. This results in both a decrease in [F] and an increase in $[CF_3]$ (section 5.4), and hence in $[C_2F_6]$, as observed. However, a decrease in [O], and hence in $[O_2]$ would also be expected but was not observed. Nevertheless, we note that $[C_2F_6] \propto [CF_3]^2$ (section 4.5.1.1), so small changes in $[CF_3]$ are enhanced through $[C_2F_6]$, whereas $[O] \propto [O_2]$ (section 4.5.3.1). Therefore, since the errors in the QMS measurements were quite large ($\approx \pm 30$ %), it is possible that a small decrease in $[O_2]$ would not be exposed.

Our results also showed that the deviation from the expected SiGe alloy behaviour is greater for SiGe with 33 mol % Ge content than with 67 mol % Ge content. Perhaps the etch rate enhancement effects caused by the addition of Ge to Si reach saturation at higher Ge content, so that novel etching effects are stronger at low Ge content.

7.7 ENDPOINT DETECTION AND PROCESS CONTROL USING QMS

Previous work in this laboratory [141] has demonstrated that the QMS technique may be used successfully to detect endpoints in a variety of different etch systems. We now discuss the use of the QMS for endpoint detection in the SiGe-on-Si system, using CF_4 + 8 vol % O_2 process gas. We then describe how the QMS monitoring technique could be used to provide not only endpoint detection, but also to provide precise process control in any RIE or plasma etching system.

For many applications, e.g. for heterojunction bipolar transistors, SiGe alloy material with a Ge content of less than around 20 % is of primary interest. In order to fabricate such devices, it is often necessary to etch through a SiGe alloy layer, stopping at the interface with the underlying Si (e.g. see reference 22). Clearly endpoint detection will prove difficult in cases of low Ge content because of the general similarity of the etch chemistry of Si and SiGe alloy.

The most obvious species which may be expected to be suitable for endpoint detection is GeF_4, because it is the only species which is present exclusively over SiGe but not over Si. However, it is possible that [GeF_4] will not be suitable for endpoint detection in device manufacture because Ge-containing species are adsorbed at the chamber walls during the etching of SiGe alloy (section 7.4.1). This effect is observed as a slow initial rise of [GeF_4] when the etching commences as the coverage of Ge-containing species at the walls increases (see figures 7.1 to 7.14). Such behaviour means that [GeF_4] will be very low during etching of SiGe alloy with low Ge content, making GeF_4 detection, and hence endpoint detection more difficult (especially for very thin layers, or if much of the wafer surface is masked by resist). In addition, under conditions of good etch uniformity, as is necessary in device manufacture, there may be a delay in the fall of [GeF_4] at the endpoint as Ge-containing species at the walls are removed as GeF_4. This would result in late detection of the endpoint, and so lead to an overetch into the underlying Si. Clearly the use of [GeF_4] as an endpoint detector would have to be checked first against an independent method of endpoint detection (e.g. with [SiF_4] as in the present work (section 7.4.1)) on a system with uniform etching properties.

It is possible that [SiF_4] may change in concentration at the endpoint by a sufficient factor to allow endpoint detection. This has been possible in all the cases studied in the present work, although, as the Ge content falls, the change in [SiF_4] at the endpoint will become smaller (especially for resist covered wafers). However, for uniform etching, the concentration changes at the endpoint will be abrupt and therefore easier to recognise. It is therefore likely that changes in [SiF_4] would provide endpoint detection.

It can be seen from the temporal QMS results (figures 7.1 to 7.14) that none of the remaining species (CF_4, O_2, CO, CO_2, COF_2 and C_2F_6) consistently gives a clear change in concentration at the endpoint under all experimental conditions. This was clearly demonstrated in section 7.5 earlier, where for example we showed that $[C_2F_6]$ shows a change at the endpoint of a factor of ≈ 4 for 33 mol % Ge SiGe alloy layers at 20 W (figure 7.11), but shows no change at the endpoint at 200 W (figure 7.13). Similarly, $[O_2]$ shows a change at the endpoint of a factor of ≈ 1.4 for 33 mol % Ge SiGe alloy layers at 10 mTorr (figure 7.7), but shows no change at the endpoint at 85 mTorr (figure 7.1). Clearly these species cannot be predicted *a priori* to be useful for endpoint detection. Nevertheless, as mentioned above, endpoints are more sharply defined for conditions of uniform etching, so it is very likely that some of these species will be suitable for endpoint detection.

It is clear from the preceding discussions that species suitable for endpoint detection must be found after the etching process has been optimised and the operating conditions decided upon. Once suitable species have been found, several species could be monitored simultaneously, providing more precise endpoint detection.

We note that the monitoring of plasma processing systems by QMS in this way could also have other advantages, namely in allowing precise process control [142]. Once the gas composition of the optimised system has been characterised by QMS, this "ideal concentration profile" could be stored in computer memory to allow a comparison to be made with profiles from subsequent etch runs. Measured deviations from the ideal profile could then be corrected for or at least minimised during the etch by making small adjustments to the process conditions. The latter may be achieved through signal feedback from the QMS to a microprocessor operating the mass flow controllers, the pressure controller, the platen temperature and the power supply. This approach can clearly be extended to any RIE or plasma etching system.

We conclude that QMS monitoring of plasma processing systems has the potential to provide not only endpoint detection, but also to provide precise process control

in any RIE or plasma etching system. It could therefore have an important role to play in the manufacture of future semiconductor devices, especially as the demands on the etching process become ever more stringent with today's novel materials and as linewidths fall to nm dimensions.

CHAPTER 8

CONCLUDING REMARKS AND FURTHER WORK

8 CONCLUDING REMARKS AND FURTHER WORK

One point which has become clear from the results of present work, is that a detailed understanding of the chemical mechanisms which are important in the plasma can only be obtained if information concerning a significant proportion of the important variables is available. These include the electron density and energy distribution, neutral species concentrations and ion densities, discharge currents and voltages as a function of time and position, gas mixture and flow geometry, as well as data concerning electron and ion kinetics, gas phase chemical kinetics, surface kinetics, and many other factors. The need for so much information is a direct consequence of the inherent complexity of the plasma system. This is illustrated by the results presented in chapter 4, where despite the large amount of species concentration data collected by QMS and OES in this work, the construction of a relatively simple kinetic model was only possible as a result of additional information provided by the Langmuir probe measurements of Welch [37], which gave the electron temperature and number density, and more importantly the LIF measurements of Hancock [46], which yielded [CF_2] and [O].

There is no "perfect" plasma diagnostic tool which will provide all the necessary information. It is therefore clear that in order to fully understand RIE and plasma etching systems, a multi-diagnostic approach is required. This would ideally include: QMS using the capillary sampling methods used in the present work, OES with a photodiode array detector (section 1.9.2) to observe excited species (especially F atoms), LIF for the measurement of radical concentrations, a Langmuir probe (section 1.9.4) for determination of the electron temperature and number density (and hence dissociation and ionisation rates), an ion energy analyser (section 1.9.7) built into the cathode to determine the energies of ions striking the wafer surface, and a surface science capability including XPS (section 1.9.5) to analyse etched samples, preferably connected to the plasma chamber in such a way as to allow the transfer of samples for surface analysis under vacuum. Once these diagnostics are attached to a single reactor, results for many process gas / substrate

systems would be obtained quite quickly. The data from all these sources could then be used to construct a model for the processes occurring in the plasma.

Clearly this represents an enormous task, both experimentally and computationally, but evidently this type of approach is required for a full and detailed understanding of plasma-based etching systems to be obtained. Otherwise it is rather like trying to make a jigsaw with only a small proportion of the pieces, and with no picture to act as a guide.

However, we have seen that it is possible to gain an understanding of small parts of the whole picture. We now outline some possible follow-up projects which have been indicated by the findings of present work.

1) A more sophisticated computer model could be developed in order to model the QMS results of chapter 4. This should be done using the gas flow rates, the pressure and the power as model inputs along with the kinetic data in chapter 4 (tables 4.2 to 4.4) to calculate species concentrations from first principles. This would be a preferable alternative to using the kinetic data and selected measured concentrations to calculate other measured concentrations as a check for model consistency, as was done in chapter 4. Although that approach did highlight many of the important reaction pathways, its predictive power is limited. Additional kinetic information concerning dissociation rates and wall reactions would also be advantageous, although such factors could be used as fitting parameters in the model. This more sophisticated model could then be extended to include the etching of wafer substrates (see also 2 below).

2) The results of the gas addition experiments (chapter 4) proved to be particularly useful in aiding the construction of the kinetic model. It is recommended that further experiments of this type be performed over a wider range of process conditions. This would further clarify the role of species in the plasma. The flow rate is a particularly useful variable because the electron density and energy

distribution are relatively constant as flow rate changes. It would also be valuable to perform experiments with additions of COF_2 to the feed gas (not possible in the present work), because dissociation of COF_2 is an important production mechanism for COF in the plasma. The level of importance of COF is difficult to ascertain, largely because, unlike CF_3, CF_2 F and O, it is not formed by direct dissociation of CF_4 or O_2 feed gas molecules; it is further along the chain of reactions. The addition of COF_2 to the feed gas would therefore allow more control over the concentration of COF.

Further, gas addition experiments should be performed with Si and Ge wafers present in order to reveal the role of some of the plasma species in etching. Of course the interpretation of all these results would be greatly aided by an improved kinetic model, such as mentioned in 1 above.

3) The kinetic model of chapter 4 indicated the importance of wall reactions in determining the plasma composition. It would therefore be interesting to perform a study of the species present on the surface of the chamber walls. This could be achieved by attaching small Al samples to chamber walls, then performing surface analysis on these samples by XPS (section 1.9.5) after running a plasma. Such a study could be performed as a function of location on the chamber walls, and also as a function of experimental plasma process conditions, especially the vol % of O_2 in the feed gas, since O atoms have been shown to be important in wall reactions.

4) Studies are currently already underway in this laboratory to shed light on the anomalous behaviour of the $3p\ ^2P$ states of F found in chapter 6. Measurements are being made of the doppler linewidths of F atom emission lines as a function of $[O_2]$ using Fabry-Perot interferometry (section 1.9.7). This will yield the temperature of the excited F atoms, and so may give further information concerning the mechanisms by which they are formed (see for example [8]).

5) We recall from chapter 6 that Hydes et al [126] found similar anomalous behaviour of the emission from the 3p ^2P excited states of F atoms to that found in the present work using a plasma etcher. However, Hydes et al found more striking anomalous behaviour in the emission from singlet, triplet and quintet excited states of F^+ during the etching of Si. It would therefore be interesting to study F^+ emission during Si etching using the present system to discover if the anomalous behaviour can be reproduced. It would then be interesting to study the F^+ emission with no wafer present as a function of feed gas composition, as was done for F in the present work. This would indicate whether the effect is caused by reactions at the wafer surface [126] or by gas phase effects, since a change in the feed gas composition would almost certainly change the concentration of all the important gas phase species in the plasma which might give rise to such an effect.

6) For further studies of the etching of SiGe alloy material, it is recommended firstly that a vacuum pumped load lock, or at least a proper N_2 glove box, be attached to the chamber in order to prevent water contamination.

The results of chapter 7 indicated that the interesting novel fast etching behaviour occurs most strongly under conditions of low ion bombardment. The Omega etcher, being an RIE reactor, is therefore not best suited to the purpose. The novel behaviour would be more likely to be revealed using either a plasma etcher operating at high pressure and low power or using an etcher in which the samples are placed downstream away from the glow. An even better approach would be to use a molecular beam system (section 1.9.7), since the level of chemical and physical etching can be controlled independently.

7) The value of the simultaneous QMS and OES approach has been clearly illustrated in the present work. This dual-diagnostic system should now be extended to other plasma-based etching systems, preferably with the addition of a photodiode array detector (section 1.9.2) to the OES system which would greatly enhance its

diagnostic power. The QMS diagnostic is especially suited to multi-component systems because it has the capability to monitor many species simultaneously. Although such systems are more complicated, in that there are more possible reactions and species which may be formed, there will almost certainly also be a number of unreactive molecules which are measurable by QMS. These are helpful for analysis because they can be used as a test for a kinetic model. In this connection, it would be advantageous to choose a system for which there is a substantial database of kinetic information available, so that important reaction pathways may be more easily determined.

REFERENCES

REFERENCES

1. P.A. Cox, *The Electronic Structure and Chemistry of Solids* (Oxford University Press, Oxford, 1987).

2. A.J. Decker, *Solid State Physics* (Macmillan, London, 1952).

3. D.J. Elliott, *Integrated Circuit Fabrication Technology* (McGraw Hill, New York, 1982).

4. I. Brodie, J.M Muray, *The Physics of Microfabrication* (Plenum Press, London, 1982).

5. J.S. Kilby; IEEE Trans. on Electron Devices **23**, 648 (1976).

6. B.E. Deal, J.M. Early; J. Electrochem. Soc., **126**, 200 (1979).

7. J. White, J. Keen; New Scientist, **1422**, 37 (1984).

8. P.W. May, Ph.D. Thesis, University of Bristol, 1991.

9. A.B. Glaser, *Integrated Circuit Engineering* (Addison-Wesley, Reading, Mass., 1977).

10. G.K. Teal, J.B. Little; Phys. Rev., **78**, 647 (1950).

11. J. Barrett, R.H. Heil Jr.; Solid State Technol., **17**, 37 (1974).

12. S.J. Moss, A. Ledwith, eds., *The Chemistry of the Semiconductor Industry* (Blackie, Chapman and Hall, New York, 1987).

13. R.V. Stuart, *Vacuum Technology, Thin Films and Sputtering, an Introduction* (Academic Press, London, 1983).

14. A.Y. Cho; J. Vac. Sci. Technol., **16**, 275 (1979).

15. J.C. Bean, L.C. Feldman, A.T. Fiory, S. Nakahara, I.K. Robinson; J. Vac. Sci. Technol., **A2**, 436 (1984).

16. Edinburgh Microfabrication Facility, Dept. Electrical Engineering, University of Edinburgh, Vacation school notes (March 1981).

17. N.G. Einspruch, D.M. Brown, eds., *VLSI Electronics and Microstructure*, Vol 8 (Academic Press, London, 1984).

18 R. People; IEEE J. Quantum Electronics, QE-22, 1696 (1988).

19. C.G. Tuppen, C.J. Gibbings, M. Hockly; J. Crystal Growth, **94**, 392 (1989).

20. D.V. Lang, R. People, J.C. Bean, A.M. Sergent; Appl. Phys. Lett., **47**, 1333 (1985).

21. H.L. Störmer, R. Dingles, A.C. Cossard, W. Wiegman, M.D. Sturge; Solid State Commun., **29**, 705 (1979).

22. G.L. Patton, J.H. Comfort, B.S. Meyerson, E.F. Crabbé, G.S. Scilla, E. de Frésart, J.M.C. Stork, J.Y.C. Sun, D.L. Harame, J.N. Berghartz; *IEEE Electron* Dev. Lett., **11**, 171 (1990).

23. J. Senior, New Scientist; **1458,** 31 (1985).

24. G.M.W. Kroesen, G.S. Oehrlein, E. De Frésart, G.J. Scilla, Appl. Phys. Lett.; **60**, 1351 (1992).

25. M.A. Gell; Physical Review B, **38**, 7535 (1988).

26. R.A. Heinecke; Solid State Elect., **18**, 1146 (1975).

27. P. Singer; Semiconductor International, **8**, 52 (1992).

28. B.N. Chapman, *Glow Discharge Processes* (J. Wiley and Sons, New York, 1980).

29. M.D. Gill; Vacuum, **34**, 357 (1984).

30. M.J. Druvestyn, F.M. Penning; Rev. Mod. Phys., **12**, 88 (1940).

31. Y.P. Song, D. Field, D.F. Klemperer; J. Phys. D: Appl. Phys., **23**, 673 (1990).

32. H.V. Boenig, *Fundamentals of Plasma Chemistry* (Technomic, Lancaster, Penn., 1988).

33. E.W. McDaniel, *Collisional Phenomena in Ionised Gases* (J. Wiley and Sons Inc., London, 1984).

34. J.H. Noggle, *Physical chemistry* (Scott, Foremason and Company, London, 1989, 2nd edn.).

35. C.E. Moore, *Atomic Energy Levels* (Nat. Stand. Data Ser., Nat. Bur. Stand. (US), 35/Vol 1, 1971).

36. Christopherou, ed., *Electron-Molecule Interactions and their Applications*, Vol 1, (Academic Press, London, 1984).

37. C.C. Welch, M.Sc. Thesis, Thames Polytechnic, London, 1987.

38. M.J. Vasile; J. Appl. Phys., **51**, 2503 (1980).

39. E.W. McDaniel, V. Cermák, A. Dalgarno, E.E. Ferguson, L. Friedman, *Ion-Molecule Reactions* (Wiley-Intercience, London, 1970).

40. P.W. May, D. Field, D.F. Klemperer; J. Appl. Phys., **17**, 3721 (1992).

41. J. Troe; J. Chem. Phys., **66**, 4758 (1977).

42. I.C. Plumb, K.R. Ryan; Plasma Chem. Plasma Proc., **6**, 205 (86).

43. K.R. Ryan, I.C. Plumb; Critical Reviews in Solid State Materials Science, **15**, 153 (1988).

44. G.A. Somorjai, *Principles of Surface Chemistry* (Prentice-Hall, Englewood Cliffs, N.J., 1972).

45. J.C. Greaves, J.W. Linnett; Trans. Faraday Soc., **54**, 1323 (1958).

46. G. Hancock; Proceedings of the Conference on Plasma and Ion Surface Engineering (Toulouse, June 1991, unpublished work).

47. L.E. Kline, M.J. Kuschner; Critical Reviews in Solid State Materials Science, **16**, 1 (1989).

48. D. Rapp, P. Englander-Golden; J. Chem. Phys., **43**, 1464 (1985).

49. N.P. Johnson, A.P. Webb, D.J. Fabian; Mat. Res. Soc. Symp. Proc., **30** (1984).

50. J.W. Coburn; Rev. Sci. Inst., **41**, 1219 (1970).

51. J.W. Coburn, E. Kay; Solid State Technol., **22**, 117 (1979).

52. C.I.M. Beenakker, R.P.J. Van de Poll; Proc. 4th Int. Symp. Plasma Chem., 125 (1979).

53. A.J. Hydes, Ph.D. Thesis, University of Bristol, 1985.

54. D.J. Thomas, Ph.D. Thesis, University of Bristol, 1989.

55. P.E. Clarke, D. Field, A.J. Hydes, D.F. Klemperer, M.J. Seakins; J. Vac. Sci. Technol., **B3**, 1614 (1985).

56. W.R. Harshbarger, R.A. Porter, T.A. Miller, P.Norton; Applied Spectrosc., **31**, 201 (1977).

57. R. d'Agostino, F. Cramarossa, S. De Benedictus, G. Ferraro; J. Appl. Phys., **52**, 1259 (1981).

58. D. Field, A.J. Hydes, D.F. Klemperer; Vacuum, **34**, 563 (1984).

59. S.M. Morley, Ph.D. Thesis, University of Bristol, 1991.

60. P.E. Clarke, Ph.D. Thesis, University of Bristol, 1988.

61. B.J. Curtis, H.J. Brunner; J. Electrochem. Soc., **125**, 829 (1978).

62. I.T. Wade, Ph.D. Thesis, University of Bristol, 1989.

63. J.W. Coburn, M. Chen; J. Appl. Phys., **51**, 3134 (1980).

64. J.W. Coburn, M. Chen; J. Vac. Sci. Technol., **18**, 353 (1981).

65. C.J. Mogab, A.C. Adams, D.L. Flamm; J. Appl. Phys., **49**, 3796 (1978).

66. V.M. Donnelly, D.L. Flamm, W.C. Dautremont-Smith, D.J. Werder; J. Appl. Phys., **55**, 242 (1984).

67. R.E. Walkup, K.L. Saenger, G.S. Selwyn; J. Chem. Phys., **84**, 2668 (1986).

68. R.A. Gottscho, V.M. Donnelly; J. Appl. Phys., **56**, 245 (1984).

69. R.A. Gottscho, G.P. Davis, R.H. Burton; J. Vac. Sci. Technol., **A1**, 622 (1982).

70. T.A. Miller; Plasma Chem. Plasma Proc., **1**, 3 (1981).

71. D. Maundrill, J. Slatter, C.C. Welch; J. Phys. D: Appl. Phys., **20**, 815 (1987).

72. M.J. Kuschner; J. Appl. Phys., **53**, 2939 (1982).

73. R.M. Clements; J. Vac. Sci. Technol., **15**, 2 (1978).

74. J.D. Swift, M.J.R. Schwar, in *Electrical Probes for Plasma Diagnostics*, (Iliffe, London, 1970).

75. G. Ertl, J Küppers, *Low Energy Electrons and Surface Chemistry* (VCH, Weinheim, 1985).

76. J.M. Walls, ed., *Methods of Surface Analysis, Techniques and Applications*, (Cambridge University Press, Cambridge, 1988).

77. O. Auciello, D.L. Flamm, eds., *Plasma Diagnostics Volume 2, Surface Analysis and Interactions* (Academic Press Inc., London, 1989).

78. G.S. Oehrlein, T.D. Bestwick, P.L. Jones, M.A. Jaso, J.L. Lindström; J. Electrochem. Soc., **138**, 1443 (1991).

79. G.S. Oehrlein, H.L. Williams; J. Appl. Phys., **62**, 622 (1987).

80. F.R. McFeely; J. Vac. Sci. Technol., **A3**, 879 (1985).

81. R. d'Agostino; J. Vac. Sci. Technol., **A3**, 2627 (1985).

82. P.W. Hawkes, *Electron Ooptics and Electron Microscopy* (Taylor and Francis, London, 1972).

83. R.M.A. Azzam, N.B. Bashara, *Ellipsometry and Polarised Light* (North Holland, Amsterdam, 1987).

84. J.W. Coburn, H.F. Winters; Surface Science Reports, **14**, 161 (1992).

85. J.W. Coburn, E.Kay; J. Appl. Phys., **43**, 4965 (1979).

86. H.H. Sawin, J. Lui, G.L. Huppert; Proc. 8th Int. Symp. Plasma Proc. (Montreal, May 1980, pub. by Electrochem. Soc.).

87. A.D. Kuypers, H.J. Hopman; J. Appl. Phys., **63**, 1894 (1988).

88. D. Field, D.F. Klemperer, P.W. May, Y.P. Song; J. Appl. Phys., **70**, 82 (1991).

89. A.C. Dickenson, D. Field, D.F. Klemperer, P.C. Johnson, R.A. Pitts; submitted to 3rd Int. Symp. on Process Physics and Modelling in Semiconductor Technology (Honolulu, 1993).

90. Tylan Mass Flow Controller Reference Manual, Tylan (UK) Ltd., Swindon, UK.

91. M.I.T. Wavelength Tables, compiled by G. Harrison (M.I.T. Press, Cambridge, Mass., Original edn. pub. 1939 and third printing 1982).

92. M.I.T. Wavelength Tables by Element, prepared by F.M Phelps III from compilation by G. Harrison, M.I.T. Press, Cambridge, Mass. 1982.

93. A.R. Striganov, N.S. Sventitskii, *Tables of Spectral Lines of Neutral and Ionised Atoms* (I.V. Kurchatov Inst. of Atomic Energy, IFP/Plenum, New York, 1976).

94. K.K. Corvin, S.J.B. Corrigan; J. Chem. Phys., **50**, 2570 (1969).

95. SPECTRALAB PC User Manual, V.G. Quadrupoles, Cheshire, UK.

96. A.P. Day, M.Sc. Thesis, University of Bristol, 1988.

97. R.W. Kiser, *Introduction to Mass Spectrometry and its Applications* (Prentice-Hall Inc., Englewood Cliffs, N.J., 1965).

98. S. Dushman, *Scientific Foundation of Vacuum Techniques* (Wiley and Sons Inc., London, 1962, 2nd edn.).

99. A. Cornu, R. Massot, *Compilation of Mass Spectral Data* (Heydon and Son with Presses Universitaires de France, 1986).

100. G. Smolinsky, D.L. Flamm; J. Appl. Phys., **50**, 4982 (1979).

101. H.L. Davis, Y.M. Smith; Proceedings of the 8th Australian Computer Conference, Vol. 1, Australian Computer Society Inc., 277 (1978).

102. T.H.J. Bisschops, Ph.D. Thesis, University of Eindhoven, Netherlands, 1988.

103. Ch. Steinbrüchel; J. Electrochem. Soc., **130**, 648 (1983).

104. J.P. Booth, G. Hancock, N.D. Perry; Appl. Phys. Lett., **50**, 318 (1987).

105. G. Hancock, M.J. Toogood; Appl. Phys. Lett., **60**, 35 (1992).

106. J.P. Booth; J. Appl. Phys., **70**, 611 (1991).

107. D.A. King, D.P. Woodruff, eds., *The Chemical Physics of Solid Surfaces and Heterogeneous Catalysis, Vol. 4; Fundamental Studies of Heterogeneous Catalysis* (Elsevier Scientific Publishing Co., 1982).

108. P.C. Nordine, O.E. Rosner; Faraday I, **72**, 1526 (1976).

109. P.C. Nordine, J.D. Legrange; AIAA Journal, **14**, 644 (1976).

110. C.D. Steinspring, A. Freedman; Appl. Phys. Lett., **48**, 718 (1986).

111. E. Kay in *Methods and Materials in Microelectronic Technology*, J. Bargon ed. (Plenum, New York, 1984).

112. A.A. Bright, S. Iyer, S.W. Robey, S.L. Delage; Appl. Phys. Lett., **53**, 2328 (1988).

113. D.L. Flamm, V.M. Donnelly, T.A. Mucha; J. Appl. Phys., **52**, 3633 (1981).

114. C.J. Mogab; J. Electrochem. Soc., **124**, 1262 (1977).

115. D.M. Manos, D.L. Flamm eds., *Plasma Etching, an Introduction* (Academic Press, London, 1989).

116. M.E. Jacox; J. Phys. Chem. Ref. Data, **17**, 269 (1984).

117. R.W.B. Pearse, A.G. Gaydon, *The Identification of Molecular Spectra* (Chapman and Hall, London, 1976).

118. K.F. Zmbov, J.W. Hastie, R. Hauge, J.L. Margrave; Inorganic Chem., **7**, 608 (1968).

119. N. Bartlet, K.C. Yu; Can. J. Chem., **39**, 80 (1961).

120. H. Takeo, R.F. Curl Jr., P.W. Wilson; J. Molecular Spectrosc., **38**, 464 (1971).

121. H.F. Winters, F.A. Houle; J. Appl. Phys., **54**, 1218 (1983).

122. Y.Y. Tu, T.J. Chuang, H.F. Winters; Phys. Rev., **B23**, 823 (1981).

123. D.R. Stull, H. Prophet; JANAF Thermochemical Tables, 2nd edn. (Nat. Bur. Stand., US GPO, Washington, 1971).

124. J.W. Coburn, E. Kay; Solid State Technol., **22**, 117 (1979).

125. J.W. Coburn, E. Kay; Proceedings of the 7th International Vacuum Congress and the 3rd International Conference on Solid Surfaces, Vienna, Vol II, 1257 (1977)

126. D. Field, A.J. Hydes, D.F. Klemperer; Surf. Sci., **171**, 654 (1986).

127. W.L. Wiese, M.W. Smith, B.M. Miles, *Atomic Transition Probabilities* (Nat. Bur. Stand., NSRDS, Washington D.C., 1969, Vol I).

128. R.P. Wayne, *Chemistry of Atmospheres* (Clarendon, Oxford, 1985).

129. B.A. Lengel, *Introduction to Laser Physics* (J. Wiley and Sons Inc., London, 1966).

130. M.J. Weber, ed., *CRC Handbook of Laser Science and Technology*, Volume II (CRC Press Inc., Boca Raton, Florida, 1982).

131. K.P. Huber, G. Herzberg, *Constants of Diatomic Molecules* (Van Nostrand Reinhold Company, London, 1979).

132. D.H. Katayama, R.E. Huffmann, Y. Tanaka; J. Chem. Phys., **62**, 2939 (1975).

133. R.E. Huffmann, J.C. Larabee, V.C. Baisley; J. Chem. Phys., **50**, 4594 (1967).

134. R.E. Huffmann, J.C. Larabee, Y. Tanaka; J. Chem. Phys., **46**, 2213 (1967).

135. G.S. Oehrlein, G.M.W.Kroesen, E. de Frésart, Y. Zhang, T.D. Bestwick; J. Vac. Sci. Technol., **9**, 768 (1991).

136. G.S. Oehrlein, Y. Zhang, G.M.W.Kroesen, E. de Frésart, T.D. Bestwick; Appl. Phys. Lett., **58**, 2252 (1991).

137. J. Harvell, P. Lessard; Semiconductor International, **7**, 88 (1991).

138. R.M. Robertson, M.J. Rossi, D.M. Golden; J. Vac. Sci. Technol., **A5**, 3351 (1987).

139. J.P. Dismukes, L. Ekstrom, R.J. Paff; J. Phys. Chem., **68**, 3123 (1964).

140. R.C. Weast, *Handbook of Chemistry and Physics*, 66th edn. (CRC Press, Boca Raton, Florida, 1985-6).

141. D. Field, Y.P. Song, D.F. Klemperer, A.P. Day; Vacuum, **40**, 357 (1990).

142. D. Field, A.J. Hydes, D.F. Klemperer, G. Mrotzek; in preparation.